Heterogeneous Catalytic CO_2 Hydrogenation to Value-Added C–C Coupled Products



Renzo A. Leeflang

Supervisor: Prof. Edman S.C. Tsang†

Co-supervisors: Dr. Yiyang Li and Prof. Luet Wong

St. Anne's College

University of Oxford

A thesis submitted for the degree of

Doctor of Philosophy in Inorganic Chemistry

Hilary Term 2026

Abstract

In recent years, the hydrogenation of CO_2 into fuels and chemicals has gained increasing attention as a key technology for achieving a sustainable circular carbon economy. This research focuses on heterogeneous thermocatalytic hydrogenation of CO_2 into value-added products containing carbon–carbon bonds (C–C coupled products). In recognition of the two subfields within thermocatalytic CO_2 hydrogenation research, this thesis includes research related to both approaches.

Before laying out the findings of the current research, Chapter 1 of this thesis provides general background to the research described in Chapters 3, 4 and 5. Chapter 1 starts with a discussion of the societal relevance of the research. This is followed by a general discussion of CO_2 hydrogenation catalysis including thermodynamics and orbital theory. Hereafter, more details are provided on the literature specifically relevant to the current research. This includes a separate discussion on direct and tandem CO_2 conversion. The experimental methods are described in Chapter 2. After presenting the findings in Chapter 3, 4 and 5, final conclusion and suggestions for future research are briefly laid out in Chapter 5.

Chapter 3 and 4 investigate the direct hydrogenation of CO_2 over CuZnFe catalysts promoted with alkali metals (K, Rb, Cs). Herein the aim is to elucidate the pathway through which the alkali metal (AM) promoters lead to the formation of higher alcohols and olefins at the expense of paraffins during CO_2 hydrogenation. The crucial role of surface AMs for the formation of alcohols and olefins is first addressed in terms of the catalyst structure in Chapter 3, then Chapter 4 goes into the effect of AM doping on the catalyst surface interactions and reaction mechanism of olefin and higher alcohol formation.

It is found that the AM promoters induce significant changes to catalyst structure and phase composition: enhanced Fe carburization and Cu^0 formation. Such transition metal related changes remain insufficient to account for the sharp shift in the product selectivity however. Hence, the research

aims to clarify the surface chemistry, structure and reactivity of the doped AM atoms. Chapter 4 builds on the AM chemical and structural data discussed in Chapter 3 by presenting a mechanistic study, which demonstrates that AM promotion opens a new reaction pathway involving CO insertion. This new pathway enables the co-formation of olefins and higher alcohols from CO_2. It is argued an alcohol dehydration step mechanistically links the formation of higher alcohols and olefins. Overall these two chapters highlight the unique surface structure and active catalytic role of AM dopants in the CuZnFe catalysts.

Chapter 5 presents a tandem catalytic approach to selective CO_2 hydrogenation to propane (C_3). A composite catalyst system was developed, combining a RhInMg layered double hydroxide-derived catalyst with a highly acidic H-ZSM-5 zeolite. By co-feeding an aromatic co-reactant (benzene), this tandem catalyst achieves highly selective propane (C_3) production under relatively mild conditions (250 °C). The benzene dramatically enhances C_3 formation with minimal impact on overall CO_2 conversion, by promoting the aromatic cycle of the hydrocarbon pool reaction inside the zeolite pores. Through mechanistic investigations using isotope labeling, solid-state NMR, GC-MS and TGA, it is shown that benzene acts as a transient scaffold that sequesters in situ generated methanol into substituted aromatic intermediates responsible for the downstream formation of propane, thereby steering the reaction toward C_3 while suppressing competing pathways generating $C_{1\text{-}2}$ and C_{4+} hydrocarbons.

Table of Contents

Abstract i
Table of Contents ii
Declaration vi
Acknowledgements vii
List of Abbreviations x
Chapter 1 1
Background 1
1.1. Societal Relevance 3
1.2. CO_2 Hydrogenation Catalysis 5
1.3. Direct CO_2 hydrogenation catalysis 14
1.3.1. The Effect of Alkali Metals on Cu-FeC_x based Catalysts 17
1.3.2. Reaction Mechanism of Higher Alcohol and Olefin formation 22
1.4. Tandem CO_2 hydrogenation catalysis 25
1.4.1. General Introduction to Zeolites 26
1.4.2. General Methanol Conversion Mechanism over Acidic Zeolites 33
1.4.3. Zeolite Socony Mobil (MFI) structure 35
1.4.4. Reaction mechanism of methanol to C_3 conversion over MFI 37
1.4.5. Tandem CO_2 hydrogenation using MFI 39
1.5. Thesis Outline 43

TABLE OF CONTENTS

Chapter 2 47
Methods and Theory 47
2.1. Introduction 49
2.2. Catalyst preparation and evaluation 51
2.2.1. Chemicals 51
2.2.2. Synthesis of $Cu_4Zn_3Fe_3$ (CZF) and alkali metal doped analogues 51
2.2.3. Synthesis of RhInMg LDH catalyst precursor 52
2.2.4. CO_2 hydrogenation using plug flow reactor 54
2.2.5. Catalytic reaction (batch reactor) 55
2.2.6. Control Experiments using batch reactor 56
2.2.7. Gas Chromatography (GC) (plug flow or batch reactor) 56
2.3. Material Characterization 58
2.3.1. X-Ray Diffraction (XRD) 58
2.3.2. Temperature Programmed Reduction (H_2-TPR) 58
2.3.3. X-Ray Photoelectron Spectroscopy (XPS) 59
2.3.4. X-Ray Absorption Spectroscopy (XAS) 61
2.3.5. Mössbauer Spectroscopy 63
2.3.6. Thermal-Gravimetric Analysis (TGA) 64
2.3.7. UV-VIS Spectroscopy 65
2.4. Reaction Mechanism Characterization 66
2.4.1. Temperature Programmed Desorption (TPD) Experiments 66
2.4.2. Pulse Transient Hydrogenation (PTH) Experiments 67
2.4.3. CO DRIFTS 67
2.4.4. Temperature Programmed Surface Reaction (TPSR) 68
2.4.5. In-situ DRIFTS 68
2.4.6. CO Adsorbed XAS Experiments 69
2.4.7. Solid-State Nuclear Magnetic Resonance (ssNMR) 69
2.4.8. Isotopic Labelling Experiments 70
2.4.8.1. GC-MS ^{13}C scrambling experiments 71
2.4.8.2. Solid State NMR ^{13}C scrambling experiments 73
2.4.9. GC-MS trapped species 73

Chapter 3 77
Effect of Alkali Metals on CuZnFe Catalyst Structure: 77
Carburization and Re-Oxidation 77
3.1. Introduction 79
3.2. Results 81
3.2.1. Catalysis 81
3.2.2. Characterization 88
3.2.2.1. Inductively Coupled Plasma Mass Spectrometry (ICP-MS) 90
3.2.2.2. Brunauer-Emmett-Teller (BET) 90
3.2.2.3. Hydrogen Temperature Programmed Reduction (H_2-TPR) 91
3.2.2.4. X-Ray Diffraction (XRD) 93
3.2.2.5. X-Ray Photoelectron Spectroscopy (XPS) 96
3.2.2.6. Mössbauer Spectroscopy 107
3.2.2.7. Transmission Electron Microscopy (TEM) 111
3.2.2.8. X-Ray Absorption Spectroscopy (XAS) 116
3.2.2.8.1. X-Ray Absorption Spectroscopy (XAS) (Transition metals) 118
3.2.2.8.2. X-Ray Absorption Spectroscopy (XAS) (Rubidium) 126
3.3. Conclusion 131

Chapter 4 135
Higher Alcohol and Olefin Formation: 135
Alkali Metals Open up a New Reaction Pathway 135
4.2. Results 139
4.2.1. TPD 139
4.2.2. Pulse Transient Hydrogenation experiments 142
4.2.3. In-situ DRIFTS 146
4.2.4. TPSR 152
4.2.5. CO-Adsorption 156
4.2.5.1. CO-Adsorption DRIFTS 159
4.2.5.2. CO Adsorption XAS 168
4.3. Conclusion 173

TABLE OF CONTENTS

Chapter 5 179
Leveraging Aromatics for the Enhanced Hydrogenation of CO_2 to Propane 179
5.1. Introduction 181
5.2. Results 185
5.2.1. Catalysis 185
5.2.2. Mechanism of Promotion 188
5.2.2.1. ^{13}C Scrambling and Control Experiments 189
5.2.2.2. Liquid Product Analysis 191
5.2.2.3. Trapped Products analysis by TGA, UV-VIS and GC-MS 191
5.2.2.4. ssNMR Analysis 195
5.2.2.4.1. Room Temperature Adsorption 195
5.2.2.4.2. Co-reaction of Methanol and Benzene 197
5.2.2.4.3. CO_2 hydrogenation 202
5.3. Conclusion 207

Chapter 6 211
Final Conclusions and Outlook 211

Literature 218

Appendix 242

Declaration

I confirm that all the research described in this thesis is my own work unless otherwise stated. All the materials used in this thesis from other sources have been properly cited and fully acknowledged.

Renzo A. Leeflang

Acknowledgements

This thesis represents the efforts of more than four years as a DPhil student at the university of Oxford. Throughout this time I have been the lucky recipient of much academic support, teaching and friendship at the Tsang group and beyond. Without the help of a great number of people this work would not have been possible.

Of course my greatest gratitude goes to my late supervisor and head of our research group professor Edman C.E. Tsang. Ultimately it is his trust and confidence that granted me the opportunity to complete this research. In my novity his advice, enthusiasm and kindness have been a great motivator and support. In his absence I remain dedicated to the curiosity and belief in sustainability that he presented. Thank you Edman.

I would like to thank all my scientific collaborators:

- Dr. Iulian A. Dugulan for performing the Mössbauer measurements and data fitting at the Technical University of Delft Reactor Institute (Netherlands) as well as providing his resources on the background of Mössbauer spectroscopy.
- Prof. Robert Weatherup and Dr. Peixi Cong of the Energy and Material Interfaces group within the Department of Materials at the University of Oxford (United Kingdom), for their expertise on X-ray Absorption Spectroscopy and their help in analysing and interpreting the measured XAS spectra presented in this thesis.
- Dr Lucy Costely-Wood and Prof. Peter P. Wells for their assistance in obtaining the Rb K-edge spectra during my BAG access at the B18 beamline of Diamond Light Source (United Kingdom).
- Dr Tai-Sing Wu for measuring the Cu, Zn and Fe K-edge XAS spectra at the National Synchrotron Radiation Research Center (NSRRC) (Taiwan).
- Msc. Hanjun for performing the TPD and Pulse Transient Hydrogenation at the University of Wuhan.
- Dr. Guangchao Li for hosting and assisting me at The Hong Kong Polytechnic University (PolyU) (Hong Kong) and Msc. Zixia Feng for measuring the ssNMR data obtained during my visit to PolyU.

ACKNOWLEDGEMENTS

While it would not have been possible to obtain the results presented in this thesis without the work of the mentioned scientific collaborators, I have received indispensable support from many of our current and former members of the Tsang group. For this I thank:

- Dr. Haokun Wang for our many discussions on zeolite chemistry and engineering;
- Msc. Sijie Huang for her companionship at PolyU and her help with the initial analysis of my XAS data;
- Dr. Constantine Lebedev and Dr. Xuelei Pan for our discussions on XAS and DFT, which have inspired the CO-adsorption XAS work presented in this thesis.
- Dr. Bruce Yiyang Li who has, in Edman's absence, shown himself to have an incredible ability to step-forward and take on the task of helping us see through with our research under less than ideal circumstances. He has been an inspiration to me and a bedrock for our group.
- Dr. Tugce Ayvali, who I have been extremely lucky to have had the privilege of being taught by during my first years at Oxford. Tugce has represented a cornerstone of the Tsang group for many years and she has helped me find my way at our lab more than anyone else. She has helped me with anything relating to my understanding of the literature to performing my first syntheses and experiments. Her commitment and generosity combined with my status as an experimental novice has more than once resulted in us sharing long hours trouble shooting equipment during my early time at Oxford. For all this I am thankful.
- Although we have not formally worked together on any work, I want to sincerely thank Amy Radford and Dori Szalay. They have, more than anyone else at our lab, pulled me through the hard parts that any DPhil student faces by being my true friends.

Throughout this thesis generative AI has been used to check spelling and grammar. It was also used to edit long sentences in previous drafts and to suggest connecting sentences between subsequent paragraphs in select cases.

ACKNOWLEDGEMENTS

Lastly, away from the lab and the work of the day my partner Maria has supported me through the hard parts and has been with me to celebrate the good. Thank you for helping me maintain my composure during the frustration and seeing this long way through with me. I don't see how I could have done it without you. With much love, met veel liefde, com muito amor thank you Maria.

List of Abbreviations

Abbreviation	Definition
AES	Auger Electron Spectroscopy
AM	Alkali Metal
ASF	Anderson–Schulz–Flory
BET	Brunauer–Emmett–Teller
BEP	Brønsted–Evans–Polanyi relation
BSE	Backscattered Electrons
CCE	Circular Carbon Economy
CZF	$Cu_4Zn_3Fe_3$ catalyst
DRC	Degree of Rate Control
DRIFTS	Diffuse Reflectance Infrared Fourier Transform Spectroscopy
E_a	Activation energy
EDX	Energy Dispersive X-ray Spectroscopy
EXAFS	Extended X-ray Absorption Fine Structure
FT-IR	Fourier Transform Infrared Spectroscopy
FTS	Fischer–Tropsch Synthesis
GC	Gas Chromatography
GC-MS	Gas Chromatography–Mass Spectrometry

LIST OF ABBREVIATIONS

HA / HAs	Higher alcohol(s)
HAS	Higher Alcohol Synthesis
HFF	Hyperfine Field
ICP-MS	Inductively Coupled Plasma Mass Spectrometry
IS	Isomer Shift
LCE	Linear Carbon Economy
MS	Methanol Synthesis / Mass Spectrometry
NMR	Nuclear Magnetic Resonance Spectroscopy
PTH	Pulse Transient Hydrogenation
QS	Quadrupole Splitting
RWGS	Reverse Water Gas Shift
SE	Secondary Electrons
SEM	Scanning Electron Microscopy
ssNMR	Solid-state Nuclear Magnetic Resonance
TEM	Transmission Electron Microscopy
TCD	Thermal Conductivity Detector
TGA	Thermogravimetric Analysis
TOF	Turnover Frequency
TPD	Temperature Programmed Desorption
TPR	Temperature Programmed Reduction

LIST OF ABBREVIATIONS

TPSR	Temperature Programmed Surface Reaction
TS	Transition State
UV-Vis	Ultraviolet–Visible Spectroscopy
XAFS	X-ray Absorption Fine Structure
XANES	X-ray Absorption Near–Edge Structure
XAS	X-ray Absorption Spectroscopy
XPS	X-ray Photoelectron Spectroscopy
XRD	X-ray Diffraction

Chapter 1

Background

CHAPTER 1: BACKGROUND

1.1.Societal Relevance

It is well known that man-induced climate change, caused by excessive emittance of greenhouse gases, will and is already an immense burden on society. The steep rise of atmospheric CO_2 is the prime culprit for this climate change, and it is therefore of utmost importance to address its emission. The vast increase in atmospheric CO_2 can be attributed chiefly to the immense rise in the consumption of fossil fuels by industry, transport, and in the generation of electricity. These sectors are collectively responsible for around 78.4% of global greenhouse gas emissions [1]. To create a more sustainable society, a significant decrease in greenhouse gas pollution from these sectors is needed. Hence, their dependence on fossil fuels must be curtailed. In line with this, the "*circular carbon economy"* (CCE) has been proposed to replace the current "*linear carbon economy"* (LCE). The latter is characterized by extraction, production, use and disposal. In contrast in the CCE, fixation of CO_2 and sustainably produced electricity replace non-renewable fossil-based resources [2]. In this way the increase in atmospheric CO_2 can be mitigated by recycling CO_2, using it as a carbon resource. More specifically CO_2 and green H_2 would form the foundation of such a cycle. Together these molecules can be converted into platform molecules to be used in the chemical, pharmaceutical and energy industries [2,3]. The required H_2 can be sourced by catalytically splitting water as a sustainable hydrogen feedstock, while CO_2 can be captured directly from the air [3]. Additionally, ammonia may play a role as a chemical hydrogen storage vector [4] alongside its application in agriculture [5]. Additionally, new chemical technologies may be used to directly recycle synthetic materials such as plastics [6]. The field of catalysis plays an integral part in reaching such a circular carbon-based society.

The development of highly stable, selective, and active catalysts is crucial to produce CO_2 derived platform molecules in an economically appreciable manner [3,7]. To this end, the current research focuses on heterogeneous catalytic hydrogenation of CO_2 into value-added coupled products. More specifically, this thesis details the results of three studies, which are divided into Part I (Direct CO_2 hydrogenation) and Part II (Tandem CO_2 hydrogenation). Part I explores the effect of alkali metals (AMs) on the catalytic behaviour of a CuZnFe catalyst. The crucial role of surface AMs for the formation of alcohols and olefins will first be addressed in terms of the catalyst structure in Chapter 3, then Chapter

4 will go into the effect of AM doping on the catalyst surface interactions and reaction mechanism of olefin and higher alcohol formation. Part II involves the conversion of CO_2 and H_2 into light hydrocarbons. Chapter 5 describes a method to selectively generate propane under mild batch conditions.

1.2. CO_2 Hydrogenation Catalysis

Research on CO_2 hydrogenation catalysis is a relatively young but rapidly expanding field. Current approaches can be broadly categorised into electro-, photo-, plasma- and thermocatalytic routes, each offering distinct advantages. Among these, thermocatalytic CO_2 conversion is presently the most viable for near-term industrial implementation due to its comparatively higher efficiencies in both conversion and selectivity [8,9]. For this reason, the present work focuses on thermocatalytic hydrogenation of CO_2.

The surge in interest in CO_2 conversion is reflected in publication trends: the field began to grow notably only after 2010, when fewer than 100 papers appeared annually (Figure 1) [10]. By 2019 the number of articles had ballooned to nearly 1000 [10], and continued growth is evident. Indeed, the number of articles on electrocatalytic CO_2 conversion alone exceeded 1200 by 2022 already [11], indicating the overall research output across all CO_2 conversion pathways to be considerably larger by the time of publication of this thesis.

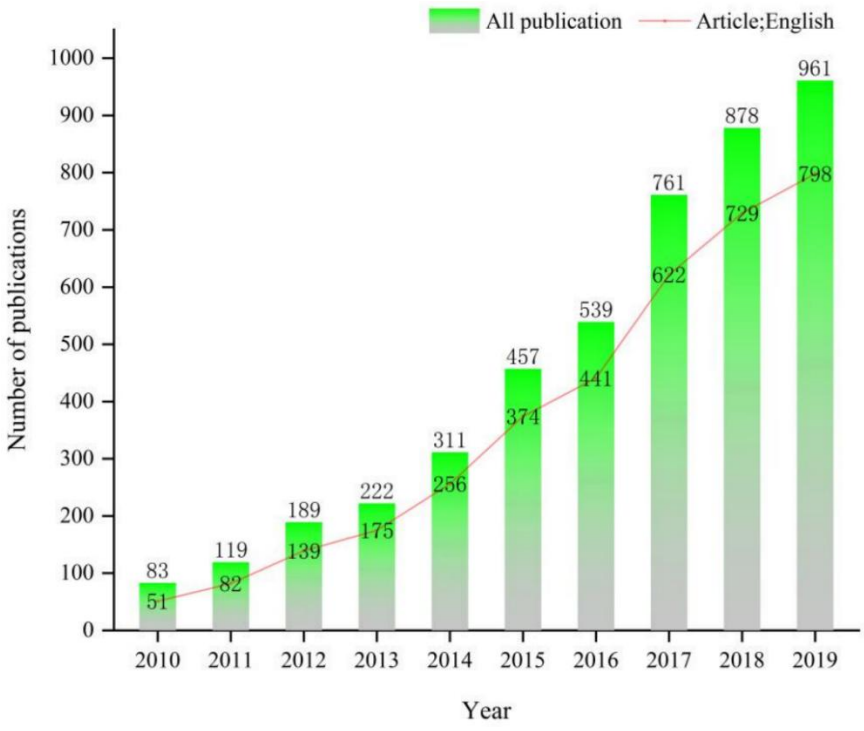

Figure 1| Annual number of publications on CO_2 conversion from 2010 to 2019. Both the total number and the articles published in English are shown. Reproduced with permission from Ref. [10].

The field of thermocatalytic CO_2 conversion can further be divided into direct hydrogenation (using a single catalyst) and tandem hydrogenation (using at least two catalysts). Both of these approaches can be used to generate valuable coupled products from reacting CO_2 with H_2. Indeed, many different single- and multi-carbon products can be generated by direct hydrogenation of CO_2. These products include methanol (H_3COH) [12–16], methane (CH_4) [17–19], carbon monoxide (CO) [19–22], higher alcohols (e.g. ethanol (H_5C_2OH)) [23–28], fuels (C_{5+}) [29,30]and olefins (C_nH_{2n}) [31–38]. Using tandem catalysis selective formation of particular hydrocarbons can be achieved, such as light paraffins [39–41] or olefins [42–45] (e.g. C_{2-4}). Furthermore, products which are entirely inaccessible to direct hydrogenation of CO_2 can be attained, namely dimethyl ether (DME, C_2H_6O) [46,47] and aromatics [48–52]. Accordingly, this thesis includes research related to both. The Chapters 3 and 4 of this thesis are dedicated to a salient topic in the direct hydrogenation of CO_2 to higher alcohols (HAs) and olefins. Chapter 5 presents a novel tandem hydrogenation method to selectively generate propane from CO_2 and H_2.

The hydrogenation of CO_2 is thermodynamically favourable particularly at low temperatures, as evidenced by the negative Gibbs free energy change of several key the reactions presented in the insert to Figure 2. Hence, the generation of any specific product is largely a kinetic challenge rather than a thermodynamic one [53]. Potentially key competing reactions are:

Higher alcohol synthesis (HAS):

$$2CO_2+6H_2 \rightarrow C_2H_5OH + 3H_2O \qquad \Delta H^0_{298k} = -173.6kJ \cdot mol^{-1} \qquad (1)$$

Methanol synthesis (MS):

$$CO_2 + 3H_2 \rightarrow CH_3OH + H_2O \qquad \Delta H^0_{298k} = -49.5kJ \cdot mol^{-1} \qquad (2)$$

Reverse water gas shift reaction (RWGS):

$$CO_2 + H_2 \rightarrow CO + H_2O \qquad \Delta H^0_{298k} = 41.2kJ \cdot mol^{-1} \qquad (3)$$

Methane synthesis :

$$CO_2 + 4H_2 \rightarrow CH_4 + 2H_2O \qquad \Delta H^0_{298k} = -252.9kJ \cdot mol^{-1} \qquad (4)$$

Alkanes formation:

$$nCO_2 + (3n+1)H_2 \rightarrow C_nH_{2n+2} + 2nH_2O \qquad (5)$$

Alkene formation:

$$nCO_2 + 3nH_2 \rightarrow C_nH_{2n} + 2nH_2O \qquad (6)$$

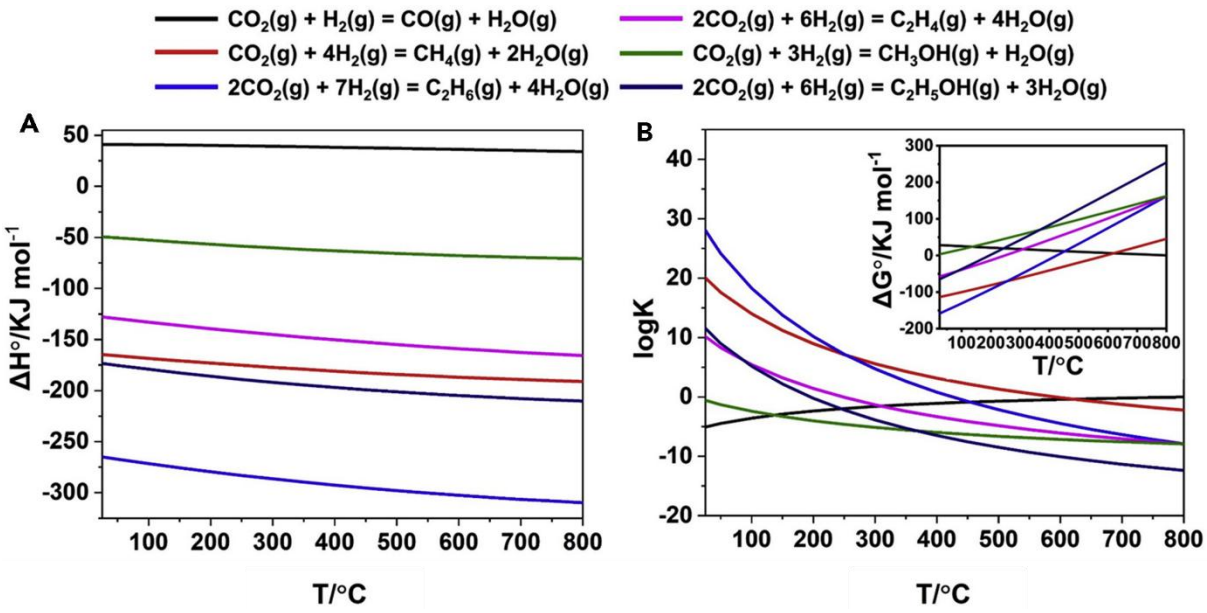

Figure 2| Thermodynamic analysis of six CO_2 hydrogenation reactions. Panel A and B show the standard enthalpy change ($\Delta H°$) and the natural logarithm of the equilibrium constant ($\log(K)$) of each reaction from 0 to 800 °C respectively. The inset in panel B indicates the standard Gibbs free energy change ($\Delta G°$). Adapted from Ref. [53] with permission from Elsevier.

The equilibrium constant (K), which is related to the standard Gibbs free energy change ($\Delta G°$), temperature (T) and gas constant (R) by the relation

$$\Delta G° = -RT\ ln(K)$$

, of the reactions is given in Figure 2B. A favourable Gibbs free energy change is reflected by positive $ln(K)$ values. Importantly, all these reactions are exothermic ($\Delta H^0_{298} < 0$) (see Figure 2| **Thermodynamic analysis of six CO_2 hydrogenation reactions.** Panel A and B show the standard enthalpy change ($\Delta H°$) and the natural logarithm of the equilibrium constant ($\log(K)$) of each reaction from 0 to 800 °C respectively. The inset in panel B indicates the standard Gibbs free energy change ($\Delta G°$). Adapted from Ref. [53] with permission A), except CO formation, which is endothermic ($\Delta H^0_{298} > 0$). Moreover, the RWGS reaction is the only reaction with a favourable standard entropy change ($\Delta S°>0$) [53,54]. Given that the ($\Delta G°$) can be written as

$$\Delta G° = \Delta H° - T\Delta S°$$

, where $\Delta H°$ and $\Delta S°$ are the standard enthalpy and entropy change respectively, the exothermic nature of RWGS reaction makes it less favourable at low temperatures (where $T\Delta S°$ is close to 0) and more favourable at high temperatures temperature where the entropy term $T\Delta S°$ becomes more prominent.

This is indicated by the decreasing $\Delta G°$ and increasing $ln(K)$ value for the RWGS reaction as the temperature increases (see Figure 2B). Conversely, the other reactions show the opposite trend: the hydrogenation of CO_2 to alcohols, or hydrocarbons becomes thermodynamically less favourable at high temperatures as suggested by the increasing $\Delta G°$ and decreasing $ln(K)$.

As a result of these thermodynamic trends, often a conversion-selectivity trade-off exists particularly for the formation of CO. This is most pertinent to the formation of methanol from CO_2, in which case CO is generally the main unwanted byproduct. Accordingly, methanol synthesis catalysts are normally operated at temperatures below 300 °C to achieve appreciable methanol yields. Besides lowering the reaction temperature, the most important way to suppress the formation of CO is the meticulous engineering of the catalyst surface. In this case the catalyst design needs to specifically focus on kinetically inhibiting the formation of CO.

Similar unwanted temperature related trends may be observed for the formation of coupled products. Here the generation of methane may be troublesome. This is due to the relatively high energy barrier for C–C coupling requiring significant energy input to overcome and therefore necessitating high temperatures. At such higher temperatures the hydrogenation to methane is strongly thermodynamically favoured compared to multi-carbon coupled products (e.g. ethane, ethylene and ethanol see Figure 2). Hence, the catalyst needs to kinetically inhibit the over-hydrogenation of CO_2 to methane. Clearly catalyst systems need to be designed appropriately to arrive at the desired products. Only by inhibiting the formation of unwanted products can the desired molecules be readily generated.

Focusing on first-row transition metals Fe, Co, Ni and Cu for the direct conversion of CO_2, a notable trend appears: the product selectivity of catalysts based on these metals depends on their d-band filling and is related to the binding strength of CO. Metals with a more filled d-band (lower d-band center relative to the Fermi level) bind CO_2 and CO less strongly. Since the d-band center lowers moving from Fe to Cu, the following trend is observed for the binding strength CO_2 on clean (100) surfaces: Fe(100) > Co(100) > Ni(100) > Cu(100) [55]. While the underlying mechanism of activation (which will be described on the next page) stays the same, depending on the system the adsorption strength over Fe, Co, Ni and Cu containing surface may change as a result of alloying [56] or isolation of single atom

binding sites [57]. For instance, the calculated adsorption strength of CO_2 on Fe, Co and Ni doped Cu surfaces shows the trend Co/Cu(100) > Fe/Cu(100) > Ni/Cu(100) > pure Cu(100) [56]. This trend is similar to the activation of CO on graphene confined single atoms of Fe, Co, Ni and Cu, in which case the binding strength follows: Co > Fe > Ni > Cu [57]. The difference between the trend observed for the clean (100) surface and the latter two mentioned systems is due to changes in the occupation of specific d-orbitals due to the chemical environment.

To understand these trends and the reason why the occupation of some particular d-orbitals may influence the binding of CO_2 and CO more than others, it is important to consider the specific orbital interactions between d-orbitals of the transition metals (see Figure 5) and the filled/unfilled molecular orbitals of CO_2 and CO during chemisorption (also see Figure 3 and Figure 4). Although CO and CO_2 binding orbital interactions are different—CO_2 chemisorption is characterized by electron transfer from filled d-states to empty anti-bonding molecular orbitals. In contrast, CO chemisorption also involves electron transfer from the CO HOMO state to empty metal d-states (σ-donation) in addition to transfer from filled metal d-states to the CO LUMO state (back-donation)—the binding strength of CO_2 and CO both depends on the ability of the TM centre to donate electron density into the antibonding states. Indeed, upon activation of CO_2 onto a metal surface a negative charge is left on the adsorbate. The magnitude of this charge correlates strongly with the CO_2 binding strength [56,58]. The electron transfer from the filled d-orbitals to CO_2 anti-bonding molecular orbitals is facilitated by bending of the linear geometry of the CO_2 molecule. This bending results in the splitting of the $1\pi_u$ (HOMO) and $2\pi_g$ (LUMO) states generating four new states, which allows for more effective charge transfer from the TM to CO_2 [58] (see Figure 5A and B). Importantly, only those TM d-orbitals with z-component ($3d_{z2}$, $3d_{xz}$ and $3d_{yz}$) have the ability to transfer electrons to unfilled molecular anti-bonding orbitals of adsorbed CO_2 or CO. Indeed, the reason why the aforementioned Co systems more strongly bind CO and CO_2 than the Fe containing analogues, is due to their relatively greater ability to transfer electron density from Co $3d_{xz}$ $3d_{yz}$ and/or $3d_{z2}$ to the CO or CO_2 adsorbates. Clearly then, the specific catalytic surface environment has clear ramifications for the catalytic behaviour.

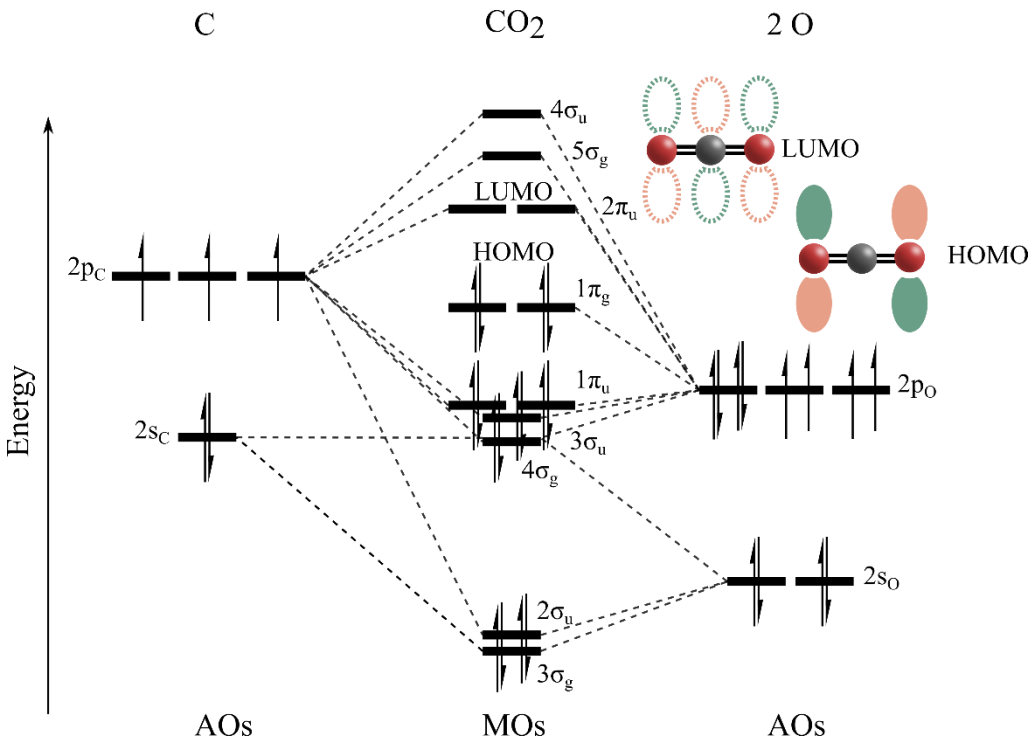

Figure 3| Molecular orbital diagram of CO_2. Based on data reported in Ref. [59]. The AO and MO levels represent the atomic and molecular orbitals respectively. The orbital shapes of the HOMO and LUMO states are indicated.

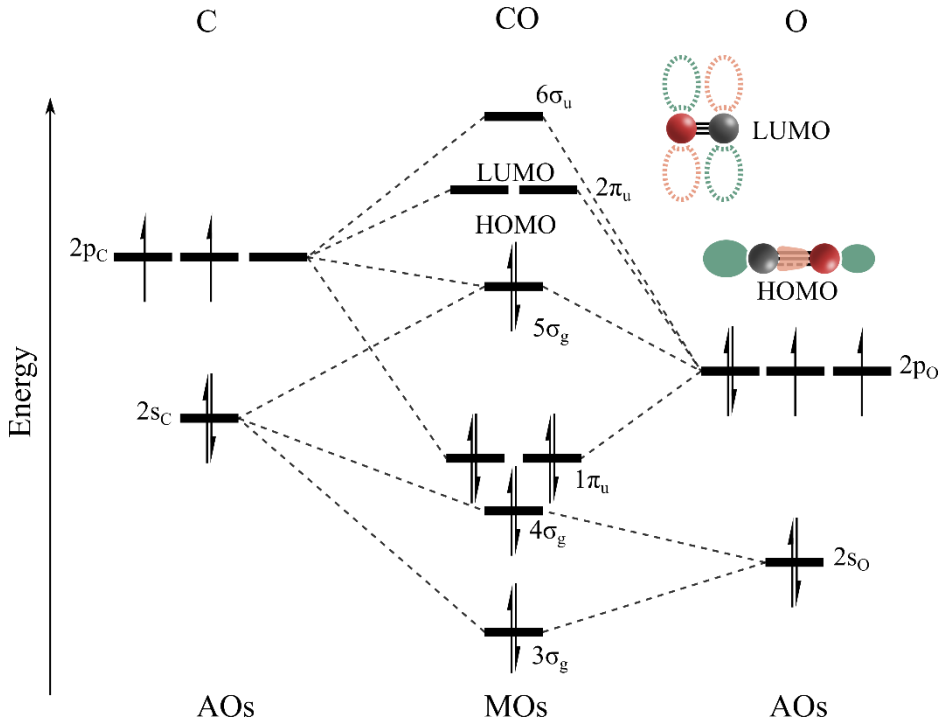

Figure 4| Molecular orbital diagram of CO. Based on data reported in Ref. [57]. The AO and MO levels represent the atomic and molecular orbitals respectively. The orbital shapes of the HOMO and LUMO states are indicated.

Nevertheless, in context of CO_2 hydrogenation catalysts, catalysts based on Co, Fe, Ni or Cu generally show consistent behaviour: the product selectivity of such catalysts can be rationalized by its ability to break both C-O bonds of CO_2 (instead of only a single C-O bond) and to perform C–C coupling. The main products of catalysts based on these metals are: CO and methanol for Cu-based catalysts (lacks C-O bond breaking); methane for Ni-based catalysts (no C–C coupling); and multi-carbon molecules (e.g. paraffins and olefins) for Co and Fe-based catalysts (CO breakage and C–C coupling). The ability of Fe and Co-based catalysts to perform scission of both C-O bonds and accomplish C-C coupling is directly related to their ability to more strongly adsorb CO and CO_2 compared to Ni and Cu.

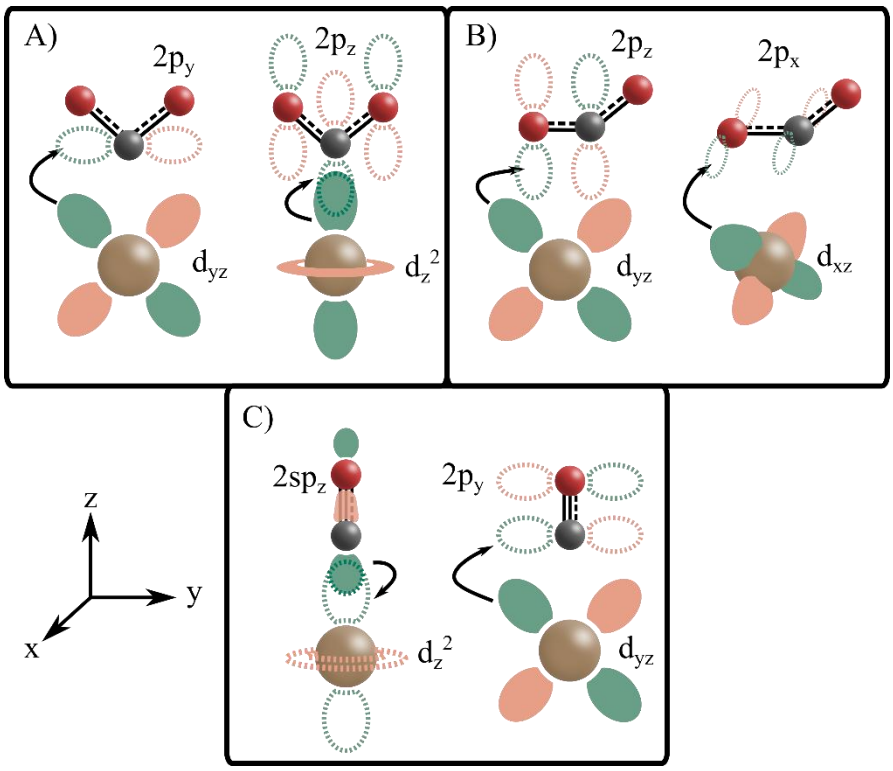

Figure 5| Schematic representation of the orbital interaction between TM d-electrons and molecular orbitals of CO and CO_2. Two modes of CO_2 activation are shown in panel A and B. Electron transfer from the filled d-orbitals (filled areas) to the empty anti-bonding orbitals (empty dotted areas) is indicated by the curved arrows. Chemisorption of CO_2 by η^1(C) linkage, and η^2(C,O) linkage are shown in panel A and B. Panel C shows the electron donation and back-donation interactions between a TM atom and CO molecular orbitals. Figure is based on information provided in Ref. [56,57].

The relative number of hydrocarbons formed with the same product carbon number is straightforwardly described by the Anderson-Schulz-Flory (ASF) distribution. Simply, the mass fraction of hydrocarbons with carbon number n (denoted M_n) depends on single variable called the growth probability (α). This gives

$$M_n = n(1-\alpha)^2\alpha^{(n-1)}$$

with

$$\alpha = \frac{r_p}{r_p + r_t}$$

, the variables r_p and r_t are the rate of chain-propagation and chain-termination respectively. The resulting product distribution is shown in Figure 6A. Under such a distribution it is impossible to generate hydrocarbons in a narrow carbon number range. For instance, the selective formation of C_2 to C_4 hydrocarbons, which are highly sought after, is not feasible. Despite this largely inevitable drawback, direct CO_2 hydrogenation remains an invaluable tool for the formation of valuable products such as olefins and higher alcohols (HAs).

Two tandem catalytic approaches have been developed, which enable the formation of hydrocarbons in more narrow range compared to direct hydrogenation, namely FTS- and methanol-mediated tandem catalytic CO_2 conversion. In both cases at least two catalysts are used including a metal(oxide) and acidic zeolite catalyst. The metal(oxide) catalyst is responsible for the initial hydrogenation of CO_2 either to methanol or an ASF-distributed hydrocarbon mixture (methanol- and FTS- mediated respectively); the acidic zeolite then converts the hydrogenated intermediate to the desired product. The final product depends on which route is chosen and the characteristics of the zeolite used. [1]

[1] An extensive discussion on the effect of zeolite characteristics can be found on pages 188–205.

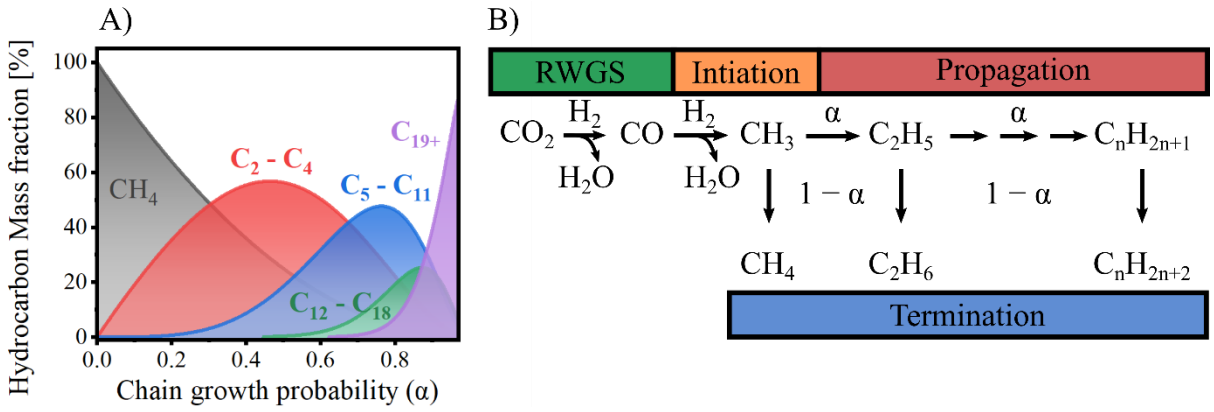

Figure 6| CO-mediated paraffin formation from CO_2. Panel A shows the theoretical hydrocarbon product distribution according to the ASF distribution. Panel B shows a generalized reaction schematic for the CO-mediated formation of paraffins from CO_2.

Direct and tandem catalytic strategies are complimentary. Their use depends on the desired reaction product and catalyst requirements. For instance, while the methanol mediated route, in principle, affords the greatest degree of control over the generated product (light paraffins [39–41] or olefins [42–45], aromatics [48–52], fuels [60] or DME [46,47]) and can nearly entirely suppress the formation of methane [61], it suffers from the same selectivity-conversion trade-off observed for direct formation of methanol: the temperature required for methanol conversion result in excessive CO formation [61]. Moreover, HAs are readily dehydrated to olefins over acidic zeolites [62]. Therefore, the use of acidic zeolites in tandem catalytic systems is inappropriate for the synthesis of HAs. Consequently, research in both direct and tandem catalytic CO2 hydrogenation is ongoing.

1.3.Direct CO_2 hydrogenation catalysis

The Chapters 3 and 4 of this thesis are dedicated to a salient topic in the field of CO_2 hydrogenation catalysis: the direct formation of olefins and higher alcohols. More specifically herein an attempt will be made to rationalize the mechanism through which alkali metals (K, Rb and Cs) enable our $Cu_4Zn_3Fe_3$ (hereafter denoted as CZF) to generate olefins and higher alcohols from CO_2 and hydrogen at the expense of the formation of paraffins.

To understand the rationale of alkali metal (AM) promotion of CuFe-based CO_2 to olefin and higher alcohols synthesis catalysts their use in Fe-based Fischer Tropsch Synthesis (FTS) catalysts should be considered. As was described earlier, the research interest in CO_2 hydrogenation catalysis is relatively new, but has been growing exponentially from the early 2010s. In contrast, a similar industrially proven reaction, namely the conversion of syngas (CO/H_2) to coupled hydrocarbons, is much older. This reaction, referred to as Fischer Tropsch Synthesis (FTS), has been researched since 1926 [63]. The industrial viability of the FTS process is evidenced by the fact that the first industrial site was opened as early as 1935 in Germany, only 9 years after its initial discovery [63,64]. During these early days the first Fischer Tropsch catalysts were based on iron (Fe) or cobalt (Co). Importantly, Fe and Co still garner the vast majority of researchers' attention both in the FTS and direct CO_2 hydrogenation. Sinisterly, these early FTS plants in part delivered the chemicals needed to drive World War II [64]. As might be expected the interest in the FTS has since mostly been driven by a combination of socioeconomic and socio political consideration [64,65]. Which were not in the least part motivated by considerations relating to the availability of oil [65]. Paradoxically, nowadays the FTS process has again garnered interest as a pivotal means to alleviate the worlds reliance on fossil fuels for reason of sustainability, not unlike CO_2 conversion research [66,67]. As a consequence of this long history there is a large body of literature on the topic of FTS catalysts. Nevertheless new research continues to be published on this topic. For the interest of this thesis the most recent literature is drawn on to understand this subject matter as it relates to Fe based hydrogenation catalysts.

One of the areas that remains elusive within the field of FTS research (and by extension CO_2 conversion) has been the beneficial effect of AMs. This is despite the fact that the promotional effect of

AMs has been reported for FTS as far back as 1956 [68,69]. It has been long known that the inclusion of alkali metals can boost the formation of olefins from syngas both by increasing the conversion of CO and by increasing the selectivity to olefins [68,69]. Additionally, AM doping was also observed to increase the chain growth probability (α). Correspondingly, AMs generally suppress methane (CH_4) formation and promote longer hydrocarbon chains [68–70].

Alongside the selective formation of olefins from syngas by AM promotion [71,72], recently much work employing AMs has focussed specifically on optimizing FTS catalyst for the formation of higher alcohols [73–76]. The fact that AMs allow for the formation of both olefins and higher alcohols rather than paraffins is incredibly useful since these are considered much more valuable coupled products. Clearly the beneficial effect of AMs has a longstanding in the scientific research.

In accordance with the reported benefits of AM doping on the conversion of syngas to olefins and higher alcohols, AMs have been reported to have a similar effect on Fe based catalysts for the hydrogenation of CO_2 (as alluded to before). Unsurprisingly, however, the exact mechanism through which AMs promote the formation of such products from CO_2 and H_2 is similarly not entirely understood. In the case of CO_2 hydrogenation often various transition metals (TMs) are used alongside Fe to achieve the desired reactivity. [37,77–80] Regarding the formation of olefins and higher alcohols such metals often include Zn and/or Cu [23,34,77,81–84]. Zn is frequently used as a structural or electronic promotor [37,77–80]. Metallic Cu on the other hand is believed to play an important role in formation of higher alcohols by facilitating CO insertion [23,34,81–83]. Furthermore, Cu additionally may promote the activation of H_2 and allow for spillover effects thereby improving the CO_2 conversion [34,82]. Chapters 3 and 4 of this thesis aim to elucidate the function of AMs and their effect on the CZF catalyst during the conversion of CO_2 and hydrogen.

To understand the promotional effect of AMs herein a two pronged approach is used: this includes a study of the catalyst properties, which focusses on AM induced changes to the TM chemical states (Chapter 3) –e.g. changes to the surface electron density, oxidation state and phase structure– and a study of the effect of AMs on the interaction between the catalyst surface and reaction intermediates.

Generally changes to the structural or electronic properties of the catalyst directly lead to changes observed in the catalytic surface interactions. It is therefore difficult to separate the contribution of AMs to their direct interaction with reactive species from their effect on the TMs contained in the catalyst. Hence the question of whether AMs simply modify the preexisting active surface or introduce an entirely new catalytic site, remains largely unaddressed in the literature.

In acknowledgement of this challenge this thesis attempts to clarify the prime source of the enhanced alcohol and olefin formation by the AM doping. To this end Chapter 3 focusses on the structural and electronic changes to our CZF catalyst upon the inclusion of K, Rb or Cs. Extensive work is presented regarding the evolution of the phase structure and the interaction between the various transition metals (TMs) and the AMs. An attempt is made to relate the reactivity of the catalysts doped with different AMs to their different surface and bulk structures. The inability to unequivocally rationalize the observed catalytic changes upon the introduction of K, Rb or Cs to differences in their structural and electronic properties leads to the need for a further investigation of the reaction mechanism. Hence, in Chapter 4 the formation of olefins and alcohols is investigated in terms of the reaction mechanism and the effect of AMs on the surface–adsorbate interactions. The combination of results presented in Chapter 3 and 4 lead us to propose a multifactorial effect of AM doping including increased carburization, enhanced reduction and direct involvement of the doped AMs with the reactive surface species.

1.3.1. The Effect of Alkali Metals on Cu-FeC_x based Catalysts

In the context of Fe-based FTS catalysts it is widely accepted that the active site is associated with iron carbide surfaces (FeC_x: Hägg carbide (χ-Fe_5C_2), pseudo-hexagonal iron carbide (ε-$Fe_{2.2}C$), hexagonal iron carbide (ε-Fe_3C), cementite (θ-Fe_3C), or Eckstrom-Adcock iron carbide (Fe_7C_3)) [85–95]. Although debate exists around which carbide phase is the most catalytically active, most often either χ-Fe_5C_2 or ε-$Fe_{2.2}C$ is claimed to display the highest activity towards syngas conversion [85–95]. In line with this, the ability of alkalis to increase CO conversion and chain growth probability has often been discussed in the context of iron carbide formation during CO conversion. Indeed, surface carburization generally increases upon the inclusion of alkali metals to Fe-based catalysts with a corresponding decrease in the formation of iron oxides [76,94,96–98]. Because the carbide surfaces provide the active sites for CO adsorption and C–C coupling an increase in carbides results in an increase in both the conversion of CO and a shift towards heavier hydrocarbons.

Considering the similarity between FTS and CO_2 hydrogenation and the salience of CO formation during the latter, it is expected that iron carbide phases play a similar role in both reactions. Therefore many publications explicitly report the degree of carburization upon catalyst modification. Increases in the formation of iron carbide phases are then frequently linked to catalyst activity and/or selectivity [23,82,94,99,100]. Nevertheless, it is unclear to what extent carburization effects can account for changes the formation of olefins and paraffins under CO_2 hydrogenation conditions. Accordingly, the research presented in Chapter 3 explicitly addresses the extent to which changes in the carburization behaviour can account for variations observed in CO_2 hydrogenation selectivity across the studied catalyst materials.

It is imperative to emphasize that iron oxides and carbides are, in principle, at some equilibrium during reaction (see Figure 7) [71,90,95,101–105]. The equilibrium constant of such reaction is affected by the reaction conditions and the catalyst material. This fact is even more pertinent for CO_2 hydrogenation than FTS, since CO_2 is strongly oxidative [101,102,105] compared to CO which is a reductant [103,106]. Hence, an increase in the presence of iron carbides can be seen as a shift of the equilibrium constant towards the carbides. Accordingly, the promotional effect may be due to either increased rate of carburization to

form carbides by deposition of carbon or a decrease in the oxidation to form iron oxides through inhibiting the retention of oxygen. On aggregate these should both result in the same observation: increased carbide phases. However, they are potentially derived from different processes and may result in differences between the bulk and surface composition.

In the case of FTS, the increase in carburization upon the addition of AMs is generally attributed to increased CO dissociative activation [69,72,94,107] at the Fe active sites alongside enhanced WGS reaction (CO oxidation) [69,107,108]. The AM induced increased dissociation of CO is related to greater CO binding at the surface as measured by CO-TPD [71,94,109]. Considering the electropositive nature of AMs it is argued that the increase in CO binding is related to electron donation from the AM to the carbide surface. The increase in the electron density may increase the back-bonding to the TM resulting in the destabilization of the C-O bond and simultaneous strengthening of the TM-C bond [110]. The increased C-O elongation (measured by red shifting of the associated IR-bands) induced by AMs has also been observed for non-Fe based materials such as Co- [111], Cu- [112], Pd [113], Pt [114] and Rh-based [115] catalysts. As such, AM promoted back-donation can be regarded as a general feature of AM doping. As a result of the strengthened M-C bond carbon is deposited on the surface at an increased rate. Together with the improved oxygen removal via WGS a higher concentration of carbon containing Fe phases is achieved at the first few layers of the catalyst. Considering these reactions take place at the surface of the catalyst, the iron carbide phase should be expected to dominate the surface, where carbon is deposited, while the bulk should remain in (partially) oxidized state.

Indeed this agrees with the structural evolution of unpromoted Fe-based FTS catalysts: the carburization of FeO_x based catalysts during FTS has been observed to result in a Fe_3O_4 @(FeC_x-Fe_3O_4) core@shell morphology [105,116]: the bulk is dominated by Fe oxides, while the surface contains a combination of Fe carbides and oxides. Increased CO activation and removal of oxygen from the surface, as observed for under AM doping, should therefore lead to even greater surface carburization. Such promotion effect ought to maintain the relatively higher oxide concentration at the bulk compared to the surface.

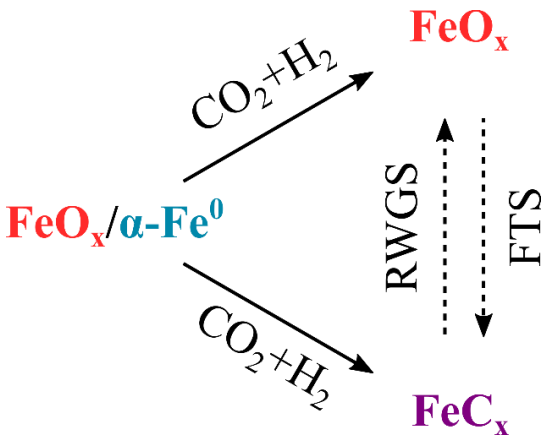

Figure 7| Schematic representation of formation and interconversion of Fe oxides and carbides during CO_2 conversion. The dotted arrows between FeO_x and FeC_x indicate the dynamic interconversion of these phases during reaction. The solid arrows show the initial rapid generation of FeC_x and FeO_x from the relatively reduced Fe phases. Figure is based on Ref. [71,90,95,101–105].

However, AM doped FTS catalysts have been reported to present a different structure altogether. In fact, upon the inclusion of AMs Fe has been observed to form a FeC_x@(FeC_x-Fe_3O_4) instead [72,117–119]. Clearly then the AMs do not only affect the surface, but cause deep carburization of the catalyst.

This AM induced deep carburization can be understood in light of the effect of AMs on the reduction of the catalyst more broadly. The result of doping various AMs (Li, Na, K, Rb and Cs) on the reduction behaviour of Fe catalyst precursors has been attributed to the mobility of oxygen between the bulk and the surface [72,119]. The rate of oxygen removal from the catalyst is greatly impacted by AMs due to their high oxophilicity. Consequently AMs increase the Fe-O binding [72,119]. The increased Fe-O binding due to the doped AMs especially inhibits the initial reduction of Fe_2O_3 to Fe_3O_4. The degree to which this initial reduction is inhibited depends strongly on the AM. Particularly Li has a strong inhibitory effect while K, Rb and Cs inhibit the conversion of Fe_2O_3 to Fe_3O_4 less strongly. Similarly the further reduction of Fe_3O_4 to FeO and α-Fe was improved by K, Rb and Cs, while it was inhibited by Li. The difference between K, Rb and Cs on the one hand and Li on the other is related to their bulk-surface distribution: Li, which has a considerably smaller radius than K, Rb and Cs, easily diffuse into the bulk of the sample, while K, Rb and Cs were largely observed at the surface. The surface presence of K, Rb, Cs enhanced the transfer of oxygen from the bulk to the surface, while bulk Li anchored oxygen under the surface [72].

The enhanced reducibility of the catalysts doped with K, Rb and Cs was directly related to the increased carburization of the catalyst [72]. This increased carburization was suggested to be the reason for the higher CO conversion observed for the K, Rb and Cs doped samples.

Similar observations have been made regarding the promotional effect of K on the formation of FeC_x under CO_2 hydrogenation rather than FTS conditions. Under such increased oxidizing environment the increase in the formation of FeC_x has been specifically related to the improved removal of oxygen in addition to increased carbon deposition [119]. By efficiently converting surface deposited oxygen to water, K stabilizes Fe_5C_2 by preventing its oxidation.

Apart from Fe carburization the oxidation state of Cu may be essential to the formation of higher alcohols and olefins. More specifically, metallic Cu has been claimed to promote CO insertion during CO_2 hydrogenation by its non-dissociative activation ability [23,34,81–83,120]. Such insertion is a necessary requirement for the formation of higher alcohols. In fact, it has previously been reported that AM doping of Cu based catalysts may lead to a suppressed Cu reducibility [20,83,121,122] . Decreased reducibility of Cu may lead to excessive oxidation of Cu and the neutralization of active sites. Such AM induced changes to the Cu oxidation state may have significant implications for the catalytic activity of the studied materials. For instance, increased reoxidation of Cu^0 has been found to retard the ability of Cs doped Cu catalysts to convert syngas to isopropanol compared to K[122]. Furthermore, recently, enhanced RWGS activity of sodium (Na) doped Cu catalysts was specifically attributed to Na induced Cu^0 reoxidation during CO_2 reduction [20]. From these examples it is clear that AM-doping may have adverse effects on the formation of Cu^0. Hence, it to build a comprehensive understanding of the effect of AM doping, such effects need to be taken into account.

It is clear that AM doping has potentially significant effects on the structure, phase composition and oxidation state of Cu-Fe based catalysts. Unfortunately, there is no comprehensive understanding of the extent to which such structural parameters can account for the beneficial effects of AMs on olefin and higher alcohol formation from CO_2 hydrogenation. Chapter 3 of this thesis will directly address this topic by attempting to relate the surface and bulk structural changes to changes in the catalytic behaviour of a Cu-Fe based catalyst doped with K, Rb or Cs.

1.3.2. Reaction Mechanism of Higher Alcohol and Olefin formation

The effect of alkali metal promoters in CO_2 hydrogenation and Fischer–Tropsch–type chemistry has been rationalised based on classical catalytic concepts such as the Sabatier principle, Brønsted–Evans–Polanyi (BEP) relations, and linear scaling relations [123–125]. According to these principles, reaction rates and selectivity are determined by the relative binding strengths of key intermediates. Hence, the enhanced conversion of CO_2 and H_2 to unsaturated products (e.g. olefins) through AM doping has described in terms of their effect on the adsorption strength of the reagents (CO_2 and H_2) and/or the products (e.g. olefins). Alkali metals are have been shown to weaken hydrogen adsorption and modify surface basicity. These changes are then often assumed to result in the suppression of the hydrogenation ability of the catalyst (its capacity to transfer hydrogen to alkyl species) generally without directly testing it. Indeed, numerous studies report that Na, K, Rb, or Cs decrease the hydrogenation ability of Fe-based catalysts, which has been correlated with enhanced olefin selectivity [28,73,80,82,126–130]. In more select cases the secondary hydrogenation ability has been studied by pulse transient hydrogenation (PTH) experiments [80,126–131]. In such cases it is found that AMs genuinely retard the catalysts ability to generate paraffins from olefins. From this perspective the formation of olefins over paraffins is not due to any fundamental change to the CH_x–CH_y surface coupling reaction, but purely the extent to which these alkyl species are hydrogenated. A schematic illustration in Figure 8 shows the reaction pathways towards olefins (green) and paraffins (red) (as well as other key products) over a Cu-FeC_x catalyst.

In contrast to olefins and paraffins, the formation of higher alcohol cannot be described purely by such a suppression of alkyl species hydrogenation. Indeed, formation of oxygenates such as alcohols requires non-dissociative CO activation and insertion steps [23,81,82,132–134], which are not trivially explained by the suppression of the hydrogenation ability. Rather, it is postulated that the formation of these oxygen containing molecules must necessarily be derived from multi-carbon surface oxygenates. Such intermediates are formed by the insertion of CO-derived surface species into alkyl chains.[2] Such

[2] Note that during thermocatalytic CO_2 hydrogenation higher alcohols are explicitly not formed by CO-CO insertion as is the case in electrocatalytic conversion of CO_2 to ethanol [337].

an insertion reaction requires dissociative and non-dissociative CO activation. In the case of Cu-FeC_x based catalysts Cu^0 provides non-dissociative sites and FeC_x provides dissociative activation of CO (leading to alkyl-species). At the interface of these sites the insertion can take place (see dark blue pathway in Figure 8).

This reading of the literature shows that there is no unified mechanistic explanation for the formation of olefins and higher alcohols, even though it is recognised that AMs may promote the formation of either during CO_2 hydrogenation. The simultaneous formation of olefins and alcohols in the current study may point toward a more fundamental, pathway-level modification induced by AMs, which is responsible for the formation of both.

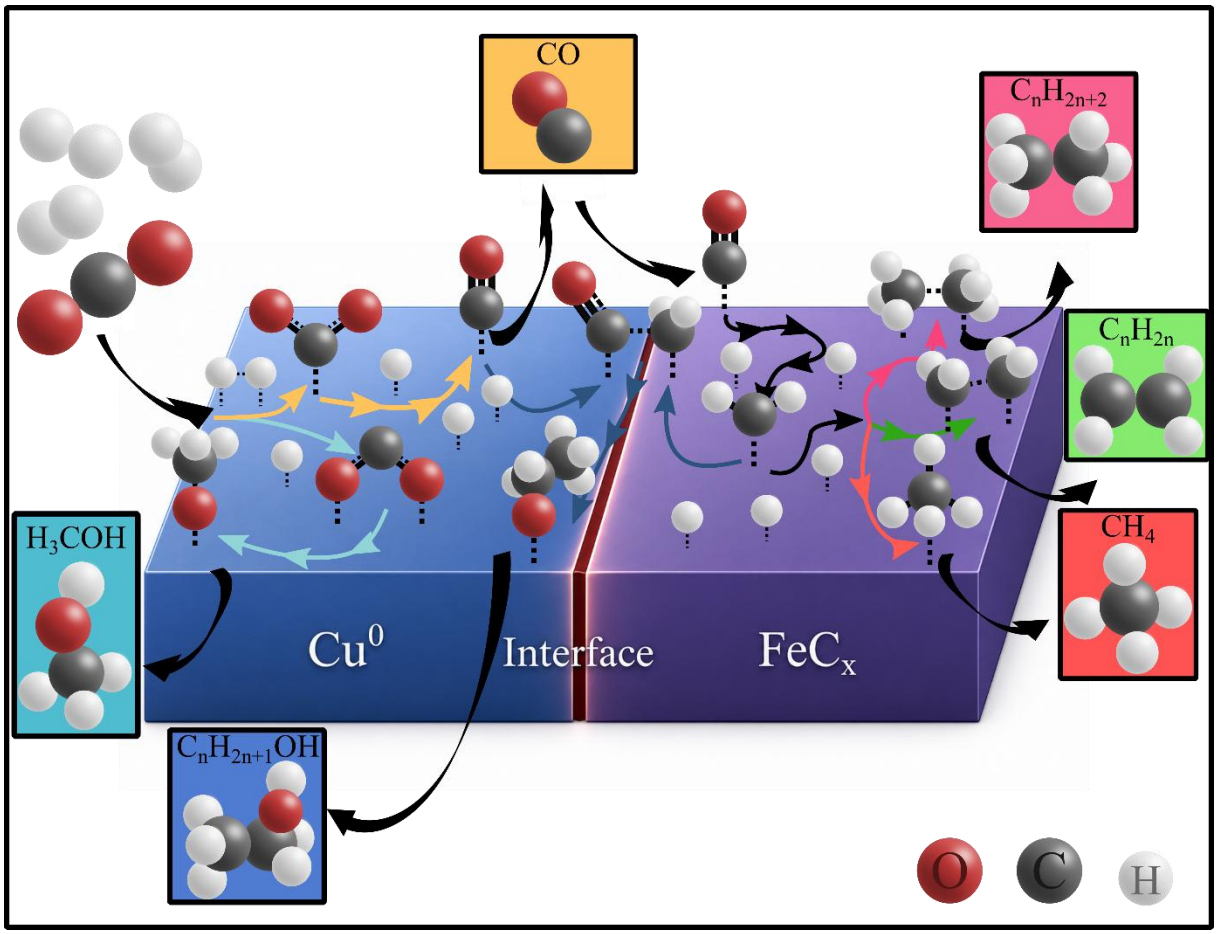

Figure 8| Schematic representation of the formation of various products from CO_2 over at the surface of a Cu^0-FeC_x based catalyst. Oxygen, carbon and hydrogen atoms are represented by red, grey and white spheres. The yellow, light blue dark blue, red, green and orange arrows indicate reaction pathways leading to, CO, methanol, higher alcohols, paraffins, olefins and methane respectively. The

figure contents is based on Ref. [23,80–82,126–135]. The graphical design was inspired by a similar scheme published in Ref. [135].

By systematically comparing undoped CZF with Cs-, Rb-, and K-promoted analogues, Chapter 4 demonstrates that alkali metals do not simply suppress hydrogenation reactions. Instead, they stabilise non-dissociative CO adsorption modes, promote carbonate–formate interconversion, and enable the formation of alkoxy intermediates that are absent on the unpromoted catalyst. These findings support the hypothesis that AMs open a distinct oxygenate-mediated reaction pathway, in which CO insertion and subsequent dehydration steps link higher alcohol and olefin formation.

In doing so, this Chapter 4 provides the mechanistic interpretation of the macroscopic selectivity trends observed during CO_2 hydrogenation. The results presented herein establish alkali metal promotion as a pathway-engineering strategy consistent with geometrical effects, rather than a simple electronic or phase structure modification, thereby offering a unified framework for understanding the enhanced formation of higher alcohols and olefins over AM-doped CZF catalysts.

1.4. Tandem CO_2 hydrogenation catalysis

As was described in Section 1.2, apart from direct CO_2 hydrogenation to form useful products, recently much work is being done in the field of tandem CO_2 hydrogenation catalysis. In such tandem schemes a metal or metal oxide catalyst is typically used to hydrogenate CO_2 to form an intermediate, which is then converted to the desired product by a zeolite catalyst. The intermediate may be either methanol, in the methanol-mediated route, or aliphatic hydrocarbons, in the FTS-mediated route. Such tandem systems can hydrogenate CO_2 into DME, aromatics, light hydrocarbons or fuels [61,136,137]. The tandem catalyst formulation gives great freedom to selectively target the particular products that are inaccessible by direct CO_2 hydrogenation [61,136,137]. The final study of this thesis describes the results of a methanol-mediated tandem catalysis system aimed at selectively forming propane from CO_2.

To introduce the Chapter 5 it is crucial to first get a deeper understanding of zeolite chemistry. To this end the literature on zeolite engineering and catalysis is laid out in the following sections. In particular, the conversion of methanol and hydrocarbons is relevant to the current research.

First, the relationship between the zeolite structure (i.e. pore structure and morphology) and the shape selective catalytic behaviour of zeolite catalysts is described in general terms. Topics that are addressed include, the catalytic function of zeolite acidity, the origin of Bronsted and Lewis acidity, the morphology of zeolites, general synthesis strategies and three types of shape selectivity.

Hereafter, the conversion of methanol over MFI (ZSM-5) zeolite specifically is discussed in detail. This discussion begins with an overview of the general reaction mechanisms of methanol conversion over zeolites, followed by a discussion of the structure of MFI. Next, the relationship between zeolite structure and the formation of light hydrocarbons from methanol is addressed. The last subsection lays out the role of ZSM-5 in tandem CO_2 hydrogenation catalysis in light of its ability to convert methanol and hydrocarbons. The differences between methanol conversion and CO_2 hydrogenation over ZSM-5 are highlighted. Moreover, the influence of the acidity on the catalytic behaviour, alongside the impact of zeolite topology is addressed. Finally, the use of MFI in the present study is rationalized.

1.4.1. General Introduction to Zeolites

Zeolites are a wide class of porous materials traditionally including only aluminosilicates [138]. Herein the term "*zeolite*" will be used slightly more loosely to refer to zeotype materials more broadly including non-aluminium containing silicates as well as silicoaluminophosphates.

Due to the unique porosity, chemistry and stability, zeolitic materials have found an incredibly wide range of applications. One such application is water treatment. This includes softening [139] , organic waste absorption [140], or even radioactive cation removal [141] . Zeolites are also used in gas separation[142] and chromatography[143], gas capture (eg. CO_2[144]) and gas cleaning (e.g. automotive exhaust fumes[145,146]). Moreover, zeolites are also used in the agricultural industry as soil conditioners [147]. Zeolites are even used in biomedical sciences in which they are used, for example, as antidiarrheal agents, antitumor adjuvants, and antibacterial agents[148]. Most relevantly, a significant portion of the zeolite market is aimed at the catalytic applications of zeolites. They are most commonly used in the petrochemical industry, in which they are used for such processes as, fluid catalytic cracking, hydrotreatment or hydrocracking, and isomerization [149,150]. The great importance of zeolites as industrial catalysts is illustrated by the fact that they are projected to constitute about a third of the refinery catalyst market in 2037 [151].

The unique catalytic behaviour of zeolites is derived from two factors: their porous structure and the tuneable acid chemistry which arises from that structure. The zeolite structure is built up of corner sharing tetrahedral units (TO_4) (see Figure 9), which combine to form a crystalline lattice with characteristic secondary structures (e.g. sodalite cages and pentasil units, see Figure 9). The interconnectivity between these secondary structures creates the complete pore structure. Critically, the openings inside the zeolite structure are at the molecular scale, typically under 2 nm wide[152]. Figure 9 shows four examples of zeolite structures containing Al, Si and O which arise from different arrangements of TO_4 units: Faujasite, which has a cage-like framework [153], as well as micro channel zeolite ZSM-12, MFI (ZSM-5 or Silicalite-1), and zeolite Theta-1 (or ZSM-22) [154]. These four structures only represent a small fraction of the 261 uniquely different zeolite structures published by the International Zeolite Association (IZA) as of August 2025 [155].

A large number of these zeolites can be synthesized by hydrothermal methods using different silica and alumina sources [156]. Importantly, however, zeolites are metastable rather than thermodynamically stable materials [157], meaning that zeolites are not the thermodynamically favoured product during their synthesis. Therefore, the synthesis of a given zeolite needs to be controlled kinetically. This is done by the use of templates that direct the crystallization of the synthesis gel. Depending on the desired framework and the specific synthesis route, a specific organic cationic template is used (called organic structure directing agents (OSDA)) [157]. Besides the template, a typical hydrothermal synthesis also requires the addition of a mineralizing agent. Which mineralizing agent is used may also affect the final zeolite [158]. These mineralizing agents, which (in part) act to compensate the positive charge of the OSDA, are usually hydroxides (e.g. NaOH or KOH [159]) or fluorides (e.g. HF [160] or NH_4F [161]). Notably, alkali metals present in the synthesis gel may also have a structure-directing role similar to the OSDAs [162,163]. By correctly choosing the hydrothermal conditions pure zeolites with the desired pore structure can be obtained.

The specific 3-dimensional pore structure is of particular importance to the diffusion of molecules into and through the zeolite structure [164]: the diffusion rate of molecules into the zeolite pores depends strongly on the size, shape and functionalities of the molecule, and zeolite pore structure [164]. For instance, the diffusion of CO_2, O_2, CH_4, N_2, and Ar is far less restricted in Faujasite (FAU) or MFI-type zeolites, in which the pore openings are substantially larger than the molecular diameters, compared to Chabazite (CHA) or DDR-type zeolites, which contain windows of a similar sizes to the molecular diameters of these gas molecules [165]. A similar effect is observed for hydrocarbons like p-xylene, which are able to diffuse into the medium size pores of ZSM-5 [166], but not into the small-window zeolite with the Chabazite structure [167]. The structure-induced variation in interactions between zeolites and different (guest) molecules is highly significant to the application of zeolites in various domains. This has been a key driver in the ongoing discovery and synthesis of an expanding array of zeolite structures.

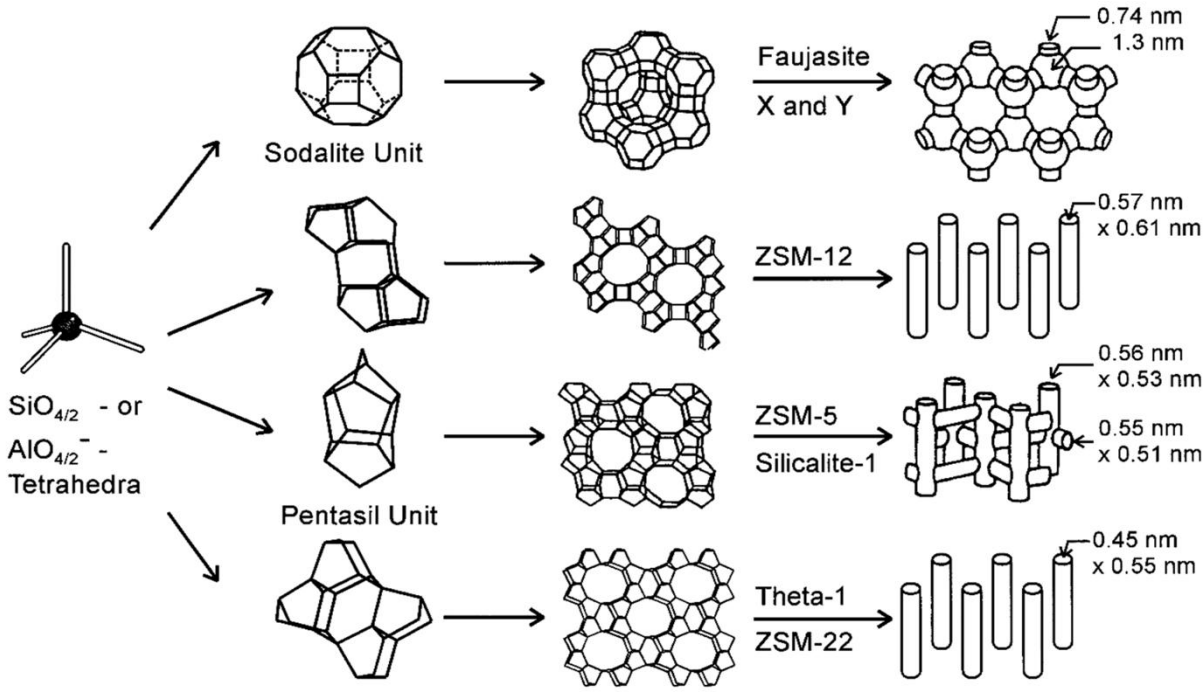

Figure 9| Four examples of zeolite structures build-up of fundamental tetrahedral units. The ordered micropore structure of faujasite (or zeolites X, Y), zeolite ZSM-12, MFI (ZSM-5 or Silicalite-1), and zeolite Theta-1 (or ZSM-22) are illustrated. Reproduced from Ref. [154] with permission from Elsevier.

However, porosity alone is insufficient for zeolites to exhibit the desired catalytic behaviour. Indeed, pristine MFI type silicalite-1 zeolite, which contains only Si and O atoms and has negligible acidic strength, shows very little to no catalytic activity [168]. Only upon the introduction of structural defects (to generate weakly acidic silanol groups [168,169]) or the introduction of dopants (either directly

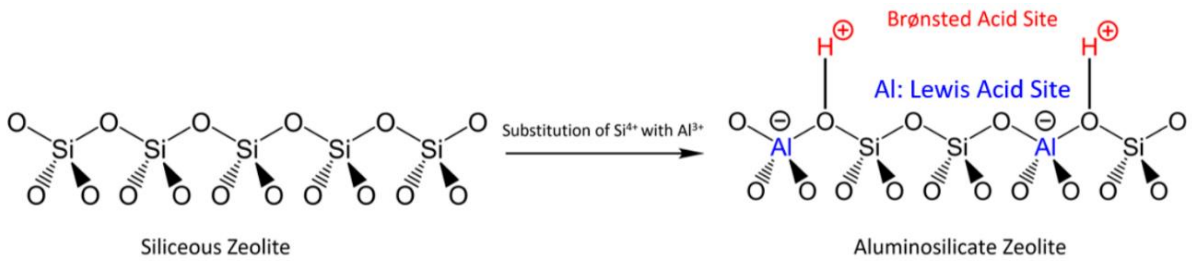

Figure 10| Brønsted and Lewis acid site formation in zeolites. Upon the substitution of Si by Al a negative charge is placed on the zeolite backbone which is compensated by acidic proton. The Lewis acid site is located on Al atom while the proton constitutes the Brønsted acid site.

into the MFI framework [170] or into its pores [171]) is the catalytic activity induced. The lack of catalytic activity of silicalite-1 is contrasted by ZSM-5, which is one of the most widely used zeolite in the petrochemical industry [172]. ZSM-5 has the same MFI structure[3], but contains Si, O and Al. Although the catalytic activity of ZSM-5 may be improved through modification, pristine ZSM-5 already shows appreciable catalytic activity. For example, it is able to catalyse the oligomerization [173] or cracking of hydrocarbons [172]. Building on this comparison, silicalite-1 also shows very poor ion exchange ability compared to its alumina containing counterpart, ZSM-5 [174]. Cleary the inclusion of Al has a great impact on the behaviour of the material.

The stark difference between silicalite-1, a SiO_2 polymorph, and ZSM-5 is due to the substitution of Si by Al in the TO_4 unit. This substitution induces the much enhanced acidity of ZSM-5 compared to silicalite-1 [175] and is the source of aluminosilicate acidity in general, as described shortly. In effect the substitution of Si^{4+} with Al^{3+}, causes a charge imbalance with the oxygen atoms (Figure 10) resulting in a negative charge on the framework. In practice this negative charge is compensated by a counter ion. After removal of the organic template (e.g. by calcination) and depending on the synthesis route (e.g. using hydroxide or fluoride media) this counter ion is typically an alkali metal (Na^+ or K^+) or a proton [156,162]. The counter ion may be exchanged to arrive at the desired material properties. In all cases the charge imbalance between the T atoms and oxygen allows for the cation incorporation.

As was alluded to before, the zeolite acidity (i.e., the number and strength of acid sites) strongly influences its catalytic behaviour. Apart from determining whether the zeolite displays any catalytic activity at all, the zeolite acidity also influences properties such as catalyst stability and selectivity of the catalyst [175]. Understanding the origin of zeolite acidity is therefore crucial.

[3] A detailed discussion on the specific geometry of the MFI structure will be appear later in this section.

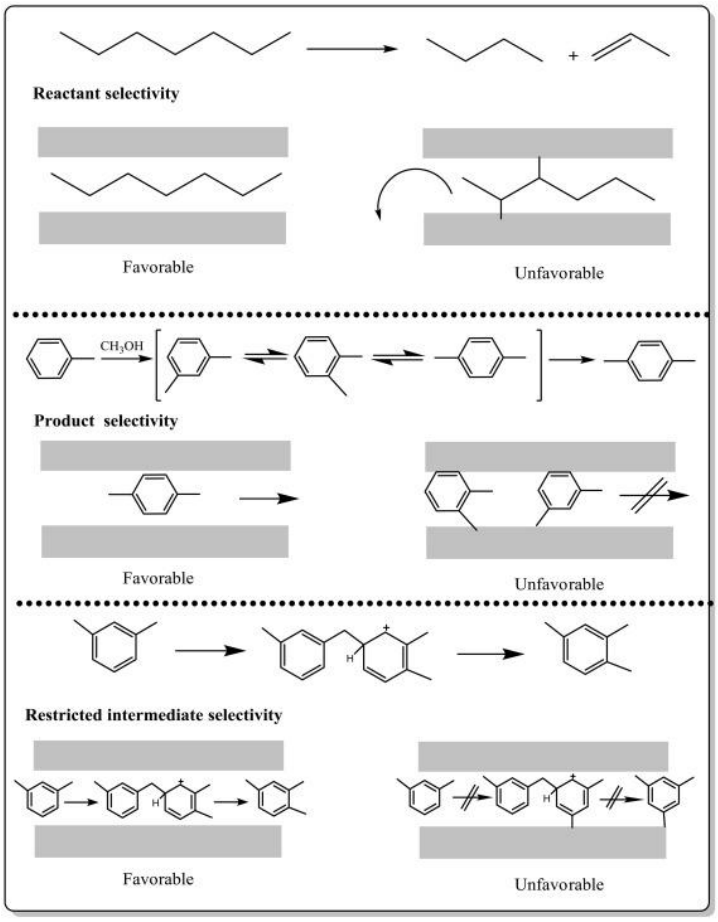

Figure 11| Three types of shape selectivity. From top to bottom the figure illustrates reactant, product and intermediate (transition) shape selectivity. Reproduced form Ref. [176] with premission from Elsevier.

The zeolite acidity depends in large part on whether the incorporated counter ion is a metal ion or a proton. In the former case the zeolite acidity may be dominated by Lewis acid sites (LAS), which can accept electrons, while in the latter case Brønsted acid sites (BAS), which can donate a proton, may be dominant [175]. It is important to note, however, that upon the inclusion of Al into the zeolite framework both LASs and BASs are formed.

Figure 10 shows the formation of these two types of active sites due to the substitution of Si^{4+} with Al^{3+}. The Lewis acidity can be understood in terms of resonance structures. Rather than describing the $Si\text{-}O^{-}(H+)\text{-}Al^{-}$ bridge as harbouring a negative charge on the Al atom and a positive charge on the proton, this structure could be seen as SiOH → Al, in which a dative bond exists between SiOH and the tetrahedral Al atom [177]. In this way a Lewis acid site is generated at the Al atom.

The combination of zeolite acidity and structure-induced diffusion limitation leads to three types of catalytic shape selectivity (see Figure 11) [178–180] :

1. Reagent shape selectivity: when two molecules with different shape and/or size are reacted over a zeolite catalyst, the relative reaction speed of the two molecules depends on their diffusion rate into the zeolite pores. In the extreme case one of the two molecules may only react at the exterior surface of the zeolite, while the other may diffuse into the pores. This is an important consideration in selecting a suitable zeolite for the desired reaction. This is exemplified by the conversion of biomass, which contains molecules like glucose with kinetic diameter >8 Å. As a result it has been found that the rate of biomass conversion is significantly lower over small window zeolites like ZK-5 and SAPO-34 (with pore size <4.5 Å) than over medium (e.g. ZSM-5, ZSM-11 and SSZ-23) or large pore zeolites (e.g. SSZ-55, Beta zeolite and Y zeolite).
2. Transition state selectivity: when at least two reaction pathways are available under catalytic conditions the relative speed of each reaction pathway depends on the geometry of the transition state. The reaction whose transition state geometry matches the zeolite pore shape is favoured. This, in turn, effects the product distribution. For example, the selective conversion of n-octane into mono-branched 2-methyl isomer, rather than 3- or 4-methyl isomers, has been attributed specifically zeolite interaction with the protonated cyclopropane ion intermediates [181].
3. Product shape selectivity: when neither the reagent or transition state is obstructed the formation of a particular product may still not be observed if the product molecule is too large to diffuse out of the pores. In the best case this allows for high control of the product distribution. In the worst case the generated molecules may bock the internal pores of the zeolite. A clear example is the formation of large aromatic species inside the pores of CHA catalysts upon the conversion of methanol [182]. Another classic example of product shape selectivity is the methylation of toluene over ZSM-5. Generally, the xylene product consists of ~90% para-xylene, which has a smaller kinetic diameter than ortho- or meta-xylene. The latter tend to isomerize inside the ZSM-5 pores to form para-xylene, which has a much higher diffusion rate [180].

In any particular catalytic system, all three types of shape-dependant selectivity may contribute to the overall reaction. Leveraging this fact enables researchers to formulate zeolite materials with high stability, selectivity and activity.

In the case of the current research, the most relevant example of zeolite-induced shape selectivity is the formation of hydrocarbons from methanol. Different types of hydrocarbons can be formed depending on the zeolite structure and acidity. In light of this fact, the following sections provide a more detailed discussion of the zeolite material, which was been used in this thesis: zeolite Socony Mobil Number 5 (MFI) (e.g., ZSM5)[4]. MFI is one of the most widely used zeotypes in tandem CO_2 hydrogenation. In this thesis ZSM-5 was used specifically for its ability to selectively convert methanol to light aliphatics (C_{2-4}) under CO_2 hydrogenation conditions.

[4] Somewhat confusingly the acronym MFI, which refers to *Mobil-5*, is typically used to refer to the zeolite structure specifically. In contrast the acronym ZSM-5 (*Zeolite Socony Mobil Number 5*) is used for the aluminosilicate zeolite originally synthesized. Hence, ZSM-5 is used for a specific zeolite, while MFI is used for a class of zeolites with the same structure [338].

1.4.2. General Methanol Conversion Mechanism over Acidic Zeolites

Before describing the specific zeolite structure of MFI it is helpful to consider the general reaction mechanism underpinning the conversion of methanol to hydrocarbons. Notwithstanding the fact that the exact reaction mechanism (e.g. which particular reaction intermediates are most relevant) depends on the specific zeolite structure. Moreover, although the exact reaction mechanism of methanol conversion has been and continues to be the subject of much research, some key aspects of the mechanism at an early stage are still not known. Nevertheless, consensus has been reached on the mechanism at working conditions.

In contrast to the RWGS-FTS reaction mechanism, which is characterised by probabilistic chain-propagation and termination (described in Section 1.2), the conversion of methanol to hydrocarbons is defined by an auto-catalytic reaction cycle called the hydrocarbon pool (HCP). As a result of the auto-catalytic nature of the reaction, generally three phases are observed (Figure 12) [183]:

1. Induction phase;
2. Active phase;
3. Deactivation phase.

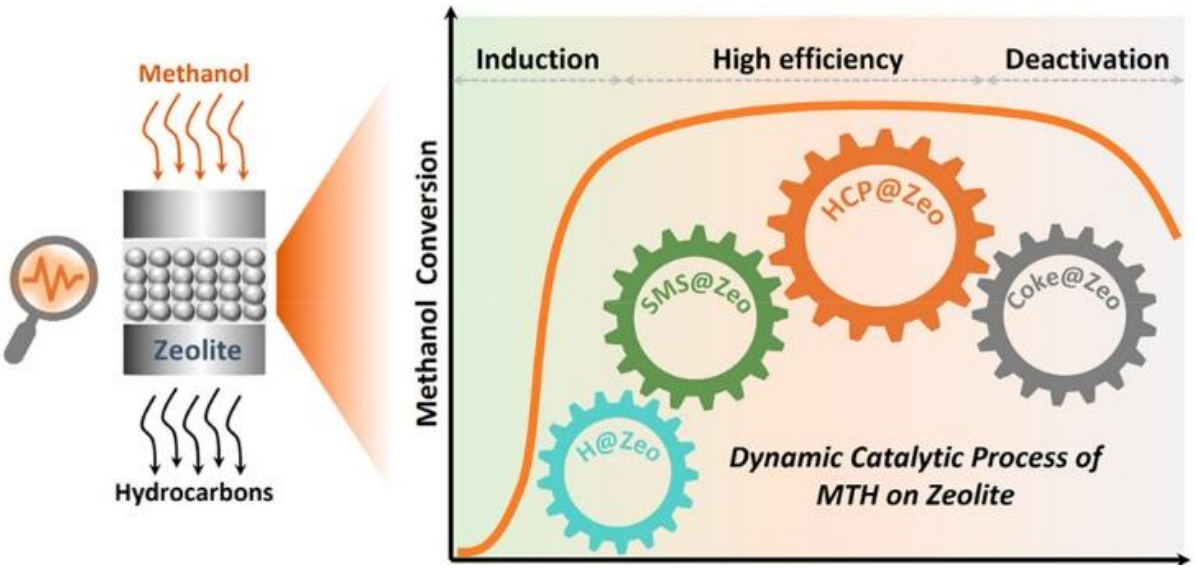

Figure 12| Three stages of methanol conversion over acidic zeolite catalysts. The induction, active and deactivation phase are shown in terms of the methanol conversion. The state of the zeolite is also indicated. Reproduced with permission from Ref. [183].

During the induction phase, methanol is converted to form short hydrocarbons via direct C–C coupling. This stage is generally associated with low methanol conversion and DME formation alongside the formation of short hydrocarbons. Although a number of reaction pathways have been proposed, no consensus exists on the mechanism of initial C–C bond formation [184]. As the reaction continues, nearly 100% methanol conversion is reached, at which point the reaction mechanism is dominated by the HCP mechanism. During the active HCP phase of the reaction methanol couples to previously generated hydrocarbons though methylation. A large number of hydrocarbons are formed via cracking, isomerization and aromatization. Consequently, two cycles emerge inside the pores of the zeolite [185]: one of these cycles consists of aliphatic hydrocarbons (the aliphatic cycle) and the other of aromatic hydrocarbons (aromatic cycle) (see Figure 13). The combination of these two cycles constitutes the HCP mechanism. Importantly, the aromatic cycle selectively produces C_2, C_3 and aromatic hydrocarbons, while the aliphatic cycle produces aliphatic hydrocarbons with a wider range of molecular weight [185].

As noted, the exact structure of the zeolite used as great impact on how the HCP reaction proceeds. Hence, to understand the HCP reaction in the ZSM-5 pores its specific structure needs to be considered.

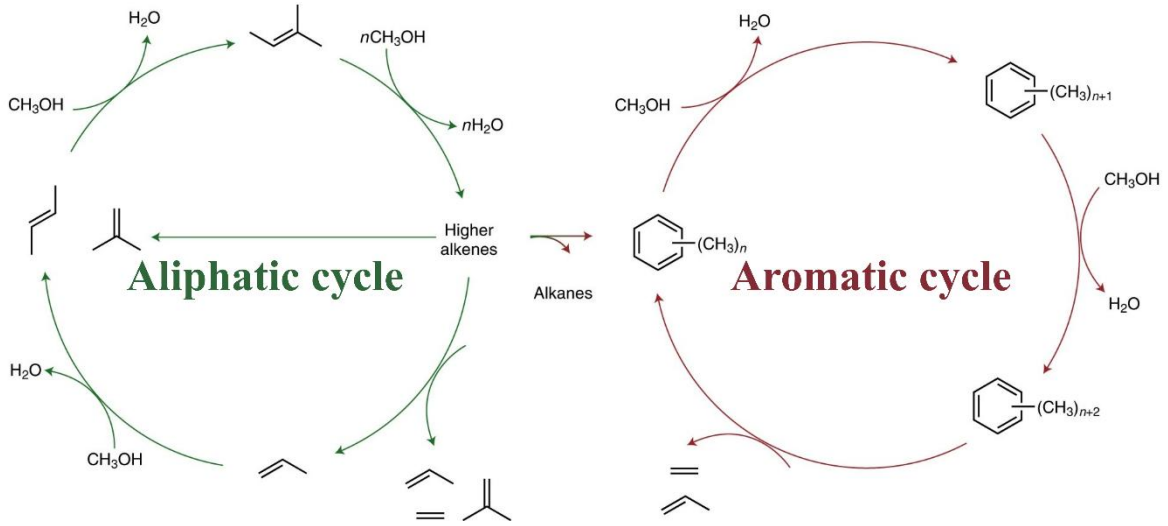

Figure 13| Methanol conversion hydrocarbon pool reaction over zeolite consisting of the aliphatic and aromatic cycle. The aliphatic cycle (on the left) proceeds by the continuous interconversion and methylation of aliphatic species during methanol conversion. The light olefin formation via the aromatic cycle is shown on the right and proceeds by the sequential methylation and dealkylation of aromatic species. Reproduced with permission from Springer Nature (Ref. [185]).

1.4.3. Zeolite Socony Mobil (MFI) structure

The MFI (or ZSM-5) structure is constructed from pentasil units [186]. The pentasil units, which contain eight 5-membered rings, assemble into characteristic ten-membered-ring straight and sinusoidal shaped pores (see Figure 9). The dimensions of these pores are 5.4 × 5.6 Å and 5.1 × 5.4 Å respectively. The combination of these two types of channels has an important role in the ZSM-5 chemistry. For instance, it results in the formation of 12 non-equivalent T sites in ZSM-5 crystal lattice. Hence, many non-equivalent BASs may exist in a given ZSM-5 structure. The combination of two types of pores also affects the diffusion of molecules like methanol, aliphatic or benzene hydrocarbons. While the former two can diffuse relatively freely through both pores, aromatic molecules (e.g. benzene, toluene, and xylene) favour diffusion along the less constrained straight pores [187–189]. Additionally, the interaction between the two channels constitute a unique chemical environment. These intersections are more spacious than either pores with a diameter of roughly 7.0 Å [189] and can therefore harbour larger molecules like highly methylated tetra methyl-benzene (TMB) [189]. In contrast, the diffusion of TMB is highly restrained in either pore [189].

The formation of the characteristic straight and sinusoidal channels in the MFI framework requires the presence of an OSDA. In practice, tetra-propylammonium hydroxide (TPAOH) (see Figure 14) is most commonly employed in the hydrothermal synthesis gel to guide crystallization. Under the typical alkaline synthesis conditions, the TPA^+ cation resides at the channel intersection, thereby stabilizing the development of both the straight and sinusoidal pores. After crystallization the template is removed by calcination to free up the zeolite pores.

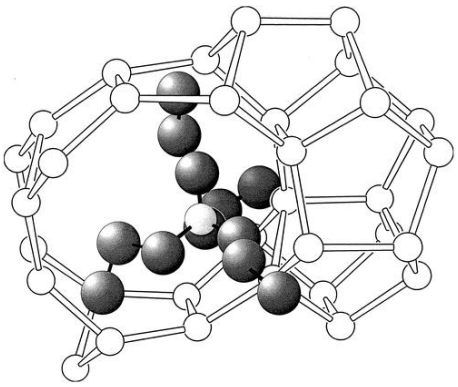

Figure 14| MFI structure unit stabilized by TPA^+. Reproduced with permission from Ref. [190].

The specific synthesis regime followed has large effects on the final zeolite structure. For example, ZSM-5 with different morphologies (e.g. sheets-like, plate-like, tube-like or globules) can be synthesised using different methods [191–193], including the addition of organic additives [194] or by using different Al or Si sources [192]. More subtle differences, such as changes in the location of Al in the crystal lattice, may also occur [194]. Considering the combination of different intersecting pores results in 12 non-equivalent T sites in the ZSM-5 crystal lattice–the location of the Al induced BASs. As a result, the placement of Al in the crystal structure may be relevant to the catalytic behaviour of the ZSM-5 material.

1.4.4. Reaction mechanism of methanol to C_3 conversion over MFI

As described in before, the conversion of methanol occurs via the HCP reaction mechanism. In the case of ZSM-5, both aromatics and aliphatics can be produced via the HCP reaction mechanism. More specifically, a range of C_2 to C_6 aliphatic hydrocarbons are produced by the aliphatic cycle inside the ZSM-5 pores, while the formation of C_2 and C_3 is favoured in the aromatic cycle alongside the generation of aromatics. In fact, C_3 formation is largely derived from the aromatic cycle rather than the aliphatic cycle.

The reaction mechanism of C_3 formation in the aromatic cycle, called the paring mechanism, involves a number of steps [195]: first, neutral and charged poly-methyl benzene (PMB) species are formed by the sequential methylation of benzene with methanol. Charged PMBs, in turn, generate propylene by ring closure and expansion. This is referred to as the paring mechanism. The formation of propylene form tetra-methyl benzene (TMB), which is the most active PMB species in ZSM-5, is shown in Figure 15. After the last methylation step, a methyl shift results in a ipso methyl structure. Then the TMB analogue undergoes a ring closure resulting in a fused ring structure consisting of 3- and 5-membered rings. The strain in this bicyclic structure is released by expelling the ipso methyl groups and

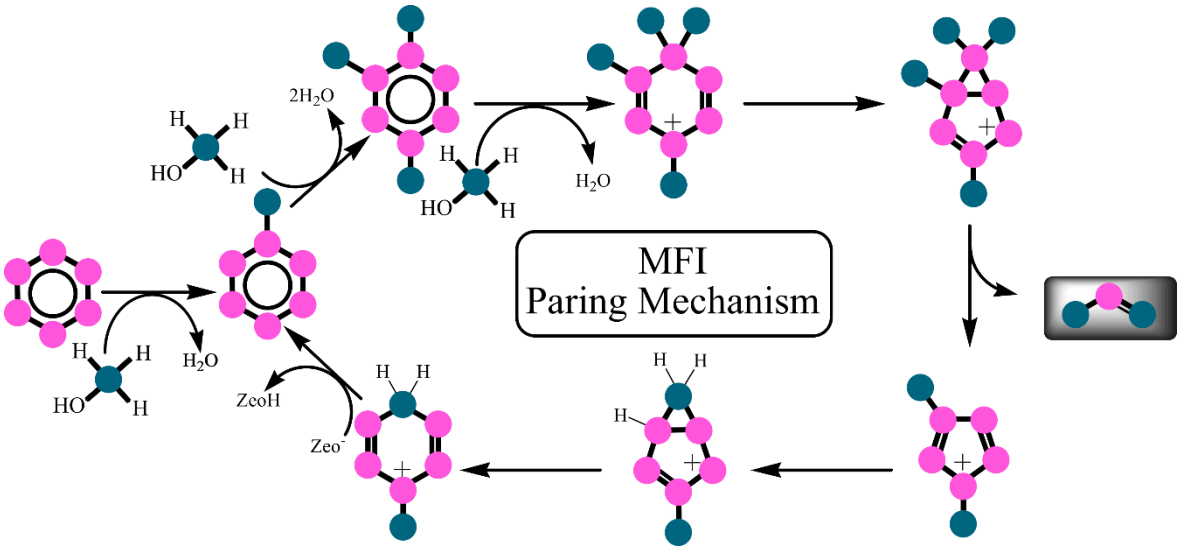

Figure 15| Paring mechanism over ZSM-5. The figure shows the formation of propylene from TMB via the pairing mechanism. Carbon atoms are shown in pink and blue to emphasize the scrambling of aromatic and aliphatic carbons. Carbons derived from aromatic rings are shown in pink. Atoms derived from aliphatic species are shown in blue. Figure is based on the mechanism described in Ref. [195].

the aromatic carbon in the form of propylene and forming the cyclopentadiene cation. This step is rate-determining with a reaction barrier of around 165.5 kJ mol^{-1} [195]. Finally, the 6-membered ring is regenerated by incorporation of one methyl ring substituent. Carbon scrambling is a hallmark of the paring mechanism–the propylene product contains both carbons derived from the methyl groups and from the aromatic ring. Similarly, after retrieval of the 6-ring, the aromatic ring contains carbons which were previously aliphatic.

1.4.5. Tandem CO_2 hydrogenation using MFI

Recently, much effort has been made to formulate bi-functional catalyst materials to facilitate the formation of aromatics and light olefins from CO_2 and hydrogen. Instead, the formation of light paraffins has received considerably less attention, even though the ability to produce products like propane from CO_2 in a sustainable way should be highly attractive. Not in the least part because these molecules have distinct applications in their own right including in aerosol propulsion, refrigeration and as potential green fuels in many industrial and agricultural settings [196–198].

ZSM-5 is most commonly used for the conversion of methanol or other hydrocarbons into mixtures of gasoline range aromatics (mostly benzene, toluene and xylene (BTX)) and olefins [199–201]. Indeed, it has been shown that, over a wide range of temperatures, both olefins and aromatics are produced from methanol when reacted over ZSM-5 with a Si/Al ratio of 42 [201]. The formation of aromatics over ZSM-5 arises from its relatively wide pores. Notably, although both straight and sinusoidal channels have a suitably large diameter to harbour aromatics [187,188], diffusion of relatively large BTX molecules is considerably more hindered in the sinusoidal channels [188]. At the same time the diffusion of methanol and light aliphatic is considerably more rapid in sinusoidal channels compared to BTX. Larger aromatic molecules like TMB are too bulky for either pore and are constrained to the more spacious intersections (~7.0 Å [189]) between the two channels [189]. This is also where benzene preferentially adsorbs. Hence the aromatic cycle preferentially takes place in the intersectional sites [202]. The difference in diffusion rate between these different molecules has large impact on the evolution of the HCP reaction mechanism and in turn has important implications for ZSM-5 catalyst engineering [202–204].

In line with the propensity of ZSM-5 to generate BTX, a number of tandem CO_2 hydrogenation catalytic systems have been reported, which are able to produce aromatics by employing ZSM-5. ZSM-5 may be used in pristine proton form [49,51] or the structure may be modified with elements including Ga, Fe [52] or B [205]. Alternatively, the acidity of ZSM-5 may be modulated to enhance BTX formation by introducing dopants including Zn [48,206], P [207,208] or Fe [207] into the pores by various methods like ion-exchange or impregnation. However, there are several reports of the preferential formation of light

hydrocarbons with a relatively low selectivity to aromatics [45,46,209]. In general. this is achieved with highly acidic zeolites with low Si/Al ratios [45,46,50]. While such high acidity ZSM-5 zeolites are typically highly susceptible to rapid deactivation in the conversion of methanol, due to the unique CO_2 hydrogenation conditions present in these tandem schemes, deactivation through coking can be minimized [46,182,210]. All in all, ZSM-5 (with a low Si/Al ratio) is also a viable candidate for tandem CO_2 hydrogenation to light paraffins. Hence, the study presented in Chapter 5 on a methanol-mediated tandem approach to convert CO_2 and H_2 to propane employs highly acidic ZSM-5 as the methanol converting catalyst component.

1.5. Thesis Outline

The following pages include one methods chapter (Chapter 2), three main results chapters (Chapter 3, 4 and 5) and a final conclusions and outlook chapter. The literature referenced throughout this thesis can be found on pages 203 to 226. Lastly, the appendix can be found at very end of the thesis.

Chapter 3 and 4 investigate the direct hydrogenation of CO_2 over CuZnFe catalysts promoted with alkali metals (K, Rb, Cs). Herein the aim is to elucidate the pathway through which the alkali metal (AM) promoters lead to the formation of higher alcohols and olefins at the expense of paraffins during CO_2 hydrogenation. In Chapter 3 the crucial role of surface AMs for the formation of alcohols and olefins is first addressed in terms of the catalyst structure (e.g. oxidation state, phase distribution, electronic effects and carburization), then Chapter 4 goes into the effect of AM doping on the catalyst surface interactions and reaction mechanism of olefin and higher alcohol formation.

Chapter 5 presents a tandem catalytic approach to selective CO_2 hydrogenation to propane (C_3). A composite catalyst system was developed, combining a RhInMg layered double hydroxide-derived catalyst with a highly acidic H-ZSM-5 zeolite. By co-feeding an aromatic co-reactant (benzene), this tandem catalyst achieves highly selective propane (C_3) production under relatively mild conditions (250 °C). The chapter focusses on clarifying this increase in C_3 formation from a mechanistic perspective using a wide-range of techniques.

Chapter 2

Methods and Theory

2.1.Introduction

Characterization of the catalyst and the reaction which occurs on its surface is integral to catalysis research. Unravelling the relationship between the formulation of the catalyst (i.e. how it is made and what elements are present), the formation of active site during activation and under reaction conditions, and the promotion of desirable reaction steps under working conditions allows for the rational design of the catalytic materials. Correspondingly, the brunt of the information presented in this thesis is concerned with characterization (as is the standard).

It is important to note that any given characterization technique can only elucidate part of the catalysis story. A collection of characterization experiments is required to build true understanding of the important factors determining the catalytic behaviour. In recognition of this fact a large number of characterization techniques have been employed throughout this thesis.

The following subsections briefly introduce the characterisation techniques used during this research. The fundamental principles underlying the techniques will be discussed to understand the information each technique can provide.

2.2. Catalyst preparation and evaluation

2.2.1. Chemicals

The following chemicals were used for the preparation of the synthesized catalysts: copper nitrate tetrahydrate ($Cu(NO_3)2{\cdot}3H_2O$, Sigma-Aldrich); zinc nitrate tetrahydrate $Zn(NO_3)_2 \cdot 6H_2O$(Sigma-Aldrich); iron nitrate tetrahydrate ($Fe{\cdot}(NO_3)_3{\cdot}\ 9H_2O$, Sigma-Aldrich); magnesium nitrate hexahydrate ($Mg(NO_3)_2.6H_2O$, 98%, Alfa Aesar); rhodium(III) nitrate ($Rh(NO_3)_3$, solution, ca. 190% (w/v) Rh in 20–25 wt% HNO_3, Thermo Scientific); indium(III) nitrate hydrate ($In(NO_3)_3.xH_2O$, Puratronic, 99.999%, metal basis, Thermo Scientific); sodium hydroxide (NaOH, reagent grade , ≥ 98%, anhydrous pellets, Sigma-Aldrich); caesium carbonate (Cs_2CO_3, Sigma-Aldrich); rubidium carbonate (Rb_2CO_3, Sigma-Aldrich); potassium carbonate (K_2CO_3, Sigma-Aldrich); and Zeolite HZSM-5 (Si/Al=18) (NKC-38, Tianjin Nanhua Catalyst Co.). Milli-Q water was used throughout all syntheses. All gas cylinders were provided by BOC. The reagents were used without further purification or modification.

2.2.2. Synthesis of $Cu_4Zn_3Fe_3$ (CZF) and alkali metal doped analogues

To study the effect of alkali metal (AM) doping in Chapter 3 and 4 AM doped $Cu_4Zn_3Fe_3$ (CZF) catalyst were synthesized by a two-stage procedure. First, a high surface area non-doped catalyst precursor was synthesised by co-precipitation. After calcination of the high surface area catalyst precursor, alkali metals (K, Rb or Cs) were introduced via incipient wetness impregnation and the dried material was calcined again.

Specifically the high surface area base material was synthesized by co-precipitation at constant pH ~10. Three solutions (A, B and C) were prepared to perform the co-precipitation. Solution A is a 1M metal precursor solution made by dissolving the Cu, Zn and Fe nitrates in 50 mL MiliQ water. Then, the precipitating solution (B) was prepared by dissolving 2.12 g $NaCO_3$ in the same amount of Milli-Q water. Finally, solution C was prepared by dissolving enough NaOH in Milli-Q water to obtain a 1 M concentrated solution. The precipitating solution B was poured into a three-neck round bottom flask

with a stirrer bar and a pre-calibrated Mettler Toledo FiveEasy™ pH/mV bench meter. To start the precipitation a syringe pump was used to transfer solution A into the flask at a rate of 1 mL/min until the pH reached around 10-10.3. At this point, solution B was fed into the flask at a variable rate using a peristaltic pump. The pH of the reaction mixture was kept at 10.0-10.3 by controlling the flow rate of the solution B. After adding all the metal solution, the pH is brought to 10.6. Finally, the reaction mixture was aged under stirring at room temperature for 16 to 24 hours.

The resulting mixture was filtered and washed with water and acetone. Then the wet solid was redispersed in acetone and stirred for another hour before refiltering and drying under vacuum for a few hours or overnight.

The obtained dry solid was calcined using a tubular furnace under air flow (30 mL/min) at 375 °C for 4 hours with a ramp rate of 5 °C/min. The undoped calcined sample is denoted CZF.

To introduce the alkali metal dopant about 1 gram of CZF was placed in a 20 mL round bottom flask. Then 1 mL of the alkali metal carbonate solution was slowly dripped into the dry powder using a syringe pump under constant stirring. The wet mass was dried under vacuum overnight and calcined as before. The obtained catalyst pre-cursor is denoted *xA*-CZF, where *A* is either K, Rb or Cs and *x* is the weight percentage. No further support material was introduced to limit the complexity of the system. The initial tests using 2 w.t.% AMs were conducted on the same batch. To verify the main observations a second batch was synthesized and retested before and after doping with 2 w.t.% Cs

2.2.3. Synthesis of RhInMg LDH catalyst precursor

The methanol synthesis catalyst component of the tandem catalyst system studied in Chapter 5, which contained Rh, In and Mg, was synthesized using a layered double hydroxide (LDH) precursor method. The LDH RhInMg catalyst precursor is prepared according to the AMOST method, which involves precipitation, aging and finally exfoliation of the LDH layers, as previously reported [16].

To make the metal precursor solution (A), 4.28 g (16.68 mmol) of magnesium (II) nitrate, 319 mL (0.31 mmol) of rhodium (III) nitrate and 1.16 g (3.86 mmol) of indium (III) nitrate were dissolved

in 40 mL of Milli-Q water. The precipitating agent (solution B) was prepared by dissolving 1.7 ± 0.01g (42.5 mmol) of sodium hydroxide in 40 mL of Milli-Q water. Another 40 mL of Milli-Q water was poured into a three-neck round bottom flask with a stirrer bar and a pre-calibrated pH meter.

A syringe pump is used to transfer the solution A into the flask at a rate of 1 mL/min. At the same time, solution B was fed into the flask using a peristaltic pump. The pH of the reaction mixture was kept at 10.1 by controlling the flow rate of the solution B. Approximately 35 mL of solution B was used in the process. After adding all the metal solution, the pH is brought to 10.6. Finally, the reaction mixture was aged under stirring at 60 ℃ for 18 hours.

After aging, the precipitate was washed using water. The solution is divided into four centrifuge tubes and filled up to 45 mL with Milli-Q water, then centrifuged at 5000 rpm for 5 minutes. This was repeated 2 more times with a centrifuge time of 10 and 15 minutes for the second and third washing. Each time the water was refreshed. After washing the LDH layers were exfoliated by adding 35 mL of acetone to each centrifuge tube and sonicating them for 1 hour. The tubes were centrifuged one last time at 5000 rpm for 5 minutes. Then, the wet LDH was dried overnight under vacuum at room temperature. Finally, the product was ground to a fine pale-yellow powder.

Approximately 500 mg fine powder LDH precursor was converted to layered double oxide (LDO) by calcination in N_2 (30 mL/min) using the following heating procedure: 1 hour 80 °C, 1 hour 150 °C and 2 hour 420 °C with a ramping rate of 2 °C/min.

For each reaction 100 mg calcined material was reduced under 5% H_2 in N_2 at 290 °C for 2 hours using a ramping time of 70 minutes. The catalyst after reduction is denoted RhIn/MgO_x. Before mixing with the reduced RhIn/MgO_x, approximately 800 mg ZSM-5 was calcined in a tube furnace under air for 5 hours at 500 °C ramping at 5 °C/min. To obtain the mixed catalyst, the reduced RhIn/MgO_x material is mixed with 100 mg of calcined ZSM-5. The final mixture is denoted as RhIn/ZSM-5.

2.2.4. CO_2 hydrogenation using plug flow reactor

In Chapter 3 all catalytic tests were conducted using a tubular plug flow reactor (see the diagram in Figure S1). The reactor body is composed of a stainless steel outer tube (with 12.7 mm diameter) in which a quartz inner tube (with 8mm diameter) is placed which holds the catalyst. The reactor is heated by a three-stage heater. Each reaction was conducted using 100 mg of catalyst in powder form (no granulation was applied), which was fixed between two beds of compressed quartz wool inside a quartz glass reactor tube. The catalyst was positioned in the centre of the third heating stage to allow for proper heating of the reactant gas before contacting the catalyst. The quartz tube was fitted with a rubber O-ring to ensure the gas properly flowed through the catalyst bed. Then the tube was placed inside the tubular reactor and sealed. Prior to reaction the catalyst was reduced using ~20 mL/min 5 % H_2 in N_2. The reduction was performed by heating to 360 °C in 1 hour 10 minutes and dwelling for 2 hours. After reduction the reactor was let to cool down to around room temperature before switching the gas stream to a mixture of 27.6 mL/min 1:3 CO_2:H_2 and 2.4 mL/min N_2 to pressurize the reactor to 45 ±1 bar. The pressure inside the reactor was regulated using a back-pressure regulator. After the desired pressure was reached a small amount of outlet gas was flowed to the Agilent 7890B GC for product analysis using a needle valve. To allow the products to reach the GC the gas line was continuously heated to 150 °C using heating tape.

The reaction was carried out sequentially at 270, 290, 310 and 330 °C. Each time the temperature was increased in 45 minutes and held for 3 hours and 45 minutes. The products and unreacted CO_2 were sampled every 45 minutes for a total of 5 measurements at each temperature step. Figure S15 shows an example of the effect of the temperature change on the product selectivity measured at each temperature step individually during CO_2 hydrogenation over CZF and Rb-CZF. The effect of the temperature change is reflected by the step-wise change in the selectivity upon increasing the temperature (e.g. from 270 to 290 °C). CO_2 and CO were detected using a TCD detector, while the remaining hydrocarbons and alcohols were measured using a separate FID detector. See Section 2.2.7 for details on the GC method.

2.2.5. Catalytic reaction (batch reactor)

In Chapter 5 a number of catalytic reactions were performed using a high pressure batch reactor under different conditions. All catalytic reactions were done using the composite catalyst in a stainless-steel autoclave (Parr General Purpose Pressure Vessel, 50 mL) with a glass-covered magnetic stirrer bar. Here we outline an example of a typical procedure for such a reaction.

The catalyst, together with the stir bar and benzene (if used) were introduced into the reactor. Then, the reactor was flushed and pressurised with Ar (2 bar) to remove the air and to provide an internal standard. Lastly, carbon dioxide/hydrogen (25% CO_2/75% H_2) was flowed into the reactor, pressurising it to 28 bar. To start the reaction the temperature was increased to 250 ℃ over 1.5 hours (increasing the pressure to 50 ± 1.5 bar) and was held at the reaction temperature for 10 hours using a heating mantle and Parr 4838 Reactor controller. Temperature feedback was done with a J-type thermal couple, which measured the gas temperature at a fixed depth. After the reaction, the products were measured using an Agilent 7890B GC. The pressurised gas was flowed through the injection loop for 1.5 minutes. Each time at least 4 measurements were done of which the last three were used to calculate the conversion and selectivity. The CO_2 conversion, CO and hydrocarbon selectivity were calculated as follows:

$$CO_2\ conversion = \left(1 - \frac{A_{CO2}/A_{Ar}}{A_{CO2\ baseline}/A_{Ar\ baseline}}\right) \times 100\% \quad (3.1)$$

$$CO\ selectivity = \frac{RRF_{CO} \cdot A_{CO\ output}}{RRF_{CO} \cdot A_{CO\ output} + + \sum_i i \cdot RRF_{CiHx}\, i \cdot A_{CiHx\ output}} \times 100\% \quad (3.2)$$

$$C_iH_x\ selectivity = \frac{i \cdot RRF_{CiHx} \cdot A_{CiHx\ output}}{RRF_{CO} \cdot A_{CO\ output} + + \sum_i i \cdot RRF_{CiHx}\, i \cdot A_{CiHx\ output}} \times 100\% \quad (3.3)$$

where A_i represents the peak areas of reactant or product measured by the GC, RRF represents the corresponding relative response factor, i is the number of carbon atoms.

2.2.6. Control Experiments using batch reactor

In addition to the main tandem catalytic data Chapter 5 presents the results of a number of control experiments using a non-tandem catalysis setup. In this case methanol, ethylene and butylene were reacted over H-ZSM5 in the presence or absence of 200 mg benzene under the same conditions as specified in Section 2.2.5. In the case of methanol, 20 bar of H_2 was used to prevent excessive coking of the catalyst due to the high initial methanol concentration. In the case of hydrocarbon reactions, no hydrogen was added.

2.2.7. Gas Chromatography (GC) (plug flow or batch reactor)

Gas Chromatography (GC) is a standard and straightforward method to perform molecular analysis of gas phase sample mixtures to determine the concentration of the individual components. As in any chromatographic technique, the molecules are separated based on their difference interaction with a specific stationary phase and then detected separately to be quantified.

In this research GC analysis of the CO_2 hydrogenation reaction was performed on the Agilent 7890B platform. Valve diagrams representing the system are shown in Figure S2-S9. The exact valve turning sequence can be found in Table S1. A typical chromatograph can be found in Figure S11 and S12. The hydrocarbon and alcohol products were measured by FID. The remaining light gases including N_2, H_2, CO and CO_2 were measured by TCD. The complete analysis took 45 minutes, during which the temperature was first ramped to 180 °C to analyse the hydrocarbons and then cooled down to 30 °C to analyse the light gases.

For the FID analysis a Split/Splitless inlet was used in Split mode to introduce the analyte into the general purpose DB-5 column (30m 0.25mm 1.0μm) by the sampling valve. Initially the peak shape (tailing or symmetrical) was used to identify alcohols from hydrocarbons (see the chromatograph examples in Figure S12). The validity of this heuristic was verified by offline GC-MS analysis. During catalysis a portion of the product gas was collected using a gas sample bag, which was manually injected into a GC-MS/FID system equipped with the sample DB-5 column.

Only light gases and hydrocarbons up to butane were analysed by TCD. To do so, two valves were used in series: a 10-port sampling-backflushing valve and a 6-port selection valve. Upon sample injection the gas introduced to Poraplot U column (10m 0.53mm 20 μm) for the initial separation. This column also acts as the backflushing column, which prevents any unwanted heavy compounds to travel to the detector. When the backflush is initiated any of the gasses remaining in the column are vented. The eluded gases are further separated by a Hayesep Q column. The fast travelling permanent gases (N_2, H_2, CH_4 and CO) are trapped inside a Molesieve 5A column 80-100 Mesh (2.0m 1.8" 2.0mm) by the selection valve. These gases are released at the end of the analysis after proper separation. CO_2 and light hydrocarbons by-pass the Molesieve and directly travel to the TCD during the heating cycle.

Relative response factors (RRF) were used to quantify the analyte components. RRFs were calculated based calibration gas measurements. The chromatographs used for the calculations can be found in Figure S10.

2.3.Material Characterization

2.3.1. X-Ray Diffraction (XRD)

X-Ray Diffraction (XRD) is one of the most commonly employed standard characterization techniques. XRD is a non-spectroscopic characterization technique: in contrast to techniques like X-Ray Photon Spectroscopy (XPS)(see Section 2.3.3) or X-Ray Absorption Spectroscopy (XAS)(see Section 2.3.4) (the use of which will be addressed in subsequent sections), in XRD the X-rays do not exchange energy with the material. In other words, XRD is concerned with elastic scattering of X-rays to study the sample. This elastic scattering can give detailed information about the crystallographic phases present in the sample. This information includes factors such as which crystalline phases are present, the lattice unit cell parameters and the crystal size.

In this thesis XRD analysis is used in Chapter 3 to study the crystallinity of CuZnFe-based catalyst samples before and after reaction. All diffractograms were measured by the Bruker D8 Advance Eco X5ray diffractometer operated at 40 kV and 25 mA with Cu $K\alpha_1$ radiation over a range of $2\theta = 5°$-90°. The obtained diffractograms were analysed using the HighScore X'pert software to compare the peak position to a reference database.

2.3.2. Temperature Programmed Reduction (H_2-TPR)

The reducibility of powder samples can easily be studied using Temperature Programmed Reduction in any reducing gas mixture (e.g. 100% H_2 or dilute H_2 in an inert carrier gas). In the context of catalysis these experiments can not only inform the required reduction temperature to generate the active phase before starting the catalytic reaction, but can also show interesting interaction between different catalyst components (e.g. the presence of one element affecting the reducibility of another).

To perform the TPR experiments the sample is placed inside a plug flow type reactor equipped with a thermal conductivity detector (TCD). To measure the uptake of the reducing gas molecules two gas streams with the same composition are used: a sample stream (passing through the sample) and a

reference stream (not passing through the sample). Any difference in composition between the two gas streams induces a proportional detector response. To make sure the generated response is entirely due to the reduction of the sample material, the response difference is set to 0 before the experiment. During the experiment, the sample is heated at a constant rate while continuously flowing the reducing gas through both channels and measuring the detector response. As the reducing gas is consumed the TCD response changes. In this way the uptake of the reducing gas molecules can be determined. The reducibility of the catalyst is reflected by the reduction temperature observed during the TPR experiment.

Temperature programmed reduction experiments were conducted using the Quantachrome ChemBET Pulsar TPR/TPD automated chemisorption analyser. Approximately 30 mg of calcined catalyst was placed inside the U-tube and plugged with loose quartz wool, then placed inside the machine. The TCD detector was left to stabilize at 150V in N_2. The H_2-TPR was performed by heating the sample to 900 ºC with a ramp speed of 10 ºC/min and monitoring the TCD response.

2.3.3. X-Ray Photoelectron Spectroscopy (XPS)

X-Ray Photon Spectroscopy (XPS) is a commonly used surface-sensitive X-Ray spectroscopic technique. Considering the surface-sensitive nature of catalysis XPS is an incredibly valuable technique to the study of catalysts. XPS gives quantitative and qualitative information related to the electronic state of near surface atoms by measuring the binding strength of core electron (commonly s- and p-electrons). This relies on the fact that the binding strength of the core electrons depends on the particular nucleus they are bound to making the technique element specific. Moreover, because the core electrons are affected by the overall electron density at the nucleus, the oxidation state of the atom can be determined and even more subtle electron donating effects can be studied.

To determine the effect of alkali metal doping on the surface oxidation states of Cu, Zn and Fe XPS spectra were measured for catalysts after reduction and after reaction. To minimize any surface oxidation the catalysts were stored and transferred to the spectrometer using a glovebox filled with

argon. All spectra were collected at Harwell Research Complex in Diamond Light Source, with the help of Dr Mark Isaacs.

The obtained spectra were analysed using the CasaXPS software. For the interest of the analysis the Fe 2p peaks were fitted to determine the presence of Fe^{2+}, Fe^{3+} or Fe^{0} oxidation states. To disentangle these spectra we relied on the peaks reported in Ref. [211]. The Zn 2p and Auger peaks were analysed without the need for fitting to determine any potential changes oxidation state. To get surface charge independent measures of the electronic states the auger parameter and transition metals 2p oxygen 2p separation were analysed. The auger parameters were calculating by the summing the binding energy 2p peak maximum and KE auger peak maximum. The relative amount of Cu^{2+}, Cu^{1+} and Cu^{0} was successfully determined after reduction and reaction by fitting the Cu Auger based on the reference data provided in Ref. [212].

2.3.4. X-Ray Absorption Spectroscopy (XAS)

X-Ray Absorption Spectroscopy (XAS) is an advanced non-surface sensitive spectroscopic technique. Just like in XPS, during XAS analysis the sample is irradiated with X-rays. These X-rays are absorbed by the sample through the photo-electric effect. Thereby, core electrons are emitted from the sample creating excited core-hole states. The X-ray absorption behaviour is used to obtain chemical and local structure information of the sample.

In contrast to XPS, however, XAS is a X-rays-in-X-rays out type of technology: rather than using a fixed energy, a tuneable X-ray source with typical energy in the range of 10^2 and 10^5 eV is used to scan through a range of energies. At each energy step the absorption of the X-rays is determined. Importantly, absorption behaviour depends on the absorbing element and chemical state of the absorbing nucleus (e.g. oxidation state, phase structure etc.). As a result, the chemical state of each element contained in the sample can be studied separately using XAS. In this thesis XAS was used to analyse Cu, Zn and Fe before and after CO_2 hydrogenation to study the effects of alkali metals (Chapter 3). Additionally the local structure of Rb after reaction is analysed by XAS (Chapter 3).

For the collection of XAS Zn, Fe and Cu K-edges samples were sent to the Taiwan Light Source NSRRC beamline TLS07A, where the samples were analysed by Dr Tai-Sing Wu. All samples were measured in transmission mode. The materials were measured using a 2 axes sample stage with a Lytle detector. All edges were measured alongside a Cu^0, Zn^0 or Fe^0 reference.

In addition, the Rb K-edge was measured in transmission mode at the Diamond Light Source B18 beamline using the fast scanning (QEXAFS) Si (111) double crystal monochromator. The sample was measured using a custom cell with Kapton tape windows. The cell is designed for sample gas exposure at around ambient pressure.

All data normalization, background subtraction and analysis was performed using the ATHENA module of the Demeter software [213]. Athena was also used to perform the linear combination fitting (LCF) analysis of the Cu, Zn and Fe spectra. The standard spectra for analysis of the Fe K-edge included α-Fe, FeO, Fe_3O_4, Fe_2O_3, $ZnFe_2O_4$ and $CuFe_2O_4$, which were taken from the Spring-8 online database.

The Fe_5C_2 standard spectrum was measured separately using a lab scale XAS setup located at the University of Oxford Materials Science Centre for Energy Materials Research (CEMR). All standard spectra for LCF analysis of the Cu and Zn K-edge were taken from the Spring-8 online database and included Cu^0, Cu_2O, CuO, $CuFe_2O_4$, ZnO, Zn^0 and $ZnFe_2O_4$. In all cases a preliminary combinatorial fit was performed. Any spectral contribution smaller than 10% was excluded from the final LCF fit. The EXAFS analysis of Rb was performed using the ARTEMIS module.

A Morlet wavelet served as the basis for the Wavelet transform analysis. The wavelet parameters were $\eta = 5$ and $\sigma = 1$.

2.3.5. Mössbauer Spectroscopy

Mössbauer spectroscopy is a highly sensitive advanced fingerprint characterization technique, which is particularly useful in studying the chemical environment of Fe. Mössbauer Spectroscopy is unique in that, in contrast to more commonly used methods like XPS or XAS, it employs high energy γ-rays to probe the material. Unfortunately, due to the fundamental principles underlying Mössbauer spectroscopy only few elements are suitable to be studied by this technique. As a consequence, Mössbauer spectroscopy is a less common characterization technique. Accordingly, in the current study (Chapter 3) Mössbauer spectroscopy was used specifically to study the chemical environment of Fe.

More specifically Mössbauer spectroscopy was primarily used to confirm the formation iron carbides during CO_2 hydrogenation. To this end *quasi in-situ* Mössbauer measurements were conducted at the Technical University Delft Reactor Institute in the Netherlands. Calcined catalyst precursors were also analysed by ex-situ Mössbauer spectroscopy. All measurements were performed by Dr A. Iulian Dugulan.

Mössbauer spectra of ^{57}Fe were collected in transmission mode at different temperatures with conventional constant-acceleration or sinusoidal velocity spectrometers using a $^{57}Co(Rh)$ source. using An α-Fe foil was used to carry out the velocity calibration at room temperature. The source and the absorbing samples were kept at the same temperature during the measurements. The Mössbauer spectra were fitted using the Mosswinn 4.0 program [214]. The experiments were performed in a state-of-the-art high-pressure Mössbauer in-situ cell – developed at Reactor Institute Delft [215]. The high-pressure beryllium windows used in this cell contain 0.08% Fe impurity whose spectral contribution was fitted and removed from the final spectra.

The *quasi in-situ* experiments were conducted by sequentially applying a temperature treatment, cooling and measuring the sample without exposure to air. Note that the sample cell is not a plugged flow reactor. During the high temperature treatment the gas flowed over, rather than through the sample (as would be the case in a plug flow reactor). As an example, 2Cs-CZF was after 5 different treatments:

1. After calcination;

2. After reduction in the Mossbauer cell
3. After CO_2 hydrogenation at 250 °C;
4. After CO_2 hydrogenation at 270 °C;
5. And after CO_2 hydrogenation at 290 °C.

The sample after calcination was measured at 27 and at -269°C to reveal the hyperfine structure. After step 2-5 the sample was cooled down to -153.15 °C before taking the measurement. The reduction was performed using 1 bar 5% H_2 in Ar at 360 °C for 2 hours with a 70 minute ramping rate. Each CO_2 hydrogenation reaction was carried out at 20 bar at a flow rate of 27.6 mL/min for 3 hours with H_2/CO_2 = 3. The same protocol was applied to the undoped sample. For the sake of efficiency, Rb- and K-doped samples were measured 4 times instead of 6: the samples were treated up to and including step 4, but not measured after step 3. The remaining measurements (after 1, 2 and 4) were performed the same.

2.3.6. Thermal-Gravimetric Analysis (TGA)

Thermal Gravimetric Analysis (TGA) is a generally used as a straightforward method to study the thermal decomposition of a material by tracking the weight of the sample under heating [216,217] . The use of TGA experiments spans various topics, such as: oxygen-nitrogen exchange to study the formation of oxynitrides [218], the thermal properties of polymers [219], measurement of the amount of organics on a sample [220], estimation of the hydration number of a sample [221], or quantification of the release of intercalated species in layered double hydroxides. In this thesis (Chapter 5) TGA is used to semi-quantitatively study organic molecules trapped in the pores of a zeolite containing multi-component tandem catalyst system after reaction.

TGA was performed using a SDT Q600 thermal analysis machine. In each experiment approximately 9 to 12 mg of sample material was used. Before starting the experiment, the sample environment was purged with air to stabilize the weight. A consistent air flow of at 100 mL/min was used. After purging, the sample weight was monitored while heating from 30 to 900 °C at a rate of 10 °C/min.

2.3.7. UV-VIS Spectroscopy

Ultra-Visible Spectroscopy (UV-Vis) is a versatile quantitative and qualitative technique used to measure electronic transitions in powder or liquid samples. Upon exposing the sample to the right energy UV-Vis light (typically in the range of around 200 to 800 nm) electrons are excited from bonding or non-bonding orbitals to anti-bonding orbitals. In other words, by scanning through a range of wavelengths in the UV-Vis range the energy required for the transition from the Highest Occupied Molecular orbital (HOMO) to the Lowest Unoccupied Molecular Orbital (LUMO) can be measured. Because the HOMO-LUMO gap varies between different chemistries, UV-Vis can be used to identify different species. The only requirement is that the HOMO-LUMO gap is sufficiently small and that the transition adheres to the selection rules. In effect this means that while aromatic or (partially) conjugated systems generate a response non-conjugated systems do not. Additionally, because the HOMO-LUMO gap is affected by charge and chemical environment, UV-Vis is a particularly convenient method to study neutral or charged molecular species trapped inside porous zeolite materials [222–224]. Indeed, in the current research (Chapter 5) UV-Vis analysis is used specifically for this purpose.

UV-Vis absorption spectra were performed using a Varian 100 Bio UV-Visible Spectrometer in absorbance mode, covering the wavelength range of 185–600 nm with a sampling interval of 2 nm. For each sample 3 measurements were taken and averaged.

2.4. Reaction Mechanism Characterization

2.4.1. Temperature Programmed Desorption (TPD) Experiments

Temperature Programmed Desorption (TPD) is a simple method to measure the adsorption strength of a given molecule chemisorbed onto the catalyst. By measuring the chemisorption strength of selected molecules, the effect of catalyst modification can be studied.

TPD experiments are performed in a similar way as TPR experiments (see 2.3.2) and can often be done on the same instrument. Briefly, the sample is placed inside a plug flow type reactor equipped with a thermal conductivity detector (TCD) or Mass spectrometry (MS) detector. After drying and pre-treating the sample (as required) the adsorption gas is introduced to the material for an extended period of time at a constant temperature (often between 20 and 50 °C). To ensure only chemisorbed molecules are measured during the desorption process, excess gas phase and physisorbed molecules are flushed away at the same temperature using an inert carrier gas. Finally, under flow of the carrier gas the temperature is increased at a constant rate while the detector response is monitored. Depending on the nature and number of adsorption sites multiple peaks with different area can be observed. The temperature at which the peak is observed can serve as a measure of the adsorption strength.

In this thesis the adsorption strength of ethylene (C_2H_4), carbon dioxide (CO_2) and hydrogen (H_2) was studied by TPD to understand the surface effects of alkali metals (Chapter 4). These experiments were conducted on the Micromeritics AutoChem 2920 instrument at Wuhan University. The calcined samples (30 mg) were reduced and carburized, First the samples were heated to 360 °C in 5% H_2/N_2 (30 mL min^{-1}) for 2 hours, then the temperature was reduced to 320 °C and the gas was switched to $1CO_2/3H_2$ (30 mL min^{-1}) for 3 h. Finally the adsorption gas (CO_2, H_2 or C_2H_4) was introduced to the sample for 30 minutes at 50 °C. The remaining gas phase or physically adsorbed gas was removed by purging with Ar at the same temperature. After 30 minutes the TPD was performed by increasing the temperature from 50 to 900 °C with a ramping rate of 10 °C/min while the MS signal is recorded.

2.4.2. Pulse Transient Hydrogenation (PTH) Experiments

Pulse Transient Hydrogenation (PTH) experiments were conducted with ethylene (C_2H_4) and ethanol (CH_3CH_2OH) using the Micromeritics AutoChem 2920 instrument at the Wuhan University. In both cases 30 mg calcined catalyst was first reduced at 360 ºC in 5% H_2/N_2 (30 mL min^{-1}) for 2 hours and then the gas was switched into $1CO_2/3H_2$ (30 mL min^{-1}) at 320℃ for 3 h. Afterwards ethylene or ethanol pulses were introduced every 10 minutes. The MS signal of C_2H_4 (m/z = 27) and C_2H_6 (m/z = 30) were collected for the C_2H_4-PTH experiments. For the CH_3CH_2OH-PTH CH_3CH_2OH (m/z = 45) was also recorded.

2.4.3. CO DRIFTS

Two types of CO adsorption experiments were conducted: room temperature adsorption-desorption experiments and temperature ramping CO adsorption experiments. In all cases the CO adsorption was done using the Harrick's Praying Mantis reactor cell equipped with a high pressure/ high temperature dome with ZnSe windows. The spectra were collected by a Thermo Fisher Nicolet IS50 spectrometer equipped with a mercury cadmium telluride (MCT) detector and KBr beamsplitter. For each spectrum 128 scans were measured at a resolution of 4 cm^{-1}. The measurement time was approximately 1 minute.

For the adsorption-desorption experiments the catalyst materials were reduced at 360 ºC for 2 hours in 5% H_2 (30 mL min^{-1}). To remove any water formed during this procedure the gas was then switched to N_2 (30 mL min^{-1}) and heated at 400 ºC until the background stabilized. The background spectrum was then measured at 25 ºC in N_2 at atmospheric pressure. CO adsorption was performed by switching to 1% CO in N_2 for at least 1 hour. The gas was let to adsorb for at least 1 hour. CO was desorbed by switching back to N_2 (5 mL min^{-1}) without increasing the temperature. The spectra were monitored from the end of the adsorption to the end of the desorption.

For the ramping experiments the procedure was similar, but an additional carburization step was performed before CO adsorption. Carburization was performed under $1CO_2/3H_2$ at 290 ºC to emulate

the *in-situ* DRIFTS conditions. The background was measured at 25 ºC in N_2. Then 5 mbar of CO was introduced into the cell. The spectral evolution was monitored during adsorption. After adsorption at 25 ºC the gas was not switched to N_2. Instead, dilute CO was used continuously throughout the measurements. To probe different sites on the catalyst the temperature was increased to 50 ºC and then further increased stepwise from 50 to 290 ºC in 10 ºC intervals. Each time the temperature was left to settle for 2 minutes before taking 5 measurement. Finally the cell was cooled down to 25 ºC again.

2.4.4. Temperature Programmed Surface Reaction (TPSR)

The CO-H_2 Temperature Programmed Surface Reaction (TPSR) experiments were conducted on reduced and carburized samples using the AutoChem HP 2950 V2.04 instrument. In all cases 50 mg of calcined catalyst was used.

For the reduction the sample was heated to 360 °C at a ramping rate of 5 °C min^{-1} in 5% H_2/Ar (30 mL min^{-1}). The temperature was maintained for 2 hours. For the carburized samples the temperature was then dropped to 320 °C. When the temperature was reached the gas was switched to $1CO_2/3H_2$ (30 mL min^{-1}) and held for another 3 hours.

After this pretreatment the samples were cooled down to 50 °C in an Ar flow (30 mL min^{-1}). To pre-adsorb CO the gas was switched was 100% CO (30 mL min^{-1}) for 30 minutes. Afterwards, the residual gas phase CO was removed by switching the gas to Ar (50 mL min^{-1}) to for 10 minutes. The TPSR was performed by immediately switching the gas to 5% H_2/Ar and heating the sample from 50 to 800 °C at a rate of 10 °C/min. The desorbed species were measured using a mass spectrometer.

2.4.5. In-situ DRIFTS

For all measurements we used Harrick's Praying Mantis reactor cell equipped with a high pressure/ high temperature dome with ZnSe windows. The spectra were collected by a Thermo Fisher Nicolet IS50 spectrometer equipped with a mercury cadmium telluride (MCT) detector and KBr

beamsplitter. For each spectrum 128 scans were measured at a resolution of 4 cm^{-1}. The measurement time was approximately 1 minute.

Before the experiments the catalyst was reduced and dried as described before. The measurements were performed at 1, 5 and 30 bar. The background was taken in H_2 at 290 °C before switching to $1CO_2/3H_2$ to observe the reaction intermediates. Spectra were measured continuously for several hours.

2.4.6. CO Adsorbed XAS Experiments

Static atmosphere XAS experiments were conducted in transmission mode at the B18 Diamond XAS beamline. The Rb K-edge of the spent (carburized) Rb-doped CuZnFe was measured under Ar and 5% CO in N_2 using a custom gas XAS cell with Kapton tape windows. The air sensitive spent sample was prepared and transferred to the cell while maintaining an inert atmosphere using a glovebox. After measuring the sample in Ar, the sample inside the XAS-cell was flushed with 5% CO. Before the second Rb K-edge measurement, CO was let to adsorb for at least 20 minutes. The whole transfer and flushing process was conducted in oxygen-free condition.

All data normalization, background subtraction and analysis was performed using the Athena module of the Demeter software [213].

2.4.7. Solid-State Nuclear Magnetic Resonance (ssNMR)

Nuclear Magnetic Resonance Spectroscopy (NMR) is an indispensable analytical technique in the study of organic molecules. Its solid state variant (ssNMR) is particularly interesting for catalysis research. In this thesis solely ssNMR will be used. By using NMR analysis the structure of compounds containing NMR active nuclei can be determined. To do so, NMR relies on the nuclear spin properties of atoms contained in the sample and their interaction with external magnetic fields. Only nuclei which display such interaction will be "*visible*" to NMR analysis. Whether a nucleus is NMR active depends

on the angular dependence of the nuclear spin angular momentum quantum number. In the case of carbon this is particularly useful, because the naturally abundant ^{12}C is NMR inactive while, in contrast, the experimentally accessible ^{13}C isotope is NMR active. Hence, NMR is able to distinguish these nuclei. This allows for the study of not only the nature of the sample carbon chemistry, but the origin of the carbon atoms when performing a reaction between different carbon containing molecules. Indeed this is the primary way ssNMR was used in this thesis research (for further information see Section 2.4.8.2).

All ssNMR experiments were conducted at the Hong Kong Polytechnic University. The ^{13}C magic angle spinning (MAS) solid state Nuclear Magnetic Resonance Spectroscopy (ssNMR) spectra were collected on a JEOL ECZ500R NMR spectrometer with the Larmor frequencies of 124.501 MHz. The chemical shifts of ^{13}C were referenced to adamantine CH_2 peak at 38.48 ppm. The data was analysed using the Delta NMR Software.

2.4.8. Isotopic Labelling Experiments

In Chapter 5 considerable attention is paid to the elucidating the mechanistic interaction between benzene and CO_2 derived during methanol-mediated tandem CO_2 hydrogenation. In order to elucidate this interaction between different reagents during reaction, it is necessary to be able to distinguish atoms derived from each molecule. However, this is usually not possible, when the reagents and products contain the same elements (as is the case for CO_2 , benzene and their hydrogenation products (see Chapter 5)). Similarly, in a benzene methylation reaction using methanol, a priori it is not possible to distinguish the carbon in benzene from the carbon contained in methanol. To differentiate the carbon from the two reagents a different isotope can be used for one compared to the other. Then physical differences between the isotopes can be used to distinguish them. For instance, because the different isotopes (e.g. ^{12}C and ^{13}C) have a different atomic weight, the isotopologue distribution of the reaction product can be studied by GC-MS to understand the interaction between the reagents.

Moreover, the difference in nuclear spin (I) of ^{12}C versus ^{13}C can be exploited by performing NMR experiments using different combinations of isotopes of the reagents. Because NMR can only

"*see*" nuclei with spin , the formation of different carbonous species can be related to different reagents. For instance, in the methylation of benzene by methanol, if natural methanol is reacted with ^{13}C benzene, the NMR signal will be dominated by carbon species derived from benzene rather than methanol. Hence, by using different isotopes in combination with GC-MS and NMR the fate of carbon derived from the different reagents may be elucidated.

2.4.8.1. GC-MS ^{13}C scrambling experiments

In order to study the reaction mechanism and prove the direct involvement of benzene during the reaction, GC-MS isotopic labelling experiments were performed using ^{13}C labelled benzene and ^{12}C CO_2. The isotopologue distribution of propane was calculated to determine the fate of benzene during reaction. The reaction was largely the same as described in Section 2.2.5: in this case 50 mL ^{13}C labelled benzene was added to the composite catalyst; the reactor pressurized using Ar and CO_2/H_2, and reacted at 250 °C for 10 hours. After naturally cooling down the reaction gasses were analysed using GC-MS by manuel injection into a Split/Splitless inlet.

To determine the isotopologue distribution of propane, the method in [225] as described in [226] was used. The mass spectra of intact carbon skeletons were compared to a baseline spectrum obtained from gas injection of a commercial disposable lighter (FlameJack), based on the following assumptions:

1. Fragmentation rates are the same for all isotopologues;

2. The contribution of naturally occurring D (0.0002%) can be neglected;

3. The ^{13}C abundance of the commercial lighter is the same as that in nature (1.1%).

Given these assumptions, the mass spectrum of an isotopologue with carbon number c and n number of ^{13}C atoms (M_n^C) should be given by the elements:

$$m_n\,(\alpha\, +\, n)\, =\, m_0(\alpha) \tag{2.1}$$

where α is the index of the mass fragment ($\alpha \in \{0,1,2, \dots ,2n + 2 + c\}$) and the first elements equal to 0. For example, for propane with one ^{13}C atom we have M_1^3 = [0, m_1 (1), m_1 (2), … , m_1 (9)] = [0, m_0 (0), $m0$ (1), … , $m0$ (8)]. Furthermore, the mass spectrum of a mixture of isotopologues ($\mathcal{M}^c$) is given by a linear combination of these vectors (M_n^C) such that:

$$\mathcal{M}^c = \sum_0^c a_i \times M_i^C \, , a_i \leq 0 \tag{2.2}$$

where the sum runs over the index i. The coefficients a_i represent the ratios of the different isotopologues and can be found by restrained Ordinary Linear Squares (OLS) Regression, where M_i^C are the basis vectors and $a_i \leq 0$. Hence, $\mathcal{M}^c$ needs to be determined stepwise. First, M_0^C is calculated based on the following equations, then the remaining M_i^C can be constructed by shifting as per Eq. (2.1). Assuming a natural ^{13}C abundance of 1.1%, the first basis vector M_0^C can be calculated by using a binomial distribution. The probability of an ion fragment with c carbon atoms, of which n are ^{13}C, is given by:

$$P_n = \binom{c}{n} \times 0.011^n (1 - 0.011)^{c-n} = \left[\frac{c!}{n!(c-n)!}\right] \times 0.011^n \times (1 - 0.011)^{c-n}. \tag{2.3}$$

Therefore, we can write the corrected spectrum by iteratively subtracting the expected contribution of ^{13}C to the experimental spectrum:

$$m_{\,0}(\alpha) = \, m_{obs}(\alpha) - \frac{\sum_{n=1}^{c<\alpha} m_{\,0}(\alpha-n) \times P_n}{(1-0.011)^{c-n}}. \tag{2.4}$$

Here $m_{obs}(\alpha)$ refers to the experimentally measured peak area of fragment with index α, and $m_{\,0}(\alpha - n)$ is the corrected peak area of the previous mass fragment.

After calculating all the required basis vectors, the restrained OLS analysis was performed in OriginPro 2023.

Finally, the contribution of each isotopologue with n carbon ^{13}C atoms (Dn) as a percentage of the total is calculated using the OLS coefficients:

$$D_n = \frac{a_n}{\sum_0^c a_i} \times 100\% \, . \tag{2.5}$$

2.4.8.2. Solid State NMR ^{13}C scrambling experiments

To study origin of the carbon residue left on the tandem catalyst studied in Chapter 5, as well as the particular mechanistic role of CO_2 and aromatic co-feeds, a number of ssNMR experiments were conducted. As noted, by using a high concentration of ^{13}C in one of the reactant molecules, the reaction trajectory of this specific molecule can be studied while strongly limiting signal interference from the other reactants.

The ssNMR samples were prepared by performing catalytic reactions with different isotopologue reactant feeds. All reactions were performed at 250 °C at 46 ±1.5 bar total reaction pressure for 10 hours. Each reaction was carried out with either high or low ^{13}C CO_2 pressure (while retaining the over-all CO_2 pressure). In the low ^{13}C CO_2 pressure condition the autoclave reactor was first purged and evacuated using a vacuum pump before introduction of ^{13}C CO_2 from a gas sample bag. The total pressure was then increased using regular ^{12}C CO_2 and H_2 to arrive at a pre-reaction pressure of 26 ±1 bar and CO_2/H_2=1/3. In the high ^{13}C CO_2 pressure condition the autoclave reactor was pressurized to 7 bars using ^{13}C CO_2 and toped up with H_2 to 26 ±1 bar.

2.4.9. GC-MS trapped species

To analyse the nature of the species trapped inside the pores of zeolites post-reaction GC-MS analysis was conducted after dissolving the zeolite structure. All sample preparation and measurements described here were conducted at the research facilities of Doğu Anadolu Yüksek Teknoloji Uygulama ve Araştırma Merkezi in Yakutiye Turkey.

After reaction, 40 mg solids were collected and dissolved in 1.0 mL hydrogen fluoride (HF, 15%) solution. Then the organic species were extracted with 1 mL dichloromethane (CH_2Cl_2) and analysed by GC-MS. The methyl yield Y_i of the trapped methylated aromatic product was calculated by Eq. (2.6):

$$Y_i = \frac{A_i}{c_i} \times m_i \tag{2.6}$$

where A_i is the area of the peak from GC-MS, c_i is the number of carbon atoms and m_i is the number of methyl groups.

Chapter 3

Effect of Alkali Metals on CuZnFe Catalyst Structure:

Carburization and Re-Oxidation

3.1. Introduction

As was described in Section 1.3.1, alkali metal (AM) doping has been observed to induce significant changes to the structure of Fe and Cu based catalysts. In case of Fe, AMs seem to have a profound promotional effect on the formation of carbide surfaces, which in turn have been proven to be essential in the related FTS process. Moreover, it has been reported that AM doping may negatively affect the reducibility of Cu. Considering the potentially crucial role of Cu^0 for facilitating CO insertion, in addition to studying the impact of AMs on the phase composition of Fe in relation to the CO_2 hydrogenation behaviour, Chapter 3 also specifically discusses the observed impact of AM doping on the reducibility and oxidation state of Cu.

It is clear that to properly understanding the role of AMs on the formation of higher alcohols and olefins during CO_2 hydrogenation it is important to first layout the effect that AM doping on the structure of the catalyst: which phases are formed upon the inclusion of AMs and what is their effect on the surface composition. In Chapter 3 first the effect of K, Rb or Cs doping on the catalytic activity of CZF reported, then their effect on the composition of this catalysts is extensively studied using a wide range of analytical techniques. It is finally concluded that the changes in catalytic activity of our CZF doped catalyst cannot be fully understood in terms of changes in phase composition, i.e. changes in oxidation state of Cu, carburization of FeO_x or electron donation effects.

Overseeing the literature it becomes increasingly clear that the scientific efforts to establish the origin of the promotional effect of AMs exceedingly focusses on their effect on the assumed FeC_x and Cu^0 active phases: through electron donation and enhanced stabilization. The actual structure of the surface AMs is rarely investigated however. Although a few efforts have been made to understand the structural evolution of K under CO_2 hydrogenation conditions, both in the case of dispersed K [227,228] and bulk K particles [229,230], but these provide little in the way of a comprehensive understanding of the AM-TM surface interaction. In light of this, alongside an in-depth analysis of the effect of AMs on the evolution of the TMs during reduction and reaction, Chapter 3 also provides an analysis of the XPS results of K, Rb and Cs after reaction as well as a tentative analysis of Rb after CO_2 reaction by XAFS and STEM-EDX.

3.2.Results

3.2.1. Catalysis

The catalytic behaviour of AM doped and undoped CZF is illustrated in Figure 16 and Figure 17. As expected the addition of AMs has a significant impact on the product selectivity. In the absence of AMs the product distribution is largely dominated by paraffins and CO (see Figure 16). No more than 1.5 % of the product consists of HAs. Methanol selectivity drops from 4.0 % at 250 °C to 0 at higher temperatures. No olefins are detected at any temperature. This may be attributed to the relatively high concentration of Cu contained in the CZF catalyst, which has been associated with increasing the overall hydrogenation ability [82].

In contrast to the undoped catalyst, the formation of paraffins is significantly suppressed in the presence of AMs and the formation of olefins and higher alcohols is promoted (see Figure 16A). Notably, the observed olefin molecules are predominantly α-olefins. The higher alcohol selectivity increases in the order CZF<<K-CZF<Rb-CZF<Cs-CZF (see Figure 16B1 and Figure 17). For all AM doped samples the HA selectivity finds a maximum at 270 °C. At this temperature the HA selectivity is 13.6 , 12.0, 10.6 and 1.4 % for Cs-, Rb-, K- and undoped CZF respectively. Although the one-to-one differences are relatively small between the doped samples, these differences may nonetheless be considered statistically significant considering that: these materials were synthesized from the same batch; the typical analysis error observed for the HA selectivity during online GC measurements to be maximally 1.3%; and the increased HA selectivity over Cs-CZF compared to Rb-CZF, and Rb-CZF over K-CZF persists at 270, 290 and 310°C. In all cases the higher alcohols formed consist of ethanol and n-propanol (no iso-propanol is detected) with the majority of the higher alcohols consisting of ethanol. Propanol only makes up between 1.1 and 2.5 % of the product depending on the temperature and catalyst. Below 270 °C HA selectivity is lower, because the formation of C_{2+} products is more limited in line with a relatively sluggish C–C coupling reaction [107]; at temperatures higher than 270 °C the higher alcohols similarly decreases, while the olefin selectivity increases. Notably, the decrease in HA selectivity is entirely due to a decrease in the formation of ethanol rather than propanol. The selectivity of the latter increase with temperature in all cases.

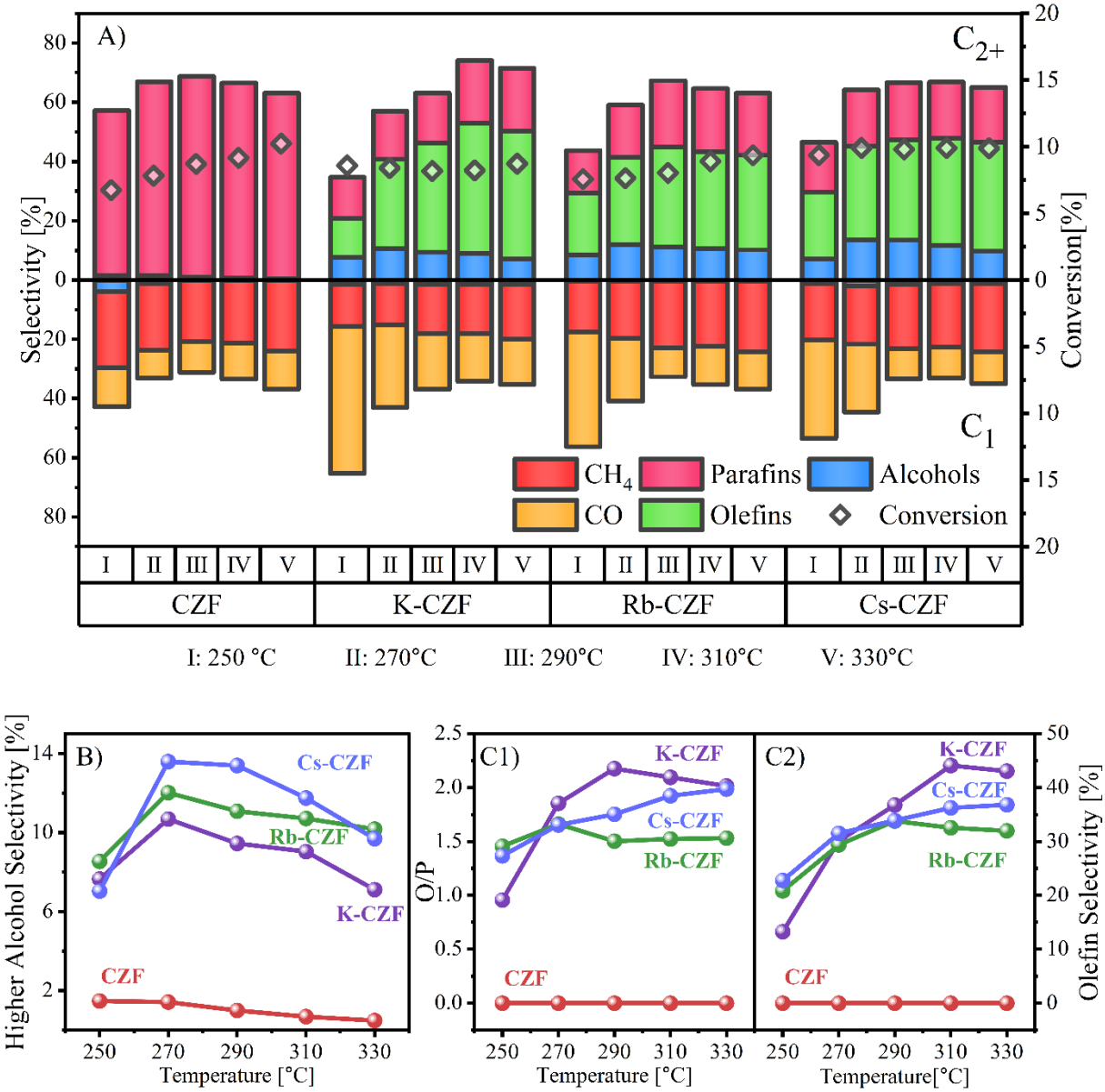

Figure 16| Catalytic results of AM doped and undoped CZF during CO_2 hydrogenation. Panel A shows the detailed catalytic data obtained for CZF, K-CZF, Rb-CZF and Cs-CZF are shown from left to right at each temperature segment from 250 to 330°C at 45 bar flowing a gas mixture of $CO_2/H_2/N_2$ with ratio 6.9/20.7/2.4: The CO_2 conversion is plotted with diamonds; the product distribution is shown as stacked columns. Products with a carbon number of 1 are plotted using negative values. The figure shows the transformation of paraffins to HAs and olefins upon AM doping. The data shown in panel B and C correspond to those reported in panel A, but highlight the trends in the selectivity towards HAs and the formation of olefins respectively. The olefin-to-paraffin ratio and olefin selectivity are shown in C1 and C2 respectively.

In contrast to the HA selectivity, the olefin-to-paraffin (O/P) ratio does not increase down the alkali metal group (see Figure 16B2). Instead, above 250 °C K-CZF has the highest O/P ratio followed by Cs-CZF, which has a higher O/P ratio than Rb-CZF. The olefin selectivity shows the same trend

above 290 °C: at 310 °C the olefin selectivity over K-CZF, Cs-CZF and Rb-CZF is 44.0, 36.2, 32.5% respectively; at 330 °C the olefin selectivity is 43.0, 36.8, 32.0% for the same catalysts. At temperatures below 290 °C the olefin selectivity is comparatively lower over K-CZF than suggested by the O/P ratio, due to relatively higher CO formation.

In fact, the formation of CO is significantly increased by K (27.8 %), Rb (21.4 %) and Cs (22.9%) at 270 °C compared to undoped CZF (9.5%). At 290 °C the CO selectivity drops most strongly for the Cs doped catalyst: 10.1% at 290 °C and 10.6 % at 310 and 330 °C. At those same temperatures CO selectivity drops consistently but less sharply over K-CZF. K-CZF shows a CO selectivity of 17.8 % (290 °C), 15.2 (310 °C) and 14.6 % (330 °C). In contrast Rb-CZF falls sharply to 9.7 % at 290 °C and then increases to 12.9 and 12.7 % at 310 and 330 °C respectively. The relatively lower CO selectivity of Cs-CZF may be related to coverage effects i.e. at the same weight percentage more K atom or Rb atoms are present at the surface than Cs atoms.

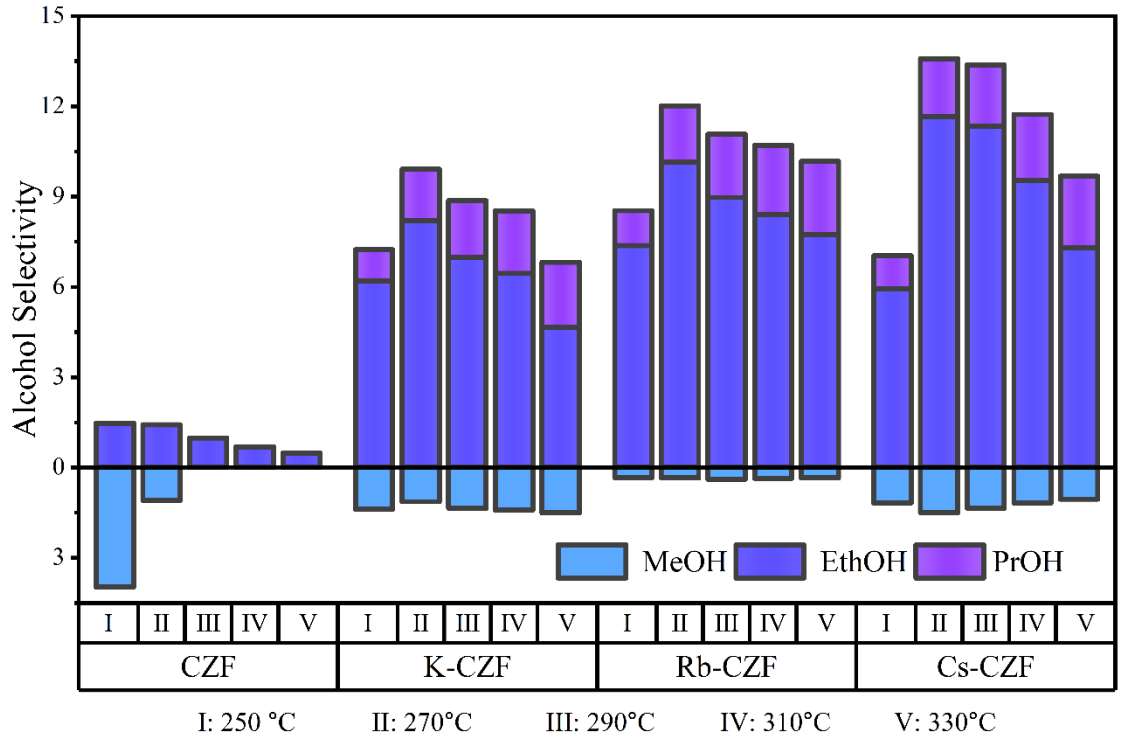

Figure 17| Detailed alcohol selectivity of CO_2 hydrogenation over AM doped and undoped CZF. Higher alcohols and methanol are plotted in the positive and negative direction respectively. These data correspond to the data presented in Figure 17.S19

Although the nature of the multi-carbon products changes considerably, as expected, the chain growth probability (α) largely remained unchanged (see Figure 18). The growth probability was calculated by taking the slope of a linear fit to the function $\ln(W_n/n)$, where W_n is the selectivity to products with carbon number n in accordance with the ASF distribution (see Section 1.2). In all cases a deviation from the ideal ASF distribution is observed: the growth probability appears smaller for hydrocarbons with carbon number <5, than for those with higher molecular weight. These different values are denoted by α_1 and α_2 respectively. While $\alpha_1$seems somewhat greater over CZF at 250 °C— 0.37 rather than 0.24, 0.27 and 0.29 for K-CZF, Rb-CZF and Cs-CZF respectively— it remains within error. At the same temperature α_2 is slightly lower for CZF at 0.60 compared to 0.68 , 0.66 and 0.65 as calculated for K-CZF, Rb-CZF and Cs-CZF respectively. No trend is observed for any other temperature and the calculated values remain largely within fitting error. Although similar *"double-ASF"* distributions have been reported previously for the hydrogenation of CO_2 over Fe-based catalysts with α values within the same range, the origin of this behaviour is not firmly established [231]. Amongst the proposed reasons it has been proposed that this type of deviation away from the ideal ASF distribution may imply the existence of two separate chain growth sites [231]. Assuming such an explanation and considering the stark change in the product distribution induced by AM doping in terms of the olefin and HA selectivity, the absence of any significant change to the chain growth probability upon AM doping is somewhat surprising. Evidently, while the nature of the coupled product clearly changes on aggregate the C-C coupling probability does not.

Nevertheless, it may be noted that some consistent changes to the specific hydrocarbon distribution are indeed observed for hydrocarbons with carbon number <5: while the selectivity of CZF towards propane is higher than towards ethane, the selectivity of AM doped catalysts towards C_2 products is higher than towards C_3 products (see Figure 18A). In fact, a linear relationship is found between the HA selectivity and the C_2/C_3 ratio (see Figure S18). To our knowledge such relationship has not been reported hitherto and the reason for such relationship remains elusive.

Evidently, doping AM has a much less pronounced effect on the total conversion of CO_2. In all cases the CO_2 conversion remains between 8.5 and 10 % depending on the catalyst. It is observed that

the conversion of doped samples are relatively less dependent on the temperature compared to their undoped CZF equivalent. In the absence of AMs the conversion increased from 6.7% at 250 °C to 10.2 % at 330 °C. In contrast, the conversion remains at 8.5±0.2, 8.5±0.9 and 9.6±0.3% for K-, Rb- and Cs-CZF respectively over the range of tested temperatures. Moreover, no significant changes were observed to the CO_2 conversion rate as the Rb or Cs amount was increased from 2 to 4 w.t.% or lowered from 2 to 0.9 w.t.% (see Figure 19).

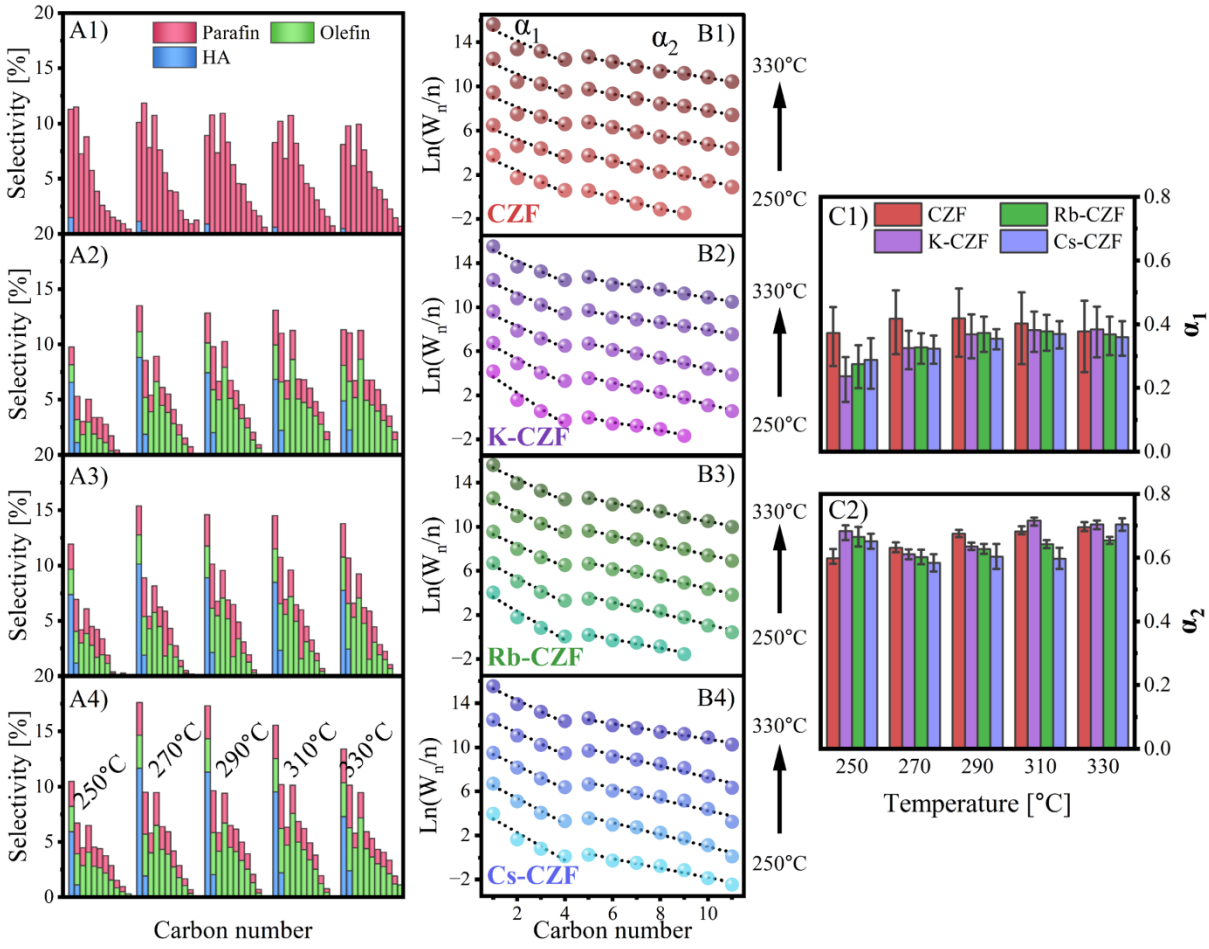

Figure 18| Distribution of multi-carbon products over alkali doped and undoped CZF catalysts. Panel A1, 2, 3 and 4 show a detailed distribution of the C_{2+} products formed over CZF, K-CZF, Rb-CZF and Cs-CZF respectively. Paraffins, olefins and higher alcohols are indicated in red, green and blue respectively. Panel B shows the result of applying the ASF function $\ln(W_n/n)$ to the raw data presented in panel A for each catalyst. The data are fitted by a double ASF model indicated by dotted lines fitted $C_{1\text{-}4}$ and C_{5+} product data points. The slope of each linear fit is used to calculate α_1 ($C_{1\text{-}4}$) and α_2 (C_{5+}). Panels C1 and C2 show the calculated α_1 and α_2 parameters for each catalyst at each temperature

Regarding the product selectivity the following observations were made: both Rb and Cs doped materials behave similarly regarding their HA selectivity when changing the doping concentration, but differently regarding the O/P ratio. In both cases the HA selectivity follows 2%>0.9%>4%. In contrast, the O/P ratio remains relatively unaltered at temperatures above 250 °C when changing the concentration of Rb on the doped catalysts, while the O/P ratio increases monotonically when going form 0.9 w.t.% Cs to 4 w.t.% for all temperatures evaluated.

To verify the consistency of these results a second batch of catalyst material was synthesized and tested before and after doping with 2 w.t.% Cs. The results of these tests are shown in Figure S14 (alongside the original data included in see Figure 16A) and remain consistent with those reported in Figure 16: little change is observed to the CO_2 conversion, but the C_{2+} products include a considerable amount of olefins and higher alcohols. Moreover, although it is observed that the repeated CZF batch shows relatively higher C_1 selectivity at 250 (58.2 %) and 270 °C (41.3 %) than the original batch (42.8 and 31.9% respectively %), this is carried over to the Cs doped analogue. The latter shows a C_1 selectivity of 59.7 versus 50.8 % at 250 °C and 43.6 versus 32.0 % compared to the original Cs-CZF catalyst. These additional tests clearly verify that the effect of Cs doping is to change the nature of the C_{2+} product, which is changed from consisting entirely of paraffins to containing a majority of olefins and higher alcohols after Cs doping.

The catalytic results clearly show the substantial effect of K, Rb and Cs on the formation of coupled products from CO_2 and H_2. It is found that all three AMs transform the paraffin rich product into olefins and higher alcohols instead. The remainder of this chapter (Chapter 3) attempts clarify the effect of K, Rb and Cs by studying their influence on the catalyst structure. This study extensively explores the catalyst carburization and oxidation state of the surface (XPS) and bulk of the catalyst (XRD, XAS and Mössbauer). The Cu and Zn XPS results will be evaluated by Wagner plots to deconvolute initial and final state effects due to the presence of AMs. Additionally, the distribution of AMs will be studied by a combination of ICP, XPS and microscopy techniques. Lastly, Rb will be used as a proxy to study the local environment of the AMs after reaction by XAS. In this way a complete picture is presented of the catalyst structural change due to AM doping.

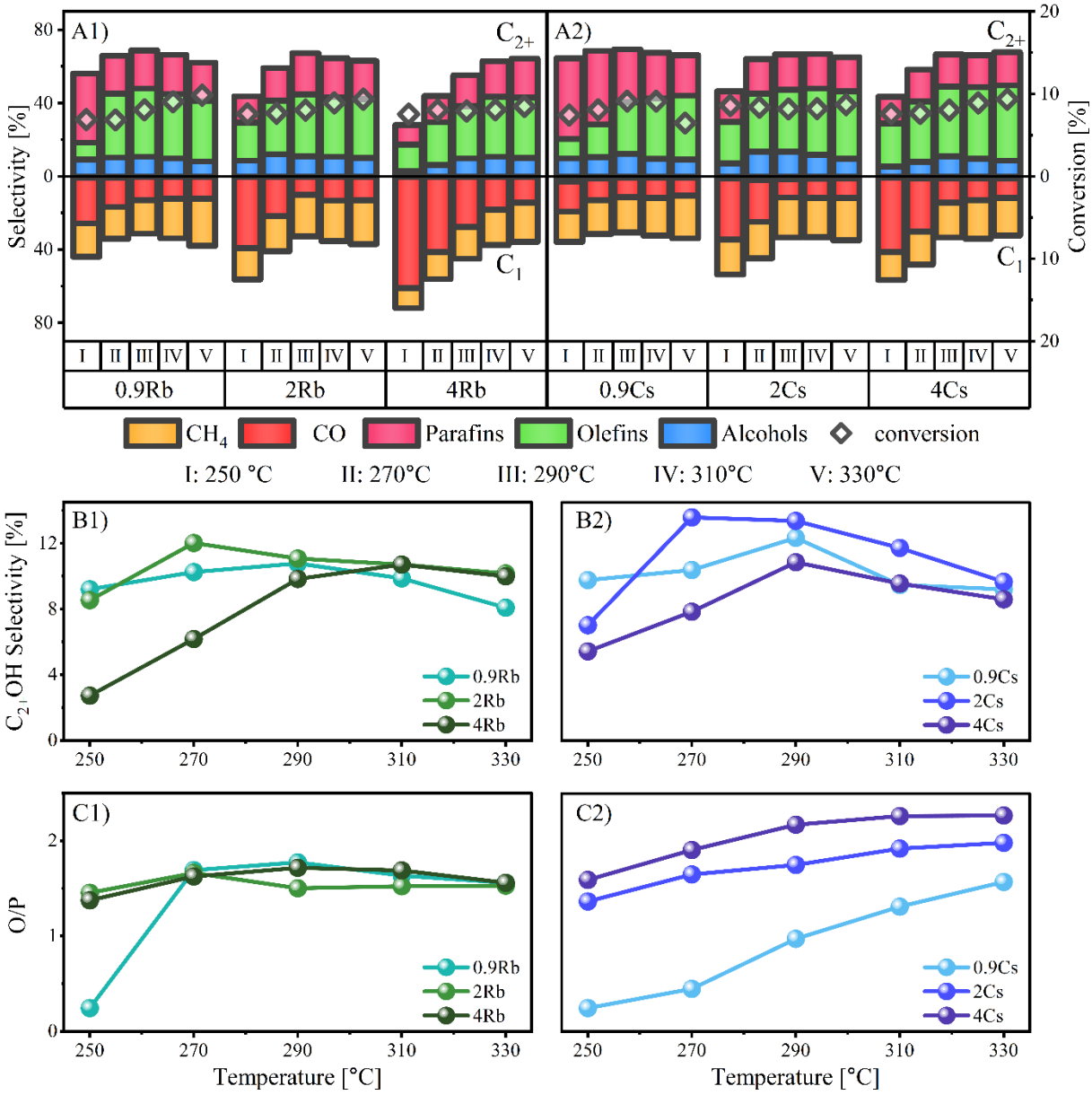

Figure 19| Catalytic results of CZF doped with varying amounts of Rb or Cs. Panel A shows the detailed product distribution and CO_2 conversion rate over catalyst doped with 0.9, 2 or 4 w.t.% Rb or Cs *from* 250 to 330°C at 45 bar flowing a gas mixture of $CO_2/H_2/N_2$ with ratio 6.9/20.7/2.Panel B1 and B2 show a comparison of the alcohol selectivity between the catalyst doped with different amounts of Rb and Cs respectively. Panel C1 and C2 show a comparison of the O/P ratio between the catalyst doped with different amounts of Rb and Cs respectively.

3.2.2. Characterization

The following sections explain the effect of AM doping on the catalyst by focussing on the catalyst structure characteristics with a focus on the formation of iron carbide and the oxidation state of Cu. In addition, the surface electron density and Madelung potential effects are investigated. To understand these effects more specifically the local environment of Rb (used as a proxy for all three AMs) is studied by EXAFS.

Before reporting the results of the advanced characterization experiments, the first few sections (3.2.2.1 and 3.2.2.2) report the ICP-MS and BET results to confirm the successful synthesis of the high surface area catalyst precursor and AM doped analogues. The ICP-MS results reported in Section 3.2.2.1. serve as a benchmark for analysing the elemental contribution measured in XPS (Section 3.2.2.5).

After showing that the synthesised catalysts have high surface area and contain the expected elemental concentrations, the effect of AM doping is explored by a number of standard and advanced characterization techniques. In addition to identifying the appropriate reduction temperature applied prior to the catalytic CO_2 hydrogenation reaction the H_2-TPR results in Section 3.2.2.3, also provide insights into the influence of alkali metal (AM) doping on the reducibility of the catalyst. The results show that AMs generally suppress the reduction of the catalyst and this depends on which AM is used. After that, Section 3.2.2.4 explores the crystallographic structure of the CZF catalyst before and after reaction and shows the effect of AM doping on the formation of Fe carbides after reaction. Compared to the non-doped catalyst the diffractograms of the AM-CZF catalysts after reaction show a steep decline in the Fe spinel phase related diffraction peaks and an increase in the χ-Fe_5C_2 crystal phase.

The final four sections of this chapter (3.2.2.5-3.2.2.7) show the advanced characterization of the AM doped and undoped catalysts to elucidate the surface and bulk effects of AM doping. The findings paint a complex picture of the effect of AM doping on the surface and bulk of the catalyst. XPS (Section 3.2.2.5.) is used to analyse the surface of the catalysts before and after reaction. In this section the surface oxidation state of the different elements is determined, the surface segregation of the AMs

is confirmed, and potential electron donation effects are discussed. The core-level excitation process (initial state effects) and Auger parameter (initial and final state effects) are analysed in terms of electron density changes and Madelung potential formation. Wagner plots are used to show that final state effects dominate the core-level peak shifts. The effect of AM doping on the TMs at the bulk of the catalyst is investigated by XAS (Section 3.2.2.6). From these results it is concluded that there is significant differences between the surface oxidation state of Cu/Fe and the bulk. Importantly the oxidation state at the bulk shows similar trends as the surface: AMs promote the formation of reduced metal centres. In the same section (Section 3.2.2.6) the local environment of Rb is also explored by EXAFS and XANES to show whether it is present as Rb pairs, clusters or single atoms. Because neither XPS nor XAS is able to entirely elucidate the transformation of Fe upon reduction and carburization *in-situ* Mössbauer Spectroscopy was performed. The results are reported in Section 2.3.5. Clear differences between the experimental results are observed and discussed. The differences between the different techniques give valuable insight into the AM promoted carburization of the tested catalysts. Lastly, the observations relating to the structure of the catalysts are confirmed by TEM-EDX analysis in Section 3.2.2.7.

3.2.2.1. Inductively Coupled Plasma Mass Spectrometry (ICP-MS)

ICP-MS was used to verify the expected elemental amounts of the doped and undoped samples after calcination. The results are shown in Table 1. Note that the weight percentages reported here do not sum to 100 due to the large proportion of oxygen present in the calcined samples. Nevertheless, after normalizing the weight percentages according to the atomic weight of each element, the measured chemical formulae are very close to the theoretical.

Table 1| ICP results of doped and undoped samples after calcination. The data show a close agreement between the theoretical and measured chemical formulae of the samples, for which oxygen represents the remainder.

Sample	Cu *[wt.%]*	Zn *[wt.%]*	Fe *[wt.%]*	AM *[wt.%]*	Measured Formula*	Theoretical Formula*
CZF	24.57	17.85	15.65	0	$Cu_{4.112}Zn_{2.905}Fe_{2.983}$	$Cu_4Zn_3Fe_3$
K-CZF	28.47	22.11	17.50	1.78	1.78K-$Cu_{4.073}Zn_{3.076}$ $Fe_{2.851}$	2K-$Cu_4Zn_3Fe_3$
Rb-CZF	27.76	21.72	17.54	1.88	1.88Rb-$Cu_{4.034}Zn_{3.067}Fe_{2.899}$	2Rb-$Cu_4Zn_3Fe_3$
Cs-CZF	26.84	20.66	16.82	1.93	1.93Cs-$Cu_{4.063}Zn_{3.039}Fe_{2.898}$	2Cs- $Cu_4Zn_3Fe_3$

**The formulae are presented in the form XAM-$Cu_xZn_yFe_z$, where x, y and z are the atomic ratios of the TMs, AM is Cs, Rb or K, and X is the weight percentage of the AM.*

3.2.2.2. Brunauer-Emmett-Teller (BET)

The BET surface area of the freshly synthesized CZF and calcined CZF have been measured by BET analysis. The BET surface area is measured to be 256 m^2/g before calcination and 176 m^2/g after calcination. Unsurprisingly, the total surface area decreases after calcination due to the formation of aggregates at high temperature. A Type II isotherm was observed in both cases, which is consistent with the expected high surface area non-porous nature of the materials [232].

3.2.2.3. Hydrogen Temperature Programmed Reduction (H_2-TPR)

H_2-TPR is a convenient method to evaluate the effect of dopants on the reducibility of the catalyst. In the current research H_2-TPR is also used to inform the minimal temperature required to fully reduce Cu before reaction. By measuring H_2-TPR profile of calcined CZF, K-CZF, Rb-CZF,Cs-CZF catalysts the hypothesis that

AM doping inhibits the reduction of Cu and Fe

is tested.

The H_2-TPR profiles of calcined CZF, K-CZF, Rb-CZF,Cs-CZF are presented in Figure 20. Broadly two regions can be distinguished, a high temperature and a low temperature region. The main lower temperature peak can be attributed to the reduction of Cu to Cu^0 [82], while the less defined broad peak from 400 to 700 °C can be attributed to the partial reduction of Fe [82].

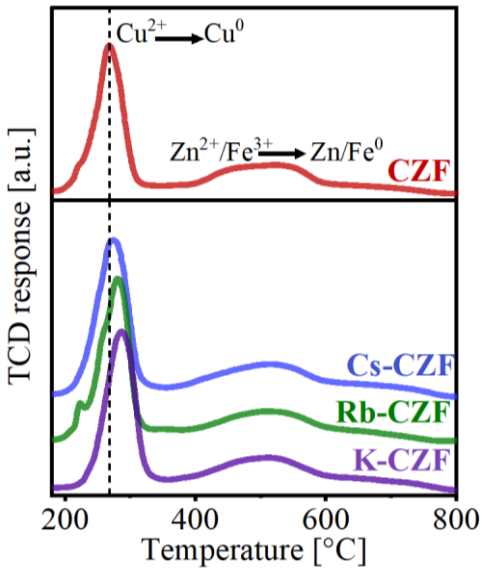

Figure 20| H_2-TPR of calcined samples using 5% H_2 in N_2. The reduction curve of CZF, Cs-CZF, Rb-CZF and K-CZF are shown in red, blue, green and purple respectively. A dotted reference line indicates the position of the main reduction peak observed for CZF.

As predicted the Cu peak shifts to higher temperatures upon AM doping in the order CZF (267 ℃) < Cs-CZF (273 ℃) < Rb-CZF (280 ℃) < K-CZF (285 ℃). Note, the increase in the Cu reduction onset temperature going up the AM group may be due to a larger coverage effect at the same weight percentage for the lighter AMs. No clear shift in the high temperature reduction region is observed upon the inclusion of AMs.

These results have educated the choice reduction temperature of 360 ℃, which, based on these results, should be sufficient to fully reduce Cu^{2+} to Cu^{0}.

3.2.2.4. X-Ray Diffraction (XRD)

Although the crystallographic data may give limited information about the surface or electronics of the catalytic site, it does provide preliminary information on phase changes during reaction as a result of AM doping.

Based on the available literature, which was discussed previously, it is hypothesized that

1. *After reduction CZF shows a combination of Cu, ZnO, Fe^0 and FeO_x;*
2. *After reaction iron carbide phases are formed from Fe^0 and FeO_x;*
3. *AM doped samples present a higher fraction of Fe carbide phases relative to Fe oxide phases than CZF;*
4. *K, Rb and Cs show similar degrees of carbide formation after reaction as indicated by XRD.*

To test these hypotheses the diffractograms of CZF, K-CZF, Rb-CZF, Cs-CZF were measured after reaction (referred to as "spent"). Additionally, CZF was measured after reduction without exposure to air. Figure 21 and Figure 22, show the result of these measurements. The reduction was performed by treating the calcined catalyst precursor in a stream of 5% H_2/N_2 at 360 °C for 2 hours in a tube furnace. After cooling down the reactor tube was flushed with N_2, sealed and transferred to a glovebox to prepare the XRD sample without contact to air.

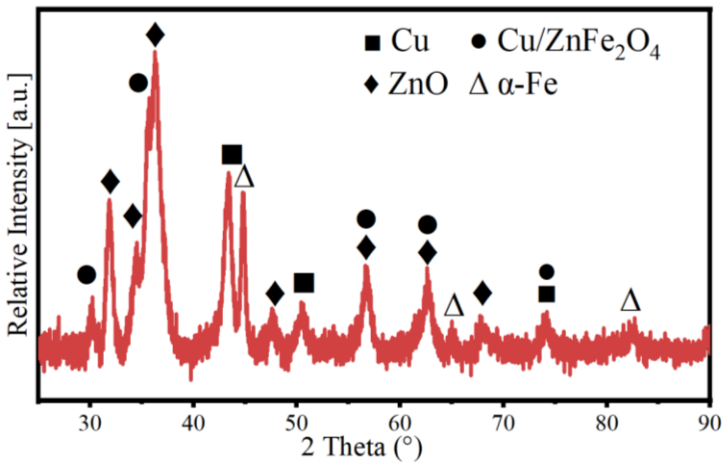

Figure 21| Diffractogram of reduced CZF sample. The diffractogram was measured after reduction of the calcined catalyst precursor by exposing it to 5% H_2/N_2 at 360 °C for 2 hours in a tube furnace. The diffraction peaks corresponding to Cu^0 , α-Fe, ZnO and the Fe spinel phases are indicated by ■, Δ, ♦ and ● respectively.

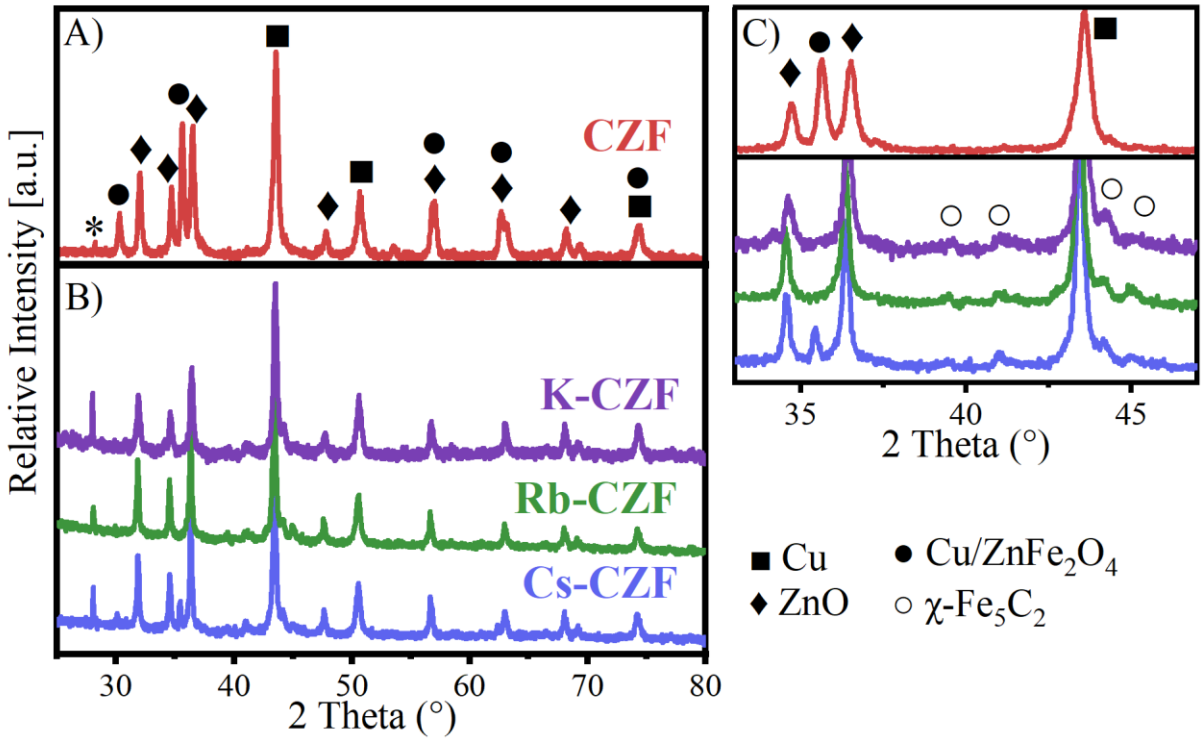

Figure 22| XRD of spent doped and undoped samples. Panel A show the diffractogram obtained from spent (after CO_2 hydrogenation) CZF in red. Panel B shows the diffractograms of K-CZF, Rb-CZF and Cs-CZF after reaction in purple, green and blue respectively. Panel C shows an enlarged region from 33 to 47 °.

As expected, after reduction characteristic peaks for ZnO (at 36.3°, 31.8° and 34.5°), α-Fe (at 44.9°, 65.0° and 82.7°) and Cu^0 (at 43.4°, 50.4° and 74.2°) are clearly visible. Similarly, a spinel phase (SP) is observed with a major peak at 35.6°. Considering the similarity between spinel Fe_3O_4, $CuFe_2O_4$, $ZnFe_2O_4$, no unequivocal statement can be made about the presence of any one of these phases in particular.

Regarding carburization during reaction, indeed after reaction small new peaks are obtained around 39.4° and 41° as well as a shoulder at 44.4° is observed. These can be assigned to either ε-Fe_2C (36-1249) or χ-Fe_5C_2 (89-8968). At the same time the diffraction peaks related to Fe^0, which was previously observed in CZF after reduction, has entirely disappeared. It must be noted that, although the FeC_x related peaks have low intensity in all cases, they seem particularly lacking in the absence of AMs, in which case only the shoulder at around 44.4° is clearly visible. Moreover, the relative peak intensity of the Fe spinel phase (e.g. at 35.6°) decreases steeply upon the introduction of AMs compared to CZF.

This clearly suggests the transformation of the crystalline SP phase into the less crystalline iron carbide phases. In the case of K and Rb the peak at 35.7 vanishes entirely, while a small peak remains for Cs-CZF. In this respect, K and Rb seem more efficient at promoting the formation of iron carbide type phases than Cs. Interestingly, the increase in carburization for K-CZF and Rb-CZF compared to Cs-CZF and CZF does not correlate positively with higher C_{2+} product selectivity (see Figure 16 in Section 3.2.1.). Nor does the selectivity to olefins or higher alcohols over K-CZF, Rb-CZF and Cs-CZF correlate with the decrease in the Fe spinel phase diffraction intensity. Hence, the changes in catalytic behaviour in terms of the olefin and higher alcohol formation cannot be reduced to the efficient conversion of crystalline SP to FeC_x. Importantly, however, these diffraction data give limited insight into the carburization at the surface of these catalyst materials. To shed light on the surface oxidation states and carburization Section 2.3.3 presents the XPS spectra of these materials obtained before and after reaction.

Lastly it can be noted that no diffraction peaks are observed for AM related crystal phases (AM carbonates, (per/super-)oxides or hydroxides). Moreover, none of the doped AMs induces a shift of the TM crystal diffraction peaks. These observations suggest that, while the AMs doped atoms are not integrated into the TM crystal lattice (as expected considering their significantly greater atomic radius), they do not form large crystalline particles either. Instead, the AMs are likely highly dispersed at the surface of the crystalline particles. The XPS results presented in the following section will further elucidate the surface presence of the doped AMs.

3.2.2.5. X-Ray Photoelectron Spectroscopy (XPS)

Here the results of the XPS measurements of both AM-doped and undoped samples are discussed. The main focus here is on the XPS spectra obtained after the reaction, but key differences between the reduced and reacted samples will be addressed as well. The samples after reaction are measured after collecting the catalysis data as previously presented and were transferred to the glovebox to prevent oxidation. Similarly, the reduced samples were transferred inertly by using a sealable tube reactor, which was transferred to a glovebox before collecting the sample material. The XPS data are incredibly valuable to build understanding of the catalysts surface. The analysis of the core-level and Auger peaks of the different elements provides invaluable information on the interaction between the AM dopants and TMs. More specifically, the effect of AM doping on the oxidation state and electron density of Cu, Zn, and Fe surface atoms in the catalyst was investigated using XPS analysis. Considering the TPR and XRD results the first hypotheses addressed here are:

1. *Cu chiefly presents as Cu^0 before and after reaction regardless of AM doping;*
2. *Zn presents as Zn^{2+} before and after reaction;*
3. *Fe presents with a combination of Fe^{2+}, Fe^{3+} and Fe^0 before and after reaction.*

Furthermore, the chemical state of the AMs was evaluated. Based on the highly electro positive nature of the AMs, it is hypothesized that:

4. *AMs are in a 1+ oxidation state with a BE indicative of adsorption on metal oxide surfaces.*

Additionally, the XPS data may further elucidate the carburization effects (as suggested by XRD) by directly quantifying the relative abundance of Fe^{2+}, Fe^{3+} or Fe^0 at the surface after CO_2 hydrogenation. The fifth hypothesis tested here is that

5. *After reaction the relative abundance of surface Fe^0 increases as K-CZF>Rb-CZF>Cs-CZF>>CZF.*

Unfortunately, Fe 2p spectra are inherently challenging to interpret, because the presence of multiple Fe phases and oxidation states may result in a large number of overlapping multiplet and satellite peaks. In the absence of a suitable theoretical model for the studied samples, a fixed set of intercorrelated

reference peaks were used as proxies for the different oxidation states [233].For each oxidation state, the total integrated area of its reference peak envelope is taken as a measure of its relative abundance.

Additionally, noting the surface sensitivity of XPS, the data presented here (combined with XAS Section 2.3.4) may further elucidate surface-bulk discrepancies: on the one hand, it has previously been suggested that carburization of FeOx type materials may result in a Fe_3O_4@(FeC_x-Fe_3O_4) core-shell structure with a relatively large amount of oxide rich surface and carbidic bulk due to continuous oxidation and carburization of the Fe surface. On the other hand, it has been shown that α-Fe is very unstable under CO_2 hydrogenation conditions and its rapid carburization might lead to an increased amount of FeC_x at the surface relative to the bulk [103]. Hence it is hypothesised that

6. *There is a significant difference in the abundance of Fe^0 at the surface and the bulk after reaction.*

This hypothesis is partially tested by XPS (surface) and partially tested by XAS and Mössbauer spectroscopy (bulk) (Section 3.2.2.6 and 3.2.2.6 respectively).

Similarly the surface-bulk distribution of the AMs can be determined by comparing the abundance measured by XPS to the total concentration determined by ICP (see Section 3.2.2.1). Based on the nature of the alkali metals, it is hypothesized that

7. *K, Rb and Cs are concentrated at the surface of the catalyst.*

The distribution of the AMs is critical considering the surface sensitive nature of catalysis. Furthermore, any electron donation effects from the AMs to the TM, as is commonly suggested [23,73,81,128,234–236] can be determined by XPS. The literature suggests that

8. *AMs donate electrons to the transition metals in the catalysts.*

To rigorously test hypothesis 8, three different factors are taken into account: the binding energy determined from the core-level peak position, the modified Auger parameter, and the TM–O absorption energy separation. Only by considering all three together can misleading effects, such as surface charging or variations in the work function, be excluded and robust conclusions be drawn.

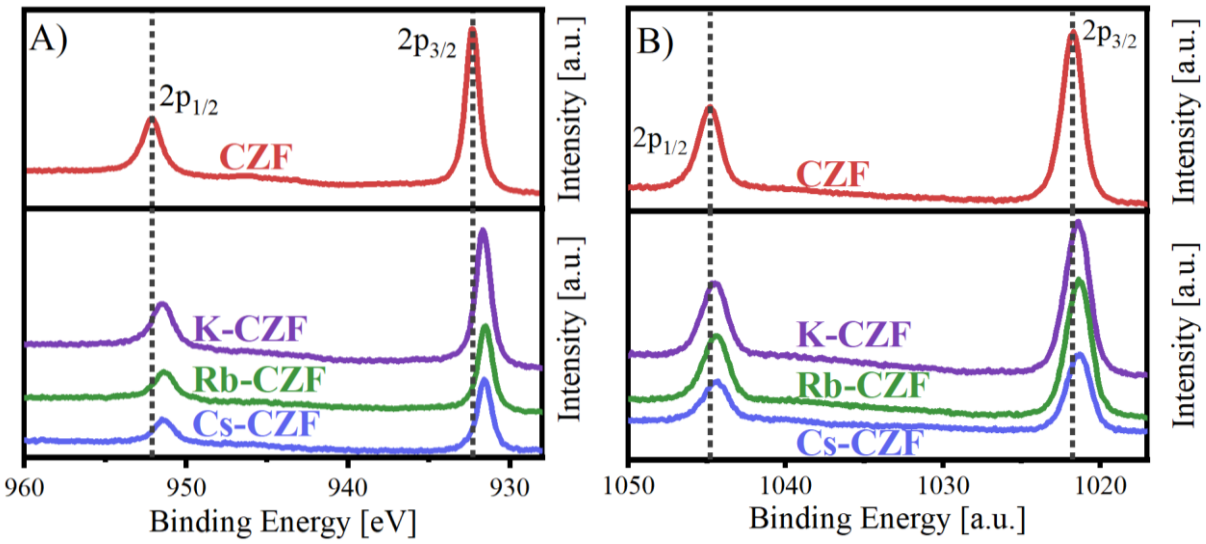

Figure 23| Cu and Zn 2p XPS spectra of spent samples. The Cu and Zn 2p spectra are shown in panel A and B respectively. In both cases a dotted reference line is centred at the CZF peaks. The data were obtained after CO_2 hydrogenation testing.

The core-level Cu 2p, Zn 2p and Fe 2p spectra obtained for CZF, K-CZF, Rb-CZF and Cs-CZF after reaction are presented in Figure 23A, Figure 23B and Figure 24 respectively. The Cu LMM Auger spectra can be found in the appendix. It can be noted qualitatively that the Cu and Zn 2p spectra of the AM doped samples present the same overall shape and peak position. Hence, the discussion here will focus mainly on differences between the AM doped and undoped samples, rather than the differences between the AM doped samples. The TM spectra of Cu, Zn and Fe are discussed in that order.

Before addressing the Cu 2p and LMM spectra, a few limitations must be noted: on the one hand, the presence of Cu^{2+}, can be easily confirmed by considering the presence of strong satellite peaks around 9 eV above the $2p_{3/2}$ core-level excitation peak [212]. In the absence of such peaks it can be concluded that Cu^{2+} is not present. On the other hand, Cu^{1+} and Cu^{0} are notoriously difficult to distinguish let alone quantify using the 2p core-level excitation spectra. This is due to the similar line shape and small BE separation (0.17 eV) of the 2p peaks expected for these two oxidation states of Cu [212]. Fortunately, the prevalence of Cu^{1+} and Cu^{0} can be determined by considering the Cu LMM spectra instead, whose shape is distinctly different for Cu^{1+} and Cu^{0} [212]. The raw and Cu LMM spectra can be found in Figure S19 and Figure S20 respectively.

The contribution of Cu^0, Cu^{1+} and Cu^{2+} to the Cu LMM spectra is shown in Figure 26. It is found that, after reaction, Cu is fully reduced to Cu^0 in the doped samples. The spectra show a single sharp peak around a KE of 918.9 eV, indicative of Cu^0. In contrast, the Cu LMM spectra of CZF presents two strong features at KE of 918.8 and 916.9 eV, which indicate both Cu^0 and Cu^{1+}. Indeed, the fitting shows the co-existence of Cu^{1+} and Cu^0 for CZF after reaction.

On the one hand, the more oxidized nature of Cu in the absence of AMs is somewhat surprising considering H_2-TPR results (Section 3.2.2.3), which showed that the presence of alkali metals suppressed the reducibility of Cu. On the other hand, the Cu LMM spectra of the samples before reaction (after reduction) show the reverse picture. In this case, Cu seems more reduced in the absence of AMs. These results indicate that the AM dopants have a critical role in stabilizing Cu^0 under reaction conditions, rather than increasing the reducibility of Cu outright.

The oxidation state of Zn can straightforwardly be done by evaluating the Auger parameter. The values of the Zn modified Auger parameters, reported in Table 2, range from 2010.0 to 2010.1 eV, which is indicative of Zn^{2+} in all cases, without any significant differences between the samples.

As noted before, the analysis of the surface oxidation state of Fe is rather difficult. Nevertheless, an important difference between the doped and undoped sample Fe 2p spectra is immediately visible. Rather than the two broad peaks centred around ~710.7 (2p 3/2) and ~724.4 eV (2p 1/2) observed for CZF, the AM doped samples show two smaller broad peaks at ~709.4 (2p 3/2) and ~718.8 eV (2p 1/2). Most strikingly, the AM doped catalysts present a strong sharp peak around 706.0 eV, which is indicative of Fe^0. The presence of Fe^0 proves of the increased surface carburization induced by AM doping.

To get some more insight into the relative amounts Fe^{2+}, Fe^{3+} and Fe^0, theoretical reference data can be used to fit the spectra. More specifically, the contribution of Fe^{3+}, Fe^{2+} and Fe^0 were determined by using a set of intercorrelated peaks previously reported [233]. The peak position was allowed to vary in a narrow range to achieve an acceptable fit.

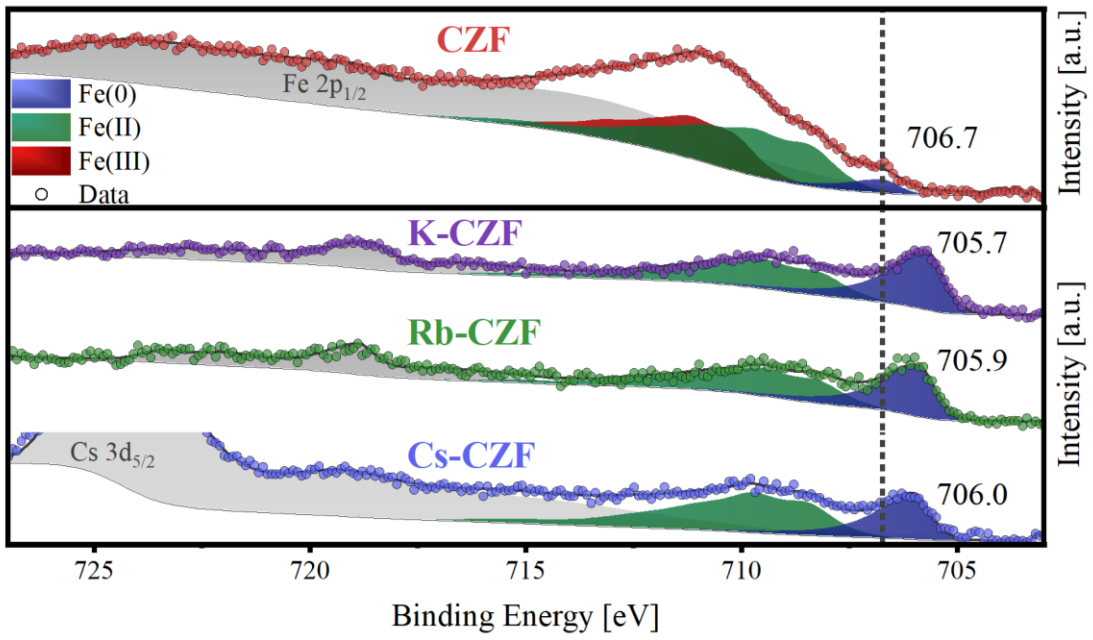

Figure 24| Fe 2p XPS spectra of spent samples. The spectra obtained for CZF, K-CZF, Rb-CZF and Cs-CZF are plotted in red, purple, green and blue respectively. The contribution of Fe^0, Fe^{2+} and Fe^{3+} is illustrated by the blue, green and red areas respectively. The grey area indicates the arbitrarily fitted $2p_{1/2}$ region. A grey line indicates the fit. The binding energy measured for the $2p_{3/2}$ of Fe^0 is indicated on the right in eV. The dotted reference line is centred at 706.7 eV (the Fe^0 $2p_{3/2}$ peak measured for CZF). The data were obtained after CO_2 hydrogenation testing.

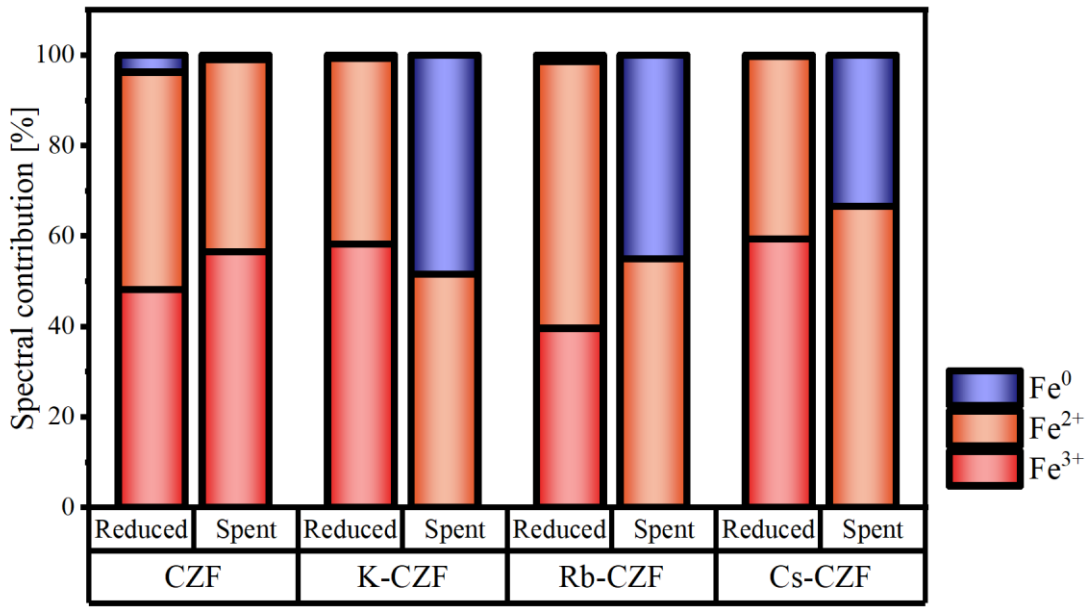

Figure 25| Fe XPS $2p_{3/2}$ peak fitting. The surface oxidation state of Fe for various samples before and after reaction based on the Fe $2p_{3/2}$ spectrum. The spectral contribution of Fe^0, Fe^{2+}, Fe^{3+} are shown in blue, orange, and red respectively. The values are calculated using the standard spectra reported in Ref. [233].

For this analysis only the $2p_{3/2}$ excitation is considered. In the absence of theoretical reference data for the Fe $2p_{1/2}$ region, it is fitted arbitrarily providing a sensible backdrop to apply the 2p 3/2 model.

The analysis reveals that the Fe surface oxidation state of the undoped sample consists chiefly of Fe^{2+} (56.5%) and Fe^{3+} (42.5%), while the AM doped samples show a combination of Fe^0 and Fe^{2+}. The Fe^0 relative amount increases in the order of K-CZF(48.4)>Rb-CZF(45.0%)>Cs-CZF(33.4%)>>CZF (1.0%). Note, that the deconvolution of the Fe 2p 3/2 region of Cs-CZF is further implicated by the Cs 1s region. Clearly, AM doping promotes the formation of reduced Fe, which is likely in the form of FeC_x.

Focusing on the alkali-metal contributions in the XPS survey spectra, the intensities associated with K, Rb, and Cs are substantially higher than would be anticipated from their bulk concentrations (~2 wt.% according to ICP; Section 3.2.2.1). Quantitative analysis of the survey spectra yields surface atomic abundances of 26% (K), 21% (Rb), and 23% (Cs). While these values should be interpreted cautiously due to their sensitivity to background subtraction and integration parameters, the fact that they exceed the ICP-derived bulk values by approximately an order of magnitude provides clear evidence that the alkali metals are concentrated at the catalyst surface.

To evaluate the high resolution scans of the spent samples, it is useful to compare the measured core level binding energy (α of the AMs (Cs $3d_{5/2}$, Rb $3d_{5/2}$, K $2p_{3/2}$)) to their pure hydroxides, oxides and carbonate analogues. Importantly, the AM BEs do not correspond to their respective carbonates, which were used during the impregnation, nor do they correspond to the BE values expected for their respective hydroxides or oxides. In fact the values obtained fall in between the latter two: the measured BEs are 0.2-0.8 eV higher than expected for the pure AM hydroxide (see Table 3); and although no data is available for K_2O, in the case of Rb and Cs the measured BEs are 0.4 and 0.6 eV lower than their oxide respectively. This clearly shows the carbonate reagent used during the impregnation was converted into a chemical species unlike the simple hydroxide or oxide.

Table 2| Auger and TM-O/2p-2s separation values of samples after reaction. All Auger parameters of Cu and Zn are within error. The TM-O/2p-2s separation of Cu, Zn and Fe shrink upon AM doping.

Sample	Cu			Zn			Fe	
	α *[eV]*	TM-O** *[eV]*		α *[eV]*	TM-O** *[eV]*		TM-O*** *[eV]*	
CZF	1851.0*	402.0	-	2010.1*	491.4	-	176.4	-
K-CZF	1851.2*	401.6	0.46	2010.0*	491.3	0.12	176.0	0.45
Rb-CZF	1851.0*	401.5	0.56	2010.0*	491.3	0.14	175.9	0.52
Cs-CZF	1851.2*	401.6	0.45	2010.0*	491.3	0.11	175.9	0.52

**This modified Auger parameter (α) is calculated as is the convention by summing the TM peak maximum BE and the Auger peak maximum KE.*

***The TM-O/2p-2s separation is calculated by subtracting the lattice oxygen peak position form the TM 2p peak maximum position. The values are rounded to 1 decimal.*

****For Fe the TM-O/2p-2s separation is calculated by subtracting the lattice oxygen peak position from the fitted Fe^0 peak position. The values are rounded to 1 decimal.*

Table 3| XPS AM core level binding energies for doped samples after reaction. The measured values are compared to literature values for the pure AM oxides and hydroxides. This comparison shows that the measured values are constantly between the oxide and hydroxide.

Sample	Measured AM BE *[eV]*	Expected* AM oxide BE *[eV]*	Expected** AM hydroxide BE *[eV]*
K-CZF	292.9	-	292.1
Rb-CZF	109.8	110.2	109.3
Cs-CZF	724.4	725.2, 725.1	724.2

** BE values correspond to K 2p 3/2, Rb 3d 5/2 and Cs 3d 5/2.*

***The expected BE values for the AM oxides can be found in Ref. [237–239].*

**** The expected BE values for the AM hydroxides can be found in Ref. [240–242].*

In fact, in the case of K, the $2p_{3/2}$ core level binding energy is consistent with previous reports of K interacting with oxide surfaces like TiO_2 (292.8-293.2 eV) [243] or FeO (292.7 eV) [244]. This behaviour shows that the electronic environment of the BEs is significantly perturbed by the catalyst surface, implying a genuine interaction between the two.

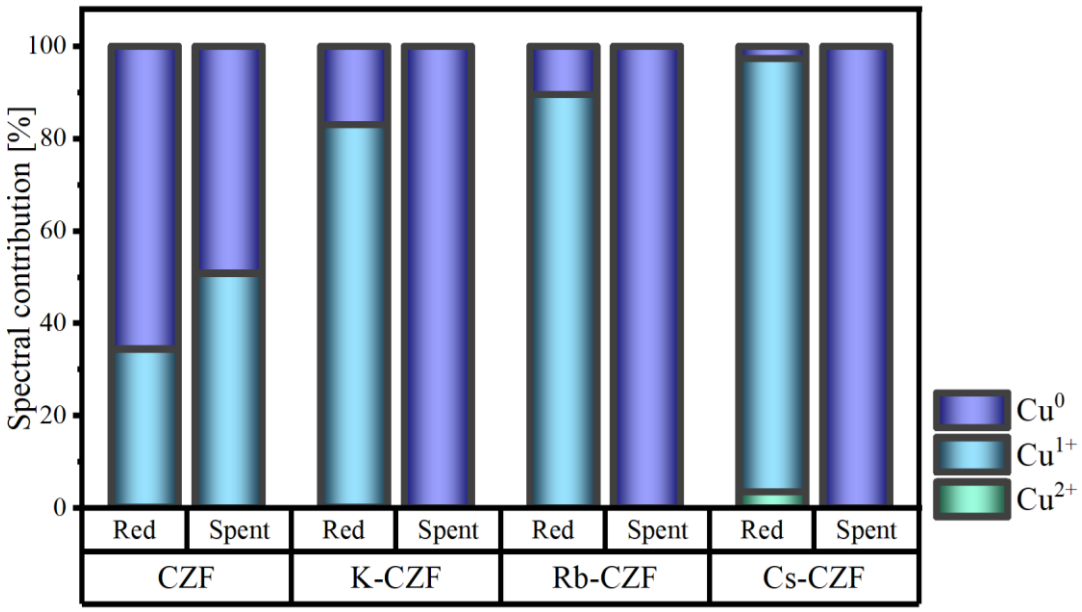

Figure 26| Cu Auger peak fitting. The surface oxidation state of Cu for various samples before and after reaction based on the Cu LLM spectrum. The spectral contribution of Cu^0, Cu^{1+}, Cu^{2+} are shown in dark blue, light blue, and green respectively. The values are calculated using the standard spectra reported in Ref. [212]

When Cs or K are deposited on metallic surfaces in the absence of oxygen the BE is reported to be considerably higher than was measured here. For instance, upon depositing Cs on Cu the Cs $3d_{5/2}$ BE is 0.8-1.1 eV higher than for Cs-CZF after reaction [245,246]. Similarly there are a number of publications on the electronics of K on metal surfaces (Ag [247], Co [248], Fe [249], Ni [250], Pd [251]). These studies also consistently show binding energies which are 0.8-1.25 eV higher than obtained for K-CZF. Such values are much closer to metallic K (294.7 eV) [249]. When deposited on such metallic surfaces K may even show plasmons loss features, which are characteristic of K metal [244,247,249,252]. Similarly, plasmon tailing features have been observed for Cs 3d spectra after deposition on metallic Cu [253]. Such features disappear upon dosing O_2. Hence the absence of plasmon loss features underpins that the doped AMs are present in oxidized from. Nevertheless, AMs may be present on reduced Cu or FeC_x surfaces if anchored by oxygen.

The interaction between of the AMs and TMs is further reinforced by closely evaluating the TM-O/2p-2s separation of Cu, Zn and Fe. This value is calculated by subtracting the O 2s lattice peak position from the TM core level peak maximum. Importantly, this value is independent of potential

surface charging occurring during measurement and is therefore a more reliable metric than the absolute core-level peak position. As can be seen in Table 2, the gap shrinks in the presence of AMs. For Cu the gap shrinks by 0.45-0.56 eV and for Zn the separation shrinks by 0.11-0.14 eV. The TM-O/2p-2s separation for Fe shrinks by roughly the same magnitude as Cu: 0.46-0.52 eV. These changes in the TM-O/2p-2s separation are entirely due to a shift of the TM peaks rather than the O 2s lattice peak. At face value, such peak shift may be attributed to electron transfer from the more electropositive AMs to the more electronegative TMs via electron donation. However, such electron donation should lead to a corresponding change in the modified Auger parameter due to stabilization of the cationic exciton. Such a change is not observed for Cu or Zn (see Table 2). The simultaneous shrinking of the TM-O/2p-2s separation with an unperturbed Auger parameter implies no genuine electron transfer has occurred. Instead the shift of the TM core level is due to the proximity of the positively charged AM cation causing a positive Madelung potential near the surface of the catalyst [254].

The contribution of initial state (Madelung potential) and final state effects (e.g. electron screening/electron donation) to the Cu and Zn spectra are clearly illustrated by the Wagner plots in Figure 27. In such plots the data are evaluated using two reference lines, which pass through some

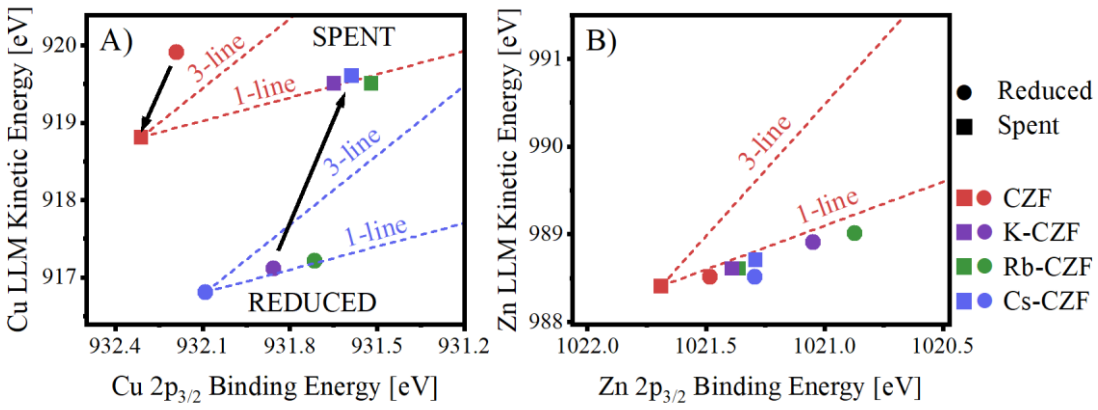

Figure 27| Cu and Zn Wagner plots for spent and reduced catalysts. Panel A and B show the data for Cu and Zn respectively. The square and round markers indicate reduced and spent samples. The data for CZF, K-CZF, Rb-CZF and Cs-CZF are plotted in red, purple, green and blue respectively. Reference lines with a slope of 3 or 1 are drawn to deconvolute initial and final state effects relative to spent CZF (red) and reduced Cs-CZF (blue).

central point. The line with a slope equal to 3 represents the final state effects. The other line with slope equal to 1 represents the initial state effects. The position of the data relative to these lines shows whether the spectral differences are due to final or initial state effects. As expected from the above analysis, after reaction the data of the doped materials cluster around the 1-line relative to the spent CZF catalyst. This is the case for both Cu (Figure 27A) and Zn (Figure 27B) . Hence, the spectral changes upon AM doping after reaction can rightfully be attributed to Madelung potential effects.

Overall the analysis of the TM-O/2p-2s separation, Wagner plots, and AM core level binding shows that the doped AMs are bond to the catalyst surface in close proximity to the TMs. While the strongly electropositive nature of AMs is expected to lead to a high propensity to donate electron density to the surface TMs, the observed spectral changes for Cu and Zn can be entirely attributed to the generation of a Madelung potential near the surface.

3.2.2.6. Mössbauer Spectroscopy

Mössbauer Spectroscopy was use to study the evolution of Fe from calcination and reduction to carburization during CO_2 hydrogenation. It was tested whether:

The Fe^{3+} species interact with the Cu^{2+} and Zn^{2+} in the calcined samples;

Fe presents as a combination of Fe^{3+},$Fe^{2+}$and α-Fe after reduction in all samples;

and

AMs facilitate the carburization during CO_2 hydrogenation.

As expected, the initial oxidation state of Fe after calcination presents as 3+ and is unaffected by the presence of alkali metal dopant (see Figure S26 and Figure S27): at room temperature both doped and undoped samples presented with single doublet with the same isomer shift, quadrupolar splitting and line width (see parameters in Table 4). The absence of any hyper fine splitting indicates a lack of an internal magnetic field. The lack of long range magnetic ordering suggests the Fe atoms are present in an amorphous phase [255–257].

This is consistent with Fe being present as amorphous Fe_2O_3 and is in line with the XRD showing no crystallographic peaks associated with any Fe oxide (see Figure S13**Figure S13**).

Cs-CZF was used as a representative sample to study the hyperfine structure of the AM doped CZF catalysts in comparison to 2%Cs-Cu_7Fe_3 (Cs-CF) and 2%Cs-Cu_7Fe_3 (Cs-ZF). Cs-CF and Cs-ZF were synthesized by the same method described before. To induce the formation of the internal magnetic field and thereby the hyperfine field, the samples were cooled down to 4.2 K, which is below the Curie temperature for these samples. At this temperature two different Fe environments are revealed to be present in Cs-CZF (see parameters in Table 4 and spectra in Figure S27**Figure S27**). These can be assigned to octahedral and tetrahedral geometries [256,257]. Both are represented by a sextuplet with a low hyper fine field 47.9 and 40.9, consistent with the amorphous nature of the Fe phase [256]. Similarly, the quadrupolar splitting is near zero indicating the symmetrical nature of the Fe nuclei in the amorphous medium.

Interestingly, the hyperfine parameters obtained for both nuclei of Cs-CZF and Cs-CF are all within measurement error. Only the hyper fine field of Fe in octahedral geometry in Cs-CZF is lower than Cs-CF (40.9 and 41.5 T respectively). In contrast, the Mössbauer spectrum of Cs-ZF is characterized by a single sextuplet with a high signal-to-noise ratio indicating a high degree of disorder of the Fe atoms. These results indicate that Fe in the Cs-CZF is likely associated with Cu, while Zn presents in a separate phase.

Similar to the data obtained from the calcined samples, the *quasi in-situ* Mössbauer measurement data after reduction show relative uniformity across the samples (see the hyperfine parameters in Table 5 and spectra in Figure S25**Figure S25**): after treatment in 5% H_2 the spectra of all samples taken at 120 K show the same degree of Fe^0 and Fe^{2+} formation (86-89% and 11-14% spectral contribution respectively). Considering the XPS, XRD and XAS data presented in Sections 3.2.2.5, 3.2.2.4 and 3.2.2.8.1 Fe^{2+} is assumed to be concentrated near the surface, while Fe^0 makes up the bulk. Surprisingly and in contrast to the XAS, XPS and XRD results reported earlier, after reaction all samples including undoped CZF show a high degree of carburization. After exposure to CO_2 and H_2 at 20 bar at 250, 270 or 290 °C, the spectra are entirely characterized χ-Fe_5C_2 and ε'- $Fe_{2.2}C$, with no contribution from Fe^{2+} or Fe^{3+}. Notably, the relative amounts of χ-Fe_5C_2 and ε'-$Fe_{2.2}C$ vary across the samples. The contribution of χ-Fe_5C_2 after reaction at 270 °C is in the order of: Cs-CZF (65±5%)>CZF (60±5%)>K-CZF (55±5%)>Rb-CZF (45±5%). Importantly, the differences in the relative amounts of χ-Fe_5C_2 and ε'- $Fe_{2.2}C$ between the AM doped catalysts does not correlated with HA or olefin selectivity.

Although the absence of any oxidized Fe phases observed by Mössbauer after reaction is surprising considering the prevalence of FeO_x phases measured by other techniques, the relative amounts of χ-Fe_5C_2 and ε'- $Fe_{2.2}C$ can also reveal interesting information about the carburization effect of AMs. It is well known that the lower carbon containing ε'- $Fe_{2.2}C$ phase behaves as an intermediate towards the higher carbon containing χ-Fe_5C_2 phase [90]. The step-wise carburization from ε'- $Fe_{2.2}C$ to χ-Fe_5C_2 is evidenced here by the progressive increase of the later under CO_2 hydrogenation conditions over Cs-CZF: for Cs-CZF the spectral contribution (SPC) of χ-Fe_5C_2 increases from 63% at 250 °C, to 65% at 270 °C, and to 72% at 290 °C. Contrastingly, for CZF the spectral contribution of χ-Fe_5C_2 decreases

from 65 % to 60 % after reaction at 250 and 270 °C respectively. This implies that, rather than only promoting the formation of χ-Fe_5C_2 outright, the presence of Cs ensures that χ-Fe_5C_2 is maintained. Furthermore, the increase in ε'- $Fe_{2.2}C$ may be an indication of onset surface oxidation [258] as is observed in XPS. While no additional data was obtained for K-CZF and Rb-CZF, it may be speculated that their relatively higher amount of ε'- $Fe_{2.2}C$ after reaction at 270 °C is not due to surface oxidation, but rather due to more limited carburization ability considering the data obtained by XPS.

Table 4|. The Mössbauer fitted parameters of the calcined samples.

Treatment	Measurement Temperature *[°C]*	Sample	*IS [mm·s^{1}]*	*QS [mm·s^{1}]*	*Hyperfine field [T]*	*Γ [mm·s^{1}]*	*Phase*	*SPC [%]*
Calcination	26.85	CZF	0.32	0.87		0.54	Fe^{3+}	100
		K-CZF	0.33	0.86		0.54	Fe^{3+}	100
		Rb-CZF	0.33	0.87		0.53	Fe^{3+}	100
		Cs-CZF	0.33	0.86		0.55	Fe^{3+}	100
Calcination	-268.95	Cs-CZF	0.49 0.43	-0.03 -0.02	47.9 40.9*	0.72 0.50	Fe^{3+} Fe^{3+}	36 64
		Cs-CF	0.49 0.43	-0.01 0.00	47.8 41.5*	0.67 0.52	Fe^{3+} Fe^{3+}	43 57
		Cs-CZF	0.65	-0.05	43.5*	1.12	$Fe^{2.5+}$	100

*Experimental uncertainties: Isomer shift: I.S. ± 0.02 mm s^{-1}; Quadrupole splitting: Q.S. ± 0.02 mm s^{-1}; Line width: Γ ± 0.03 mm s^{-1}; Hyperfine field: ± 0.1 T; Spectral contribution: ± 5%; *Average magnetic field.*

Table 5| Mössbauer fitted parameters of reduced (5% H_2) and reacted (30 bar $1CO_2/3H_2$) samples measured at -153.15 °C.

Treatment	Sample	*Treatment Temperature [°C]*	*IS [mm·s^{-1}]*	*QS [mm·s^{-1}]*	*Hyperfine field [T]*	*Γ [mm·s^{-1}]*	*Phase*	*SPC [%]*
Reduction	CZF	360	-0.01		34.1	0.35	Fe^0	89
			0.91	2.12		0.65	Fe^{2+}	11
	K-CZF		-0.01		34.1	0.36	Fe^0	87
			1.04	2.32		0.65	Fe^{2+}	13
	Rb-CZF		-0.01		34.1	0.34	Fe^0	86
			0.93	2.12		0.65	Fe^{2+}	14
	Cs-CZF		-0.01		33.8	0.32	Fe^0	87
			0.95	2.35		0.65	Fe^{2+}	13
Reaction	CZF	250	0.20		24.7	0.49	χ-Fe_5C_2	25
			0.18		20.4	0.49	χ-Fe_5C_2	27
			0.21		13.9	0.49	χ-Fe_5C_2	13
			0.23		18.5	0.37	ε'-$Fe_{2.2}C$	35
		270	0.21		24.3	0.42	χ-Fe_5C_2	26
			0.18		20.5	0.42	χ-Fe_5C_2	23
			0.21		13.9	0.42	χ-Fe_5C_2	11
			0.24		18.4	0.35	ε'-$Fe_{2.2}C$	40
	Cs-CZF	250	0.18		24.5	0.42	χ-Fe_5C_2	31
			0.15		21.0	0.42	χ-Fe_5C_2	22
			0.21		13.9	0.42	χ-Fe_5C_2	10
			0.22		18.4	0.34	ε'-$Fe_{2.2}C$	37
		270	0.19		24.7	0.35	χ-Fe_5C_2	28
			0.15		20.9	0.35	χ-Fe_5C_2	23
			0.21		13.6	0.35	χ-Fe_5C_2	14
			0.21		18.5	0.34	ε'-$Fe_{2.2}C$	35
		290	0.18		24.5	0.32	χ-Fe_5C_2	29
			0.16		21.1	0.32	χ-Fe_5C_2	28
			0.21		13.8	0.32	χ-Fe_5C_2	15
			0.22		18.4	0.34	ε'-$Fe_{2.2}C$	28
	K-CZF	270	0.21		24.1	0.33	χ-Fe_5C_2	22
			0.18		20.6	0.33	χ-Fe_5C_2	23
			0.21		13.8	0.33	χ-Fe_5C_2	10
			0.23		18.4	0.35	ε'-$Fe_{2.2}C$	45
	Rb-CZF	270	0.19		24.3	0.39	χ-Fe_5C_2	18
			0.15		20.5	0.39	χ-Fe_5C_2	18
			0.21		13.2	0.39	χ-Fe_5C_2	9
			0.23		18.4	0.38	ε'-$Fe_{2.2}C$	55

*Experimental uncertainties: Isomer shift: I.S. ± 0.02 mm s^{-1}; Quadrupole splitting: Q.S. ± 0.02 mm s^{-1}; Line width: Γ ± 0.03 mm s^{-1}; Hyperfine field: ± 0.1 T; Spectral contribution: ± 5%; *Average magnetic field.*

3.2.2.7. Transmission Electron Microscopy (TEM)

Microscopic experiments were conducted to further investigate the structure of the catalyst as well as the interaction between catalyst TMs and surface AMs in terms of their relative distribution. These experiments included a combination of Transmission Electron Microscopy (TEM), Energy Dispersive X-ray Spectroscopy (EDX) and Selected Area Electron Diffraction (SAED). Herein Rb-CZF is used as a proxy for the AM doped samples, which is compared to CZF.

Although the XRD results show the formation of crystalline phases after the reaction, hitherto no information has been obtained regarding the spatial distribution of these Cu, Zn and Fe phases. Hence, EDX, TEM and SAED were first used to confirm that

Different crystal domains rich in Cu, Zn and Fe are formed in close contact after reaction.

EDX was used to confirm the presence of the various elements in the selected areas, while SAED was employed to reveal the crystallinity.

The XPS, ICP and XRD results imply that the doped AM atoms are highly dispersed at the surface of the catalyst. However it is not known whether doped AMs are uniformly distributed or are concentrated at any particular Cu, Fe or Zn rich surface. In lieu of any evidence to the contrary it is hypothesized that

Rb is uniformly distributed on catalyst surface.

To test this hypothesis three representative regions were analysed. Two of these regions contain appreciable amounts of Cu, Zn and Fe, while one is low in Fe. Considering the relatively low concentration of Rb contained in the sample (2 w.t.%) EDX spectra were used to gain further confidence in the measured EDX maps by evaluating the Rb-L, Rb-Kα and/or Rb-Kβ bands.

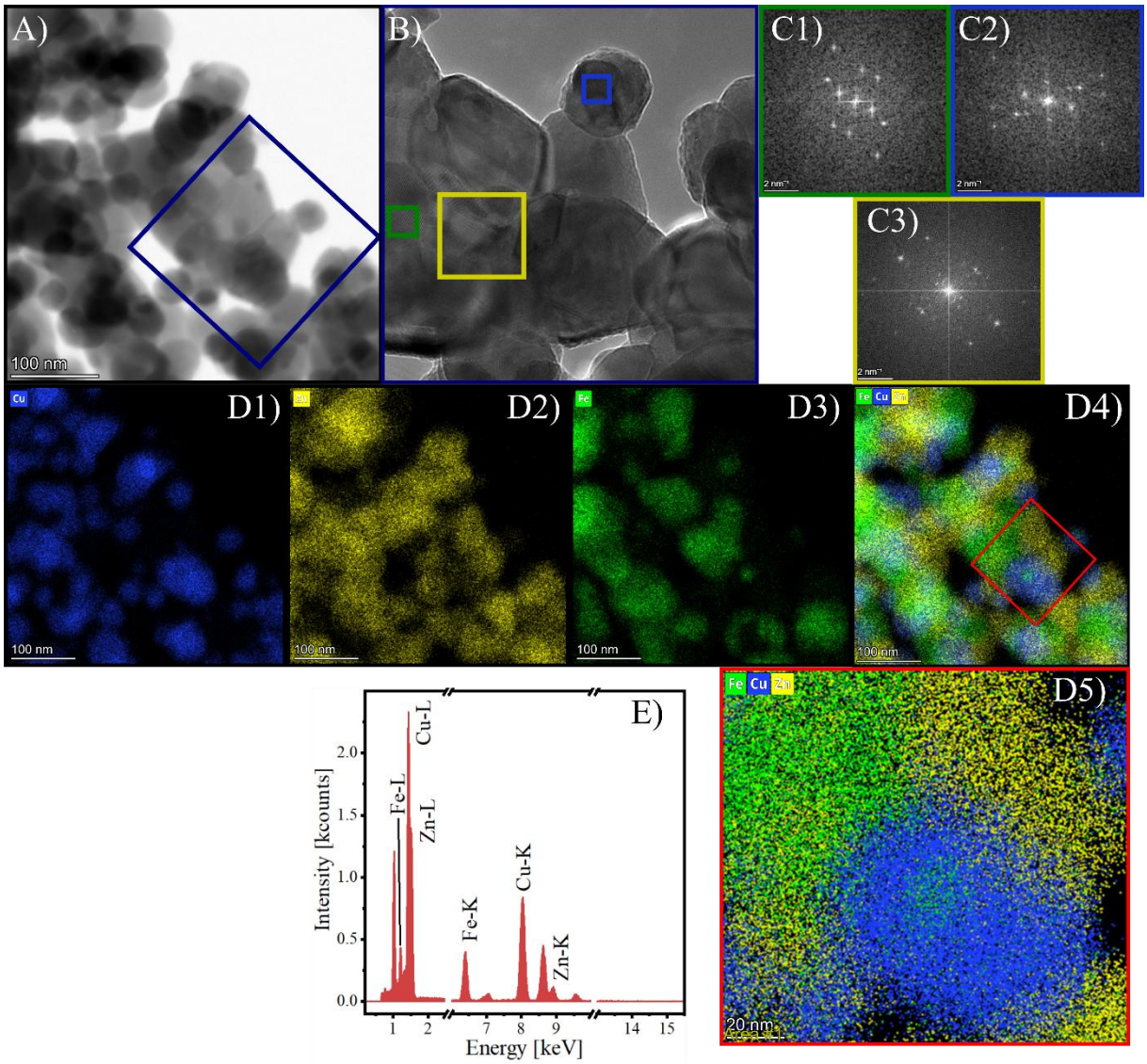

Figure 28| Combined microscopic analysis of CZF after CO_2 hydrogenation reaction. Panel A shows the Bright-Field TEM image in scanning mode of the selected area. The image in panel B corresponds to the region indicated by the dark blue box in panel A measured in TEM mode. The SAED results obtained in the green blue and yellow boxes in panel B are indicated in panels C1, C2 and C3 respectively. As indicated by the EDX mapping these regions are rich in Fe, Cu and Zn. Panel D1-3 show the EDX mapping of Cu, Zn and Fe respectively. Panel D4 shows the overlapping elemental maps. The region in D5 corresponds to the red box in D4. Lastly panel E shows the EDX spectrum of the area in D5.

The results obtained for CZF confirm the close contact between Cu, Zn and Fe crystal domains. Indeed the STEM image and EDX mapping results in Figure 28 show to coexistence of Cu, Zn and Fe rich particles of ranging sizes. A TEM image of the surrounding area can be found in the appendix (Figure S28). The crystallinity of the various domains rich in Fe, Cu and Zn is corroborated by the SAED patterns in Figure 28C1-3.

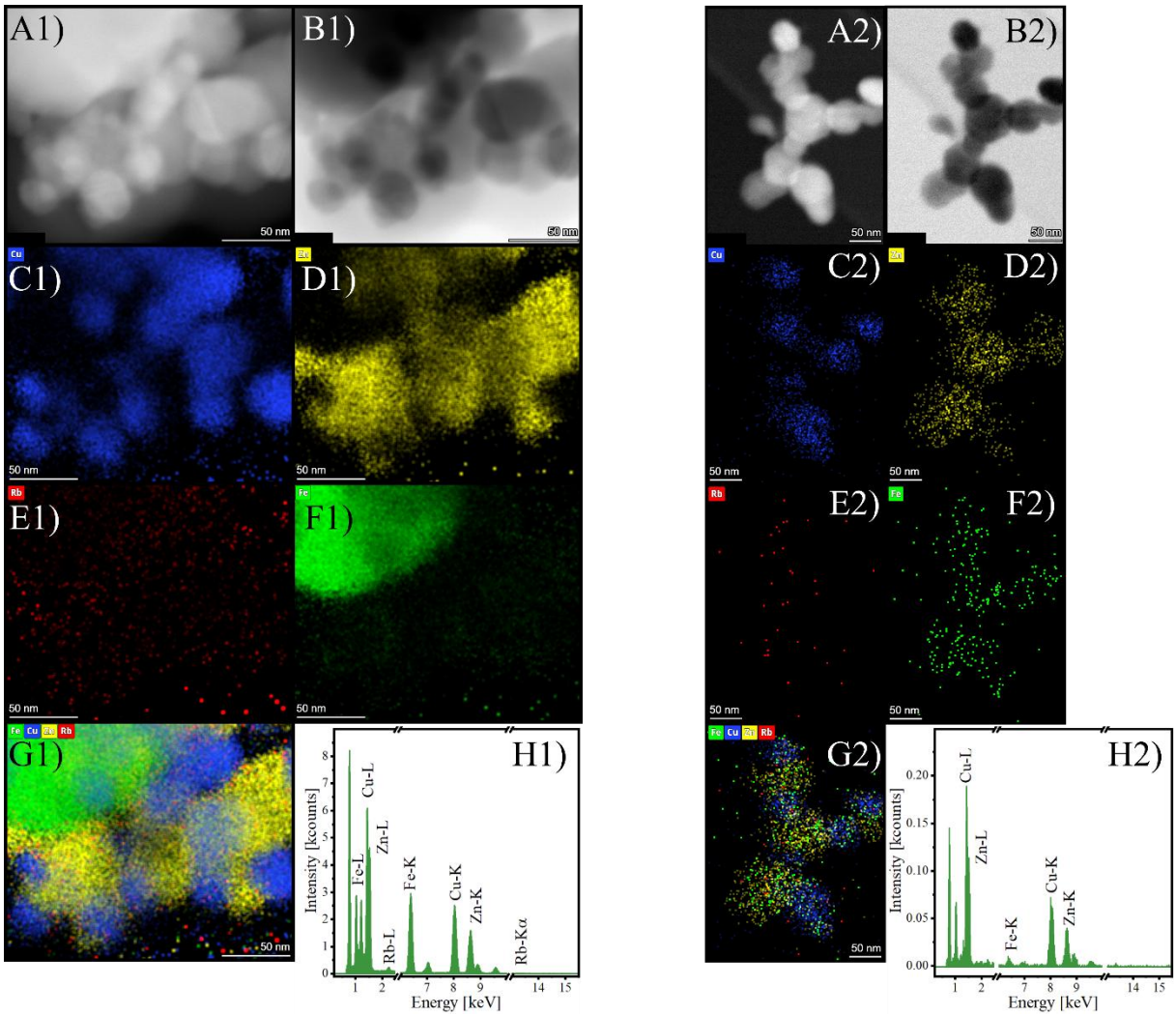

Figure 29| Combined microscopic analysis of Rb-CZF after reaction Region 1 and 2. Region 1 and 2 correspond to the panels labelled with 1 and 2 respectively. Panel A and B shows the Dark-Field and Bright-Field TEM images in scanning mode. Panels C, D, E and F show the EDX mapping of Cu, Zn, Rb and Fe respectively. Panel G shows the overlapping elemental maps. Lastly Panel H1 and H2 show the EDX spectra of the two regions.

No significant differences in the catalyst morphology between Rb-CZF and CZF were observed by the microscope experiments (see Figure S28): similar to CZF the result show close contact between Fe, Zn and Cu in Rb-CZF after reaction (see Figure 29 and Figure 30). Importantly, however, a number of interesting observations were made regarding the distribution of Rb. The results presented in Figure 29 and Figure 30 suggest a distinct role of Fe in distributing Rb.

The STEM and EDX mapping results of two regions of Rb-CZF (denoted region 1 and 2) are illustrated in Figure 29. Region 1 is rich in Fe relative to Cu and Zn, while region 2 has a relatively low

amount of Fe as illustrated by the EDX mapping (panel C-G) and EDX spectra (panel H). Although the Rb is strongly dispersed in both regions, the amount of Rb seems considerably higher in the Fe rich region 1.

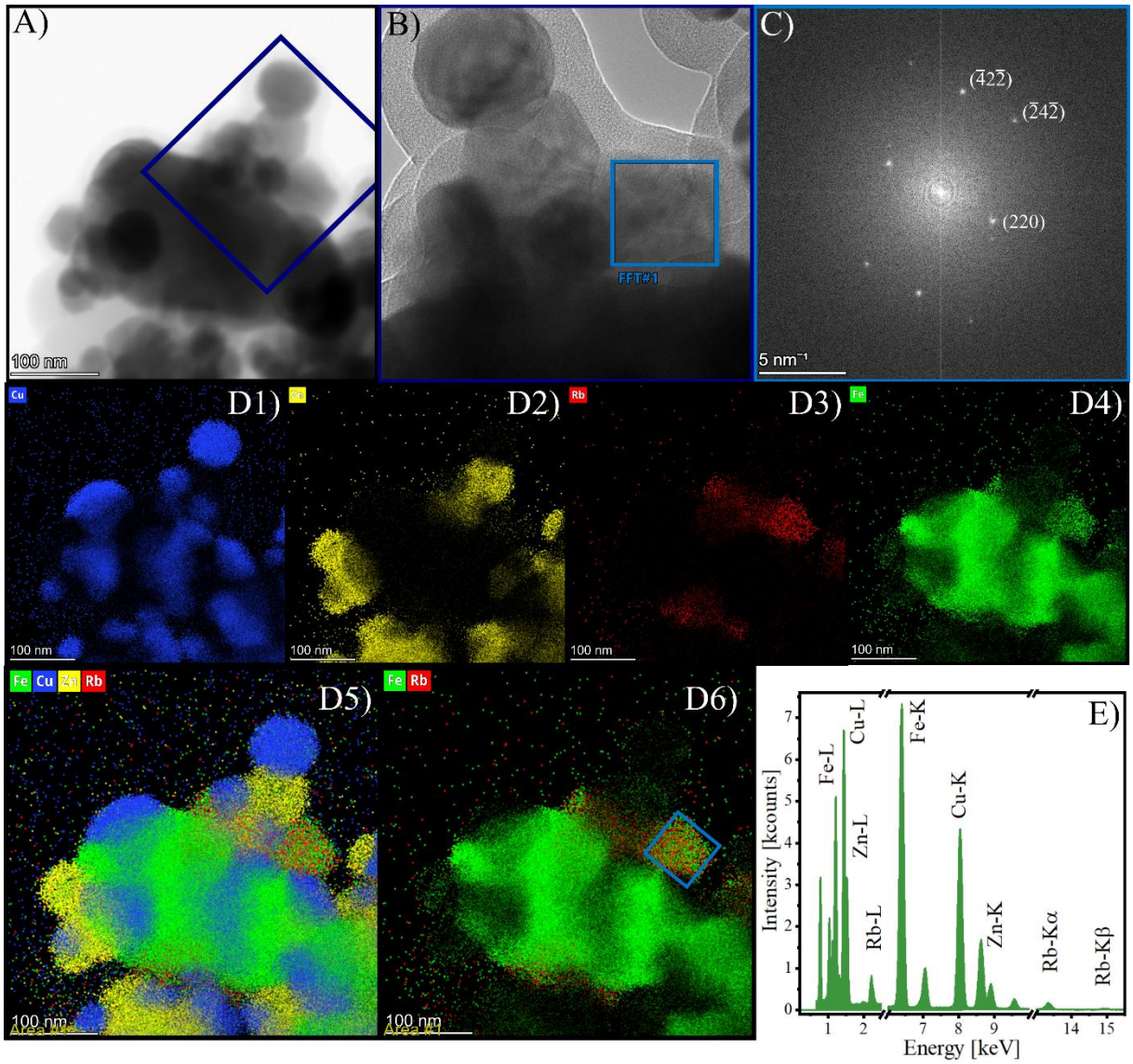

Figure 30| Combined microscopic analysis of Rb-CZF after reaction Region 3. Panel A shows the Bright-Field TEM image in scanning mode. The image in panel B corresponds to the region indicated by the dark blue box in panel A measured in TEM mode. The SAED results obtained in the light blue boxes in panel B is indicated in panel C. As indicated by the EDX mapping this region is rich in Fe and Rb. Panel D1-4 show the EDX mapping of Cu, Zn, Rb and Fe respectively. Panel D5 shows the overlapping maps of all four elements. Panel D6 shows the overlapping Fe and Rb maps with a light blue box corresponding to the box in panel B. Lastly panel E shows the EDX spectrum of the entire area.

The relation between Fe and Rb is further confirmed by the analysis of region 3. Alongside clearly showing the proximity of Cu, Zn and Fe, region 3 presents distinct regions rich in Rb and Fe. One such region (highlighted by the light blue box in Figure 30) is analysed by SAED to reveal crystalline Fe_3O_4. The presence of crystalline Fe_3O_4 in this region is evidenced by close similarity between the measured SAED pattern and the simulated diffraction pattern of Fe_3O_4 shown in Figure S29**Figure S29**. Based on this simulation the diffraction spots in Figure 30C are indexed (220), $(\bar{4}2\bar{2})$ and $(\bar{2}4\bar{2})$. Indeed the measured and simulated angle between the and plane are within 0.5° (107.3 and 106.8° respectively). The relatively high concentration of Rb at the surface of redox active Fe_3O_4 [259] may explain the absence of Fe^{2+} as measured by XPS.

Moreover, combined with the redox activity of Fe_3O_4, the close association between Rb and Fe_3O_4 (rather than FeC_x) can be attributed to the high oxophilicity of Rb combined with a high mobility AMs at the catalyst surface: in the presence of Fe_3O_4 Rb concentrates on its surface; upon carburization of Fe_3O_4 Rb atoms are dispersed across all surfaces; and in the absence of Fe (as is the case in region 2) Rb concentration remains low. It can be hypothesized that the high dispersion of Rb observed in region 1 is due to Rb spillover from Fe to Cu and Zn surfaces. For such mechanism to hold Fe in region 1 must be highly carburized. Unfortunately the current results are unable to reveal the phase of Fe in this region. While no direct evidence is obtained to test this hypothesis, it is in line with the considerably higher adsorption strength of AMs on Fe_3O_4 [260] compared to Fe_5C_2 [261], ZnO [262] and Cu [263], while maintaining a high degree of mobility on all such surfaces [260–263]. The combination of high mobility with preferential adsorption on Fe_3O_4 may result in carburization modulated AM dispersion.

3.2.2.8. X-Ray Absorption Spectroscopy (XAS)

X-Ray Absorption Spectroscopy (XAS) measurements were performed to further investigate the effect of AM doping on the catalyst structure. For consistent analysis of the bulk and surface these data were collected on the same batch as the XPS measurements while ensuring inert atmosphere was maintained. To this end The Fe, Zn and Cu X-ray absorption K-edges were measured and analysed to obtain information about the local structure, oxidation state and presence of different phases at the bulk before and after reaction. This includes XANES, EXAFS and Linear Combination Fitting (LCF) data. Additionally, Rb was measured and is used as a proxy for the used AMs to investigate the local structure of the AMs

Considering the data present so far a number of well formulated hypotheses could be tested with respect to the evolution of the TMs under the influence of AMs:

AM doping has no effect on phase or electron structure of Zn, and remains unchanged before and after reaction, while it promotes the reduction of Cu^{1+} *to* Cu^{0}.

Considering the XPS and Mössbauer results the following hypotheses are tested regarding Fe:

A combination of reduced and oxidized Fe phases are formed after reduction;

and

AMs promote formation of FeC_x *species relative to Fe oxides during reaction.*

Due to the large number of potential phases produced by Fe during reaction the LCF analysis included a large number of standards. The LCF analysis of Cu included up to 4 standards. Any phase which contributed less than 10% was excluded from the fit.

In contrast to the evolution of the TM during reduction and reaction, little is known about the structure of the surface AMs. The literature is especially lacking in the analysis of Rb. Although a relatively comprehensive XAS study on Rb doped oxide materials has been published [264], the structure of AMs at the catalyst surface remains elusive and EXAFS data are scarce. To our knowledge only two papers have reported Rb K-edge XANES for catalytic materials relevant to the current thesis, neither of

which provide EXAFS data [108,265]. Although the obtained Rb K-edge spectra are very similar and only subtle differences between the sample spectra and the reference spectra are found, different conclusions are reached regarding the local structure of Rb: Sarkar et al. concluded that Rb is likely present as Rb_2CO_3 on their Rb doped Fe catalyst. This conclusion is based on a qualitative comparison of their Rb reference and sample spectra. Conversely, a similar analysis of Rb doped Mo_2C/MgO, which shows nearly identical spectra, suggests structural changes to Rb at the catalyst surface [265]. Similarly, despite the relatively more frequent use of K and Cs as dopants of FTS or CO_2 hydrogenation catalysts, only two XANES studies were found for the former [227,228] and none for the latter. These studies ascribe the evolution of the K-edge spectra during FTS to either agglomeration of the K atoms (without providing EXAFS data) or formation highly dispersed K_2CO_3 or KHCOO [227,228]. Clearly there is a need for further investigation of the Rb local structure, especially by EXAFS analysis.

To this end the Rb K-edge was measured of the spent Rb-CZF sample taking care to transfer it entirely inertly. Considering the sparse literature no firm hypotheses can be formulated. Nevertheless,

Based on the XRD, which shows separation of any Rb phase, and the XPS results, which indicate perturbation of the Rb electronic structure, it is hypothesized that

During reaction Rb is present as highly dispersed Rb_2CO_3 like species.

To test this hypothesis the K-edge of Rb was measured after reaction and was analysed compared to Rb_2CO_3, which was used for the synthesis.

3.2.2.8.1. X-Ray Absorption Spectroscopy (XAS) (Transition metals)

As expected, the Zn K-edge spectra [12] obtained for all samples before (Figure 31**Figure *31* Zn K-edge X-Ray Absorption Spectroscopy data of reduced samples.** Panel A shows the Zn K-edge. Panels B and C show the EXAFS data in the frequency domain (K-space) and spatial domain (R-space). The data corresponding to CZF, K-CZF, Rb-CZF and Cs-CZF are plotted in red, purple, green, and blue respectively.) and after reaction (Figure 32) are indicative of ZnO with no differences in the measured spectra. Indeed, the XANES spectra in both Figure 31A and Figure 32A show the absorption edge at 9662.5 eV (the energy at half of the edge step), which is consistent with ZnO. Moreover, the interatomic distance between the absorbed and the first and second nearest neighbour, which correspond to Zn-O and Zn-Zn, are observed to be ~1.82-1.89 and 3.20-3.32 Å, indicative of Zn in ZnO. Similarly, no peak is observed around 2.3 Å indicating the absence of metal like Zn-Zn scattering. Finally, the LCF analysis showed no formation of Zn^0 in any sample. These results clearly demonstrate the high degree of stability at the bulk of ZnO.

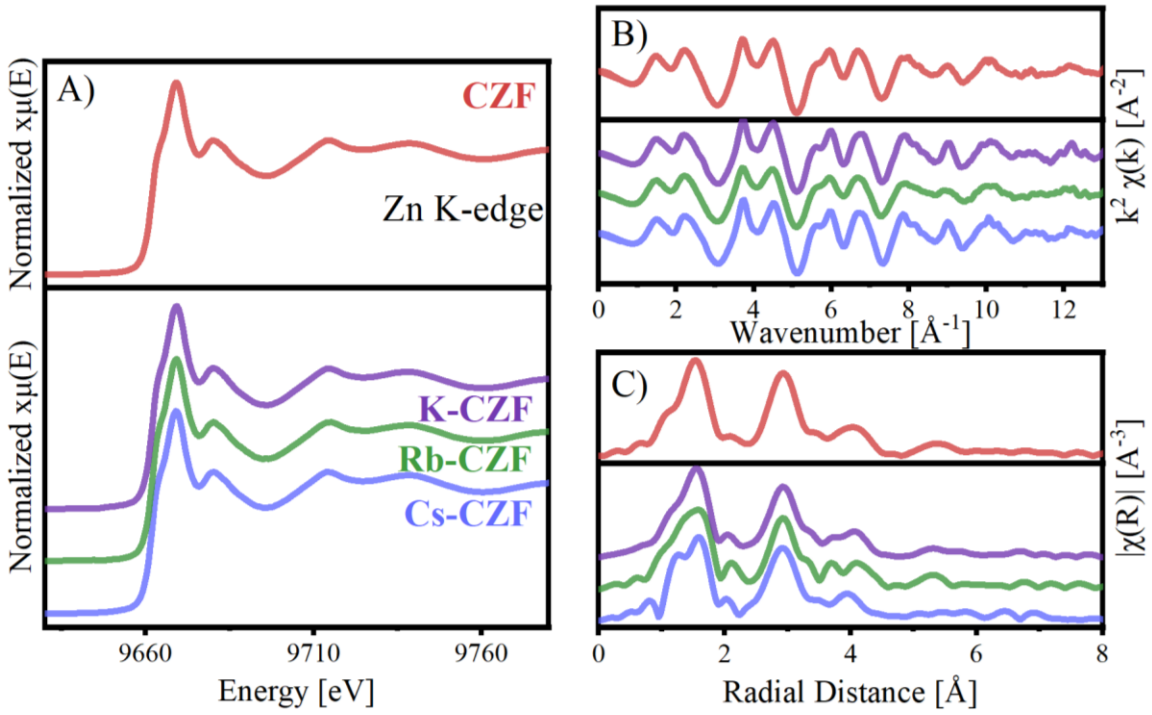

Figure 31 Zn K-edge X-Ray Absorption Spectroscopy data of reduced samples. Panel A shows the Zn K-edge. Panels B and C show the EXAFS data in the frequency domain (*K*-space) and spatial domain (*R*-space). The data corresponding to CZF, K-CZF, Rb-CZF and Cs-CZF are plotted in red, purple, green, and blue respectively. The data were obtained after reduction in 5% H_2 in N_2.

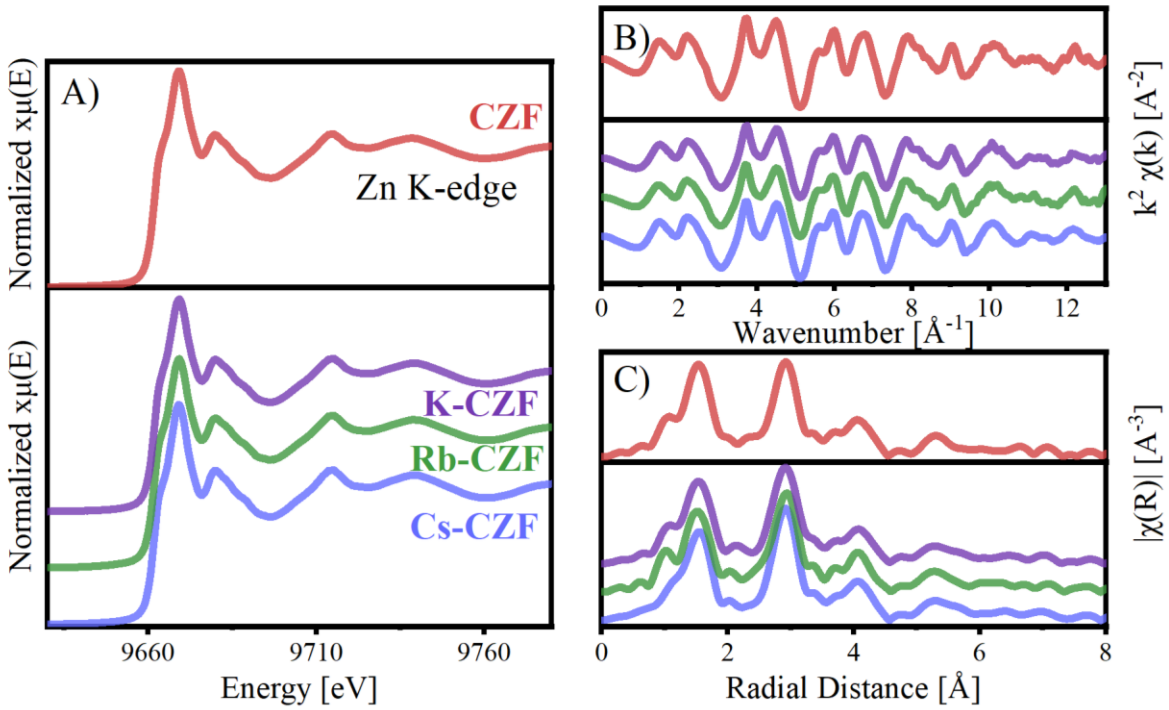

Figure 32| Zn K-edge X-Ray Absorption Spectroscopy data of spent samples. Panel A shows the Zn K-edge. Panels B and C show the EXAFS data in the frequency domain (*K*-space) and spatial domain (*R*-space). The data corresponding to CZF, K-CZF, Rb-CZF and Cs-CZF are plotted in red, purple, green, and blue respectively. The data were obtained after CO_2 hydrogenation testing.

The fact that the edge position is independent of AM doping shows the AMs do not change the electron density of Zn atoms at the bulk. In other words, these Zn nuclei do not experience any shielding through electron donation by the AMs. Note, on the one hand, the absence of any AM induced chemical shift may be due to the small concentration of AMs at the bulk. On the other hand, AM induced shielding at the surface, as measured by XPS (Section 3.2.2.5), was similarly absent.

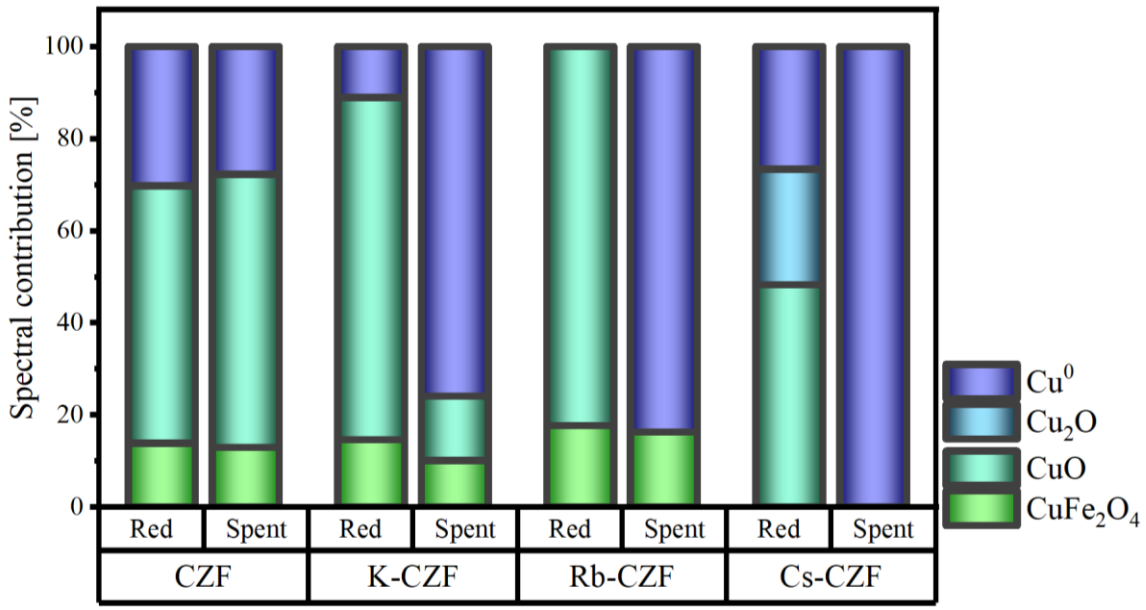

Figure 33 | Linear Combination fitting of Cu K-edge. The spectral contribution of $CuFe_2O_4$, CuO, Cu_2O, and Cu^0 to the Cu K-edge of samples before and after reaction are plotted in green, cyan, light blue and dark blue respectively.

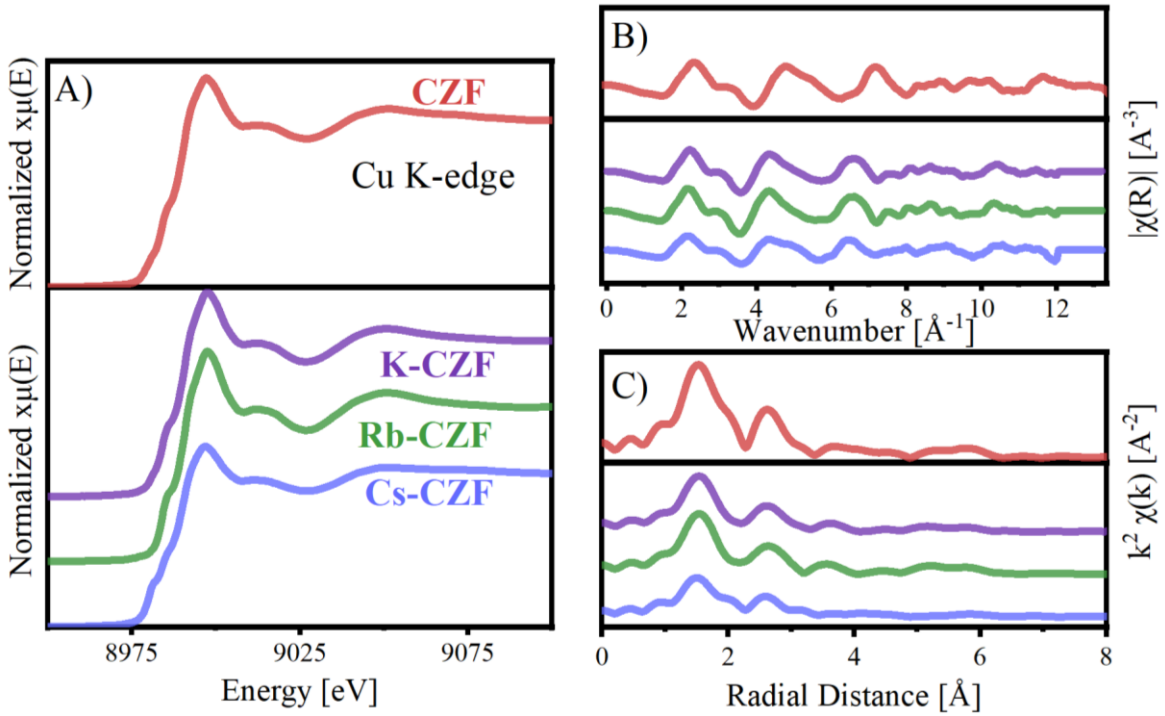

Figure 34| Cu K-edge X-Ray Absorption Spectroscopy data of reduced samples. Panel A shows the Cu K-edge. Panels B and C show the EXAFS data in the frequency domain (*K*-space) and spatial domain (*R*-space). The data corresponding to CZF, K-CZF, Rb-CZF and Cs-CZF are plotted in red, purple, green, and blue respectively. The data were obtained after reduction in 5% H_2 in N_2.

The Cu K-edge spectra show significant changes before and after reaction, in contrast to Zn. Critically, these changes depend on whether the samples is doped with AMs. Before reaction all the measured spectra show the coexistence of multiple Cu oxidation states. Surprisingly, a large fraction (54 to 86%) of the spectrum can be attributed to Cu^{2+}, as the LCF reveals (Figure 33). Notably, Cs-CZF is the most reduced with Cu^0 accounting for 51% of the measured spectrum compared to 32% in CZF and only 12 and 0% in K-CZF and Rb-CZF respectively. Furthermore, the oxidized nature of Cu is reinforced by the absence of a nearest neighbour around 2.5 Å, which would be indicative of metallic Cu^0. Instead, the first and second nearest neighbours are observed at 1.80-1.84 Å and 2.88-2.95 Å. These correspond to Cu-O and Cu-Cu in a CuO_x.

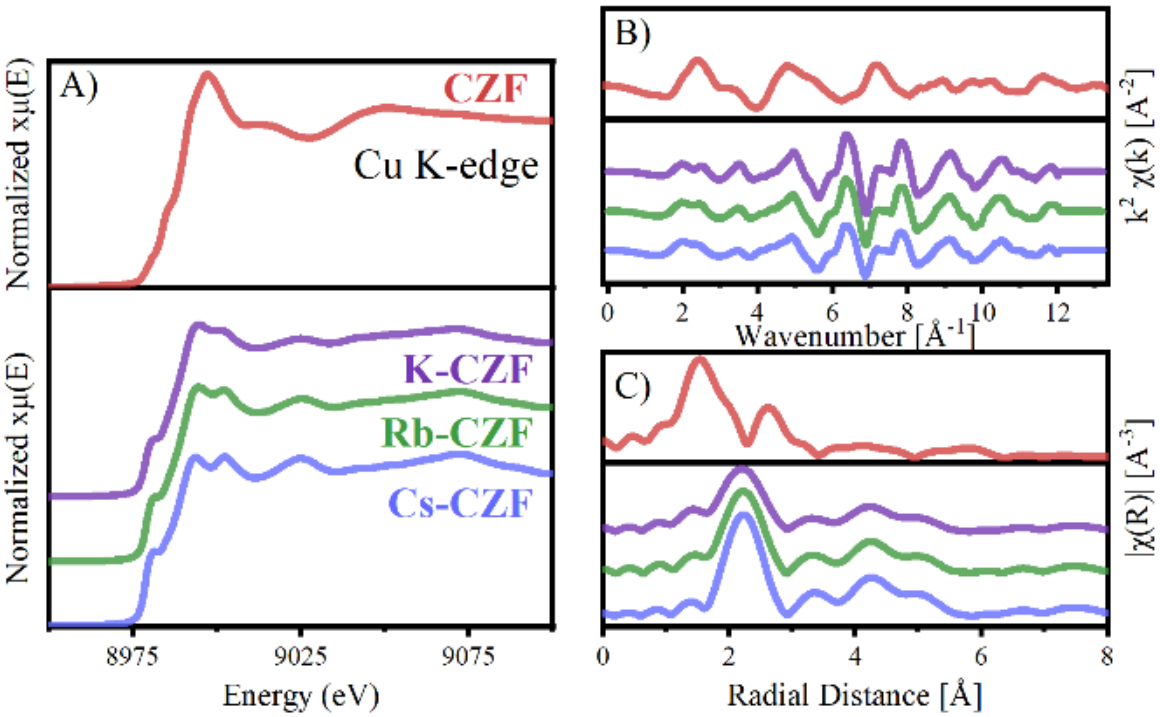

Figure 35| Cu K-edge X-Ray Absorption Spectroscopy data of spent samples. Panel A shows the Cu K-edge. Panels B and C show the EXAFS data in the frequency domain (*K*-space) and spatial domain (*R*-space). The data corresponding to CZF, K-CZF, Rb-CZF and Cs-CZF are plotted in red, purple, green, and blue respectively. The data were obtained after CO_2 hydrogenation testing.

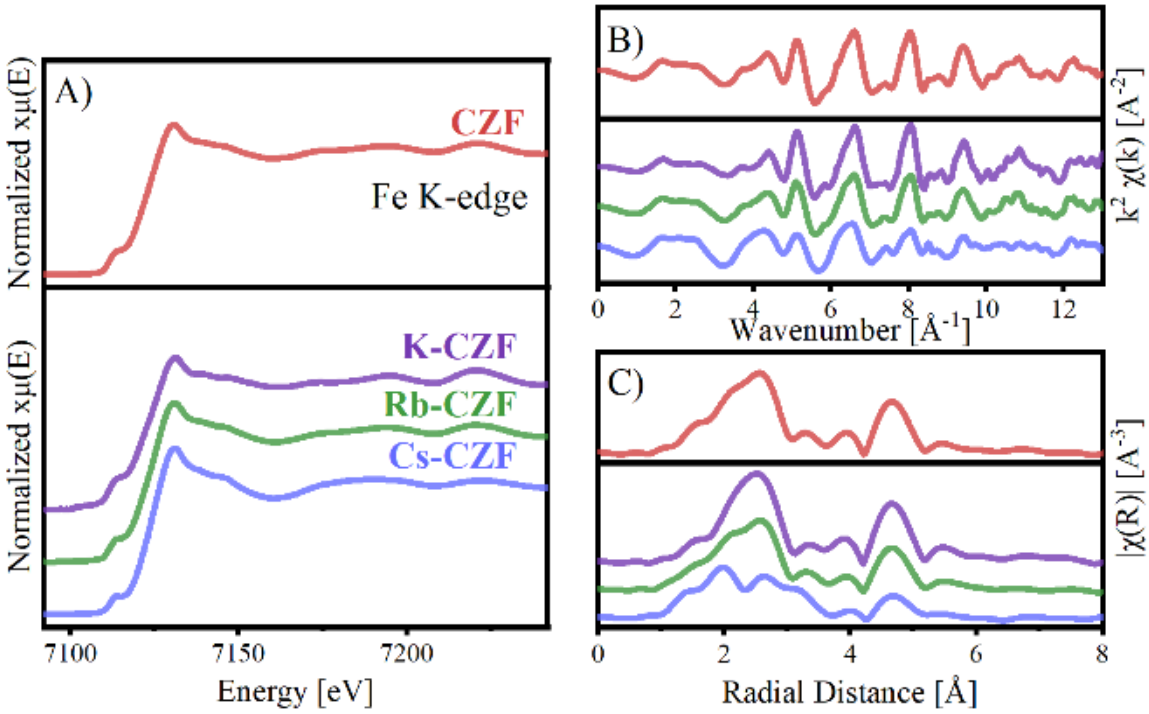

Figure 36| Fe K-edge X-Ray Absorption Spectroscopy data of reduced samples. Panel A shows the Fe K-edge. Panels B and C show the EXAFS data in the frequency domain (*K*-space) and spatial domain (*R*-space). The data corresponding to CZF, K-CZF, Rb-CZF and Cs-CZF are plotted in red, purple, green, and blue respectively. The data were obtained after reduction in 5% H_2 in N_2.

Interestingly, while Cu at the bulk is highly oxidized before reaction in all samples, after reaction AM containing samples show a large degree of Cu^0 formation. This change is clearly observed by the change in absorption edge shape and position. All spectra obtained for the doped samples show two peaks at 8993.6 and 9002.4 eV with intensity around the edge maximum, which is indicative of reduced Cu^0 species. In contrast, for CZF the single peak at 8997.1 eV is observed at the absorption maximum indicating Cu is oxidized. Given no strong pre-edge feature is observed around 8882 eV (as observed in Cu_2O) Cu in CZF is likely present as Cu^{2+} rather than Cu^{1+}. Similar trends are observed for the edge position: the edge position is lowest for Cs-CZF at 8984.9 followed by both K-CZF and Rb-CZF at 8986.1 eV, and CZF at 8988.8 eV. Note that these variations in the absorption edge position are likely not due to electron donation effects, but differences in the contribution of different Cu phases. This is reinforced by the LCF results (Figure 33): the samples with the lowest the edge position have the greatest Cu^0 amount. Cs-CZF has the greatest Cu^0 amount at 83% followed by K-CZF and Rb-CZF, with 71 and

64 % respectively. Only 25% Cu^0 is found for CZF. The metallic nature of Cu in AM doped samples after reaction is further indicated by the dominant scattering peak around 2.49-2.52 Å shown in Figure 35C, which is absent for CZF. Instead CZF shows nearest and second nearest neighbour interatomic distance of 1.84 (Cu-O) and 2.93 (Cu-Cu) Å respectively, which is similar to the reduced sample.

Together with the XPS results it is clear that the AMs assist the reduction of Cu under working conditions at the surface and bulk. In the absence of AMs the catalyst surface consists of a combination of Cu^{1+} and Cu^0 while the bulk contains a large amount of Cu^{2+}. Considering the XRD results the Cu^{2+} species are likely present in a spinel phase with Fe or contained in a non-crystalline phase.

A similar discrepancy between the XPS and XAS results are observed for Fe after reduction: the XPS results obtained after reduction show that none of the samples contain any Fe^0 at the surface. Instead the surface of all samples contains a combination of Fe^{2+} and Fe^{3+}. In contrast, however, the LCF analysis of the Fe K-edge clearly shows the formation of α-Fe in all samples. This is consistent

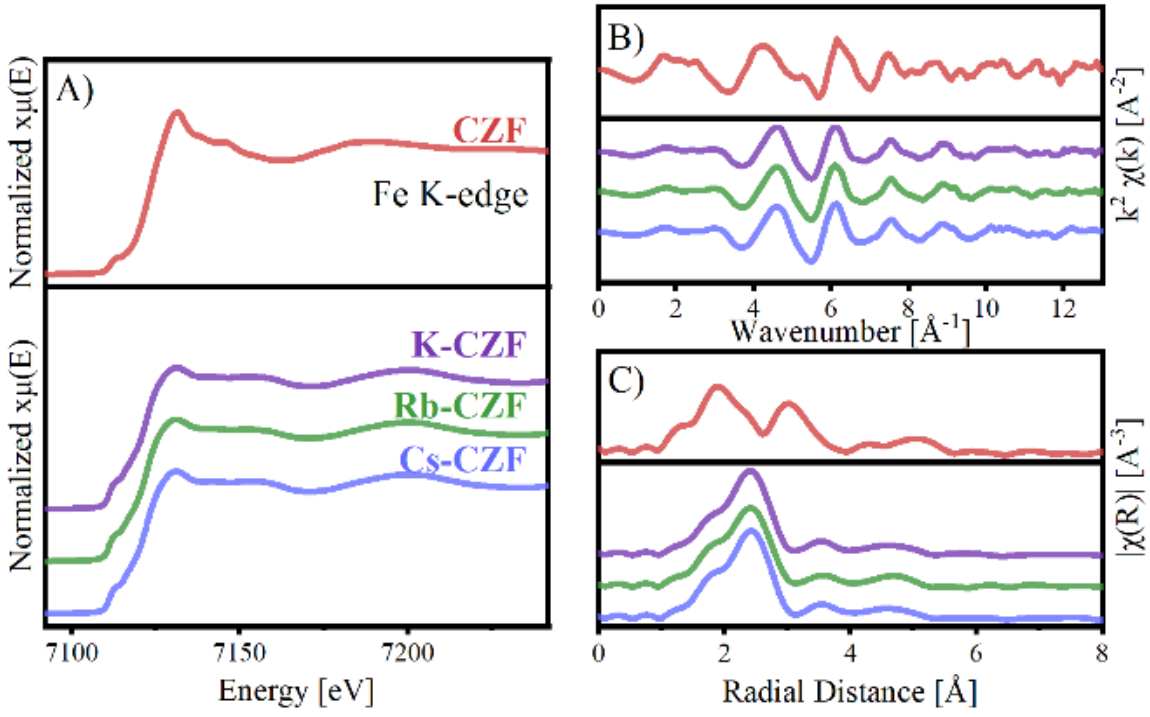

Figure 37| Fe K-edge X-Ray Absorption Spectroscopy data of spent samples. Panel A shows the Fe K-edge. Panels B and C show the EXAFS data in the frequency domain (*K*-space) and spatial domain (*R*-space). The data corresponding to CZF, K-CZF, Rb-CZF and Cs-CZF are plotted in red, purple, green, and blue respectively. The data were obtained after CO_2 hydrogenation testing.

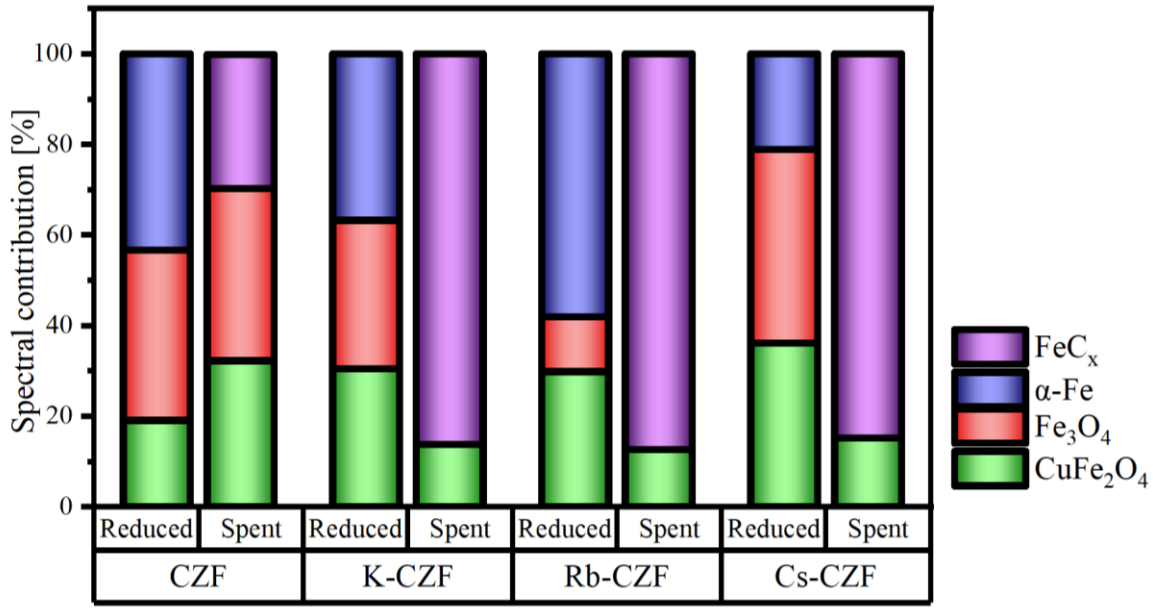

Figure 38| Linear Combination fitting of Fe K-edge. The spectral contribution of $CuFe_2O_4$, Fe_3O_4, α-Fe, and FeC_x to the Fe K-edge of samples before and after reaction are plotted in green, red, blue and purple respectively.

with the XRD results of CZF after reduction (Figure 21), which indicated the formation of crystalline α-Fe before reaction. Taken together, it can be concluded that after reduction all samples show a core@shell type structure with a combination of Fe^0, Fe^{2+} and Fe^{3+} at the core and only Fe^{2+} and Fe^{3+} at the shell.

Furthermore, the LCF results clearly show the disappearance of α-Fe and the formation of FeC_x during CO_2 hydrogenation (Figure 38). Interestingly, the degree of α-Fe formation after reduction does not correlated with the formation of FeCx during reaction: although the doped samples show different amounts of α-Fe after reduction (36.7, 58.0 and 21.1 % for K-,Rb-, and Cs-CZF respectively), after reaction all AM doped samples show primarily FeC_x (86.2, 87.3 and 84.8 % respectively). Importantly, the FeC_x amount in CZF is found to be considerably lower after reaction, only accounting for 29.6 %. Clearly these results show that all AMs significantly increase the carburization of the catalyst surface during reaction.

The LCF results are corroborated by EXAFS local scattering behaviour. Regarding the relatively lower α-Fe formation after reduction on Cs-CZF, it is observed that a significantly decreased scattering

intensity is observed around 2.42-2.50 Å compared to the other samples. This scattering path is related to the Fe-Fe nearest neighbour scattering in α-Fe. An additional scattering peak related to crystalline α-Fe All is observed at 4.66-4.70 Å. This peak can be assigned to the second nearest neighbour Fe-Fe scattering in α-Fe.

Such longer range scattering is not observed for the doped samples after reaction after reaction, as should be expected upon the disappearance of highly crystalline α-Fe and formation of less crystalline FeC_x phases. The promotional effect of the AMs to form such carbides during CO_2 hydrogenation is reflected by the high scattering intensity at 2.36-2.41 Å, which shows a shoulder at 1.87-1.90 Å. These peaks are related to Fe-C and Fe-C-Fe scattering in Fe carbide materials [89,95]. The lacking carburization of CZF is manifested in a significantly diminished intensity at 2.4 Å and increased intensity at 1.87, 2.89 and 3.27 Å. These can attributed to the formation of Fe_3O_4 or $CuFe_2O_4$ [89,266,267]. More specifically the peak

at 1.87 Å may be attributed to Fe-O nearest neighbour scattering, while the peaks at 2.89 and 3.27 Å are due to scattering between metal ions. The peak at 2.89 is the result of scattering between two octahedral metal ions. The scattering peak at 3.27 Å reflects scattering between tetrahedral metal ion with any other metal ion in the spinel structure [266]. Assuming the formation of $CuFe_2O_4$, the scattering at 2.89 Å is in part due to scattering between Fe^{3+} and Cu^{2+}, which both reside in the octahedral sites [266]. The tetrahedral sites are occupied by Fe^{3+}, which results the distinct peak at 3.27 Å [266]. Clearly then, the local Fe environment of CZF after reaction is in line with spinel rather than carbide structure.

3.2.2.8.2. X-Ray Absorption Spectroscopy (XAS) (Rubidium)

Finally, the Rb K-edge of the spent Rb-CZF catalyst was probed to investigate changes to the local structure and oxidation state of Rb. Figure 39 shows the sample data in blue and the data obtained from the Rb_2CO_3 standard material in grey. The XPS results showed that, although Rb remains in oxidation state 1+, it's environment is likely much different from Rb_2CO_3 or RbOH. This is corroborated by the XAS data.

These data show a significant perturbation of the local structure of Rb through interaction with the catalyst surface (where Rb is located). From the edge position of the sample spectrum (15201.1 eV), which is not significantly different from Rb_2CO_3, it is clear that Rb remains in 1+ oxidation state. Furthermore, no pre-edge feature, which is associated with 1s→3d electron transition and d-sp hybridization [268,269], is observed. This is consistent with a closed shell electron configuration as is the case of the Rb in Rb_2CO_3.

Interestingly, a kind of peak splitting is observed around the edge maximum resulting in a shoulder at 15206.0 eV and a maximum at 15210.1 eV (see the inset in Figure 39A). These features lay on either side of the maximum observed for Rb_2CO_3, which is located at 15208.4 eV. Similar features have been observed for Rb on MgO [264], which were absent for other oxide surfaces [264]. Furthermore, these near-edge features strongly resemble those obtained after heating Rb_2CO_3-Mo_2C/MgO [265]. However, entirely unique spectral features are observed in the case of Rb-CZF, which are absent from Rb_2CO_3 or any previously reported material (to our best knowledge). These features are indicative of a larger range structure around the Rb atoms: two doublet peaks are observed at 15236.4/15249.7 and 15275.8/15284.8 eV. The latter is well within in the EXAFS region. These doublets are the result of two frequency components, which are clearly observed in *K*-space (Figure 39B). After Fourier transforming the data into *R*-space an additional scattering path becomes prominent for Rb-CZF compared to Rb_2CO_3. Both Rb_2CO_3 and Rb-CZF show a scattering peak at 2.48 Å, but Rb-CZF shows an additional scattering peak at 4.96 Å. To our knowledge such scattering behaviour has not been previously observed for Rb on oxide surfaces, bulk RbOH or bulk Rb_2O [108,264,265]. this longer range scattering may be attributed to the interaction of the Rb species with the catalyst surface.

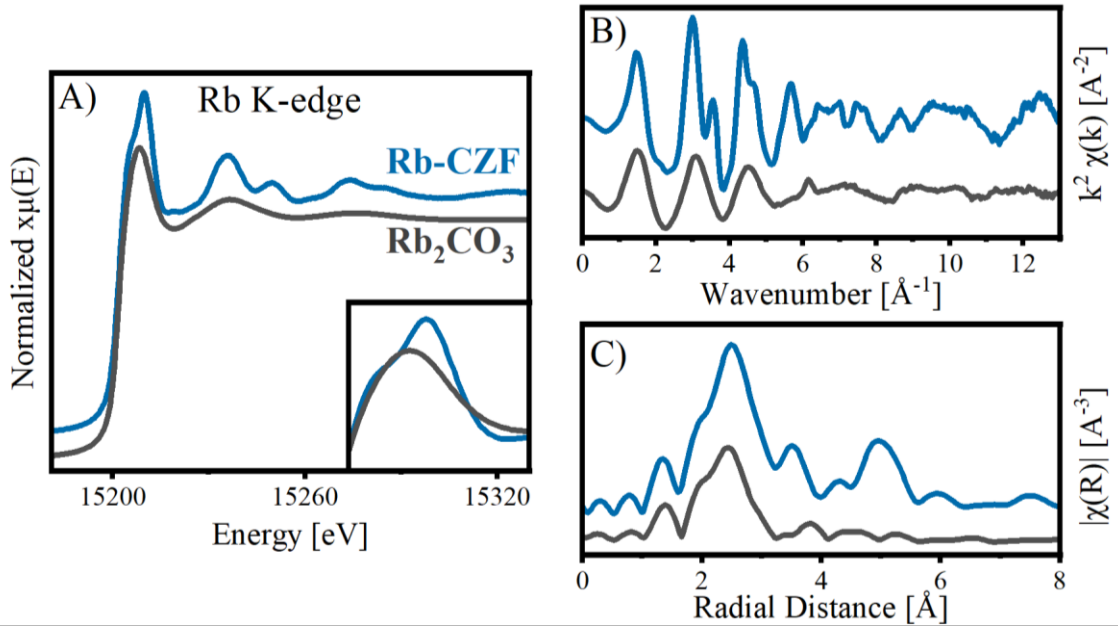

Figure 39| Rb K-edge X-Ray Absorption Spectroscopy data of spent Rb-CZF. Panel A shows the Rb K-edge. The main window shows the spectra with a small off-set. The inset shows the region around the edge maxima without an off-set. Panels B and C show the EXAFS data in the frequency domain (*K*-space) and spatial domain (*R*-space). The data corresponding to Rb-CZF is plotted in blue. Rb_2CO_3 is used as a reference and is plotted in grey. The data were obtained after CO2 hydrogenation testing.

To gain further insight into the local scattering around the Rb cations a Morlet wavelet transform was applied to the Rb K-edge EXAFS data. Figure 40A and B show the result of this transformation on the sample and Rb_2CO_3 spectra. The wavelet transformed data reveal an additional scattering body close to the first shell O at 2.81 Å, which was not observed in *R*-space. This scattering body may tentatively be assigned to surface TM atoms. Such assignment is based on the wavenumber of this scatter (4.72 $Å^{-1}$) and the fact that no such scattering path is observed for Rb_2CO_3. (The wavelet transformed EXAFS data of the Cu, Zn and Fe K-edges of this samples can be found in Figure S30.) Furthermore the wavelet analysis suggests that the long range scattering path (observed at 4.96 Å in *R*-space after Fourier transform) is likely the result of multiple scattering involving the surface TMs and O. This is evidenced by the large blob centred at (3.51 $Å^{-1}$, 4.54 Å). In lieu of any EXAFS fitting, the combination of XANES as well as the Fourier and wavelet transformed EXAFS clearly illustrate the restructuring of Rb at the catalyst surface compared to Rb_2CO_3. Although the presence of Rb clusters or pairs cannot be unequivocally excluded, this analysis shows the intimate interaction between the catalyst surface and the isolated Rb species.

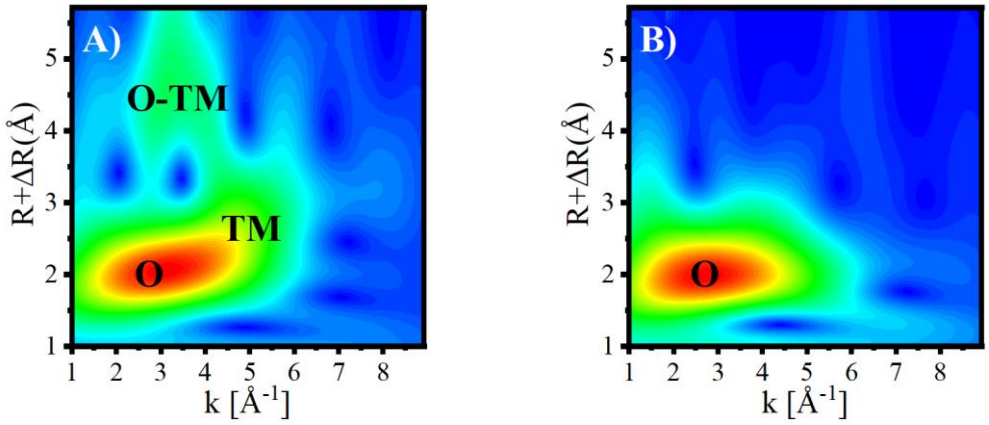

Figure 40| Wavelet transformed Rb K-edge EXAFS data. Panel A and B show the wavelet transform of Rb-CZF and Rb_2CO_3 respectively. The tentative assignment of the atoms involved in the scattering paths are indicated.

3.3. Conclusion

The extensive analysis of the CZF and AM-CZF samples reported in this chapter paints a complex picture of the effect of AM doping on the surface and bulk of the catalyst. It can be found that AMs, which are highly dispersed at the surface of the catalyst, have a critical role in facilitating the formation of iron carbide phases during reaction. Upon the inclusion of AMs deep carburization of the catalyst occurs during CO_2 hydrogenation catalysis. The Mössbauer spectroscopy results show that the iron carbide phase consists of χ-Fe_5C_2 and ϵ'-$Fe_{2.2}C$. The ratio between these two carbide phases depends on the catalyst material (CZF, K-CZF, Rb-CZF or Cs-CZF) and the temperature of reaction. In the presence of Cs the proportion of χ-Fe_5C_2 increases at higher temperatures, while ϵ'-$Fe_{2.2}C$ decreases. The opposite trend is observed in the absence of AMs. Interestingly, while XPS, XAS and XRD analysis constantly show the formation of oxidized iron species after reaction in the absence of AMs, no such iron oxide phases were observed during the Mössbauer analysis. This was attributed to the Mössbauer cell configuration, in which the reactant gases flow over rather than through the sample. The combined results of XPS, XAS, XRD and Mössbauer spectroscopy imply that carburization is promoted mainly by suppressing the oxidation of the catalyst: in the presence of AMs the formation of oxidized Cu species at the surface –as the XPS results reveal– and the formation of oxidized Cu and Fe phases at the bulk –as is revealed by XAS and XRD analysis of the spent catalysts– is suppressed.

Critically, however, it is found that, while carburization clearly increases upon the inclusion of K, Rb or Cs, the concentration of FeC_x at the surface of these AM doped samples does not positively correlate with the formation of AHs and olefins during reaction. In fact, amongst the AM doped samples, the FeC_x surface concentration is negatively correlated with total AH and olefin formation: while the FeCx surface concentration increases in the order Cs-CZF<Rb-CZF<K-CZF, the AH and olefin formation increases in the opposite order K-CZF<Rb-CZF<Cs-CZF. From this result it can be stipulated that the formation of AH and olefins upon the introduction of AMs to the surface of the catalyst cannot be simply ascribed to the increase in FeC_x formation during reaction. Instead it may be hypothesized that play a more direct role in influencing the reaction mechanism. This hypothesis is further explored in Chapter 4.

Beyond carburization and oxidation effects induced by AM doping the proximity between the surface TMs and doped AMs was studied. The in depth XPS analysis revealed an intimate interaction between the doped AMs and the TM catalyst surface. This interaction is characterized by the generation of a Madelung potential, as evidenced by the core-level peak shift observed for all three TM spectra, and a perturbation of the electron cloud around the surface AM atoms. Importantly no electron donation effects could be confirmed by the XPS spectra obtained here.

To further understand investigate the local structure of the AM atoms extensive XAS analysis was performed on the Rb K-edge of spent Rb-CZF. The distinctness of the Rb chemical environment is clarified by direct comparison between the obtained sample and standard spectra. The analysis suggests a direct interaction between the surface Rb atoms and the TM atoms via a multiple scattering pathway involving O. To our knowledge no such scattering pathway has been observed hitherto. These data suggest a unique chemical environment present around the AM atoms, in which the AMs are stabilized at the catalyst surface by O atoms.

To understand the role of these surface anchored AM atoms on the reaction Chapter 4 explores how the inclusion of AMs influences the interaction between the catalyst and reaction intermediates.

Chapter 4

Higher Alcohol and Olefin Formation:

Alkali Metals Open up a New Reaction Pathway

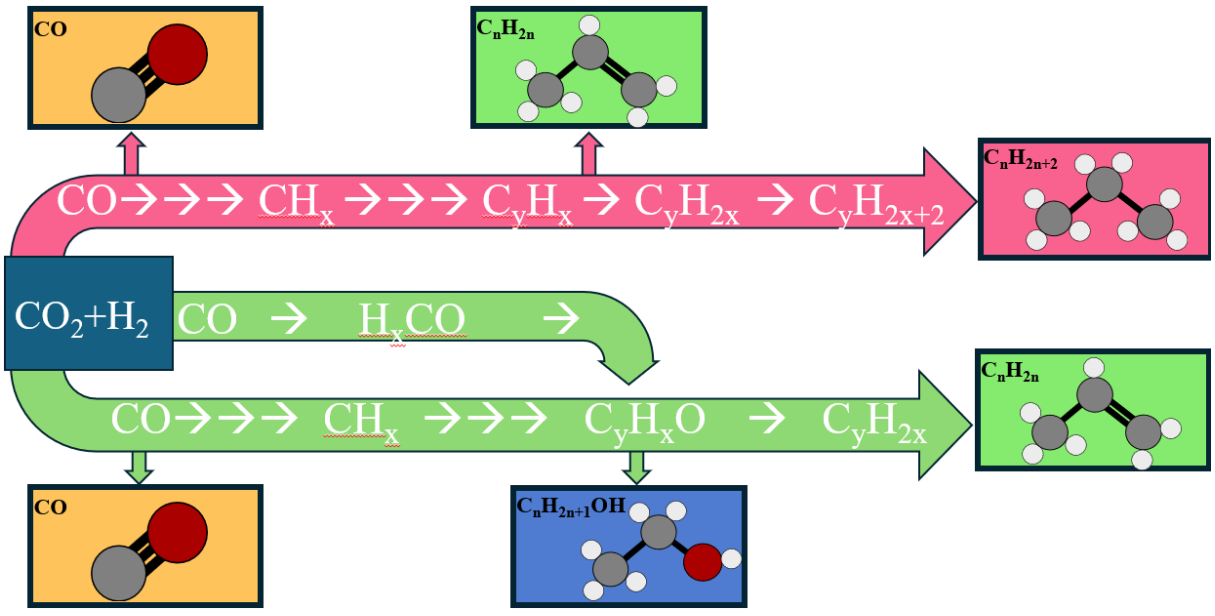

4.1.Introduction

The results of the investigation presented Chapter 3 have established that alkali metal (AM) promotion has a profound impact on the surface chemistry of our CZF catalysts under CO_2 hydrogenation conditions: notably, AMs enhances the formation of metallic Cu^0 and χ-Fe_5C_2 phases. This enhancement is achieved by surface AM species, which are in intimate contact with surface TMs. While such changes in surface phase composition are frequently correlated with increased C–C coupling and alcohol formation, the presence of these phases alone cannot fully account for the pronounced shift toward higher alcohols and olefins observed upon AM doping. Building on the structural and compositional insights developed in Chapter 3, the following chapter focuses on elucidating the degree to which AMs modify surface reaction pathways by altering the surface-adsorbate interaction. Herein there is a particular emphasis on adsorption, activation, and transformation of CO and CO-derived intermediates during CO_2 hydrogenation, which are assumed to be responsible for the AM induced catalytic change.

Chapter 4 aims to address the following central question: *Do alkali metals merely tune adsorption strengths within an existing reaction pathway, or do they open an entirely new pathway for CO_2 hydrogenation, which leads to both higher alcohols and olefins?* To answer this question, a comprehensive experimental strategy is employed, combining adsorption studies (TPD), intrinsic hydrogenation tests (C_2H_4-PTH), alcohol conversion tests (CH_3CH_2OH-PTH), mechanistic probing of CO activation (TPSR and CO-DRIFTS), and direct observation of reaction intermediates under working conditions (in-situ DRIFTS). Crucially, apart from the extensive implementation of these routine techniques, this research attempts to confirm a possible direct interaction between surface AMs and CO. Such direct interaction may be the prime driver behind the change in the CO_2 hydrogenation products upon the introduction of AMs. In this case, contrary to what is generally assumed in experimental studies, AM induced changes may be more accurately be attributed to geometrical effects rather than electronic effects. To this end, alongside CO adsorption DRIFTS experiments–which observe CO binding "*from the perspective of CO"*–CO adsorption Rb K-edge XAS experiments were conducted to observe CO surface interaction "*from the perspective of Rb"*.

4.2. Results

4.2.1. TPD

Understanding how the doped AMs (K, Rb and Cs) modify the CO_2 hydrogenation pathway first requires assessing their influence on the adsorption strengths of key surface species, namely the reactants (H_2 and CO_2) and representative products/intermediates (here ethylene as a model olefin). Adsorption strength is directly linked to reaction pathways through three fundamental catalytic concepts: the Sabatier principle, Brønsted–Evans–Polanyi (BEP) relations, and linear scaling relations. Collectively, these principles dictate that reaction kinetics are governed by the relative stabilities of reactants, intermediates, and products on the catalyst surface [123–125].

Due to the relative accessibility of TPD experiments numerous publications have correlated TPD-derived adsorption strengths profile with the observed shift the from paraffins to olefins during CO_2 hydrogenation catalysis. Specifically the suppression of paraffin formation in favour of olefins has frequently been attributed to weaker adsorption (or lower surface coverage) of either H_2 [28,73,80,82,126–130] or olefins [34,78,126,129] at the surface, both may decrease the hydrogenation ability of the catalyst [28,73,80,82,126–130]. The suppression of the hydrogenation ability by Na [80,126,129,130], K [28,73,128] and Cs [82] specifically has been rationalized in this way. Based on this prior work, the following hypothesis was formulated:

AMs decrease the H_2 desorption temperature, consistent with a reduced hydrogenation ability and suppressed paraffin formation.

Similarly, as noted, enhanced olefin selectivity has been related to the reduced surface binding strength of olefins (ethylene [34,78,126] and/or propylene [78,129]).Therefore, the C_2H_4-TPD behaviour was expected to follow:

The addition of AMs decreases the desorption temperature during C_2H_4-TPD analysis in line with the suppression of paraffin formation.

Additionally, although several works report the effect of AMs on the adsorption of CO_2 by the introduction of basic sites, these results are not generalizable: while several publications show an increase in the CO_2 binding strength of strongly bound CO_2 by doping AMs [33,126,130], others show a reduction in binding strength or promotion of less strongly bound CO_2 [81,82]. Nonetheless all these studies show a change in the CO_2 surface binding. Consequently, it was hypothesized that

AMs influence the binding of CO_2 by the catalyst leading to a change in the CO_2-TPD profile.

All TPD results show significant changes to the desorption profiles upon the inclusion of AMs (see Figure 41). Indeed, the CO_2-TPD profiles (Figure 41A) reveal substantial promoter-induced restructuring of CO_2 adsorption. Undoped CZF exhibits a single, relatively narrow CO_2 desorption envelope from 350-520 °C, with a maximum at 430°C. In contrast, the doped catalysts display broader desorption profiles: the desorption of CO_2 is clearly enhanced at 325-360 °C and 498-520 °C, accompanied by a marked suppression of the original 420 °C feature. Moreover, all AM-doped catalysts show lowered CO_2 desorption onset temperatures, indicating an altered distribution of surface basic sites or modified carbonate stability.

K-CZF additionally displays a high-temperature desorption band above 700 °C, which is well above typical reaction temperatures for CO_2 hydrogenation and hence may be catalytically less relevant. Overall, the strong changes in the activation of CO_2 may be derived from the increased carburization

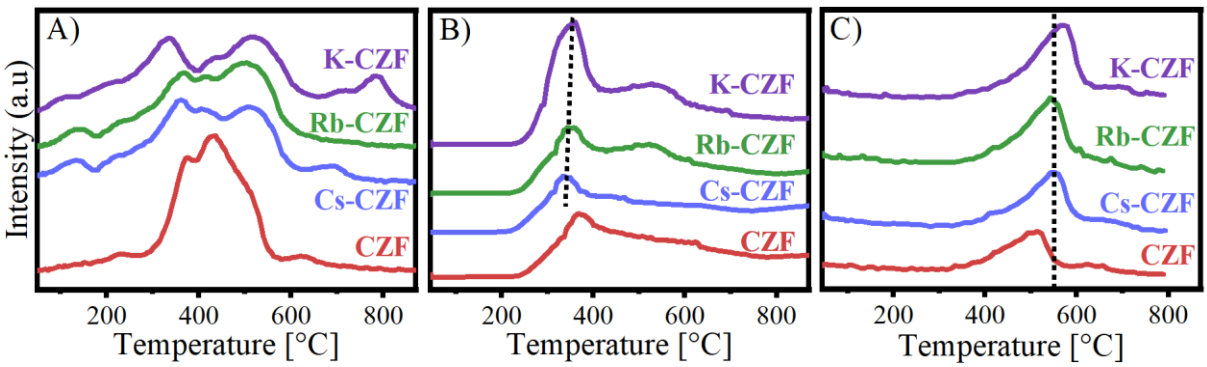

Figure 41| CO_2, H_2 and C_2H_4-TPD results. Panel A, B and C show the CO_2-, H_2 and C_2H_4- TPD results respectively. The profiles for CZF, Cs-CZF, Rb-CZF and K-CZF are shown from the bottom to the top

in red, blue, green and purple respectively. The dotted line in in Panel B shows the evolution of H_2 desorption over the doped samples. The dotted reference line in panel C is centred at 551 °C.

and reduction of Cu at the surface as was proven by XPS before or more complex surface interactions including electron transfer or direct AM-CO_2 interactions.

Curiously, the H_2-TPD and C_2H_4-TPD show opposite results: AM doping induces a weaker binding of H_2, but a stronger binding of C_2H_4. The former result is in line with the literature, while the latter differs. The weaker surface binding of H_2 at the doped surfaces is reflected by a lowering of the main desorption band: compared to CZF the main desorption band is shifted from 360 °C to 338, 348 and 353 °C when Cs, Rb or K are doped. Although the position of the main H_2 desorption band is similar for K-CZF and CZF, a noticeably larger amount of H_2 desorbs from the K doped surface between 240 and 353 °C. In contrast to CZF, Rb-CZF and K-CZF also exhibit additional higher-temperature features at 534 and 547 °C, respectively. Overall, the H_2-TPD results are in line with literature reports that alkali promoters reduce H_2 adsorption strength, thereby suppressing paraffin-forming hydrogenation pathways.

This is contrasted by to the activation of C_2H_4, for which the desorption peak is shifted to higher temperatures over the doped surfaces. The desorption peak at 508 °C on CZF is shifted up by 53 °C to 551 °C for Cs-CZF and Rb-CZF, and by a further 21 °C to 571 °C for K-CZF. The stronger retention of olefins like C_2H_4 is expected to lead higher probability of secondary hydrogenation resulting in a higher paraffin selectivity.

All-in-all the H_2- and C_2H_4-TPD results show a destabilization of the adsorbed H_2 species at catalytically relevant temperatures, but an increase in the binding of C_2H_4. The former ought to lead to a decrease in the hydrogenation ability due to AM doping, the latter to an increase in the secondary hydrogenation of olefins and its intermediates. Due to the ambiguity of these results no strong conclusions can be drawn regarding the effect of AM doping on the hydrogenation ability of these catalysts.

4.2.2. Pulse Transient Hydrogenation experiments

To further investigate the effect of AMs on CO_2 hydrogenation pathways, two sets of Pulse Transient Hydrogenation (PTH) experiments were performed: ethylene-PTH and ethanol-PTH. Using these experiments the ability of the catalysts to hydrogenate olefins (secondary hydrogenation) and the ability to decompose alcohols into hydrocarbons can be determined. These reactions are assumed to be potentially relevant steps towards the formation/retention of olefins during CO_2 hydrogenation.

By using a relatively uncomplicated molecule like ethylene (C_2H_4) the overall hydrogenation ability (OHA) can be tested without having to contest with a potentially highly complicated reaction mechanism consisting of many reaction intermediates. Additionally, the C_2H_4-PTH data gives direct proof for the hydrogenation ability. No further reliance on scaling relations or Sabatier principle is required, in contrast to TPD.

Considering the CO_2 hydrogenation results reported in this thesis and the available literature on the effects of alkali metal doping [80,126–131] it is hypothesized that:

The addition of AMs suppresses the hydrogenation ability of the catalyst.

The MS-response during the C_2H_4-PTH experiments over the four catalysts of interest are shown in Figure 42A. The peaks correspond to the periodic pulsing of ethylene gas over the catalyst materials. The scaled average peak area ratio of the reaction products ((100*ethane)/ethylene) are reported in Figure 42B. This unitless variable constitutes a measure of the OHA of the catalysts. The error bars indicate the standard deviation of the measured data for each sample. Surprisingly, the results in Figure 42B show no clear trend regarding the OHA of the catalyst and the presence of AMs: while Cs-CZF has a lower OHA than CZF within error (3.24 and 3.64 respectively), Rb- and K-CZF show a higher OHA (5.10 and 5.05 respectively). Hence, in the case of these materials, the presence of AMs does not outrightly suppress the ability of the catalyst to transfer hydrogen atoms to unsaturated hydrocarbons. In other words, the formation of olefins during CO_2 hydrogenation cannot be the result of a lower rate

of hydrogen transfer reaction. Consequently the primary route for the formation of olefins is likely separate from the formation of paraffins.

A possible route for the formation of olefins may be the dehydration of alcohols, which is a well-known route to produce olefins in industry [270]. Although this reaction generally requires acidic zeolite or Al_2O_3 catalysts [270], the conversion of alcohols to olefins has also been reported over Fe [271,272] or Zn [273] based catalysts in the absence of such acidic zeolites. To determine viability of this reaction route over our catalysts CH_3CH_2OH-PTH experiments have been performed. Drawing on the BEP relations, the increase in ethylene adsorption strength (as measured by TPD in Section 2.4.1) might drag down the reaction barrier for the formation of ethylene from ethanol (CH_3CH_2OH) resulting in a higher conversion of ethanol. Therefore it is hypothesized that:

The addition of AMs increases the catalyst' ability to convert ethanol into ethylene and ethane.

Indeed, the data in Figure 43 support this hypothesis. All catalysts have the ability to convert ethanol to hydrocarbons both in the absence and presence of AM promotors, but clear changes are observed. The MS shows that the transient hydrogenation of the ethanol primarily results in the formation of ethylene (m/z = 27) with smaller amounts of ethane (m/z = 30). Furthermore, the total ethanol conversion changes according to the following order CZF<Cs-CZF<Rb-CZF<K-CZF (see Figure 43B). More specifically the ethylene- and ethane-to-ethanol peak ratios change from 2.41/0.44 for CZF to 2.79/0.52, 3.49/0.64 and 4.30/0.76 for Cs-CZF, Rb-CZF and K-CZF respectively. The higher degree of ethanol conversion over the different AMs may be due to a number of factors such as: the larger number of AM atoms present at the surface for the lighter AMs; the relatively higher degree of surface carburization induced by the lighter alkalis; or may arise from a more favourable interaction between the lighter AMs and ethanol. In summary, these findings demonstrate that ethanol readily undergoes conversion to olefins over CZF-based catalysts and that alkali-metal promotion significantly enhances this reactivity.

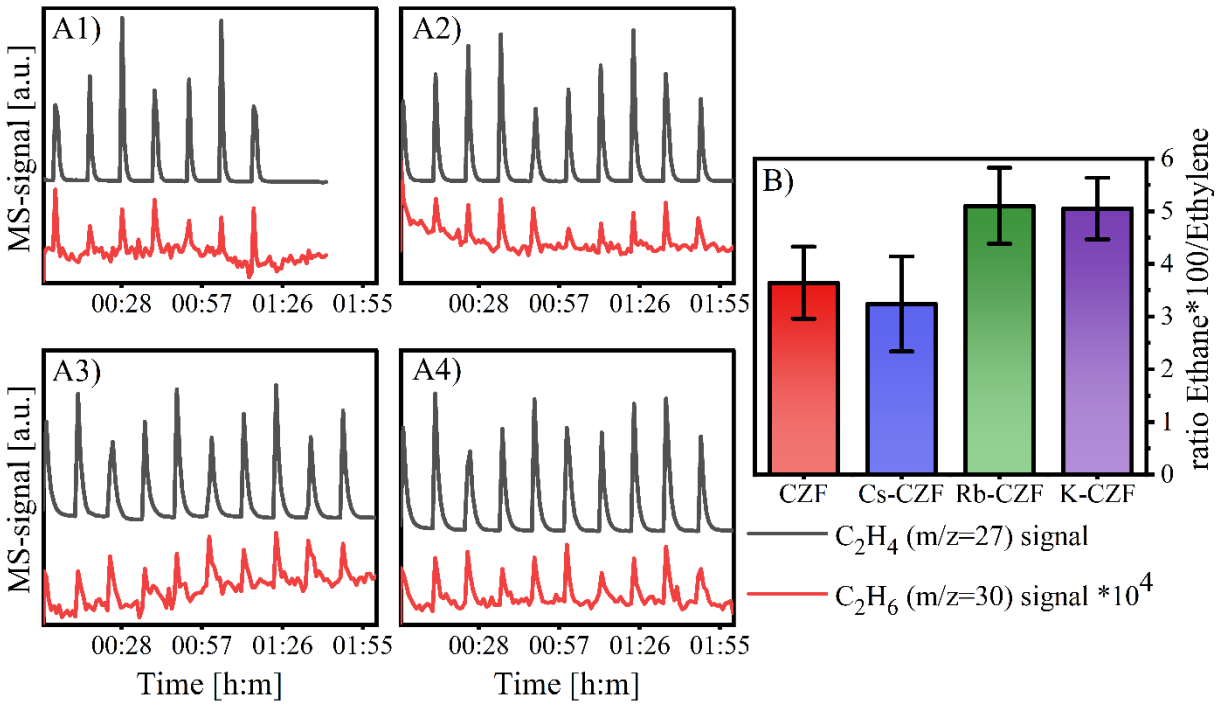

Figure 42| Ethylene Pulse Transient Hydrogenation. The MS response during the ethylene PTH experiments are indicated for CZF, Cs-CZF, Rb-CZF and K-CZF in panels A1, 2, 3 and 4 respectively. The data are obtained at 320 °C, while continuously flowing H_2 at atmospheric pressure. Fragments m/z=27 (ethylene) and 30 (ethane) are plotted in grey, and red respectively. The ethane signal is multiplied by 10^4 for clarity. From left to right panel B shows the averaged ratio of ethane*100 to ethylene for CZF (red), Cs-CZF (blue), Rb-CZF (green) and K-CZF (purple), which is a measure of their OHA. The error bars indicate the standard deviation of the measured data for each sample.

Although these PTH experiments give valuable insight into the intrinsic catalytic ability of these materials in terms of OHA and ethanol conversion, these experiments only provide proxies for the catalytic behaviour under CO_2 hydrogenation conditions. They cannot prove whether ethanol decomposition indeed occurs during CO_2 hydrogenation. As a consequence, although these PTH experiments prove that the suppression of OHA is not a viable route to the generation of olefins and they prove that ethanol decomposition might be a possible route, no direct claim can be made about the reaction mechanism of CO_2 hydrogenation at this point. To this end the next section shows the results of in-situ DRIFTS experiments using Cs-CZF and CZF to verify the reaction intermediates generated under CO_2 hydrogenation conditions.

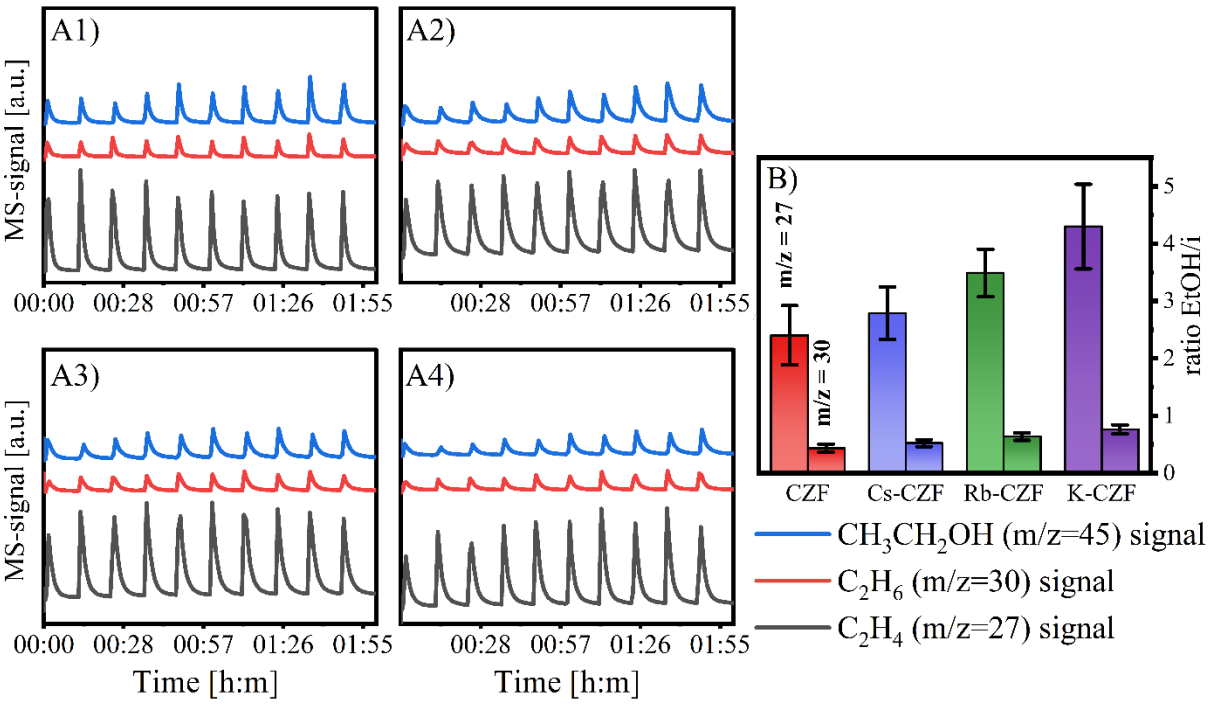

Figure 43| Ethanol Pulse Transient Hydrogenation. The MS response during the ethanol PTH experiments are indicated for CZF, Cs-CZF, Rb-CZF and K-CZF in panels A1, 2, 3 and 4 respectively. The data are obtained at 320 °C, while continuously flowing H_2 at atmospheric pressure From bottom to top the fragments m/z=27, 30 and 45 are plotted in grey, red and blue respectively. Panel B shows the averaged ratio of ethylene (m/z=27) and ethane (m/z=30) to ethanol (m/z=45).

4.2.3. In-situ DRIFTS

To understand the reaction mechanism for the formation of HA and olefins it is necessary to investigate the surface species generated during reaction. As has been shown, the formation of HA and olefins does not correlate with the OHA of the catalysts (Section 4.2.2). Instead, it has been hypothesized that the reaction pathway of HA and olefins may be related via a dehydration reaction step. In effect, it is expected that the AMs facilitate the generation of entirely new oxygenated intermediates. These intermediates constitute an entirely new reaction mechanism which efficiently forms HAs and olefins. The formation of oxygenated intermediates is a necessary condition for such a reaction mechanism. More precisely, in this section we investigate the hypothesis:

AMs facilitate the formation of oxygenate intermediates via insertion of CO (/H_xCO) species.

To this end *in-situ* DRIFTS experiments were performed at 30 bar, 5 bar and atmospheric pressure. In all cases the obtained spectra showed the similar features. Here only the results of the experiments at 5 bar are reported. At these conditions all features are clearly discernible without large amounts of hydrocarbons obscuring the surface species between 3100 and 2700 cm^{-1}. These data thus enable a direct comparison of the surface chemistry on Cs-CZF and CZF under representative reaction conditions.

Figure 44 shows the spectral evolution indicating the formation of surface species upon switching from pure H_2 to CO_2/H_2 mixture over Cs-CZF and CZF at 290 °C and 5 bar. The spectra are measured sequentially without delay at 290 °C. The data have been plotted such that the relative intensity of the bands between the different regions is maintained.

Upon introduction of CO_2 characteristic bands confirm the formation of CO reaction: three CO-related features appear at 2200–2150, 2140–2050 and 1960–1910 cm^{-1}. Corresponding respectively to the R-branch of gas-phase CO (CO(g)) [274], monodentate adsorbed CO (m-CO) overlapping with the P-branch of CO (g) [274], and bidentate adsorbed CO (b-CO) [23,81] . These bands form more rapidly over Cs-CZF than CZF. Furthermore, the b-CO band on Cs-CZF appears stronger and red-shifted relative CZF. The accelerated formation of CO over Cs-CZF reflects the promotional effect of Cs. The red-

shifting of b-CO suggests a different environment for the adsorption of CO at the Cs doped surface resulting in greater back-donation. Hence Cs affects the catalytic behaviour not only by increasing the number of catalytic sites through promoting carburization, but also by generating entirely new catalytic sites.

A second major difference between CZF and Cs-CZF is observed in the region from 3050 to 2800 cm^{-1}. This region is characteristic of the C-H vibrations for different functional groups. Alongside the sharp symmetrical stretching vibrational band of methane (CH_4) at 3015 cm^{-1} [234,275] a number of additional bands are observed between 2970 and 2850 cm^{-1}. The former is related to the band at 1303 cm^{-1}, which can be attributed the bending vibrational mode of CH_4 [235,236,275,276]. The latter are likely the result of multi-carbon species: while the methane peak is formed relatively rapidly over both catalysts (as indicated by both stretching and bending features), the remaining bands in this region increase more slowly, in line with a relatively more sluggish C–C coupling reaction [107]. Throughout the reaction the methane features remain dominant over CZF, while they are significantly suppressed over Cs-CZF.

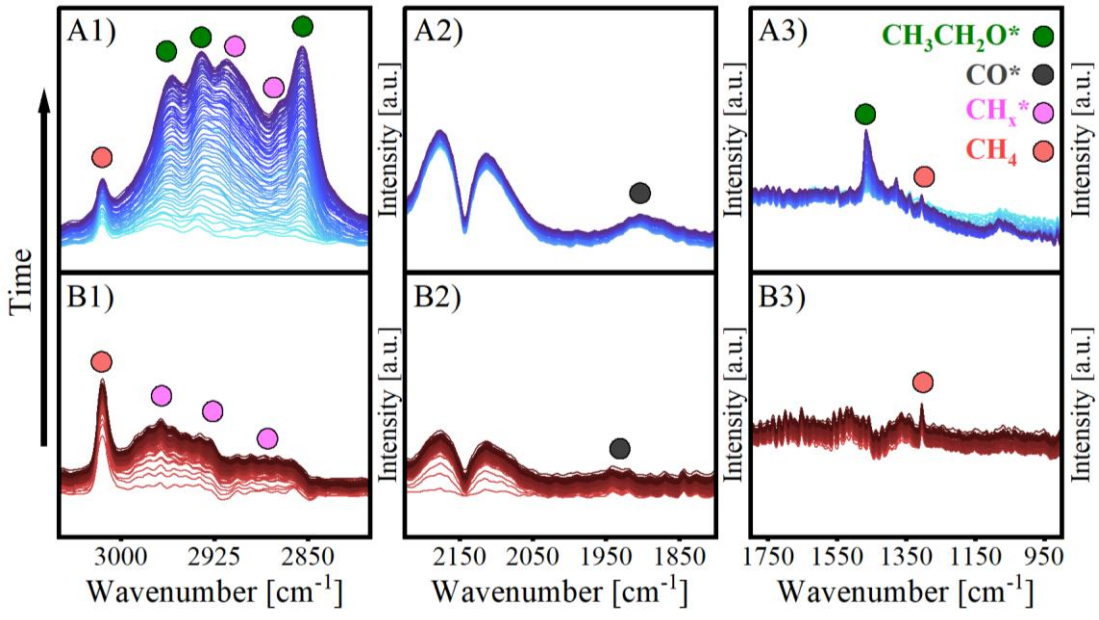

Figure 44| In-situ CO_2 hydrogenation DRIFTS. The evolution of surface species during CO_2 hydrogenation over Cs-CZF (A1–3) and CZF (B1–3) at 5 bar and 290 °C. Spectra are taken consecutively after switching the gas feed from pure H_2 to CO_2/H_2 (1/3). The main absorption bands related to CH_3CH_2O*, CO*, CH_x* and CH_4 are indicated with green, grey, pink and orange markers respectively.

For CZF the remaining bands in this region are dominated by three broad features: the two bands at 2968 and 2908–2862 cm^{-1} are related to alkyl species, CH_3* and CH_2* respectively [276]. The assignment shoulder at 2938 cm^{-1} is more difficult. Although similar wide indistinct bands, including the shoulder at 2938 cm^{-1}, have previously been attributed explicitly to the formation of alkanes [79,132,276–278], the shoulder at 2938 may alternatively indicate the formation of formate species instead (HCOO*) [81]. In the latter case, such formate feature may be related to the band observed at 1363 cm^{-1}, which could be indicative of the symmetric O-C-O vibration of formate [19,79,81,132,277,279]. The corresponding asymmetric vibrational band between 1550 and 1580 cm^{-1} [19,35,79,277,279] is not clearly discernible however. Thus, while alkyl species dominate the CZF spectrum, minor formate formation cannot be excluded.

Over Cs-CZF, the formation of formate species is considerably clearer: the 2938 cm^{-1} band is more pronounced and a formate band at 1377 cm^{-1} is observed to grow steadily after 20 minutes (in line with the increasing intensity at 2938 cm^{-1}). Notably, the increase in HCOO* is not accompanied by an increase in methoxy (CH_3O*) species, which are identified by the characteristic CH_3 rocking vibrational mode between 1078 and 1042 cm^{-1} : the formation of CH_3O* is typically observed over Cu-based methanol synthesis catalysts and is derived from HCOO*. Here the conversion of HCOO* to CH_3O remains negligible here, indicating that the increased formate coverage is does not lead to increased methanol formation.

In addition to formate, Cs-CZF uniquely presents clear signatures of CH_3CH_2O* species, with CH_3 bands at 2959 (asymmetric) [23–25,81,82,132,234,235,280,281] and 2871 (symmetric) [82,280], and CH_2 bands at 2920 (asymmetric) [77,275,280] and 2855 cm^{-1} (symmetric) [81,275,276,281]). Importantly, the existence of the $CH_3CH_2O^*$ species is verified by the band at 1466 cm^{-1}, which corresponds to the CH_2 bending vibrational mode of CH_3CH_2O* [23,275,282]. All these features are entirely absent on CZF. Surface CH_3CH_2O* is widely considered a key intermediate toward higher alcohols [81,275,276,281], yet the expected precursor CH_3CHO* cannot be confidently identified in the expected region above 1700 cm^{-1} [133,235,275,283] due to excessive noise. This difficulty in identifying CH_3CHO* has been reported before over a similar catalyst [82]. The appearance of CH_3CH_2O* nevertheless confirms the formation of

oxygenated multi-carbon intermediates over Cs-CZF, in contrast to the non-oxygenated hydrocarbon-dominated pathway over CZF.

Despite previous reports suggesting that b-CO dissociation over FeCx surfaces may be responsible for the formation of methane [134,235], such dissociative CO conversion seems to be considerably inhibited by Cs in this case: although the b-CO band is stronger over Cs-CZF, the early-stage CH_4 band is weaker compared to CZF. This suppression is consistent with the destabilization of H_2 at the surface as observed by H_2-TPD (Section 4.2.1) and suggests that Cs stabilizes b-CO relative to its dissociation products. In this sense, considering the C_2H_4-PTH experiments, paraffin formation during CO_2 hydrogenation is disfavoured due to the stabilization of b-CO relative to methane, rather than suppression of secondary hydrogenation. Such changes to the relative stability prevent the conversion of the former into the later by dissociation and hydrogenation.

In light of the ethanol-PTH results presented earlier (Section 4.2.2), it can be concluded that the further hydrogenation and dehydration of $CH_3CH_2O^*$ leads to the formation of HAs as well as olefins. The current results therefore suggest that the formation of olefins and higher alcohols can be attributed to a shared reaction pathway. Based on these results an updated version of Figure 8, which shows a schematic representation of the reaction pathways leading to various products over a Cu-FeC_x based on the literature, is presented in Figure 45.

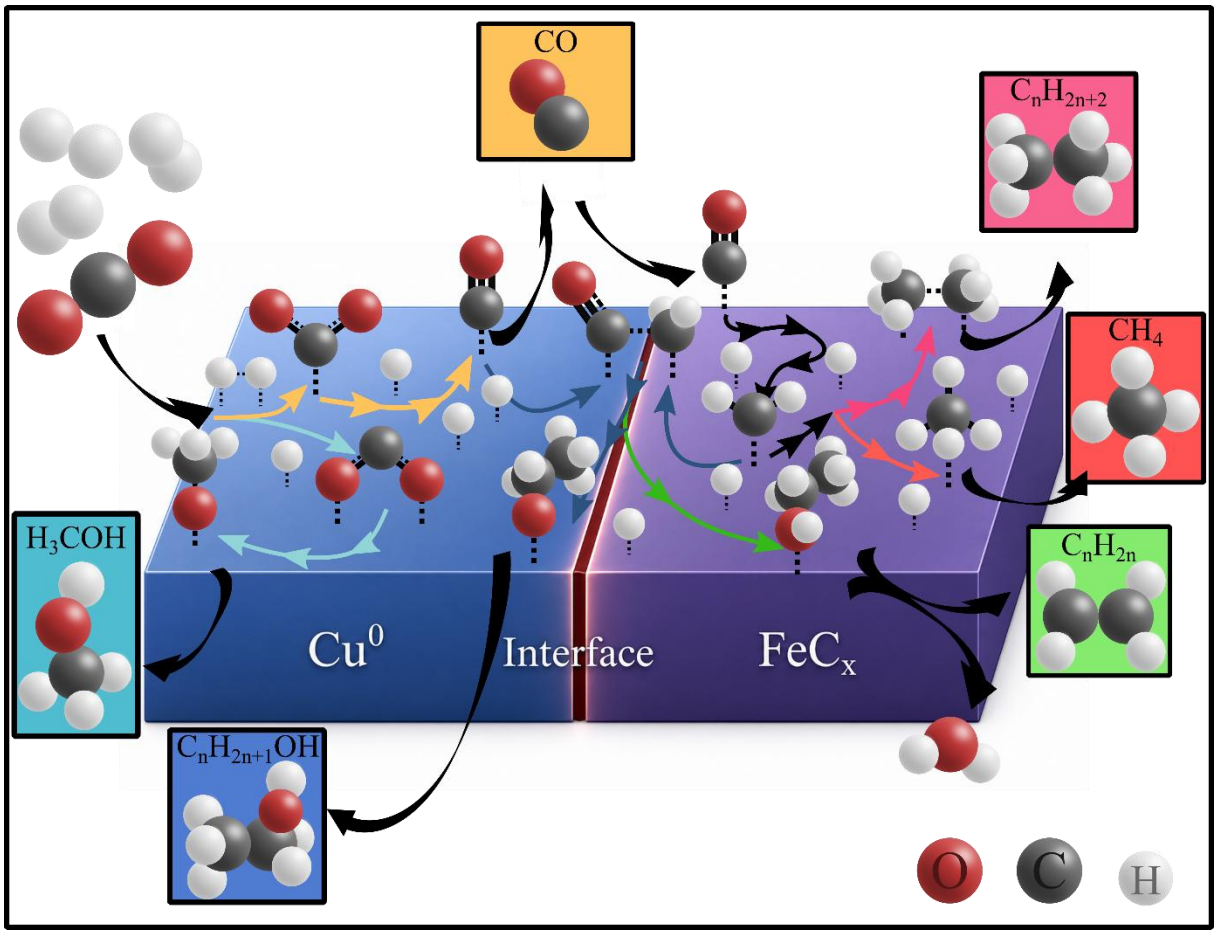

Figure 45| Updated schematic representation of the formation of various products from CO_2 over at the surface of a Cu^0-FeC_x based catalyst. Oxygen, carbon and hydrogen atoms are represented by red, grey and white spheres. The yellow, light blue dark blue, red, green and orange arrows indicate reaction pathways leading to, CO, methanol, higher alcohols, paraffins, olefins and methane respectively. The figure contents is based on Ref. [23,80–82,126–135] and modified based on the results obtained in Chapter 4 of this thesis including a shared pathway for the formation of higher alcohols and olefins. The graphical design was inspired by a similar scheme published in Ref. [135].

As discussed earlier, alcohol formation is often attributed to CO insertion into alkyl chains over carbide phases or Cu-carbide interfaces [23,81,82,132–134]. Therefore, the increased formation of alcohols and olefins over AM doped catalysts may be attributed to their ability to promote carburization through the suppressing of re-oxidation (Chapter 3). However, the present results indicate that the increase in Cu^0 and Fe_5C_2 phases alone is insufficient to account for the behaviour of AM-promoted catalysts. Instead, the current DRIFTS experiments demonstrate that even at an early stage of the reaction (when presumably FeC_x is rapidly formed from Fe^0) different chemical species are formed in the presence of Cs than in its absence. The increased prevalence of multi carbon intermediates at the steady state might

straightforwardly be attributed to an increase in the FeC_x at the surface compared to FeO_x , but the generation of $CH_3CH_2O^*$ at an early stage may not be. Instead, the formation of these intermediates is likely facilitated by the increased binding of CO relative to its dissociation products. Consequently, the observed increase in higher alcohol and olefin formation is best rationalized by Cs-driven changes in CO binding and insertion kinetics, rather than by carburization effects alone.

Sections 4.2.4 and 4.2.5 are dedicated to understanding the increase in the CO surface activation due to the presence of AMs.

4.2.4. TPSR

To understand the ultimate fate of CO generated by RWGS during CO_2 hydrogenation and the effect of alkali metals on this process, Temperature Programmed Surface Reaction (TPSR) experiments have been conducted. Such experiments are able to illustrate changes in the dissociative and non-dissociative activation of CO. The balance between such sites is believed to be crucial for the formation of higher alcohols during reaction [23–25,81–83,120,284,285].

Regarding the non-dissociative CO activation, reduced Cu species are assumed to provide the necessary binding sites [23,34,81–83,120]. However, the inclusion of AMs like K [23,81,286] and Cs [82] have been found to have the ability to further facilitate such binding of CO. Hence, it is hypothesized that

the presence of alkali metals increases the temperature of desorption of CO.

Considering the proposed electron charge transfer as a mechanism of AM promotion, it is hypothesized that:

the temperature of CO desorption increases with the electro positivity of the AM.

Furthermore, by performing these experiments on both reduced and carburized samples, the effect of the FeC_x can be elucidated. While the dissociative activation of CO is has been consistently associated with FeC_x surfaces [23,25,81–83], the effect of the pre-formation of such carbide surfaces on the activation of CO has been neglected [23–25,81–83,284,285]. Hence, here the TPSR results of reduced and carburized samples are compared to confirm the role of FeC_x. This carburization was performed after an initial reduction by exposing the samples to CO_2/H_2 (ratio 1/3) and heating at 320 °C. This allows for testing the hypothesis:

There are three hypotheses to be evaluated:

The presence of FeC_x promotes the formation of coupled hydrocarbons by providing dissociative CO binding sites at an appropriate binding strength.

The MS response for m/z=28 ($[CO]^+$ or $[C_2H_4]^+$) and m/z=16 ($[CH_4]^+$) during the TPSR experiments are plotted in Figure 46.[5] The TPSR results clearly show a dependence on the presence of AMs and the pre-treatment (reduced or spent).

It is shown that binding strength of weakly held CO on the reduced catalyst surfaces is significantly increased by the presence of AM doping (see Figure 46A1). More specifically, while a clear CO desorption peak is observed at around 170 °C for reduced CZF, this peak is absent for doped samples. Instead a higher temperature desorption peak is observed between 250 and 260 °C. At the same time the medium temperature desorption peak remains around the same temperature for all samples after reduction as indicated by the reference line at 416 °C. Interestingly this medium temperature desorption peak increases with the presence of AMs and is maximal for Rb-CZF followed by K-CZF and Cs-CZF. An additional high temperature peak is observed for K-CZF, which is absent for all other samples. The addition of binding these strongly CO bastion sites may be related to the increased CO selectivity observed during reaction.

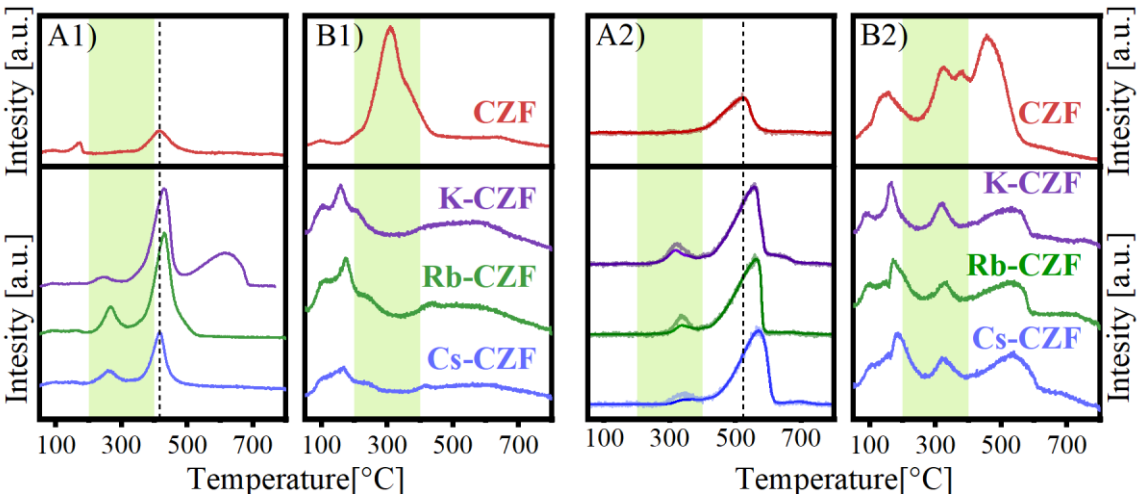

Figure 46| Temperature Programmed Surface Reaction over reduced (1) and spent (2) samples. The data are obtained after pretreatment (see methods) and pre-adsorption of CO. After flushing away gas phase CO, the gas stream is switched to H_2 and the data is collected while ramping to 800°C. Panels A and B show the MS detector response for mass fragments m/z= 28 and m/z=16 respectively. Panel A2 also shows the MS response for fragment m/z=27. For comparison, the m/z=27 response is scaled such that the peaks maxima of m/z=28 and m/z=27 overlap. Samples CZF, K-CZF, Rb-CZF and Cs-

[5] Note that for all experiments the ratio of the peak maxima of m/z=28 and m/z=27 is between 0.012 and 0.017 indicating that the majority of the desorbed species are likely derived from $[CO]^+$ rather than $[C_2H_4]^+$.

CZF are plotted in red, purple, green and blue respectively. The temperature range appropriate for CO_2 hydrogenation is highlighted in green (200–400°C).

Regarding the dissociative activation of CO, it can be noted that the CH_4 desorption behaviour changes significantly upon doping K, Rb or Cs, while the difference between the doped samples remains minimal. Compared to CZF doped samples produce significantly less CH_4 and the desorption temperature changes strongly. For the doped samples the majority of CH_4 is generated at low temperatures (between 100 and 200 °C) compared to CZF, which generates CH_4 around 306 °C. At high temperatures (400 to 700 °C) a broad desorption peak is observed for the doped samples, which is minimal for CZF.

These results illustrate two important effects of AM doping on the dissociative and non-dissociative activation of CO at temperature appropriate for CO_2 hydrogenation (250 and 330 °C). Firstly, at such conditions, the dissociative activation of CO (generation of CH_4) is suppressed in the presence of AMs. This is illustrated by the lack of desorption peaks in this region (Figure 46B1). Secondly, the weakly held non-dissociative CO species may play a more prominent role during CO_2 hydrogenation due to their increased binding strength. This increased surface binding brings these species into the CO_2 hydrogenation regime.

Interestingly the desorption curves change sharply after carburization under CO_2 hydrogenation conditions, however the general conclusions noted above remain the same. The change in the TPSR results can be attributed to the preformation of the carbide phase.

The desorption of CO and coupled hydrocarbons are illustrated in Figure 46A2. In the absence of AMs a single desorption peak is observed at 522 °C. This high temperature desorption peak is shifted to higher temperatures in the presence of AMs by 40-50 °C. Both the peak shape and temperature of this desorption peak closely resemble the desorption of ethylene during the TPD experiments reported earlier. Indeed, when the MS response for m/z=27 ($[C_2H_3]^+$) [6], which should be absent for CO, is overlaid and scaled it closely follows the m/z=28 curve. This shows that CO desorbs alongside hydrocarbons. In

[6] Note that m/z=27 is the main fragment associated with olefinic hydrocarbons.

contrast to the reduced samples no significant difference in the high temperature desorption peak area is measured in this case. Interestingly, a second low temperature desorption peak is observed only in the presence of AMs, which is not shown in the simple TPD experiment. Importantly this desorption happens in the CO_2 hydrogenation region and the m/z=27 response is relatively higher than the higher temperature peak. This shows that the interaction between pre-adsorbed CO and H_2 enables the formation of and desorption of coupled hydrocarbons at much more tractable temperatures.

Regarding the dissociative activation of CO, a mismatch exists for the undoped sample, which is alleviated by the presence of AMs: dissociative activation of CO readily takes place in CO_2 hydrogenation region over CZF, while non-dissociative activation lacks (as described above). In fact, carburization of the sample extends that range at which dissociative CO activation occurs, while non-dissociative CO activation remains inadequate. In contrast, the doped samples are able to provide both modes of activation granted the surface is carburized: while the doped samples after reduction lack the ability to dissociatively activate CO in the appropriate temperature range, this restriction is alleviated after carburization. This is in line with the FTIR results reported earlier, which showed a gradual formation of hydrocarbons during reaction as a consequence of carburization. This clearly illustrates the role of carbide phase to dissociate CO and the ability of the AMs to regulate this dissociation.

Taken together the TPSR results clearly illustrate the role of AMs in regulating the dissociative and non-dissociative activation of CO. The co-establishment of these binding modes with appropriate binding strength to be utilised during CO_2 hydrogenation may explain the ability of these materials facilitate CO insertion.

4.2.5. CO-Adsorption

As evidenced by the previous sections the presence of AMs induces the catalytic ability to generate oxygenated species at the surface via insertion of CO (or CO-like intermediates) into alkyl chains. This insertion is likely facilitated by the coexistence of CO dissociative and CO non-dissociative activation under the relevant temperatures. However, it remains elusive through what means Cs, Rb and K are able to facilitate this insertion. Presumably, and as implied by the TPSR experiments, their surface presence increases the binding strength of the non-dissociated CO surface species, thereby making their insertion possible.

A priori, the relative electro-positivity of AMs may lead to the hypothesis that they increase the surface electron density of the transition metals, consequently increasing the back bonding to the C-O bond and increasing the TM-C bond. However, as outlined in Section 3.2.2.5 no electron donation is observed as measured by XPS. Nonetheless the TPSR data show an increase in the non-dissociative activation of CO.

The results of a number of recent computational studies provide useful insight into the surface effects of AMs in this respect. Such work has shown that the electron donation by AMs is highly localised, effecting only the nearest surface atoms [261,287,288]–which may explain the XPS results. More importantly, a direct interplay between oxygen containing adsorbates (CO or H_xCO_2), the surface TMs and surface AMs was observed (see the schematic summarizing this interaction in Figure 47) [261,287–294]. These computational results are reinforced by atomic resolution microscopic studies showing the proximal interaction of surface AMs and adsorbates [291,293]. The proximity between surface AMs and oxygen containing adsorbates results in an interaction which includes two factors involving electrostatics and charge compensation [261,287–294]: the electrostatic interaction exists between the positively charged surface AMs and negatively charged CO or H_xCO_2 adsorbates; the charge compensation is characterized by the additional electron transfer from the surface AMs to surface TMs induced by the oxygen containing adsorbates. Both of these factors contribute to the strengthened surface binding of oxygen containing adsorbates.

The electrostatic interaction, which exists in addition to TM-H_xCO_y interaction, anchors the oxygen containing species to the surface [261,288–290,293,294]. The positive and negative charges on the surface AMs and adsorbates are a consequence of their interaction with the clean TM surface (see Figure 47A2 and B1): while AMs donate electrons to the TM surface (generating lightly negative charged), the oxygenated adsorbates accept electrons from the TM surface (generating lightly positive charged) instead [261,288–290,293]. Accordingly, upon the coexistence of such negative and positive surface species an electrostatic force is expected between them (indicated by the hashed line in Figure 47B2). Indeed, such interaction is credited to more strongly bind the adsorbates in the presence of AMs.

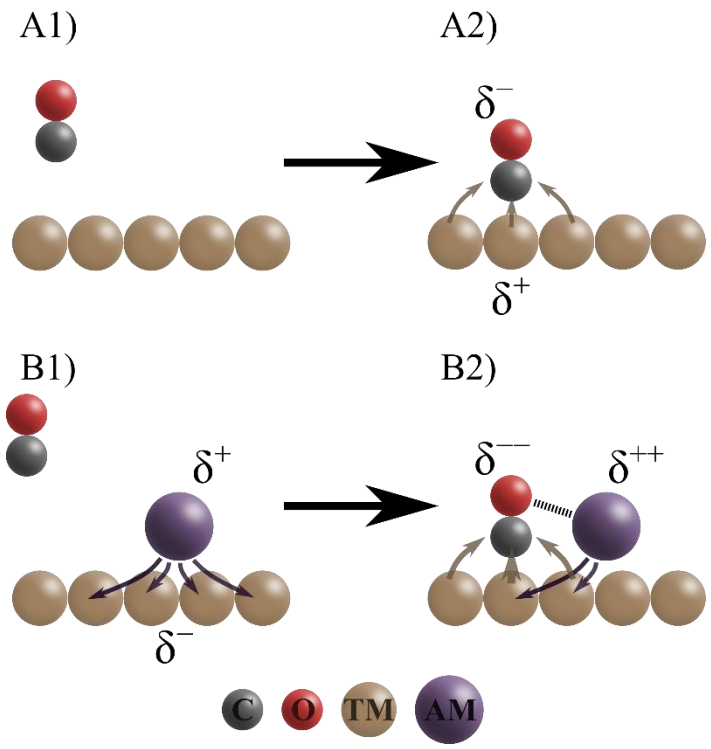

Figure 47| Generalized schematic representation of the interaction between adsorbed CO and surface AMs based on DFT literature. The electron density redistribution relative to the clean TM surface is indicated by curved arrows. Panel A shows the adsorption of CO on a metallic TM surface resulting in negative and positive charge buildup on the adsorbate and surface TMs respectively. Panel B1 shows the electron donation of surface AMs to TM atoms before the introduction of the adsorbate. Panel B2 shows the adsorption of CO in the presence of an AM atom. An electrostatic interaction is indicated by a hashed line. The additional adsorbate induced electron transfer and resulting charges are indicated.

Moreover, AM adatoms provide charge compensation to the surface TMs [261,288,290,292–294]: upon introduction of the oxygen containing adsorbate the charge on the surface AM atom increases due to enhanced electron transfer to the electron deprived surface TMs (see the schematic in Figure 47). In other words, rather than accepting electron density from the electron rich oxygenate, AMs donate additional electron density to the positively charged TM atoms, thereby modulating the excessive surface charge build up. Such behaviour results in greater occupation of the C-O anti-bonding states (back-donation) [294]. Hence these DFT results show a dynamic interplay between surface AMs, TMs and adsorbates, which goes beyond simple electron donation effects. However, to our knowledge no direct experimental evidence exists for the interplay between CO and surface AMs.

To gain a more in depth understanding of the interaction between the catalyst and CO, the following two sections (Section 4.2.5 and 4.2.5.2) focus on this interaction respectively "*from the perspective of CO"* using CO-DRIFTS experiments and *"from the perspective of the AMs"* using CO adsorption XAS experiments.

4.2.5.1. CO-Adsorption DRIFTS

This section presents the results of a series of CO adsorption DRIFTS experiments employed to investigate the effect of AMs on the catalyst CO surface interaction. The following hypotheses guided the experimental design:

AMs influence the surface binding of different CO adsorption modes on oxygen rich and reduced surfaces;

and

CO can be adsorbed in a bridged configuration on reduced surfaces at elevated temperatures.

To investigate these hypotheses different pretreatments and experimental designs have been employed.

Figure 48 shows the room temperature CO-DRIFTS absorption bands for CZF and Cs-CZF after reduction using 5% H_2. Panel A shows the region from 1800 to 2225 cm^{-1} , in which the linear CO stretching vibration is expected. Inconveniently, gas phase CO overlaps with the linearly vibration of monodentate adsorbed CO (m-CO*). The former generates 2 peaks around 2111 and 2170 cm^{-1} corresponding to P- and R-branch of its rotational-vibrational spectrum. The P-branch generally overlaps with surface bond CO band in this region [274]. To reveal the surface bound species, the spectra were measured during CO desorption. The peak around 2111 cm^{-1} rapidly disappears during flushing with N_2 (within 10 minutes), while the peak at lower wavenumber remains. After prolonged flushing the linear CO band shifts down by 3–4 cm^{-1}. The disappears of the R-branch band indicates the removal of CO in the gas phase, hence from this point onwards (after 10 minutes) the band around 2100 cm^{-1} peak can be exclusively assigned to surface bound CO.

Importantly, the results in Figure 48A show a red shift of the surface CO band for Cs-CZF relative to CZF: the bands are centred at 2099 and 2111 cm^{-1} respectively. The same red-shift is measured for Rb-CZF, while the red is 10 cm^{-1} greater for K-CZF. This downward shift of the band evidences an increase in the C-O bond. This bond elongation indicates greater backdonation into the

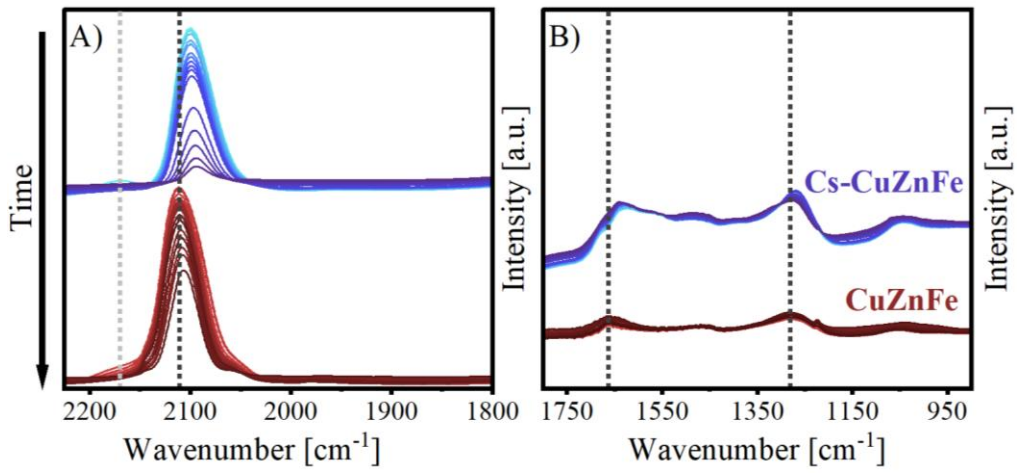

Figure 48| CO-DRIFT over Cs-CZF and CZF. The figure shows the evolution of the DRIFT absorption bands during the desorption of CO from Cs-CZF (blue/top) and CZF (red/bottom) during flushing with N_2. For comparison the black dotted reference lines are centred at the initial band positions for CZF. The grey reference line indicates the CO band which can be exclusively be attributed to the gas phase. The regions for CO and carbonate like species are shown in panel A and B respectively.

empty π* anti bonding orbital of CO and a strengthening of the surface interaction in the presence of AMs. Curiously, this redshift occurs only in the presence of Cu, Fe and AMs: when only Fe and Cs or Cu and Cs are present no such shift is observed relative to the non-AM-doped sample (see Figure S32). This implies the existence of a unique active site consisting of Cu, Fe and the AM to more strongly bind linear CO.

Figure 48B shows the formation of carbonates (CO_3^*) with major bands at 1640─1680 and 1270─1280 cm^{-1}. It is notable that no carbonate peaks are observed in the absence of Fe (see Figure S32B). This implies that the carbonates, which chiefly present as bidentate carbonates, are formed on the Fe oxide surfaces. The existence of monodentate carbonate (1460-1480 [104,132,277,295] and 1390-1445 cm^{-1} [78,79,104,277,296] are the result of room temperature oxidation of CO over oxide surfaces [297–300]. Note that the band between 1460 and 1480 may also be derived from the formation of monodentate bicarbonate species [19,79,132,277], which could be the result for CO reacting with surface hydroxyl groups [301]. Upon AM doping of CZF the relative strength of the carbonate region (compared to the linear CO) increases. Furthermore, additional bands generally associated with the formation of formate like surface

species (1560–1585) is observed in the presence of AMs [19,35,79,132,277,279,302]. Hence, AMS modify the adsorption of CO over the Fe oxide surface.

Furthermore, the position of the peaks associated with the symmetric (1270–1280cm^{-1}) and asymmetric (1640–1680 cm^{-1}) carbonate vibrations change depending on which AM is present. Most strikingly, while the changes are subtle in the presence of Cs and Rb, when K is doped additional peaks are observed around 1667, 1573.7, while no band is at 1270–1280 cm^{-1}. The stark change in the non-linear CO adsorption in the presence of K is in line with the additional high temperature desorption peaks observed previously during the TPSR experiments. Possibly the additional CO adsorption sites at the FeOx surface by the K doped sample account for the relatively higher surface carburization as measured by XPS and reported in Section 3.2.2.5. Alternatively, these sites may be related to the relatively high CO selectivity observed during CO_2 hydrogenation (e.g. at 290 °C) over K-CZF (17.8 %) than over Rb-CZF (9.7 %) or Cs-CZF (9.2 %). Furthermore, the monodentate carbonate band (1476 cm^{-1}) is much increased showing an increased CO oxidation rate. these sit account for the higher CO selectivity observed during CO_2 conversion.

These findings inspired a new set of experiments to investigate the evolution of CO adsorption under increasing temperature. Rather than adsorbing CO at 25 °C on reduced samples and flushing it away using N_2, now the spectra are monitored during adsorption and heating. Before analysis CO_2 and H_2 are introduced and heated (see methods for details), then the sample is purged with N_2 at 400 °C to remove any surface species. Subsequently the temperature is lowered to 25 °C and the background spectrum is measured at 5 bar N_2. Hereafter, the adsorption process of CO is monitored until it reaches a partial pressure of 5mbar. After the spectra stabilize the temperature is increased and the spectra are measured continuously. In this way the favourability of CO adsorption at conditions closer to CO_2 hydrogenation can be investigated.

Figure 49 shows the evolution of the IR spectra during CO adsorption from 0 to 5mbar on carburized CZF and Cs-CZF respectively. As before distinct bands are observed for linear CO, and asymmetric and symmetric bidentate carbonate species. At these conditions after carburization the linearly adsorbed CO band on Cs-CZF (2103 cm^{-1}) is blue shifted by 5 cm^{-1} compared to reduced Cs-CZF. On CZF the band is centred at 2110 cm^{-1}. Both CZF and Cs-CZF show a shoulder at 2130 and 2132 cm^{-1} respectively. This may indicate the presence of CO adsorbed on Cu^{1+} or Fe_3O_4 [303–306], but overlaps with the P-branch of CO gas [274]. Additionally CZF presents a weak shoulder at 2058 cm^{-1} indicates the formation of linear CO on Fe carbide surfaces [116,307]. This band is not observed for Cs-CZF. No bands for b-CO exists at this point. Interestingly, for Cs-CZF as the partial pressure of CO increases from 0 mbar to 2 mbar a band develops preferentially around 1550 cm^{-1} while a shoulder is observed at 1630 cm^{-1}. As the partial pressure is increased further to 5 mbar the shoulder grows and shifts to 1643 cm^{-1}. Such behaviour is not observed for CZF.

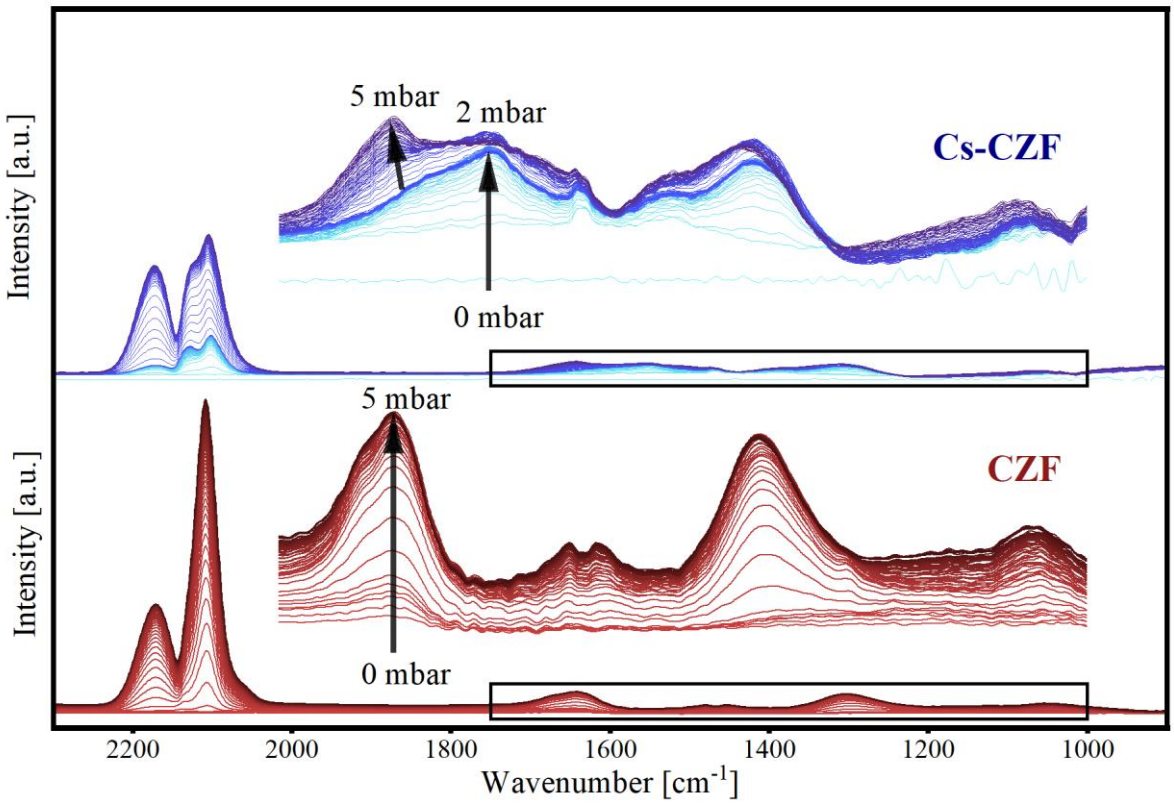

Figure 49| CO-DRIFTS over carburized CZF and Cs-CZF. The figure illustrates the evolution of the DRIFTS spectra during the adsorption of CO (5 mbar). Arrows highlight the change in the bands during increasing CO pressure. The spectra for Cs-CZF and are plotted in blue and red respectively. The region of the spectra between 1000 and 1750 cm^{-1} (indicated by the box) is enlarged.

Substantive changes to the spectra are observed while increasing the temperature from 50 to 290 °C. Figure 51 shows the spectra obtained upon heating carburized CZF, Cs-CZF, Rb-CZF, and K-CZF in the presence of 5 mbar CO. The temperature driven evolution of vibrational bands in the regions from 1800 to 2250 cm^{-1} and 1000 to 1700 cm^{-1} are shown separately. Linearly adsorbed CO* species rapidly diminish upon heating. It is observed that above 100 °C the shoulder at 2130–2133 cm^{-1} becomes indiscernible in the doped samples, while it persists clearly up to 290 °C on CZF. Overall, these observations indicate that linearly adsorbed CO* species are progressively destabilized upon heating, accompanied by extensive thermal restructuring of surface carbonate species.

Notably in all cases the relative intensity between 1600 and 1280 cm^{-1} decreases drastically relative to the increasing background: a narrow negative band is observed at 1461-1475 cm^{-1} indicating the decomposition of monodentate carbonate or bicarbonate species at elevated temperatures [19,79,104,132,277,295]. For K-CZF, Rb-CZF and Cs-CZF an additional negative band appears at 1615-1605 cm^{-1}, while the carbonate features at higher wavenumber (asymmetric O-C-O at 1640–1680 cm^{-1} [19,35,79,132,277,279]) vanish. Low vibrational mode bands display a similar behaviour. The symmetrical O-C-O vibration of bidentate carbonate on K-CZF, Rb-CZF and Cs-CZF (1270, 1285 and 1320 cm^{-1} respectively [19,35,79,132,277,279]) shifts to lower wavenumber and flatten out. The simultaneous loss of the symmetric and asymmetric carbonate vibrations marks the onset carbonate decomposition and formate (HCOO*) formation at elevated temperatures.

The formation of surface formate is evidenced by two positive bands which develop at 1360 and 1570 [19,35,79,132,277,279,302]. Focusing on K-CZF, the positive band at 1350 cm^{-1} shift up to 1364 cm^{-1} upon heating. While the band feature in this region is less prominent during CO adsorption at 25 °C over Cs-CZF and Rb-CZF, at higher temperatures discernible features appear: Rb-CZF and Cs-CZF show a peak and a shoulder respectively at 1360 cm^{-1}, both of which intensify during sequential heating. The band at 1570 cm^{-1} behaves similarly, growing most prominently over K-CZF compared to Rb-CZF and remaining barely identifiable for Cs-CZF. Note that this band is close to 1550 cm^{-1}, which forms rapidly over Cs-CZF during CO adsorption. Considering the additional band at 1294 cm^{-1} observed over Rb-CZF, the generated formate species are likely adsorbed monodentately, as expected under CO-rich and

H_2-poor conditions in the absence of CO_2. Such monodentate formate species may result directly reaction of CO with surface hydroxides [301,308] or hydrogenation of bidentate carbonate species [309]. These temperature-dependent spectral evolution confirms the ability of the AM doped samples to facilitate the formation and stabilization of CO derived formate species.

In contrast, CZF does not display the growth of any new absorption bands between 1000 and 1800 cm^{-1}. This clearly shows that AMs facilitate the interconversion of carbonate to formate species at elevated temperatures, even in a hydrogen-poor environment where undoped CZF remains largely inert to such conversion. Hence, alkali promoters enhance the surface reactivity of the catalyst by enabling carbonate-to-formate conversion under CO-rich conditions.

As expected from the *in-situ* DRIFTS experiments, b-CO species also emerge at elevated temperatures over all catalysts. The position and relative intensity of the b-CO band vary across the series. Doping CZF with Cs or Rb shifts the b-CO band from 1956 cm^{-1} to 1913 cm^{-1}, while K doping produces a further red-shift to 1903 cm^{-1}. Stronger binding of these bidentate species in the alkali-doped samples may promote CO insertion steps leading to oxygenate intermediates. However, increased back-donation alone does not enhance b-CO formation: although K-CZF exhibits the greatest CO bond elongation (1903 cm^{-1}), it displays a weaker b-CO band intensity than Rb-CZF and Cs-CZF. Moreover, the b-CO band intensity on K-CZF increases much slower than over Rb-CZF and Cs-CZF. Figure 50 shows the b-CO* peak intensity during heating over CZF, Cs-CZF, Rb-CZF and K-CZF, in red, blue, green and purple respectively. Although the maximum b-CO band intensity was similar between Rb-CZF and Cs-CZF, the growth kinetics differ: Rb-CZF shows a higher initial intensity but slower increase, whereas Cs-CZF grows more rapidly. Both decrease again after their maxima, reached at 190 °C and 230 °C, respectively. Undoped CZF develops b-CO only at higher temperatures, peaking at 240 °C, while K-CZF continues increasing until 290 °C. At 290 °C, the intensity follows the order Cs-CZF ≈ Rb-CZF > K-CZF > CZF. Thus, despite inducing stronger π^* back-bonding, K appears less effective

in generating b-CO species. Altogether, these results reveal distinct kinetic and thermodynamic profiles for b-CO formation, depending strongly on the specific alkali dopant.

These changes in the rate of b-CO formation may be related to the product selectivity during CO_2 hydrogenation. The comparatively higher propensity of Rb- and Cs-CZF to form b-CO compared to K-CZF correlates with their lower CO selectivity during CO_2 hydrogenation (9.7, 9.2, and 17.8 % at 290 °C, respectively). These results mirror the favourable overall effect of alkali-metal doping on alcohol and olefin production via CO_2 hydrogenation. The increased surface binding strength of CO may facilitate CO insertion to generate the oxygenated intermediates observed in Section 4.2.3. Furthermore, the enhancement in CO binding at FeOx (as carbonates) and FeCx (as b-CO) sites aligns with the higher degree of surface carburization observed upon alkali doping. Considering the carburization trend (CZF ≪ Cs-CZF < Rb-CZF < K-CZF), it is more likely that the efficient generation of carbonates promotes subsequent carbide formation, rather than the stronger b-CO binding alone.

Considering these observations together with the b-CO band position it can be noted that Rb-CZF and Cs-CZF possess the greatest ability to generate strongly adsorbed b-CO. As noted before, all samples exhibit b-CO species at the surface, but undoped CZF shows a higher CO bond vibrational frequency (1956 cm^{-1}) relative to the K, Rb and Cs doped samples (respectively 1903 , 1913 and 1913 cm^{-1}). Furthermore, K-CZF shows a weaker relative b-CO band compared to Rb-CZF and Cs-CZF (see Figure 50 and Figure S33). Thus, the Rb- and Cs-modified catalysts exhibit the strongest ability to generate bridged CO species on their FeCx surfaces.

Fascinatingly, after the temperature is decreased again from 290 °C back to 25 °C, b-CO band is maintained on Cs-CZF (see Figure S31**Figure S31**). Although the band shifts to 1949 cm^{-1} (compared to 1913 and 1956 cm^{-1} for Cs-CZF and CZF, respectively, during heating), the intensity does not decrease. The bands corresponding to formate (1550–1570, 1360–1380 and 1280–1294 cm^{-1}) and bidentate carbonate (1640–1680 and 1308–1320 cm^{-1}) are recovered, but with markedly lower intensity. An even stronger reduction occurs between 1390 and 1440 cm^{-1}, indicating diminished capacity to oxidize CO to monodentate carbonate. This loss in intensity can be attributed to surface reduction after prolonged CO exposure, since CO can act as a reductant at elevated temperatures [103,106]. More

specifically the Fe oxide type surfaces are likely converted to carbides [103]. The fact that the b-CO band intensity remains unchanged despite reduction suggests that these bridged CO species reside on carbide rather than oxide sites. The persistence of b-CO upon cooling therefore demonstrates the remarkable stability of this adsorption configuration on the carbide-rich surfaces.

From these combined observations it can be concluded that, while FeCx phases can adsorb CO in a bridged configuration, an activation barrier is associated with such adsorption. The maintenance of b-CO after cooling proves that this CO adsorption mode is inherently stable. Furthermore, the red-shift of the b-CO peak in the presence of alkali metals shows that not only linear CO and carbonates, but also bridged CO located on FeCx is affected by alkali doping. Collectively, these findings demonstrate that alkali metal promoters not only modulate the carbonate–formate equilibrium but also stabilise bridged CO adsorption on FeCx domains, underscoring their multifaceted influence on CO binding and surface reactivity.

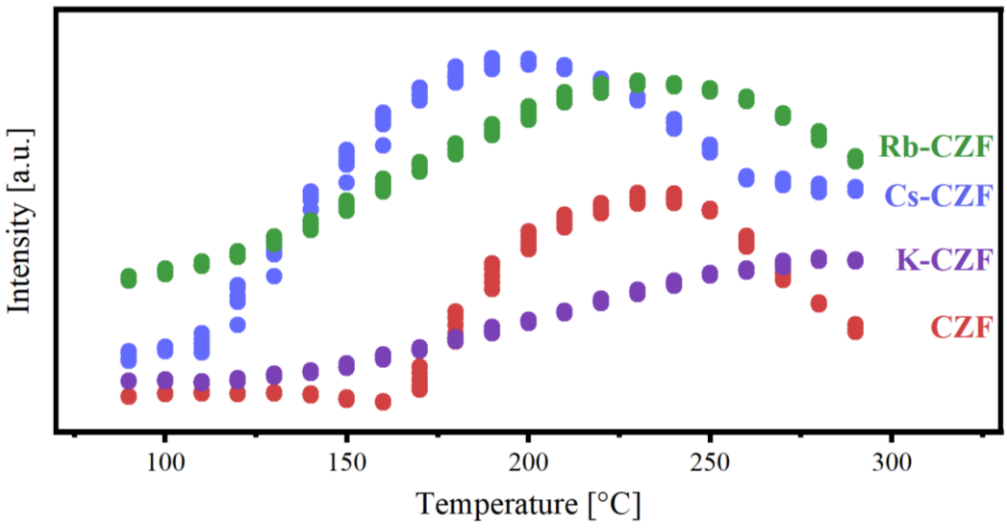

Figure 50| Evolution of b-CO band during temperature dependent CO adsorption. The peak intensity of b-CO on CZF (red), K-CZF (purple), Rb-CZF (green) and Cs-CZF (blue) are plotted at different temperatures.

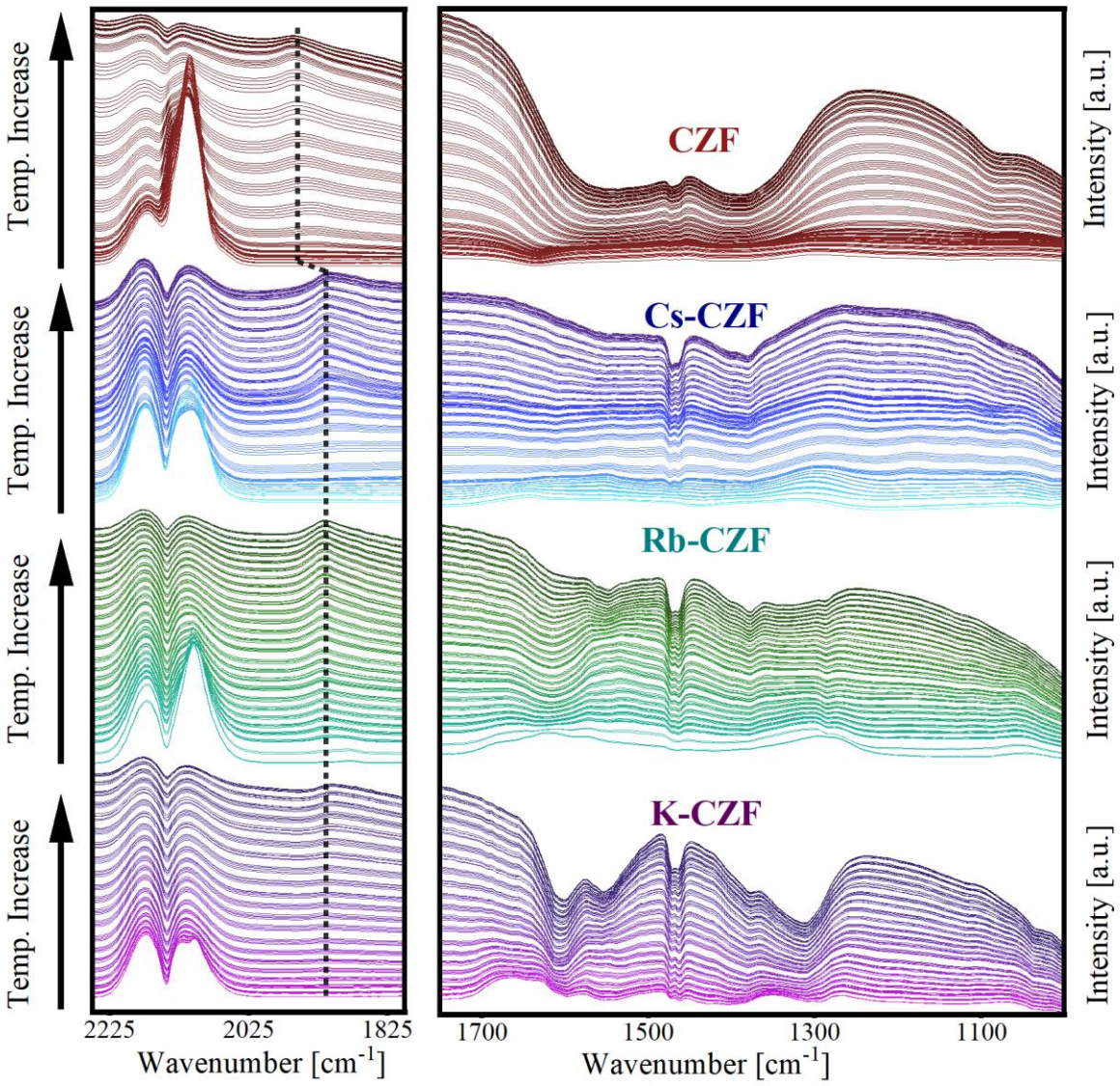

Figure 51| Temperature dependant CO adsorption DRIFTS. The evolution of the measured DRIFTS spectra are plotted from 50 to 290 °C with temperature steps of 10 °C under continuous flow of 1% CO in N_2 . From top to bottom the figure shows CZF (red), Cs-CZF (blue), Rb-CZF (green) and K-CZF- (purple). The dotted reference line indicates the position of the b-CO band.

These results mirror the favourable overall effect of AM doping on alcohol and olefin production via CO_2 hydrogenation. The overall increase in the surface binding strength of CO may facilitate the CO insertion to generate the oxygenated intermediates observed in Section 4.2.3. Furthermore, the increase in the binding at the FeO_x (as carbonates) and FeC_x (as b-CO) is consistent with to the increase in the surface carburization. In this respect, considering the surface carburization trend is CZF<<Cs-CZF<Rb-CZF<K-CZF, it is more likely the efficient generation of carbonates is what leads to the increase in carbides, rather than the stronger b-CO binding.

4.2.5.2. CO Adsorption XAS

To establish a clear interaction between the AM promoter and CO *"from the AM perspective"* CO adsorption XAS measurements were performed. Based on the available computational literature the following was hypothesized:

The surface interaction between adsorbed CO and Rb lead to an increase in charge on Rb.

To test this hypothesis the Rb K-edge spectra are analysed before and after exposure to 5% CO. Hereafter these spectra will be referred to as spectrum A and B respectively. The prepared Rb-CZF catalyst was treated as described before and tested in the same fashion (flowing $6.9CO_2/20.7H_2/2.4N_2$ at 45bar from 250 to 330 °C for 3h and 45 min at each temperature interval with 45 min ramp). After reaction the reactor was cooled down, depressurized and flushed with N_2 to get rid of any remaining gases, then the inlet and outlet ball valves were closed. The entire reactor body was then removed and transferred to the glovebox where the spent Rb-CZF was collected. The sample was then mixed with degassed cellulose, pressed into a pellet and placed in the XAS cell in a glovebox under Ar gas. Finally, the initial Rb K-edge (spectrum A) was measured . For the CO exposed measurement (spectrum B) the gas transfer line was connected to the XAS cell and thoroughly flushed with 5% CO in Ar. Hereafter, the diluted CO was allowed to flow into the cell for 20 minutes. Lastly, spectrum B was measured.

Although no additional spectral features are observed upon exposure of 5% CO, a CO induced chemical shift is clearly observed. The striking similarity between the spectra shown in Figure 52A illustrate the lack of any covalent bonding between the adsorbed CO and surface Rb. Hence, any change in the edge position can be attributed to CO induced charge transfer. Indeed the expanded region around the adsorption edges (shown in Figure 52B) indicates such a shift with a magnitude of 0.2 eV. For clarity the difference spectrum is plotted in Figure 52C. This spectrum is obtained by subtracting spectrum B from A. Note the at the 0 crossing of the difference curve (15210.1 eV) appears after the edge maximum of spectrum A (15209.8 eV). The relatively higher intensity of spectrum A before the edge maximum is indicated by the blue area, while decreased edge intensity directly after the maximum is indicated by the

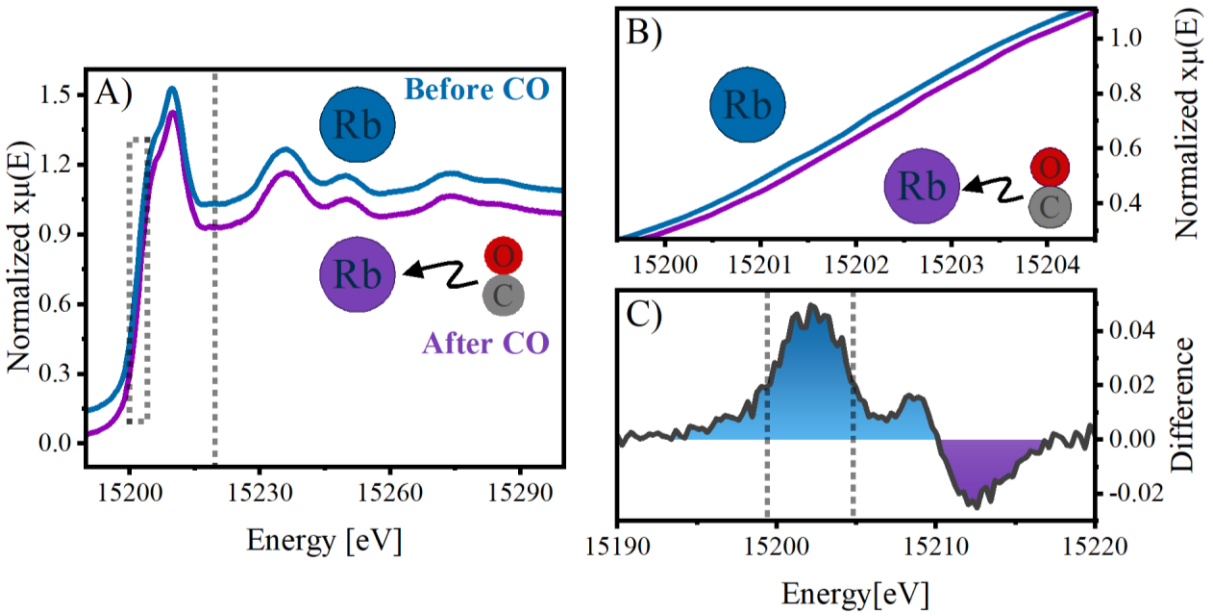

Figure 52| Rb K-edge XANES before and after CO adsorption. The initial Rb K-edge measured under Ar atmosphere is shown in blue. The Rb K-edge measured after switching to 5% CO atmosphere is shown in purple. Panel A shows both spectra with a small offset. Panel B shows the segment of the two spectra indicated by the dotted rectangle in Panel A. The difference spectrum from 15190 to 15220 eV (indicated by the dotted line in Panel A) is shown in Panel C. The dotted lines in Panel C indicate the region plotted in Panel B.

purple area. Note the difference spectrum reaches its maximum exactly at half the edge step (15201.1 eV) at which the difference amounts to 4% of the edge step. From this analysis it can be concluded that there is an increase in charge on Rb upon surface adsorption of CO. Such charge increase may be indicative of ligand induced charge transfer of Rb towards surface TM atoms near the CO adsorption site.

Indeed these results are in line with the computation studies discussed previously (see Section 4.2.5). As was noted, these studies show that the effect of alkali metals is in part adsorbate induced and highly localised. Upon the adsorption of CO or H_xCO_2, which become negatively charged due to electron transfer from the surface to the adsorbate, it has been found that the AM adatoms act as positively charged anchors, which interact electrostatically with the adsorbate. Importantly the interaction between the charged surface species is a dynamic phenomenon. In fact, the calculated positive Bader charge further increases at the AM when oxygen containing species are co-adsorbed [261,288,290,292–294,310]. Similarly, the charge on the TM atoms increases as well. However, the positive charge built up on the

surface TMs is considerably smaller in the presence of AM adatoms than in their absence (see Figure 47). In fact, the increased charge on the AMs upon the adsorption of (e.g.) CO is largely due to enhanced electron donation to the surface TMs involved in binding CO. As a result it has been concluded that the AMs not only serve to electrostatically anchor the intermediates, but also facilitate surface charge transfer towards the adsorbate by compensating the generated charge on the surface TMs.

In this light the observed edge shift of the Rb K-edge upon CO adsorption can be understood as an interplay between surface TM atoms, CO and Rb, rather than simply a lateral electrostatic CO-Rb interaction. Taking this together with the previous results, it may be concluded that the increase in the CO binding strength is directly related to the surface AM active site modification.

4.3. Conclusion

In summary, the results presented in this chapter demonstrate that AM doping introduces a fundamental change in the reaction pathway for CO_2 hydrogenation over the studied catalysts. Through a combination of TPD, PTH, *in-situ* DRIFTS, TPSR, CO-DRIFTS and XAS experiments, it has been shown that the addition of AMs alters the catalyst adsorbate interaction giving rise to new reaction intermediates.

In contrast to numerous publications, here the TPD and PTH experiments revealed that the hydrogenation ability (OHA) of the catalyst is not significantly suppressed by AM addition. The lack of such suppression was evidenced by the ambiguous changes to the adsorption strength of ethylene and H_2 upon AM doping, as well as the unexpected increase in the rate of ethylene hydrogenation during the PTH experiments over Rb-CZF and K-CZF compared to CZF. Hence, the formation of HAs and olefins cannot be explained by a suppression of hydrogen transfer during CO_2 conversion. Instead, it was proposed that the formation of olefins may be the result of alcohol dehydration. Indeed the enhanced conversion of ethanol during the CH_3CH_2OH-PTH experiments suggests that AMs facilitate the decomposition of oxygenates to form hydrocarbons. This implies that the formation of olefins cannot be ascribed to a reduced hydrogen transfer ability but rather to an alternative reaction route involving oxygenate intermediates.

The *in-situ* DRIFTS experiments further supported this conclusion by showing that the presence of Cs leads to the formation of CH_3CH_2O* species during CO_2 hydrogenation, whereas such species are absent at the surface of the undoped material. The emergence of such oxygen-containing intermediates indicates that AMs open up a new mechanistic pathway in which CO (or CO-like) surface intermediates are inserted into alkyl chains to form alcohol-related species that can subsequently dehydrate to olefins. In effect alcohols and olefins are proposed to share a reaction pathway, which is enabled by AMs.

Note, that the current results do not exclude the possibility of increasing olefin or higher alcohols selectivity by means of suppressing the overall hydrogenation ability. Hence, modulating the relative adsorption of H_2 and olefins to decrease hydrogen transfer may remain a viable strategy for selective

formation of olefin or higher alcohols from CO_2 and H_2. However, such suppression did not lead to the increased selectivity to such products in this study. Based on these results it is expected that AM induced hydrogen transfer suppression is likely auxiliary to the prime functioning of surface AMs, which is to induce a fundamental change in reaction pathway.

To rationalize the AM induced changes to the catalytic reaction mechanism TPSR and CO-DRIFTS experiments were conducted. Their results reveal that AMs increase the surface binding strength of CO and modify its adsorption modes at the catalyst surface. In this respect the TPSR data obtained after carburization were particularly insightful. These data show that, after carburization, AMs introduce CO dissociative and non-dissociative adsorption sites with similar binding strength, which may be relevant under CO_2 hydrogenation temperatures. Such co-existence of dissociative and non-dissociative activated CO species with similar adsorption strength is absent in the non-doped catalyst. Regarding the CO-DRIFTS experiments, the AM induced increase in CO binding manifests as a red-shift in the linear/bridged CO bands and modification of the carbonate/formate region of the spectra. Moreover, it was found that AMs promote the formation of bridged CO species, which are assumed to be key reaction intermediates. These experiments establish an enhanced interaction between CO and the catalyst surface due to the presence of AMs. The presence of these new adsorption environments likely facilitates CO insertion.

Finally, in light of the results obtained in Chapter 2 and recent DFT publications, a possible interaction between the CO adsorbates and the surface AMs was proposed as the source of the increased CO adsorption. XAS measurements show a CO-induced shift of the Rb K-edge, providing direct evidence for ligand-induced charge transfer between the AM and the transition metal surface upon CO adsorption. This observation confirms that the interaction between CO and the catalyst is not purely electrostatic but involves a dynamic redistribution of charge between the AM, TM and adsorbate as predicated by previous DFT studies. To our knowledge, no such experimental confirmation of the dynamic adsorbate-AM interaction has been reported previously.

Taken together, these findings demonstrate that alkali metal promotion modifies interaction between the catalyst surface and reactive intermediates. By strengthening CO adsorption and stabilising

oxygenate intermediates, AMs open a new reaction pathway that favours the formation of higher alcohols and olefins. This new pathway emerges from the interplay between non-dissociative CO activation, CO insertion, and the regulation of surface charge by the alkali metals.

Chapter 5

Leveraging Aromatics for the Enhanced Hydrogenation of CO_2 to Propane

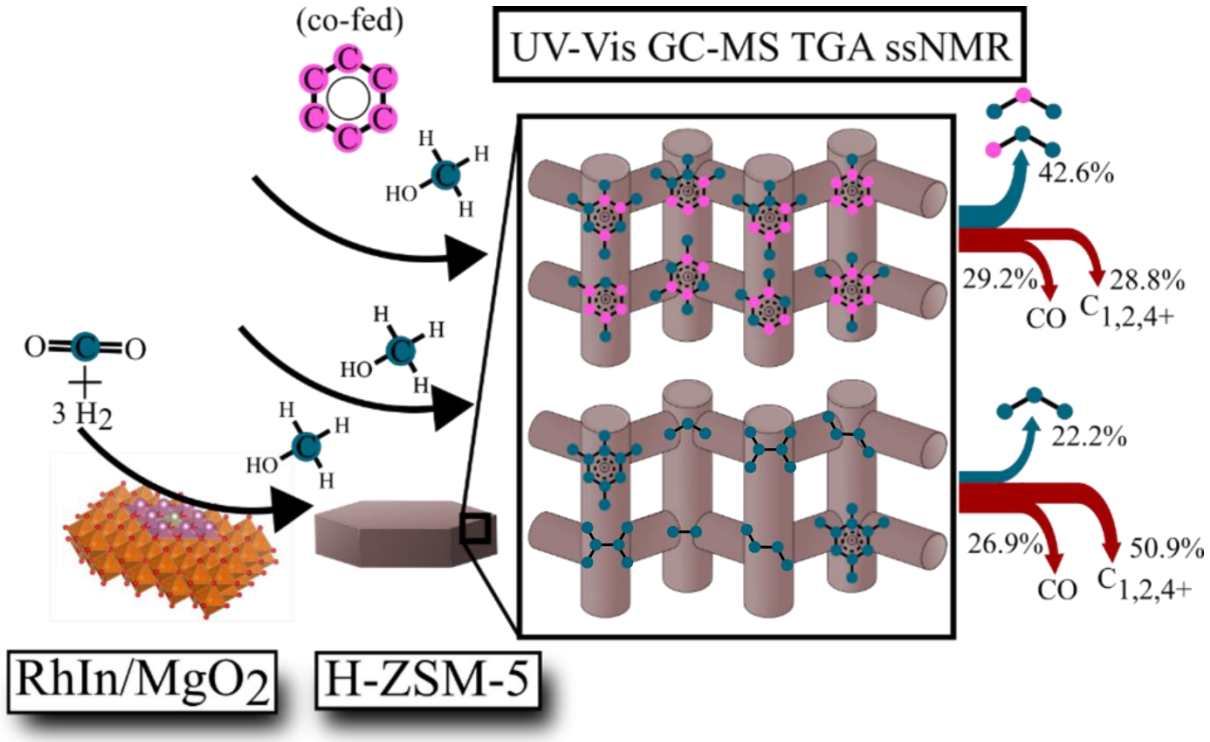

CHAPTER 5: LEVERAGING AROMATICS FOR CO_2 CONVERION

5.1.Introduction

Here we describe a method of selectively converting CO_2 to propane under relatively low temperature (230-270 °C) batch conditions. This is achieved by specifically promoting the aromatic cycle by co-feeding a small amount of benzene to the reaction.

As described in section 1.4.4, the hydrocarbon pool reaction inside the pores of ZSM-5 consist of aliphatic/olefinic and aromatic cycles. The combination of these two catalytic paths leads to a range of hydrocarbon species. Importantly, while the aliphatic cycle leads to products from C_2 to C_6, the aromatic cycle leads to C_3. (Although the aromatic cycle can lead to the formation of C_2 as well, the ratio between C_2 and C_3 originating from the aromatic cycle can be tuned by the reaction temperature. This leads to a typical conversion-selectivity trade-off [7].)

We find that benzene can act as a scaffold to "*grab*" the *in-situ* produced methanol, thereby forming methyl-benzene intermediates, which forms the core of the aromatic cycle. These methylated aromatics subsequently lead to the selective formation of propane at the expense of C_{1-2} and C_{4+} hydrocarbons.

To prove the promotion of the aromatic and a shift away from the aliphatic cycle the following hypotheses have been tested:

1) *Propane selectivity increases relative to other hydrocarbons upon co-feeding of benzene;*

A range of experiments varying the co-fed benzene amount has been used to test this hypothesis.

2) *The concentration of substituted aromatic molecules inside the pores of the zeolite increases upon co-feeding of benzene;*

This is shown by a combination of post-reaction TGA, GC-MS trapped species analysis and ssNMR.

3) *The concentration of cationic substituted aromatics inside the pores of the zeolite increases upon co-feeding of benzene.*

[7] Here "selectivity" refers specifically to the distribution of hydrocarbons, i.e. not including CO.

The protonation of the aromatic ring causes a change in the HOMO-LUMO gap compared to the non-protonated molecule. UV-Vis spectroscopy is a suitable technique to evaluate electronic energy transitions and is well suited to evaluate both the neutral molecule and cationic species. Hence, it is used here to measure the effect of benzene co-feeding on the generation of charged cationic aromatic species during reaction.

Lastly it is hypothesized that

4) *Upon co-feeding benzene in-situ produced methanol no longer polymerizes, but rather acts to methylate benzene leading to exclusively trapped methyl benzene rather than aliphatics.*

The effective suppression of the aliphatic cycle should lead to a decrease in the direct C–C bond formation of methanol. Rather, as per the aromatic cycle, methanol should act to methylate the existing aromatic moieties, which in turn lead to propane formation. In this research, ssNMR is used extensively to show a clear change in the chemical environment of carbon atoms trapped inside the pores, thereby proving the shift away from the aliphatic cycle towards the aromatic cycle.

CHAPTER 5: LEVERAGING AROMATICS FOR CO_2 CONVERION

5.2.Results

In the following Section the effect of co-feeding benzene on the formation of hydrocarbons during CO_2 hydrogenation is reported. Section 3.1. outlines the main catalytic results obtained. These results show the increase in propane selectivity upon the co-feeding of benzene. It also illustrates the effect of different reaction conditions such as benzene amount, reaction pressure and temperature. After this, in Section 5.2.2, we investigate the mechanism through which benzene co-feeding leads to an increase in the formation of propane using a combination of ^{13}C scrambling experiments (5.2.2.1), control experiments (5.2.2.1), liquid product analysis (5.2.2.2), trapped products analysis using UV-VIS and GC-MS (5.2.2.3), and ssNMR experiments (5.2.2.4). The conclusions are presented in Section 5.3.

5.2.1. Catalysis

This section addresses the hypothesis that

1) Propane selectivity increases relative to other hydrocarbons upon co-feeding of benzene

Figure 53A shows the main catalytic result, namely the effect of the addition of 200 mg benzene to a reaction of CO_2 and H_2 at 250 ℃ at 46 ±1.5 bar for 10 hours over our composite catalyst (RhIn/ZSM-5). Three key observations are made. Firstly, in the absence of benzene the hydrocarbon product ranges from methane (C_1) to hexane (C_6), with a large fraction coming from butane (C_4) and pentane (C_5). This can be ascribed to a relatively uncontrolled sequential methylation of hydrocarbon intermediates in the olefinic cycle under these conditions. In contrast, when 200 mg benzene is co-fed, the hydrocarbon distribution shows a clear shift towards propane (C_3) from 27.2 to 36.8% at the expense of all other hydrocarbons. Secondly, the conversion of CO_2 drops from 60 ± 2% to 55 ± 2% when benzene is added. Thirdly, the selectivity of CO increases drastically from 17.3 % to 45.1% in the benzene co-feeding condition. These two experiments clearly indicate the addition of benzene can influence the products of CO_2 hydrogenation over our composite catalyst under relatively mild conditions.

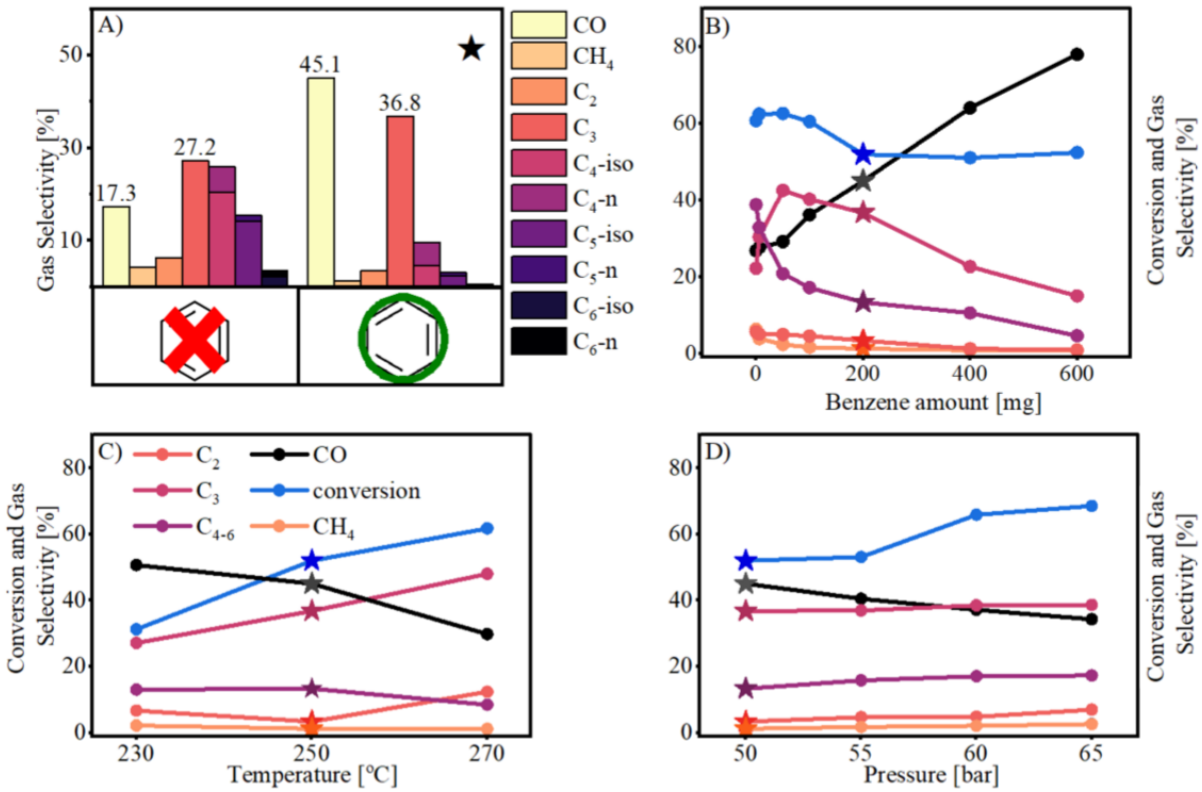

Figure 53| CO_2 hydrogenation catalysis results under various conditions. In all cases the reactant gas is $CO_2/3H_2$. Panel A directly compares the reaction product selectivity in the absence of benzene with co-feeding 200 mg benzene. A clear increase in the propane selectivity is observed at the expense of other hydrocarbons. Panels B, C and D show the effect of the co-fed benzene amount, the temperature and pressure on the selectivity and conversion relative to co-feeding 200 mg benzene indicated by a star.

These initials results motivated a further study on the effect of different reaction conditions to explore the possibility of mitigating the negative effects of benzene co-feeding on the CO selectivity and CO_2 conversion to maximize the propane yield. In particular, the effect of the amount of benzene, temperature and pressure have been investigated. In all these cases only one of the variables is changed.

As shown in Figure 53, the benzene amount and the temperature of reaction have a large effect on the reaction selectivity, while the reaction pressure has a more moderate effect.

Importantly, it is observed that the benzene co-feeding amount shows an optimum around 50 mg. As the benzene co-fed amount is increased from 0 to 50 mg the non-propane hydrocarbon selectivity is reduced from 50.9 to 28.2 %, while the propane selectivity is almost doubled from 22.2 to 42.6%. Above 50 mg benzene the CO selectivity is increased and CO_2 conversion is decreased. The negative effect of

excessive benzene addition (in terms of the CO selectivity and CO_2 conversion) may be attributed to competitive absorption of in-situ produced methanol and co-fed benzene in the zeolite pores [311]. This competitive absorption may slow down the rate of methanol conversion, thereby reducing the pulling effect of the tandem reaction set-up. Alternatively, the addition of large amounts of benzene might be able to interfere with the selective conversion of CO_2 and H_2 to methanol.

Varying the temperature from 230 to 270 ℃ reveals two trends: firstly, the hydrocarbon distribution is dependent on the temperature. As can be observed, the selectivity towards C_2 dips from 230 to 250 and increases at 270 ℃, while the selectivity of C_4 remains relatively the same from 230 to 250 ℃ and dips at 270 ℃. At the same time the C_3 selectivity increases from 27.1 to 48.0% going from 230 to 270 ℃. Hence, these results show that changing the temperature can tune the C_3/C_2 ratio. In this case the highest C_3/C_2 ratio is attained at 250 ℃.

Secondly, the CO selectivity decreases at higher temperatures, and the overall CO_2 conversion similarly increases. Given that CO formation is generally favoured at higher temperatures [42] this is a surprising result. The decreased CO selectivity at 270 ℃ can be attributed to a more efficient *"pulling effect"* exerted by the zeolite catalyst on the CO_2 hydrogenation, which occurs over the $RhIn/MgO_x$ catalyst. Thereby the hydrogenation catalyst can work more efficiently leading the lower overall CO formation.

5.2.2. Mechanism of Promotion

In order to rationalize the increase in propane selectivity upon co-feeding benzene during the tandem CO_2 hydrogenation catalysis we need to consider the reaction mechanism of methanol conversion as outlined on page 34–37. As has been noted, the hydrocarbon pool mechanism of methanol conversion over ZSM-5 has been widely adopted and hence it can provide a useful framework to judge current results. In effect, the following Sections provide evidence for the hypothesis that benzene acts as scaffold to exhaustively pick up in-situ produced methanol producing substituted aromatics, which results in the promotion of the aromatic cycle. This aromatic cycle in turn leads to the preferential formation of propane.

First, in Section 5.2.2.1 the active involvement of benzene in the formation of propane is proven by isotopic scrambling experiments. Additionally, control experiments prove that the interaction between in-situ produced methanol and benzene in particular is essential to give rise to the increase in propane.

Section 5.2.2.3 clearly shows an increase in products associated with the aromatic cycle when co-feeding benzene. More specifically, the concentration of molecular and cationic substituted aromatics inside the pores of these zeolite, as measured by TGA, UV-Vis and GC-MS, are shown to increase when benzene is added.

Lastly, the ssNMR results in Section 5.2.2.4 definitively prove that the addition of benzene induces a diversion away from the aliphatic cycle towards the aromatic cycle.

5.2.2.1. ^{13}C Scrambling and Control Experiments

Figure 54 shows the catalytic results of a number of control experiments. In these experiments only the ZSM-5 zeolite catalyst is used. Unsurprisingly, no appreciable amount of gas products are obtained and the CO_2 conversion is 0% when CO_2 and H_2 are reacted in the absence of the $RhIn/MgO_x$ catalyst irrespective of benzene co-feeding (Figure 54A). Only trace amounts of hydrocarbons are observed when benzene is added. This can be attributed to impurities in the benzene used (see the chromatograph in Figure S36 and S37**Figure S37**). In contrast, methanol can be fully converted to hydrocarbons under an H_2 atmosphere (Figure 54B). As expected, in this case, the propane yield increases upon the co-feeding of benzene. This emphasizes the crucial role of the $RhIn/MgO_x$ catalyst to hydrogenate CO_2 to methanol, which can be further reacted over the zeolite.

The crucial role of methanol to methylate benzene is also reaffirmed by the results obtained for the conversion of 2 bar ethylene or butylene (Figure 54 C/D). In fact, it is shown that the propane selectivity is decreased when benzene is added to either of these hydrocarbon feeds, from 82.1 to 58.4% and 84.5 to 64.4 % in the case of ethylene and butylene respectively. No CO is generated in any of these

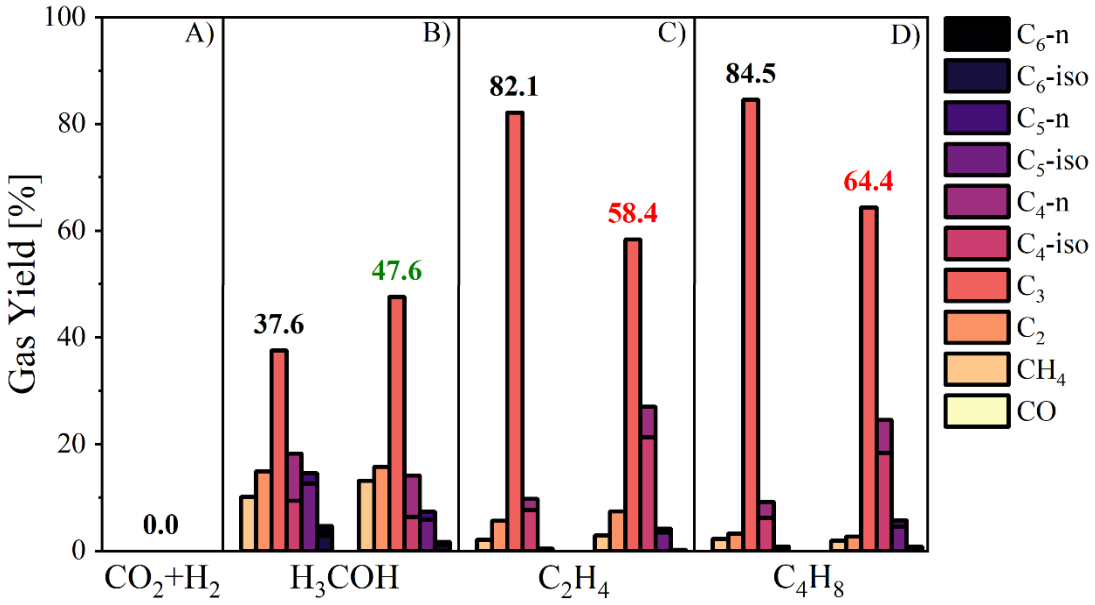

Figure 54| Control experiments selectivity using ZSM-5 only. The figure shows the conversion of CO_2 and hydrogen (A), methanol (B), ethylene (C) and butylene (D) over ZSM-5 in the absence (left) and benzene cofeeding conditions (right). Methanol is converted in an H_2 atmosphere. The increase or decrease of the propane selectivity upon benzene co-feeding is shown in green (increase) or red (decrease).

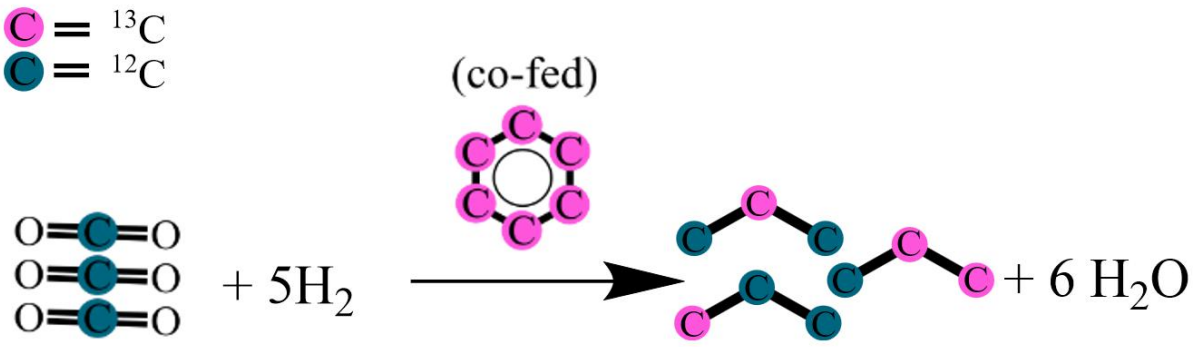

Figure 55| Isotope labelling experiment. The figure illustrates the result of ^{13}C labeling of benzene during CO_2 hydrogenation. The propane product is shown as a combination of ^{13}C from benzene (pink) and ^{12}C from CO_2 (blue).

experiments. This confirms that CO is generated primarily from the RWGS reaction during CO_2 hydrogenation.

To further prove the interaction between methanol and benzene, carbon labelled scrambling experiments were conducted. As per the paring mechanism, it is expected that methylated benzene species lead to propane via sequential methylation followed by contraction and expansion of the aromatic ring causing a scrambling of the aliphatic methyl groups and aromatic ring carbons. To show this effect, ^{13}C benzene was used to distinguish the carbon originating from benzene from those originating from ^{12}C CO_2.

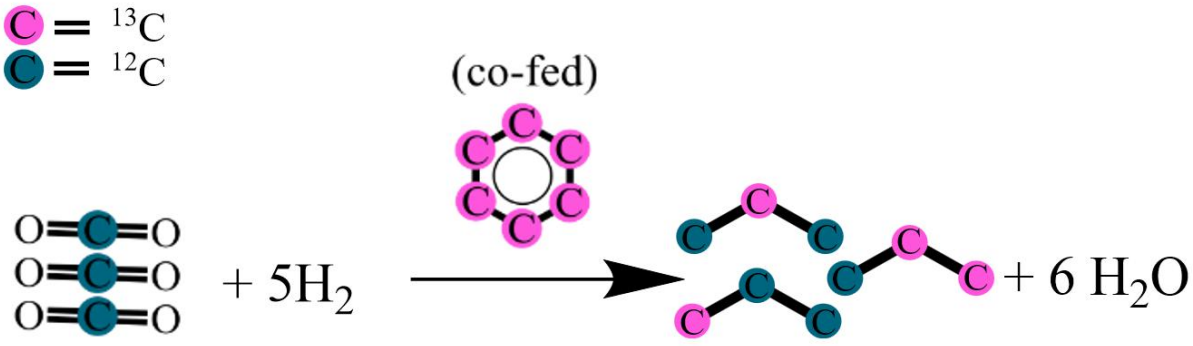

shows the isotopologue distribution of this reaction. The data clearly shows the propane product to be a combination of carbon atoms originating from benzene and CO_2. Hence, benzene actively participates in the reaction.

Table 6| Propane isotopologue distribution. Values reported here indicate the isotopologue distribution of propane generated by a ^{12}C CO_2 hydrogenation reaction while co-feeding ^{13}C benzene.

Number of ^{13}C in Propane	Fraction in total propane [%]
0	64.5
1	30.7
2	4.5
3	0.3

5.2.2.2. Liquid Product Analysis

To confirm the nature of the liquid C_{6+} product GC-MS analysis was performed by extracting any such traces from the spent catalyst using dichloromethane (CH_2Cl_2). The analysis shows that all liquid products are aromatic in nature and their carbon number ranges from 6 to 10 including a number of isomers (see Table S2). In the case of 50 mg benzene, the amount of these molecules are very low and constitute trace amounts. Naturally, when excessive amounts of benzene are co-fed the concentration of liquid aromatics increases. In all cases only trace amounts of naphthalene and substituted naphthalene molecules are observed, which is important granted these may act as precursors to coke [312–314].

5.2.2.3. Trapped Products analysis by TGA, UV-VIS and GC-MS

To investigate the amount and nature of the carbon residue on the composite catalyst TGA and trapped product GC-MS and UV-Vis experiments were conducted. The results of these experiments are summarized in Figure 56 and Figure 57.

The trapped product GC-MS results show that the hydrocarbons in the pores of the zeolite consist of substituted aromatics. More specifically, tetra-methyl benzene is the only trapped product, when benzene is not added, while when benzene is added substituted aromatics from toluene to tetra-

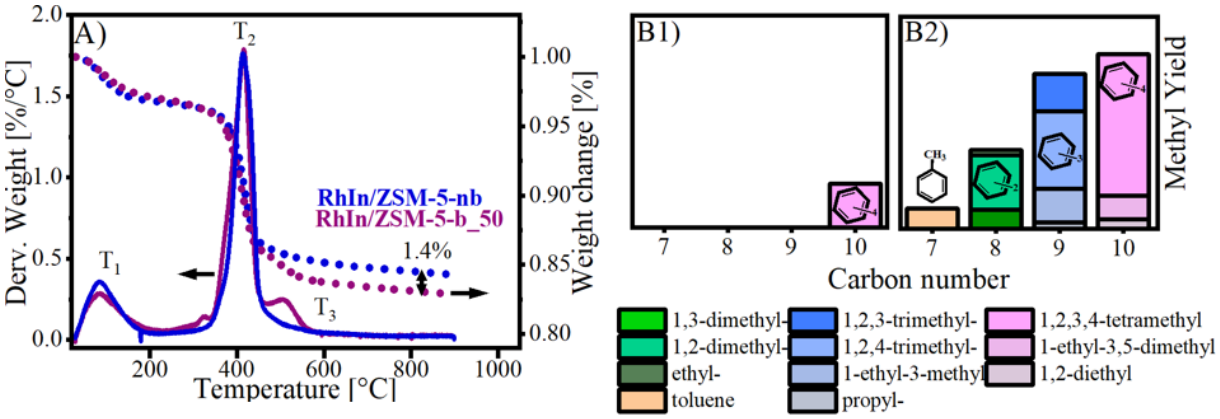

Figure 56| Trapped products analysis. Panel A shows the TGA results of the composite catalyst after reaction when cofeeding 0 or 50 mg of benzene under air flow. Panel B1 and B2 show the corresponding trapped product GC-MS results.

methyl benzene are formed. Furthermore, the formation of these products is favoured when 200 mg benzene is added, resulting in a higher yield of products with carbon number of 10 on a per methyl basis.

The post-reaction TGA results indicated in Figure 56A, show three weight loss regions: around 80 °C (attributed to the loss of water), around 400 °C (attributed to the decomposition of $Mg(CO_3)$ and $Mg(OH)_2$[315–317]), and around 500 °C (corresponding to trapped hydrocarbons). The formation of carbonates is confirmed by the ssNMR results, which can be found in the Appendix (Figure S35).The high temperature (compared to the boiling point of mono-cyclic aromatics) at which hydrocarbons are liberated shows that these species are indeed trapped inside the pores of the zeolite.

Moreover, besides molecular species measured by GC-MS and TGA, the UV-VIS spectra presented in Figure 57 prove the presence of benzonium cations. Figure 57 shows the spectra of 4 samples: the pristine composite catalyst after reduction, the composite catalyst after reaction in the absence of benzene, the composite catalyst after reaction co-feeding 50 mg of benzene, and the composite catalyst after reaction co-feeding 200 mg of benzene.

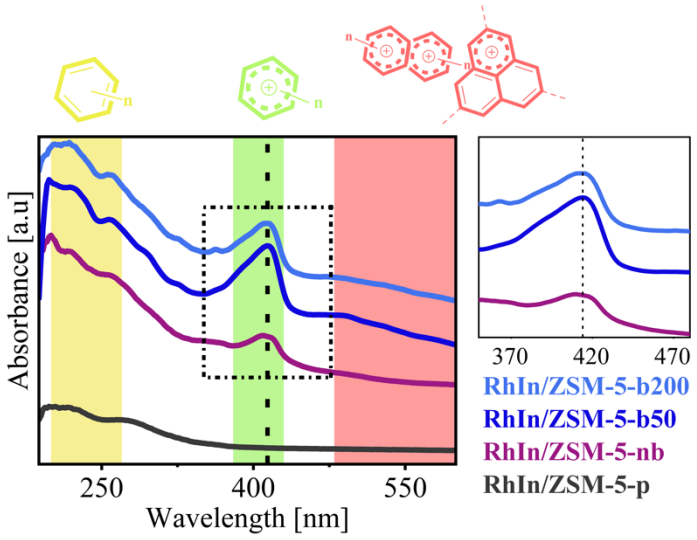

Figure 57| UV-VIS results. The UV-VIS spectra of the composite catalyst after reaction in the absence of benzene (purple) in the presence of 50 mg benzene (dark blue) and upon 200 mg benzene co-feeding (light blue) are shown. The UV-Vis spectrum of the catalyst before reaction is shown in grey as a reference. The inset shown an enlarged portion of the spectra after reaction. The shaded regions correspond to neutral (beige) and charged (green) mono-cyclic PMBs. Polycyclic species are expected in red region.

In order to understand the information embedded in the post-reaction sample spectra the pristine sample is shown as a reference. As can be seen, the pristine sample exhibits no peaks above 350 nm, and only shows broad features between 185 and 300 nm consistent with the expected signal generated by the sample ZSM-5 (190-290 nm)[318] and MgO (260-330 nm) [319].

All spectra of post-reaction samples show an increase in the absorption around 185–285 nm compared to the pristine sample, consistent with the presence of neutral molecules [222]. Importantly, an entirely new peak is observed around 410 nm with a shoulder around 380-390 nm, which is separate from the neutral aromatic molecules and can be assigned to methylated cationic benzonium ions [222]. Presumably, species are derived from PMBs coordinated to the zeolite BAS sites. Notably, these data indicate an increase in the amount of methylated benzonium cations when benzene is co-fed (either 50 or 200 mg). Interestingly, their concentration increases more strongly when 50 mg of benzene is added compared to 200 mg.

Taken together the results in this section indicate an increase in hydrocarbon species associated with the aromatic cycle inside the pores of the zeolite upon co-feeding benzene. These hydrocarbons include both neutral methylated aromatic molecules and methylated cationic benzonium ions.

Furthermore, it is found that 50 mg co-fed benzene generates a higher amount of benzonium cations compared to 0 or 200 mg of benzene.

5.2.2.4. ssNMR Analysis

To further justify the proposed mechanism and show the interaction between in-situ produced methanol and the zeolite catalyst a number of ssNMR experiments were conducted. These include room temperature adsorption (Section 5.2.2.4.1), methanol-benzene co-reactions (Section 5.2.2.4.2) and isotopic CO_2 hydrogenation experiments (Section 5.2.2.4.3).

5.2.2.4.1. Room Temperature Adsorption

To show the interaction between benzene and methanol with the zeolite catalyst, room temperature adsorption experiments have been performed. Isotopic methanol and benzene were transferred to the zeolite catalyst by evaporation under vacuum at room temperature. After evaporation the transfer line was closed and flushed to get rid of any remaining vapour. In this way all signals attained are due to chemical species adsorbed on the zeolite. Together with the analysis of the pristine zeolite structure (see appendix) these can prove the chemical adsorption of methanol and benzene at the BAS site inside the pores of the zeolite.

Firstly, the ^{13}C ssNMR of room temperature adsorbed (99% ^{13}C) methanol presented in Figure 58A2 shows the characteristic methanol peak at 52 ppm which is downshifted from molecular methanol which presents at 50 ppm [320]. This downfield shift is due to the deshielding effect induced by the hydrogen bonding interaction between methanol and the BAS site [321].

The claim that the BAS site and methanol are directly interacting is further consolidated by the more complex ^{1}H ssNMR of adsorbed methanol as shown in Figure 58B2. A strong broad peak is observed round 3.8 ppm, which corresponds to overlapping signals of unreacted BAS sites as well as methyl and hydroxyl protons of methanol interacting with the catalyst surface [322,323]. The hydroxyl proton in particular is expected to be upshifted due to its interaction with the frame work Si-O-Al oxygen. More interestingly, additional peaks are observed at 8.9, 7.2 and 6.8 ppm. These can unequivocally be assigned to BAS protons which form a complex with adsorbed methanol [323–325].

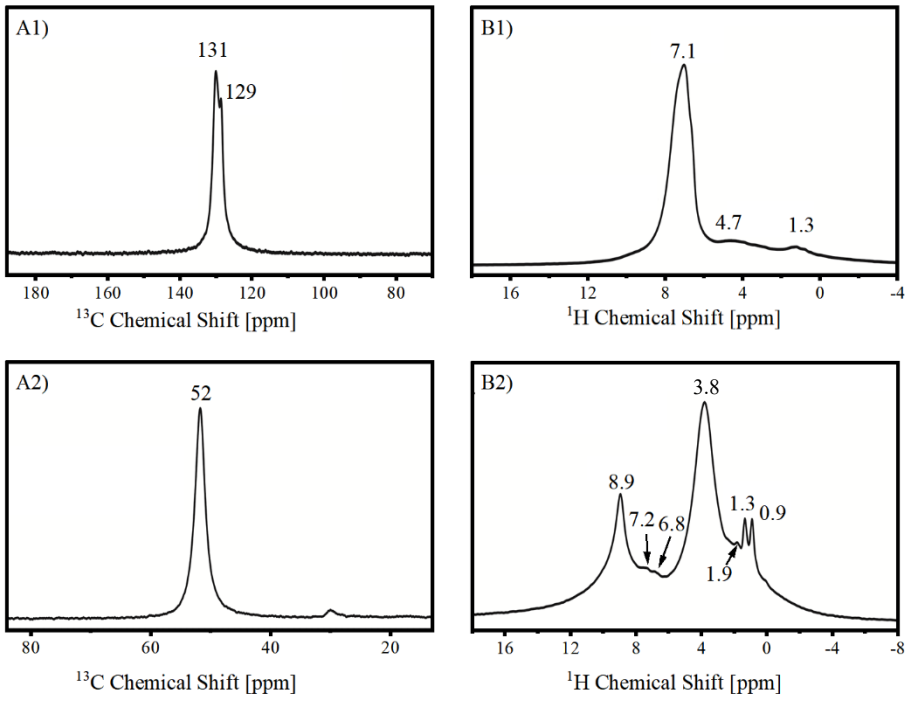

Figure 58| ssNMR of room temperature adsorption of benzene and methanol. The ssNMR results for benzene and methanol adsorption are shown in the first and second row respecively. The ^{13}C and ^{1}H spectra for each experiment are shown in panels A and B respectively.

Secondly, Figure 58A1 and A2 show the ^{13}C and ^{1}H ssNMR spectra of adsorbed (99% ^{13}C) benzene. Due to the symmetry of benzene a typical ^{13}C NMR spectrum is expected to present a single peak at 128 ppm. Instead, the adsorbed benzene shows two peaks at 129 and 131 ppm, which correspond to mobile and rigid benzene species in the ZSM-5 pores [326]. Similarly, the ^{1}H NMR data shows an ensemble of different aromatic proton environments as evidenced by the broad peak centred at 7.2 ppm [326]. Notably, no peak is observed at 8.9 ppm emphasizing that benzene, with a relatively lower proton affinity, interacts differently with the zeolite than methanol, which strongly effects the BAS proton. In contrast to methanol, the BAS proton is observed at ~4.7 ppm only [327], which is upshifted rather than downshifted relative to the pristine zeolite. This effect is due to electron transfer from benzene to the BAS proton. These data prove the chemical interaction between benzene and the acid sites of the zeolite.

While the methanol and benzene adsorption experiments show significant shifts due to their interaction with the acidic zeolite, both molecules stay intact. That is, none of the internal molecular bonds are broken.

5.2.2.4.2. Co-reaction of Methanol and Benzene

To illustrate the reactivity of methanol and benzene over the acidic zeolite two co-reactions were performed. In the first experiment (99% ^{13}C) benzene and (99% ^{13}C) methanol are transferred to the zeolite under vacuum (as before) and heated to 380 °C to complete the reaction. In the second experiment (99% ^{13}C) methanol is reacted with regular benzene under $CO_2/3H_2$ atmosphere to approximate the CO_2 hydrogenation conditions. Both sets of data are presented here.

As was shown in Section 2.4.8 when isotopic CO_2 is reacted with regular benzene the propane product contains carbons derived from both molecules. Similarly, the ssNMR data suggest formation of methylated aromatics generated from the co-reaction of isotopic methanol and benzene. The 1D ssNMR data of the first experiment are shown in Figure 59. Compared to the room temperature adsorption, clearly new chemical species are attained in the co-reaction. Specifically, for the ^{13}C ssNMR data, the absence of a peak around 52 ppm indicates the full conversion of methanol, while the peaks around 129, and 140 ppm imply the formation of neutral and charged aromatic species [326,328]. Additionally, the peaks at 19 and 17 ppm can be assigned to aliphatic carbon centres [326,328]. Correspondingly, the ^{1}H ssNMR data

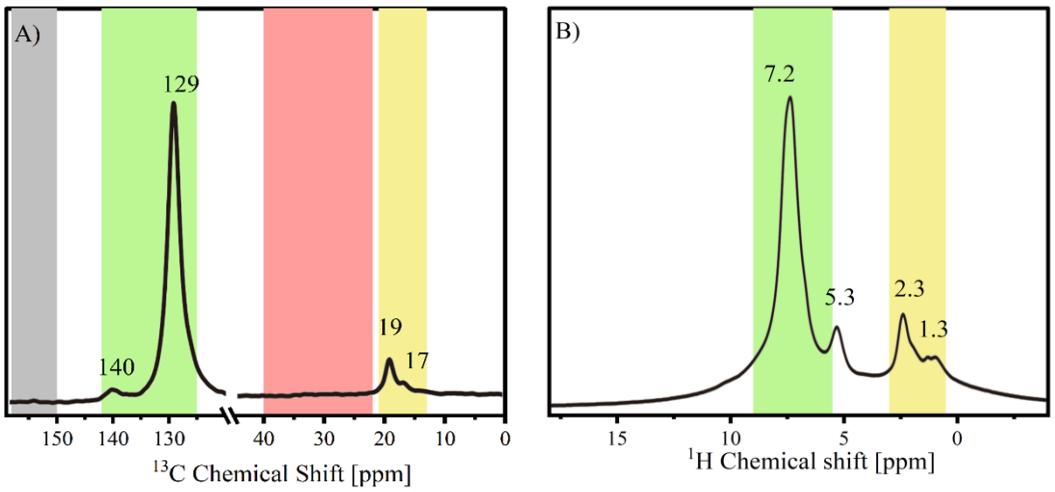

Figure 59| ssNMR result of a methanol-benzene co-reaction at 380 °C after de-gassing. Panel A shows the ^{13}C spectrum. The poly-ene (grey), aromatic (green), aliphatic/oxygenate (red) and alkyl-aromatic (beige) regions are shown. Panel B shows the ^{1}H spectrum. The aromatic (green) and aliphatic region are indicated in green and beige respectively.

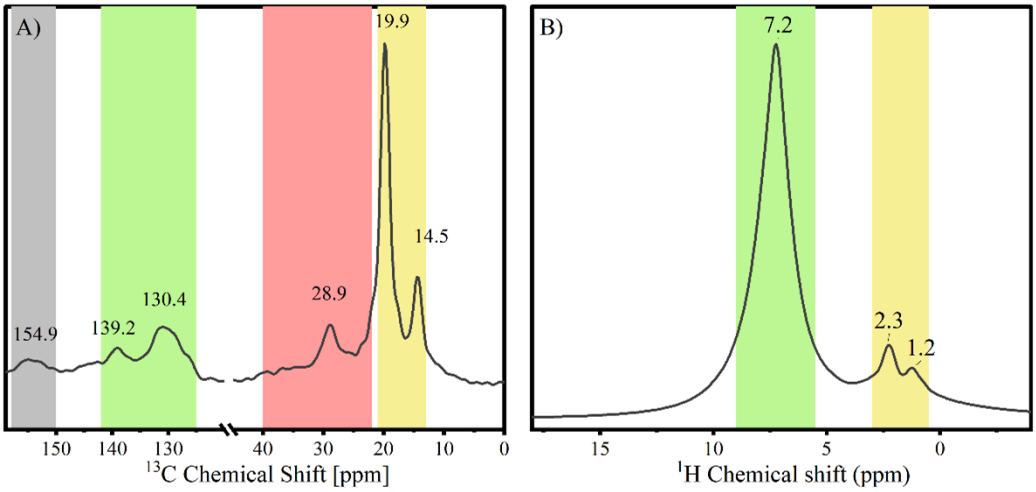

Figure 60| ssNMR of co-reaction of methanol and benzene under CO_2 and H_2 at 250 °C. Panel A and show the ^{13}C and ^{1}H spectra respectively. The ^{13}C poly-ene(-yl) (grey), aromatic (green), aliphatic/oxygenate (red) and alkyl-aromatic (beige) regions are shown. Panel B shows the ^{1}H spectrum. The aromatic (green) and aliphatic region are indicated in green and beige respectively.

in Figure 59B show aromatic protons at 7.2 alongside aliphatic protons at 2.3 and 1.2 ppm [320,326,328]. Water is measured at 5.3 ppm [329,330]. The coexistence of charged aromatics and aliphatic at these peak positions suggests the formation of methylated aromatics.

A similar result is obtained when isotopic methanol is reacted with regular benzene under CO_2-hydrogenation conditions. In this case the 2D ssNMR results prove the interaction between the aliphatic and aromatic species. As before, the 1D ^{1}H ssNMR shows a single strong and broad peak at 7.2 ppm with two smaller peaks at 2.3 and 1.2 ppm indicating the presence of aromatic and aliphatic protons [326,328]. In this case the 1D ^{13}C ssNMR data is more complicated. Aromatic carbon species are observed at 129, 137 and 143 ppm while aliphatic carbon species are measured at 14, 19, and 29 ppm [326,328]. An additional resonance is observed at 154.9 ppm, which shows the formation of polyenyl) moieties [326,328].

Moreover, the hetero- and homonuclear 2D experimental data, presented in Figure 61A and B respectively, confirm the presence of poly-methylated aromatic species as well as polyenyl type species. As expected, the carbon atoms at 129–143 ppm are correlated with the aromatic proton at 7.2 ppm confirming their aromatic nature. In the same way, the presence of alkyl groups is confirmed by the

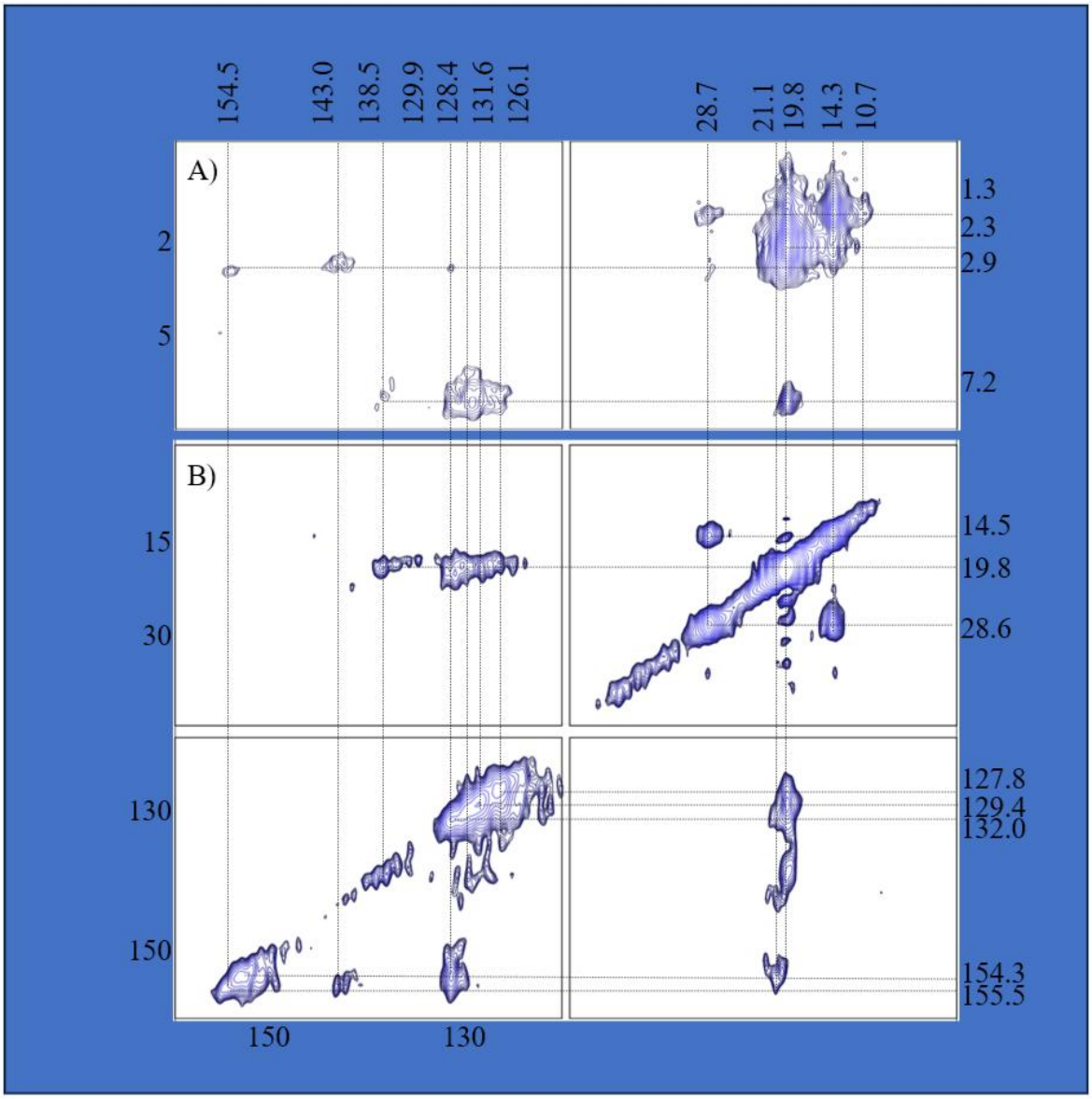

Figure 61| 2D ssNMR results of methanol conversion in the presence of H_2 and CO_2. Panel A shows the heteronuclear HETCOR ^{13}C-^{1}H spectra. Panel B shows the homonuclear PDSD ^{13}C-^{13}C spectra. Dotted reference lines indicate the approximate position of the self- and cross-correlation peaks.

correlation peak between the aliphatic carbons atoms at 14-29 ppm and the aliphatic protons at 1.2 and 2.3 ppm. The strong peak at (19, 2.3) can unambiguously be assigned to methyl groups (-CH_3), while the remaining aliphatic moieties may be derived from longer aliphatic chains like ethyl-groups. The wide spread of the main peak at (19, 2.3) in the ^{1}H dimension from 2 to 1 ppm may imply the proximity between the methyl and remaining aliphatic chains. This would be consistent with the wide range of substituted aromatic species reported in Section 2.4.9. Moreover, three weak peaks located at (128, 2.3), (143, 2.3) and (154, 2.3) are observed. These may suggest the proximity between the alkyl species

with the aromatic and poly-olefinic species. It is interesting to note that, in this case, the peak at (19, 7.1) has a much stronger intensity compared to the peak at (129, 7.1). This is presumably due to the use of non-isotopic benzene in this experiment, which should be entirely *invisible* to NMR. Indeed, the fact that the peak at (129, 7.1) is observed at all implies a transfer of carbon atoms from ^{13}C methanol to the non-isotopic benzene via carbon scrambling as would be predicted by the pairing mechanism. To get more insight in the C–C bonding homonuclear ssNMR data is presented in Figure 61B. In this case there is clear coupling between the carbon centres at 29 and 14 ppm suggesting these carbons represent the α and β carbons of an ethyl- functional group respectively. Unfortunately, due to the relatively low concentration of these species no clear correlation peak is observed between the α or β carbon with any of the carbons in the aromatic range. The methyl group carbon on the other hand shows clear cross peaks at (19, 129), (19, 137) and (19, 143) proving its proximity to aromatic atoms with different chemical environment. This highlights the presence of various neutral and charged PMB species inside the pores of the zeolite.

Furthermore, there is cross-correlation between the peaks around 154 ppm, the peaks at 130 ppm and the peak at 19 ppm. This suggests the presence of poly-ene(-el) species possibly coupled to aromatic species.

Similar to the results attained by heteronuclear NMR, the aliphatic carbon regions (14-29 ppm) show much higher intensity than the aromatic region (129-143 ppm), which is expected. As before, the generation of aromatic carbon peaks implies a carbon transfer from ^{13}C methanol to the non-isotopic benzene via the pairing mechanism.

This relatively high intensity of the aliphatic regions in the 2D data is contrasted by the 1D ^{1}H data (Figure 60 B). In this case the dominant peak is the aromatic one located at 7.2 ppm. This proves that the concentration of aromatic protons is in fact higher than the aliphatic ones. Therefore, the low aromatic carbon intensity in the 2D experiments can rightfully be ascribed to the use of ^{13}C methanol with naturally abundant benzene. Hence, the methanol not only serves to methylate benzene, but also

undergoes incorporation into the aromatic ring by sequential ring contraction and expansion as par the pairing mechanism [331].

All-in-all these data show that a range of trapped products are formed upon the co-reaction of benzene and methanol and methyl not only serves to methylate benzene, but also is incorporated into the aromatic ring. This process results primarily in the formation of PMB species, which are integral to the HCP mechanism [331].

5.2.2.4.3. CO_2 hydrogenation

To definitively show the analogy between the methanol-benzene co-reaction and the tandem CO_2 hydrogenation catalytic reaction, three sets of NMR experiments were conducted with isotopic (99%) ^{13}C CO_2: high concentration, low concentration and naturally abundant ^{13}C CO_2 experiments. By comparing the results of the different experiments with varying amounts of $^{13}CO_2$ the function of benzene can be understood in terms of its anchoring function and its promotion of specific products. Firstly, the 1D and 2D ^{13}C ssNMR data obtained from the following three samples are reported and compared:

1. 7 bar ^{13}C CO_2 reacted in the absence of benzene (N1);
2. 7 bar ^{13}C CO_2 reacted in the presence of natural abundance benzene (N2);
3. 7 bar ^{12}C CO_2 reacted in the presence of 99% ^{13}C benzene (N3).

Secondly, these data are briefly contrasted with the 1D ssNMR data attained in the low ^{13}C CO_2 pressure experiments:

1. 1 bar ^{13}C CO_2 + 6 bar natural abundance CO_2 reacted in the absence of benzene (N4);
2. 1 bar ^{13}C CO_2 + 6 bar natural abundance CO_2 reacted in the presence of natural abundance benzene (N5).

Figure 62 shows the 1D data of experiments N1-3. The species generated in the absence of benzene (N1) show a wide variety of different aliphatic hydrocarbon species in the range of 10.6-41.9 ppm as well as relatively small amounts of aromatics at 129.4 and 136.0 ppm. Unsurprisingly, an increase in the signal related to aromatic carbon species is observed when natural benzene is co-reacted with $^{13}CO_2$ (N-3). As evidenced by the peaks around 129.2 and 136.0 ppm. More strikingly and in contrast to N1, however, a much more narrow range of aliphatic carbon species is obtained with a dominant peak around 19.5 ppm. Because of the high concentration of ^{13}C in CO_2 than the natural abundance benzene used in experiment N3, the aliphatic carbon signal is much stronger than the aromatic signal. N2 shows the opposite trend: the aromatic peaks (128.9, 131.2 and 136.2 ppm) dominate

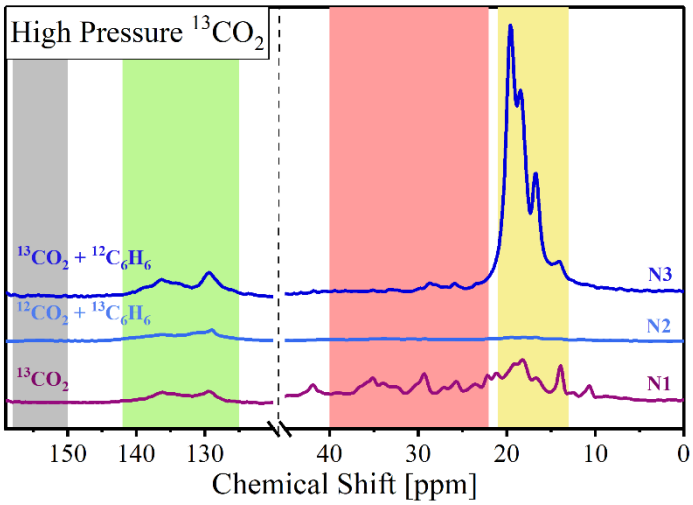

Figure 62| 1D ^{13}C ssNMR spectra of experiment high pressure $^{13}CO_2$ hydrogenation experiments. Experiments N1, N2 and N3 are shown in purple, light blue and dark blue respectively. The ^{13}C polyene(-yl) (grey), aromatic (green), aliphatic/oxygenate (red) and alkyl-aromatic (beige) regions are shown. Panel B shows the ^{1}H spectrum.

the spectrum with a relatively small broad peak ranging from 19.4 to 16.7 ppm (see the expanded spectrum of N2 in Figure S35). This shows benzene is not cracked at any appreciable rate.

To understand the relationship between the aliphatic and aromatic carbon species 2D ssNMR data of these experiments are presented in Figure 63 . As expected from the 1D data, N1 shows a wide range of coupled aliphatics as well as a methylated aromatics. The former is indicated by (for example) the cross correlation peaks at (36.0, 17.9 ppm), (25.6, 13.8 ppm), (13.8, 23.0 ppm) and (10.8, 29.3 ppm). The latter is evidenced by the aliphatic-aromatic cross-correlations regions (129.8-136.6, 17.9) and (18.0, 129.8-136.6 ppm).

The 2D ssNMR results of N2 and N3 show complementary results. On the one hand, as expected, the data obtained from experiment N2 show the formation of methylated aromatics under these conditions. This is evidenced by the cross-correlation regions at (129.1-135.6, 16.8-19.5 ppm) and (16.8-19.6, 129.1-136.0 ppm). These regions show that the aliphatic carbons species observed around (18.0, 18.0) are coupled to the aromatic species measured between (129.1, 129.1) and (136.0, 135.6). On the other hand, the aliphatic region of N3 shows a number of spread-out peaks at (10.4, 9-14) and (17.8-14.8, 9-14.7). These peaks imply the existence of different aliphatic carbon chains in the sample.

A variety of aromatic carbon atoms are also shown by the region ranging from (125.1, 127.4 ppm) to (143.4, 143.6 ppm). Crucially, no correlation peaks are observed. Hence, these aliphatic and aromatic species are not chemically bonded. In this case, the aliphatics might be derived from trapped light hydrocarbons such as propane, which are made-up of both ^{12}C from CO_2 and ^{13}C from the isotopic benzene via the pairing mechanism carbon scrambling. The aromatics are derived from the methylation of co-fed isotopic benzene by CO_2.

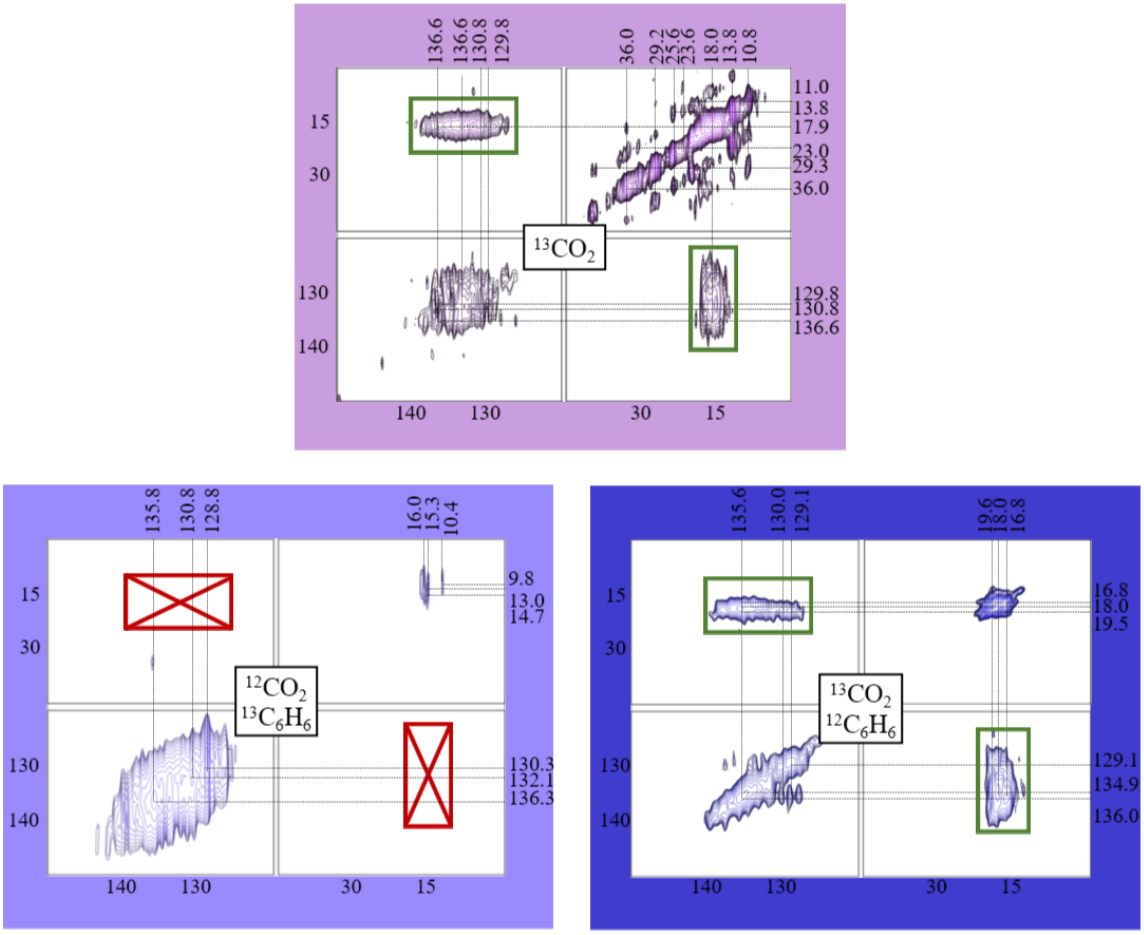

Figure 63| 2D ssNMR results of high pressure experiments. The different reaction compositions are indicated in each panel. Experiments N1, N2 and N3 are shown in the purple, light blue and dark blue panels respectively. Dotted reference lines indicate the approximate self- and cross-correlation peak positions.

The 1D data attained from experiments N4 and N5 are reported in Figure 64. Although the signal-to-noise ratio is significantly lower than in N2 due to the lower ^{13}C present, similarly to N2 experiment N4 shows the generation of both aliphatic and aromatic carbons via the mechanism referenced before. However, in the case of N5 no signal is attained due to an insufficient concentration of trapped hydrocarbons. This clearly shows that the presence of benzene increases the amount of trapped hydrocarbons.

Taking these results together it is evident that: in the presence of benzene, methanol primarily acts to methylate benzene to generate PMB species rather than to generate aliphatic chains outright (such as in the absence of benzene (N1 and N4)). This increases the concentration of active carbon species retained inside the pores of the zeolite (evidenced by N4 and N5). In turn, these PMB species give rise to aliphatic hydrocarbons via incorporation of both aromatic ring and methyl carbons via the pairing mechanism. In this way co-fed benzene acts to *"grab"* the available methanol before it can polymerize. In effect the olefinic cycle is bypassed and the aromatic cycle is instigated. Consequently, the C_3 product is increased.

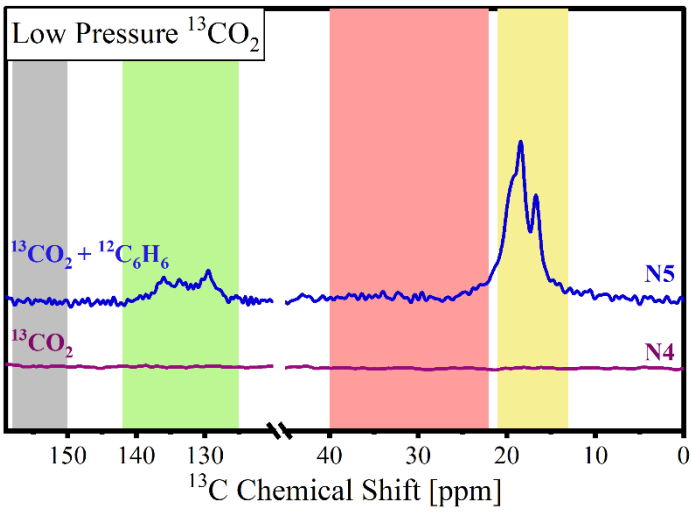

Figure 64|1D ^{13}C ssNMR spectra of experiment low pressure $^{13}CO_2$ hydrogenation experiments. Experiments N4 and N5 are shown in purple,dark blue respectively. The ^{13}C poly-ene(-yl) (grey), aromatic (green), aliphatic/oxygenate (red) and alkyl-aromatic (beige) regions are shown. Panel B shows the ^{1}H spectrum.

5.3. Conclusion

It has been shown that the addition of benzene can aid the selective tandem hydrogenation of CO_2 to propane under relatively mild conditions by promoting the aromatic HCP cycle. Co-feeding 50 mg of benzene to the RhIn/ZSM-5 composite catalyst can greatly increase the CO_2 hydrogenation selectivity to propane under the conditions chosen, while having a minimal impact on the CO_2 conversion or CO formation. The enhanced C_3 selectivity comes at the expense of both lighter (C_{1-2}) and heavier (C_{4+}) hydrocarbons. A combination of techniques including TGA, UV-VIS, GC-MS, control experiments, isotopic labelling experiments and extensive ssNMR measurements prove the active role of benzene during reaction: benzene acts as a scaffold to *"grab" in-situ* produced methanol, thereby increasing the amount of active PMB species inside the pores of the zeolite. As a consequence, methanol is diverted away from direct C–C coupling and oligomerisation at Brønsted acid sites, which would otherwise promote the aliphatic cycle. Instead, the accumulation of neutral and cationic PMB species inside the zeolite pores promotes the aromatic HCP cycle.

The formation of methylated benzonium ions, identified by UV–Vis spectroscopy, together with the ssNMR evidence for extensive methyl–aromatic coupling and carbon scrambling, confirms that these PMB species act as active intermediates rather than spectators. The isotopic composition of propane further shows that carbon atoms originating from both CO_2-derived methanol and benzene are incorporated into the final product, consistent with a pairing-type mechanism involving ring contraction and expansion within the aromatic pool. In this way, the aromatic cycle selectively favours propane formation while suppressing competing hydrocarbon pathways.

Overall, these findings show that selective manipulation of the hydrocarbon pool chemistry provides a viable strategy to control product selectivity in tandem CO_2 hydrogenation without the need for catalyst structure engineering.

Chapter 6

Final Conclusions and Outlook

Final Conclusions and Outlook

Over the recent years increased interest has gathered around the field of heterogeneous CO_2 hydrogenation catalysis. It is recognized that the conversion of CO_2 to specific molecules, which are traditionally derived from fossil fuels, is an invaluable technology to reaching a sustainable circular economy. This increased attention has led a vast body of research with the aim of understanding existing catalysts and developing new catalyst systems which are able to selectively transform CO_2 and H_2 into desired products.

The research presented here has specifically focused on the formation of value-added coupled (rather than single carbon) products. In recognition of the various strategies to achieve such conversion this thesis was separated in two parts: direct and tandem hydrogenation. Both these strategies continue to be researched and developed. Controlling the product selectivity and achieving high conversion rates are of prime interest in both cases. To achieve this increased understanding is required and new systems need to be explored.

Accordingly, in Chapters 2 and 3 a salient topic in the direct CO-mediated conversion of CO_2 to valuable olefins and higher alcohols was explored, namely the alkali metal (AM) doping of CuFe based catalysts. Although the beneficial effects of AMs on the formation of such products from either CO_2 and H_2 or syngas has been widely reported and the industrial use of alkali metals in FTS catalysis is well established, little is known about their specific role. Hence, developing a thorough understanding of their role remains needed to advance the design of highly active and selective CO_2 hydrogenation catalysts. To further this understanding, here the effects of AMs on a unsupported catalyst was studied. Using an unsupported catalyst (which are not the standard in industry) for this research limits introducing any further complicating variables. Therefore, the current study on AM doping should be regarded as an attempt clarify the AM surface interactions and effects on the reported active sites associated with Cu^0 and FeC_x phases, rather than an attempt to illustrate an optimised catalyst system. In order to move towards industrial application further research is required. To move towards industrial

application, future research ought to focus on the structure of surface AMs under working conditions as well as potential support effects.

Herein, chapter 2 has shown that AMs have a profound effect on the product selectivity of the catalyst. These findings are in line with the wider literature on AM doping of FTS and CO_2 hydrogenation catalysts [26,37,79,81,82,133,234,286]. Moreover, significant changes to the phase contribution and distribution of Fe carbides and Cu^0 were observed after reaction upon the inclusion of AMs. The increase in reduced Cu and carburized Fe phases at the bulk and surface were similarly consistent with the structural effect of AMs as reported in the wider literature [72,79,119,332]. Indeed, such changes can be largely understood by the oxophilicity and the surface segregation of the doped AMs (as was elaborated on in Section 1.3.1). Importantly, however, the observed structural changes to the TMs upon the inclusion of AMs are insufficient to rationalize the formation of higher alcohols and olefins at the expense of paraffins. This is a key insight of the current research which may educate future optimisation of CO_2 hydrogenation catalyst development. To further advance the research, the proximal interaction between the TMs and AMs was studied.

Unfortunately, in contrast to the TMs, little is known, of the structure of the doped AMs. Therefore, a first attempt was made here to show the distinct structure of Rb after reaction by the use of EXAFS analysis. To our knowledge no such analysis has been reported hitherto. Yet, further work is clearly required to clarify the local chemical environment of doped surface AMs. The EXAFS findings demonstrated here may simply be taken as confirmation of the strength of XAS to study AMs in this context.

Indeed, our EXAFS analysis was supplementary to XPS and XRD characterization, which implied that the doped AMs are highly dispersed at the catalyst surface and reside in a unique chemical environment proximal to surface TM atoms (while retaining an oxidation state of +1). The EXAFS analysis further proved the distinctness of the Rb speciation after reaction: for the first time an additional high frequency component was observed, clearly showing the local structural perturbation of the doped Rb atoms. By using wavelet analysis the measured high frequency component could be tentatively assigned to a multi-scattering pathway involving the surface AM and TM atoms. Based on this

promising result further analysis of doped surface AMs by EXAFS analysis is expected to be highly fruitful in expanding our understanding of the AM local structure. To this end, simplified model materials (containing fewer TM elements) may lend more credence to the assignment of observed spectral features. Moreover, considering the mobility of AM atoms at the surface of different metal (oxide/carbide) phases, changes to the AM local environment may be studied by EXAFS during the catalyst activation and CO_2 conversion in the future. Although dynamic changes to the AM environment has previously been eluded to for K [227,228]. In-situ EXAFS measurements should be able to further elucidate the nature of such dynamic changes under different conditions. To fully understand the structure of the AM doped CO_2 hydrogenation catalyst in situ EXAFS analysis is expected to yield incredible insight into the local structure of surface AMs. Such results may help to inform our understanding of the mechanistic changes upon AM doping as described in Chapter 3.

The work described in Chapter 3 has offered a unified mechanistic explanation for the co-formation of higher alcohols and olefins: olefins and higher alcohols are derived from a shared reaction pathway which involves CO insertion as a key reaction step. It was proposed that AM induced CO insertion is a result of direct interaction of surface AMs with reactive oxygen containing intermediates. The suggested interaction between CO and surface AMs was studied by TPSR and DRIFT measurements. These showed significant changes to the binding mode of CO in the presence of surface AMs. It was hypothesized that these changes are derived from the direct involvement of surface AMs. To test this hypothesis CO-adsorption XANES experiments were conducted. By evaluating the position of the Rb K-edge a clear CO induced decrease of the electron density around Rb was observed. Crucially, this adsorbate induced electron depletion of Rb has been predicted by recent DFT publications [261,288,290,292–294]. To our knowledge no such element specific adsorption experimental data have been reported before. In this way this thesis has provided a novel analysis of CO adsorption *from the AM perspective* in addition to extensive CO-adsorption DRIFTS experiments. Further such adsorption XAS experimental work may prove useful to investigate the adsorbate induced AM-TM interactions as described by the computational work which was discussed herein.

CONCLUSION AND OUTLOOK

Chapter 4 of this thesis has described a straightforward method to enhance the propane C_3 selectivity of a RhIn/ZSM-5 composite catalyst by co-feeding benzene into a batch reactor. Although similar composite catalysts involving ZSM-5 have been reported to be able to convert CO_2 and H_2 to light hydrocarbons before [45,46,209], the current reaction setup requires much milder conditions (only 250 °C). Such low temperatures allow for sufficient suppression of the RWGS reaction which generally dominates methanol mediated CO_2 to coupled hydrocarbon synthesis without compromising on the selective hydrocarbon formation. In this way the method described here constitutes a viable alternative to traditional methods involving structural modifications.

It was concluded that the addition of benzene enables the enhanced C_3 selectivity by promoting the aromatic cycle of the HCP reaction inside the pores of the zeolite. Interestingly, a similar type of enhancement has recently been observed to be beneficial to the selective hydrocracking of polyolefins to propane at similar conditions by ZSM-5 without structure modification. In fact, analogously to the current research, high yields of propane rich gas were achieved simply by the cofeeding of aromatic compounds during hydrocracking reaction [333] Moreover, separately a recent publication has suggested the possibility of combining CO_2 reduction with polyolefin decomposition [334–336]. The combination of such seemingly different reactions may indeed prove possible considering the similarity in reaction conditions and congruous use of acidic ZSM-5 in both reactions. Although highly speculative, in this context it may be possible to selectively produce propane simultaneously from polyolefin plastics and CO_2.

Altogether it is clear that the current thesis leaves considerable avenues for future research.

Literature

(1) Ritchie, H.; Roser, M. CO_2 and Greenhouse Gas Emissions. *Our World in Data* **2020**.

(2) Alsarhan, L. M.; Alayyar, A. S.; Alqahtani, N. B.; Khdary, N. H.; Raganati, F.; Ammendola, P.; Sa, A. S. A.). Sustainability Circular Carbon Economy (CCE): A Way to Invest CO 2 and Protect the Environment, a Review. **2021**. https://doi.org/10.3390/su1321.

(3) Schlögl, R. The Revolution Continues: Energiewende 2.0. *Angew. Chem. Int. Ed.* **2015**, *54* (15), 4436–4439. https://doi.org/10.1002/ANIE.201405876.

(4) Aziz, M.; Wijayanta, A. T.; Nandiyanto, A. B. D. Ammonia as Effective Hydrogen Storage: A Review on Production, Storage and Utilization. *Energies (Basel).* **2020**, *13* (12), 3062. https://doi.org/10.3390/en13123062.

(5) Ojelade, O. A.; Zaman, S. F.; Ni, B.-J. Green Ammonia Production Technologies: A Review of Practical Progress. *J. Environ. Manage.* **2023**, *342*, 118348. https://doi.org/10.1016/j.jenvman.2023.118348.

(6) Thiounn, T.; Smith, R. C. Advances and Approaches for Chemical Recycling of Plastic Waste. *Journal of Polymer Science* **2020**, *58* (10), 1347–1364. https://doi.org/10.1002/pol.20190261.

(7) Klankermayer, J.; Wesselbaum, S.; Beydoun, K.; Leitner, W. Selective Catalytic Synthesis Using the Combination of Carbon Dioxide and Hydrogen: Catalytic Chess at the Interface of Energy and Chemistry. *Angew. Chem. Int. Ed.* **2016**, *55* (26), 7296–7343. https://doi.org/10.1002/ANIE.201507458.

(8) Zhang, S.; Wu, Z.; Liu, X.; Hua, K.; Shao, Z.; Wei, B.; Huang, C.; Wang, H.; Sun, Y. A Short Review of Recent Advances in Direct CO2 Hydrogenation to Alcohols. *Topics in Catalysis*. Springer May 1, 2021, pp 371–394. https://doi.org/10.1007/s11244-020-01405-w.

(9) Ray, D.; Ye, P.; Yu, J. C.; Song, C. Recent Progress in Plasma-Catalytic Conversion of CO2 to Chemicals and Fuels. *Catal. Today* **2023**, *423*, 113973. https://doi.org/10.1016/j.cattod.2022.12.004.

(10) Xing, Y.; Ma, Z.; Su, W.; Wang, Q.; Wang, X.; Zhang, H. Analysis of Research Status of CO2 Conversion Technology Based on Bibliometrics. *Catalysts* **2020**, *10* (4), 370. https://doi.org/10.3390/catal10040370.

(11) Wang, H.; Yu, Z.; Zhou, J.; Li, C.; Jayanarasimhan, A.; Zhao, X.; Zhang, H. A Scientometric Review of CO2 Electroreduction Research from 2005 to 2022. *Energies (Basel).* **2023**, *16* (2), 616. https://doi.org/10.3390/en16020616.

(12) Nikolajsen, M. T.; Grivel, J.-C.; Gaur, A.; Hansen, L. P.; Baumgarten, L.; Schjødt, N. C.; Mentzel, U. V.; Grunwaldt, J.-D.; Sehested, J.; Christensen, J. M.; Høj, M. Surface ZnO on Zirconia Is Highly Active for High Temperature Methanol Synthesis. *J. Catal.* **2024**, *431*, 115389. https://doi.org/10.1016/j.jcat.2024.115389.

(13) Yang, F.; Zhou, W.; Yang, C.; Zhang, T.; Huang, Y. Enhanced Methanol Selectivity in CO2 Hydrogenation by Decoration of K on MoS2 Catalyst. *Acta Physico-Chimica Sinica* **2024**, *40* (7), 2308017. https://doi.org/10.3866/PKU.WHXB202308017.

(14) Li, M. M.; Zou, H.; Zheng, J.; Wu, T.; Chan, T.; Soo, Y.; Wu, X.; Gong, X.; Chen, T.; Roy, K.; Held, G.; Tsang, S. C. E. Methanol Synthesis at a Wide Range of H_2 /CO_2 Ratios over a Rh-In Bimetallic Catalyst. *Angewandte Chemie* **2020**, *132* (37), 16173–16180. https://doi.org/10.1002/ange.202000841.

(15) Huš, M.; Dasireddy, V. D. B. C.; Strah Štefančič, N.; Likozar, B. Mechanism, Kinetics and Thermodynamics of Carbon Dioxide Hydrogenation to Methanol on Cu/ZnAl2O4 Spinel-Type Heterogeneous Catalysts. *Appl. Catal. B* **2017**, *207*, 267–278. https://doi.org/10.1016/j.apcatb.2017.01.077.

(16) Li, M. M. J.; Chen, C.; Ayvall, T.; Suo, H.; Zheng, J.; Teixeira, I. F.; Ye, L.; Zou, H.; O'Hare, D.; Tsang, S. C. E. CO2 Hydrogenation to Methanol over Catalysts Derived from Single Cationic Layer CuZnGa LDH Precursors. *ACS Catal.* **2018**, *8* (5), 4390–4401. https://doi.org/10.1021/acscatal.8b00474.

(17) Martin, N. M.; Velin, P.; Skoglundh, M.; Bauer, M.; Carlsson, P.-A. Catalytic Hydrogenation of CO_2 to Methane over Supported Pd, Rh and Ni Catalysts. *Catal. Sci. Technol.* **2017**, *7* (5), 1086–1094. https://doi.org/10.1039/C6CY02536F.

(18) Tang, X.; Song, C.; Li, H.; Liu, W.; Hu, X.; Chen, Q.; Lu, H.; Yao, S.; Li, X.; Lin, L. Thermally Stable Ni Foam-Supported Inverse CeAlOx/Ni Ensemble as an Active Structured Catalyst for CO2 Hydrogenation to Methane. *Nat. Commun.* **2024**, *15* (1), 3115. https://doi.org/10.1038/s41467-024-47403-4.

(19) Yan, B.; Zhao, B.; Kattel, S.; Wu, Q.; Yao, S.; Su, D.; Chen, J. G. Tuning CO2 Hydrogenation Selectivity via Metal-Oxide Interfacial Sites. *J. Catal.* **2019**, *374*, 60–71. https://doi.org/10.1016/j.jcat.2019.04.036.

(20) Rabee, A. I. M.; Vuong, T. H.; Kraußer, L.; Abed, H.; Atia, H.; Rockstroh, N.; Lund, H.; Bartling, S.; Kondratenko, E. V.; Brückner, A.; Rabeah, J. Unveiling Alkali-Induced Redox Modulation: In-Situ Spectroscopic Insights from RWGS on Alkali-Modified ZrO_2 -Supported Cu Catalysts. *Advanced Science* **2025**. https://doi.org/10.1002/advs.202506401.

(21) Barberis, L.; Versteeg, C. I.; Meeldijk, J. D.; Stewart, J. A.; Vandegehuchte, B. D.; de Jongh, P. E. K and Na Promotion Enables High-Pressure Low-Temperature Reverse Water Gas Shift over Copper-Based Catalysts. *ACS Catal.* **2024**, *14* (12), 9188–9197. https://doi.org/10.1021/acscatal.4c02293.

(22) Liu, H.-X.; Li, S.-Q.; Wang, W.-W.; Yu, W.-Z.; Zhang, W.-J.; Ma, C.; Jia, C.-J. Partially Sintered Copper–ceria as Excellent Catalyst for the High-Temperature Reverse Water Gas Shift Reaction. *Nat. Commun.* **2022**, *13* (1), 867. https://doi.org/10.1038/s41467-022-28476-5.

(23) Liu, T.; Xu, D.; Song, M.; Hong, X.; Liu, G. K–ZrO_2 Interfaces Boost CO_2 Hydrogenation to Higher Alcohols. *ACS Catal.* **2023**, *13* (7), 4667–4674. https://doi.org/10.1021/acscatal.3c00074.

(24) Xu, D.; Yang, H.; Hong, X.; Liu, G.; Edman Tsang, S. C. Tandem Catalysis of Direct CO_2 Hydrogenation to Higher Alcohols. *ACS Catal.* **2021**, *11* (15), 8978–8984. https://doi.org/10.1021/acscatal.1c01610.

(25) Wang, Y.; Zhang, X.; Hong, X.; Liu, G. Sulfate-Promoted Higher Alcohol Synthesis from CO_2 Hydrogenation. *ACS Sustain. Chem. Eng.* **2022**, *10* (27), 8980–8987. https://doi.org/10.1021/acssuschemeng.2c02743.

(26) Witoon, T.; Numpilai, T.; Nijpanich, S.; Chanlek, N.; Kidkhunthod, P.; Cheng, C. K.; Ng, K. H.; Vo, D. V. N.; Ittisanronnachai, S.; Wattanakit, C.; Chareonpanich, M.; Limtrakul, J. Enhanced CO2 Hydrogenation to Higher Alcohols over K-Co Promoted In2O3 Catalysts. *Chemical Engineering Journal* **2022**, *431*, 133211. https://doi.org/10.1016/J.CEJ.2021.133211.

(27) Hilmen, A.-M.; Xu, M.; Gines, M. J. L.; Iglesia, E. *Synthesis of Higher Alcohols on Copper Catalysts Supported on Alkali-Promoted Basic Oxides*.

(28) Luk, H. T.; Mondelli, C.; Mitchell, S.; Siol, S.; Stewart, J. A.; Curulla Ferré, D.; Pérez-Ramírez, J. Role of Carbonaceous Supports and Potassium Promoter on Higher Alcohols Synthesis over

Copper–Iron Catalysts. *ACS Catal.* **2018**, *8* (10), 9604–9618. https://doi.org/10.1021/acscatal.8b02714.

(29) Yao, B.; Xiao, T.; Makgae, O. A.; Jie, X.; Gonzalez-Cortes, S.; Guan, S.; Kirkland, A. I.; Dilworth, J. R.; Al-Megren, H. A.; Alshihri, S. M.; Dobson, P. J.; Owen, G. P.; Thomas, J. M.; Edwards, P. P. Transforming Carbon Dioxide into Jet Fuel Using an Organic Combustion-Synthesized Fe-Mn-K Catalyst. *Nat. Commun.* **2020**, *11* (1), 6395. https://doi.org/10.1038/s41467-020-20214-z.

(30) He, Z.; Cui, M.; Qian, Q.; Zhang, J.; Liu, H.; Han, B. Synthesis of Liquid Fuel via Direct Hydrogenation of CO_2. *Proceedings of the National Academy of Sciences* **2019**, *116* (26), 12654–12659. https://doi.org/10.1073/pnas.1821231116.

(31) Gao, P.; Dang, S.; Li, S.; Bu, X.; Liu, Z.; Qiu, M.; Yang, C.; Wang, H.; Zhong, L.; Han, Y.; Liu, Q.; Wei, W.; Sun, Y. Direct Production of Lower Olefins from CO_2 Conversion via Bifunctional Catalysis. *ACS Catal.* **2018**, *8* (1), 571–578. https://doi.org/10.1021/acscatal.7b02649.

(32) You, Z.; Deng, W.; Zhang, Q.; Wang, Y. Hydrogenation of Carbon Dioxide to Light Olefins over Non-Supported Iron Catalyst. *Chinese Journal of Catalysis* **2013**, *34* (5), 956–963. https://doi.org/10.1016/S1872-2067(12)60559-2.

(33) Sun, Z.; Chen, X.; Lu, F.; Zhou, L.; Zhang, Y. Effect of Rb Promoter on Fe3O4 Microsphere Catalyst for CO2 Hydrogenation to Light Olefins. *Catal. Commun.* **2022**, *162*, 106387. https://doi.org/10.1016/j.catcom.2021.106387.

(34) Lu, H.; Li, X.; Li, G.; Hong, X.; Tsang, S. C. E. Na-Decorated Binary Spinel Ferrite Catalysts for the Hydrogenation of CO_2 to Olefins. *Catal. Sci. Technol.* **2025**, *15* (7), 2229–2237. https://doi.org/10.1039/D5CY00033E.

(35) Sun, X.; Guo, T.; An, M.; Guo, X.; Han, Z.; Zhai, D.; Ma, J.; Hu, X.; Zhang, J.; He, Y.; Guo, Q. The Bifunctional Oxygen Carrier K/LayCoxFe1-XO3 for the Production of C2–C4 Olefins via CO2 Hydrogenation. *Int. J. Hydrogen Energy* **2024**, *51*, 368–381. https://doi.org/10.1016/j.ijhydene.2023.06.217.

(36) Liu, Y.; Gong, X.; He, R.; Han, Z.; Chen, J.; Feng, B.; Xu, X.; Xing, A.; Jin, R.; Ren, P.; Wang, B.; Wang, Z. J. Stable Three-Dimensional Macroporous Iron-Foam Catalyst for Direct Conversion of CO2 to Olefins. *ACS Catal.* **2024**, *14* (16), 12425–12436. https://doi.org/10.1021/acscatal.4c03148.

(37) Zhang, Z.; Huang, G.; Tang, X.; Yin, H.; Kang, J.; Zhang, Q.; Wang, Y. Zn and Na Promoted Fe Catalysts for Sustainable Production of High-Valued Olefins by CO2 Hydrogenation. *Fuel* **2022**, *309*, 122105. https://doi.org/10.1016/J.FUEL.2021.122105.

(38) Ning, S.; Ou, H.; Li, Y.; Lv, C.; Wang, S.; Wang, D.; Ye, J. Co0−Coδ+ Interface Double-Site-Mediated C−C Coupling for the Photothermal Conversion of CO2 into Light Olefins. *Angew. Chem. Int. Ed.* **2023**, *62* (23). https://doi.org/10.1002/anie.202302253.

(39) Zhang, L.; Li, M.; Li, G.; Liu, W.; Ye, L.; Liu, K.; Ma, Q.; Peng, H. Catalytic Cycle Network: Boosting CO2 Hydrogenation to Propane. *Appl. Catal. B* **2024**, *358*. https://doi.org/10.1016/j.apcatb.2024.124372.

(40) Wang, S.; Zhang, L.; Wang, P.; Jiao, W.; Qin, Z.; Dong, M.; Wang, J.; Olsbye, U.; Fan, W. Highly Selective Hydrogenation of CO2 to Propane over GaZrOx/H-SSZ-13 Composite. *Nat. Catal.* **2022**, *5* (11), 1038–1050. https://doi.org/10.1038/s41929-022-00871-7.

(41) Liu, Z.; Ni, Y.; Sun, T.; Zhu, W.; Liu, Z. Conversion of CO2 and H2 into Propane over InZrO and SSZ-13 Composite Catalyst. *Journal of Energy Chemistry* **2021**, *54*, 111–117. https://doi.org/10.1016/j.jechem.2020.04.069.

(42) Chernyak, S. A.; Corda, M.; Marinova, M.; Safonova, O. V.; Kondratenko, V. A.; Kondratenko, E. V.; Kolyagin, Y. G.; Cheng, K.; Ordomsky, V. V.; Khodakov, A. Y. Decisive Influence of SAPO-34 Zeolite on Light Olefin Selectivity in Methanol-Meditated CO_2 Hydrogenation over Metal Oxide-Zeolite Catalysts. *ACS Catal.* **2023**, *13* (22), 14627–14638. https://doi.org/10.1021/acscatal.3c03759.

(43) Chen, S.; Wang, J.; Feng, Z.; Jiang, Y.; Hu, H.; Qu, Y.; Tang, S.; Li, Z.; Liu, J.; Wang, J.; Li, C. Hydrogenation of CO_2 to Light Olefins over $ZnZrO_x$ /SSZ-13. *Angew. Chem. Int. Ed.* **2024**, *63* (8). https://doi.org/10.1002/anie.202316874.

(44) Dokania, A.; Dutta Chowdhury, A.; Ramirez, A.; Telalovic, S.; Abou-Hamad, E.; Gevers, L.; Ruiz-Martinez, J.; Gascon, J. Acidity Modification of ZSM-5 for Enhanced Production of Light Olefins from CO2. *J. Catal.* **2020**, *381*, 347–354. https://doi.org/10.1016/j.jcat.2019.11.015.

(45) Li, W.; Wang, K.; Zhan, G.; Huang, J.; Li, Q. Design and Synthesis of Bioinspired ZnZrOx&Bio-ZSM-5 Integrated Nanocatalysts to Boost CO2 Hydrogenation to Light Olefins. *ACS Sustain. Chem. Eng.* **2021**, *9* (18), 6446–6458. https://doi.org/10.1021/acssuschemeng.1c01384.

(46) Ruiz Esquius, J.; Bahruji, H.; Bowker, M.; Hutchings, G. J. Identification of C_2 –C_5 Products from CO_2 Hydrogenation over PdZn/TiO_2 –ZSM-5 Hybrid Catalysts. *Faraday Discuss.* **2021**, *230*, 52–67. https://doi.org/10.1039/D0FD00135J.

(47) Frusteri, F.; Bonura, G.; Cannilla, C.; Drago Ferrante, G.; Aloise, A.; Catizzone, E.; Migliori, M.; Giordano, G. Stepwise Tuning of Metal-Oxide and Acid Sites of CuZnZr-MFI Hybrid Catalysts for the Direct DME Synthesis by CO2 Hydrogenation. *Appl. Catal. B* **2015**, *176–177*, 522–531. https://doi.org/10.1016/j.apcatb.2015.04.032.

(48) Rasouli, M.; Yaghobi, N. Bifunctional ZnO/HZSM-5 Catalysts in Direct Hydrogenation of CO2 to Aromatics; Influence of Preparation Method. *Catal. Letters* **2023**, *153* (5), 1450–1463. https://doi.org/10.1007/s10562-022-04073-5.

(49) Shi, Y.; Gao, W.; Wang, K.; Zhang, L.; Feng, H.; Guo, X.; He, Y.; Feng, X.; Liu, Q.; Li, T.; Pan, Y.; Ma, Q.; Tsubaki, N. Direct Conversion of CO2 to Light Aromatics by Composite ZrCr-C/ZSM-5 Catalyst. *Applied Catalysis B: Environment and Energy* **2024**, *353*, 124068. https://doi.org/10.1016/j.apcatb.2024.124068.

(50) Zhou, J.; Miao, Y.; Ding, H.; Ren, Y.; Ye, L.; Yue, B.; He, H. Direct and Stable Hydrogenation of CO2 to Aromatics over a Tandem Catalyst Zn0.1Ti0.9Ox/HZSM-5. *iScience* **2024**, *27* (7), 110360. https://doi.org/10.1016/j.isci.2024.110360.

(51) Wen, C.; Xu, X.; Song, X.; Lu, L.; Zhuang, X.; Jin, K.; Jiang, Q.; Zhang, X.; Chen, L.; Wang, C.; Ma, L. Selective CO_2 Hydrogenation to Light Aromatics over the Cu-Modified Fe-Based/ZSM-5 Catalyst System. *Energy & Fuels* **2023**, *37* (1), 518–528. https://doi.org/10.1021/acs.energyfuels.2c03414.

(52) Shah, D. R.; Nezam, I.; Zhou, W.; Proaño, L.; Jones, C. W. Isomorphous Substitution in ZSM-5 in Tandem Methanol/Zeolite Catalysts for the Hydrogenation of CO_2 to Aromatics. *Energy & Fuels* **2024**, *38* (3), 2224–2234. https://doi.org/10.1021/acs.energyfuels.3c03755.

(53) Xu, D.; Wang, Y.; Ding, M.; Hong, X.; Liu, G.; Tsang, S. C. E. Advances in Higher Alcohol Synthesis from CO2 Hydrogenation. *Chem* **2021**, *7* (4), 849–881. https://doi.org/10.1016/J.CHEMPR.2020.10.019.

(54) Guo, S.; Wang, H.; Qin, Z.; Li, Z.; Wang, G.; Dong, M.; Fan, W.; Wang, J. Feasibility, Limit, and Suitable Reaction Conditions for the Production of Alcohols and Hydrocarbons from CO and CO_2 through Hydrogenation, a Thermodynamic Consideration. *Ind. Eng. Chem. Res.* **2022**, *61* (46), 17027–17038. https://doi.org/10.1021/acs.iecr.2c02898.

(55) Liu, C.; Cundari, T. R.; Wilson, A. K. CO_2 Reduction on Transition Metal (Fe, Co, Ni, and Cu) Surfaces: In Comparison with Homogeneous Catalysis. *The Journal of Physical Chemistry C* **2012**, *116* (9), 5681–5688. https://doi.org/10.1021/jp210480c.

(56) Qiu, M.; Fang, Z.; Li, Y.; Zhu, J.; Huang, X.; Ding, K.; Chen, W.; Zhang, Y. First-Principles Investigation of the Activation of CO2 Molecule on TM/Cu (TM=Fe, Co and Ni) Surface Alloys. *Appl. Surf. Sci.* **2015**, *353*, 902–912. https://doi.org/10.1016/j.apsusc.2015.06.165.

(57) Perilli, D.; Chesnyak, V.; Ugolotti, A.; Panighel, M.; Vigneri, S.; Armillotta, F.; Naderasli, P.; Stredansky, M.; Schied, M.; Lacovig, P.; Lizzit, S.; Cepek, C.; Comelli, G.; Brune, H.; Africh, C.; Di Valentin, C. CO Adsorption on a Single-Atom Catalyst Stably Embedded in Graphene. *Angew. Chem. Int. Ed.* **2025**, *64* (11). https://doi.org/10.1002/anie.202421757.

(58) Wang, S.-G.; Liao, X.-Y.; Cao, D.-B.; Huo, C.-F.; Li, Y.-W.; Wang, J.; Jiao, H. Factors Controlling the Interaction of CO_2 with Transition Metal Surfaces. *The Journal of Physical Chemistry C* **2007**, *111* (45), 16934–16940. https://doi.org/10.1021/jp074570y.

(59) Paparo, A.; Okuda, J. Carbon Dioxide Complexes: Bonding Modes and Synthetic Methods. *Coord. Chem. Rev.* **2017**, *334*, 136–149. https://doi.org/10.1016/j.ccr.2016.06.005.

(60) Wei, J.; Ge, Q.; Yao, R.; Wen, Z.; Fang, C.; Guo, L.; Xu, H.; Sun, J. Directly Converting CO2 into a Gasoline Fuel. *Nat. Commun.* **2017**, *8*. https://doi.org/10.1038/ncomms15174.

(61) Xie, J.; Olsbye, U. The Oxygenate-Mediated Conversion of CO_x to Hydrocarbons─On the Role of Zeolites in Tandem Catalysis. *Chem. Rev.* **2023**, *123* (20), 11775–11816. https://doi.org/10.1021/acs.chemrev.3c00058.

(62) Sun, J.; Wang, Y. Recent Advances in Catalytic Conversion of Ethanol to Chemicals. *ACS Catal.* **2014**, *4* (4), 1078–1090. https://doi.org/10.1021/cs4011343.

(63) Schulz, H. Short History and Present Trends of Fischer–Tropsch Synthesis. *Appl. Catal. A Gen.* **1999**, *186* (1–2), 3–12. https://doi.org/10.1016/S0926-860X(99)00160-X.

(64) Casci, J. L.; Lok, C. M.; Shannon, M. D. Fischer–Tropsch Catalysis: The Basis for an Emerging Industry with Origins in the Early 20th Century. *Catal. Today* **2009**, *145* (1–2), 38–44. https://doi.org/10.1016/j.cattod.2008.08.032.

(65) James, O. O.; Chowdhury, B.; Mesubi, M. A.; Maity, S. Reflections on the Chemistry of the Fischer–Tropsch Synthesis. *RSC Adv.* **2012**, *2* (19), 7347. https://doi.org/10.1039/c2ra20519j.

(66) Okonye, L. U.; Yao, Y.; Hildebrandt, D.; Meijboom, R. Contributing to Energy Sustainability: A Review of Mesoporous Material Supported Catalysts for Fischer–Tropsch Synthesis. *Sustain. Energy Fuels* **2021**, *5* (1), 79–107. https://doi.org/10.1039/D0SE01442G.

(67) Meurer, A.; Kern, J. Fischer–Tropsch Synthesis as the Key for Decentralized Sustainable Kerosene Production. *Energies (Basel).* **2021**, *14* (7), 1836. https://doi.org/10.3390/en14071836.

(68) Kuei, C. K.; Lee, J. F.; Lee, M. D. The Promoter Effect of Alkali Metal to Supported Iron Catalyst in Carbon Monoxide Hydrogenation, the Influence of Alkali on Carbon Depositions. *Chem. Eng. Commun.* **1991**, *101* (1), 77–92. https://doi.org/10.1080/00986449108911603.

(69) Dragomir, S.; Bukur, B.; Mukesh, D.; Patel, S. A. *Promoter Effects on Precipitated Iron Catalysts for Fischer-Tropsch*; 1990; Vol. 29. https://pubs.acs.org/sharingguidelines.

(70) Uner, D. O. *A Sensible Mechanism of Alkali Promotion in Fischer-Tropsch Synthesis: Adsorbate Mobilities*; 1998. https://pubs.acs.org/sharingguidelines.

(71) Li, J.; Cheng, X.; Zhang, C.; Wang, J.; Dong, W.; Yang, Y.; Li, Y. Alkalis in Iron-based Fischer–Tropsch Synthesis Catalysts: Distribution, Migration and Promotion. *Journal of Chemical Technology & Biotechnology* **2017**, *92* (6), 1472–1480. https://doi.org/10.1002/jctb.5152.

(72) Li, J.; Cheng, X.; Zhang, C.; Chang, Q.; Wang, J.; Wang, X.; Lv, Z.; Dong, W.; Yang, Y.; Li, Y. Effect of Alkalis on Iron-Based Fischer-Tropsch Synthesis Catalysts: Alkali-FeOx Interaction, Reduction, and Catalytic Performance. *Appl. Catal. A Gen.* **2016**, *528*, 131–141. https://doi.org/10.1016/j.apcata.2016.10.006.

(73) Ding, M.; Tu, J.; Qiu, M.; Wang, T.; Ma, L.; Li, Y. Impact of Potassium Promoter on Cu–Fe Based Mixed Alcohols Synthesis Catalyst. *Appl. Energy* **2015**, *138*, 584–589. https://doi.org/10.1016/j.apenergy.2014.01.010.

(74) Woo, H. C.; Nam, I. S.; Lee, J. S.; Chung, J. S.; Kim, Y. G. Structure and Distribution of Alkali Promoter in K/MoS2 Catalysts and Their Effects on Alcohol Synthesis from Syngas. *J. Catal.* **1993**, *142* (2), 672–690. https://doi.org/10.1006/jcat.1993.1240.

(75) Tienthao, N.; Hassanzahediniaki, M.; Alamdari, H.; Kaliaguine, S. Effect of Alkali Additives over Nanocrystalline Co–Cu-Based Perovskites as Catalysts for Higher-Alcohol Synthesis. *J. Catal.* **2007**, *245* (2), 348–357. https://doi.org/10.1016/j.jcat.2006.10.026.

(76) Ding, M.; Ma, L.; Zhang, Q.; Wang, C.; Zhang, W.; Wang, T. Enhancement of Conversion from Bio-Syngas to Higher Alcohols Fuels over K-Promoted Cu-Fe Bimodal Pore Catalysts. *Fuel Processing Technology* **2017**, *159*, 436–441. https://doi.org/10.1016/j.fuproc.2017.02.010.

(77) Pan, Y.; Ding, X.; Zhang, C.; Zhu, M.; Yang, Z.; Han, Y. F. Effects of Different Reductive Agents on Zn-Promoted Iron Oxide Phases in the CO2–Fischer–Tropsch to Linear α-Olefins. *Catalysts* **2023**, *13* (3). https://doi.org/10.3390/catal13030594.

(78) Zhang, C.; Xu, M.; Yang, Z.; Zhu, M.; Gao, J.; Han, Y. F. Uncovering the Electronic Effects of Zinc on the Structure of Fe5C2-ZnO Catalysts for CO2 Hydrogenation to Linear α-Olefins. *Appl. Catal. B* **2021**, *295*. https://doi.org/10.1016/j.apcatb.2021.120287.

(79) Han, J.; Liu, W.; Zhang, L.; Ren, H.; Wu, C.; Zhang, J.; Gong, C.; Yang, G.; Yang, H.; Zhang, S.; Wang, H.; Ji, T.; Li, J.; Gao, P. Highly Efficient CO2 Hydrogenation to Linear α-Olefins on FeZnK Catalysts with Balanced Zn-O-Fe Interfaces and Fe5C2 Species. *ACS Catal.* **2025**, 3940–3954. https://doi.org/10.1021/acscatal.4c07784.

(80) Zhai, P.; Xu, C.; Gao, R.; Liu, X.; Li, M.; Li, W.; Fu, X.; Jia, C.; Xie, J.; Zhao, M.; Wang, X.; Li, Y.; Zhang, Q.; Wen, X.; Ma, D. Highly Tunable Selectivity for Syngas-Derived Alkenes over Zinc and Sodium-Modulated Fe_5C_2 Catalyst. *Angew. Chem. Int. Ed.* **2016**, *55* (34), 9902–9907. https://doi.org/10.1002/anie.201603556.

(81) Xu, D.; Ding, M.; Hong, X.; Liu, G. Mechanistic Aspects of the Role of K Promotion on Cu–Fe-Based Catalysts for Higher Alcohol Synthesis from CO_2 Hydrogenation. *ACS Catal.* **2020**, *10* (24), 14516–14526. https://doi.org/10.1021/acscatal.0c03575.

(82) Xu, D.; Ding, M.; Hong, X.; Liu, G.; Tsang, S. C. E. Selective C_{2+} Alcohol Synthesis from Direct CO_2 Hydrogenation over a Cs-Promoted Cu-Fe-Zn Catalyst. *ACS Catal.* **2020**, *10* (9), 5250–5260. https://doi.org/10.1021/acscatal.0c01184.

(83) Wang, Y.; Xu, D.; Zhang, X.; Hong, X.; Liu, G. Selective C_{2+} Alcohol Synthesis by CO_2 Hydrogenation *via* a Reaction-Coupling Strategy. *Catal. Sci. Technol.* **2022**, *12* (5), 1539–1550. https://doi.org/10.1039/D1CY02196F.

(84) Li, S.; Guo, H.; Luo, C.; Zhang, H.; Xiong, L.; Chen, X.; Ma, L. Effect of Iron Promoter on Structure and Performance of K/Cu-Zn Catalyst for Higher Alcohols Synthesis from CO 2 Hydrogenation. https://doi.org/10.1007/s10562-013-0977-7.

(85) Lyu, S.; Wang, L.; Li, Z.; Yin, S.; Chen, J.; Zhang, Y.; Li, J.; Wang, Y. Stabilization of ε-Iron Carbide as High-Temperature Catalyst under Realistic Fischer–Tropsch Synthesis Conditions. *Nat. Commun.* **2020**, *11* (1), 6219. https://doi.org/10.1038/s41467-020-20068-5.

(86) Wezendonk, T. A.; Sun, X.; Dugulan, A. I.; van Hoof, A. J. F.; Hensen, E. J. M.; Kapteijn, F.; Gascon, J. Controlled Formation of Iron Carbides and Their Performance in Fischer-Tropsch Synthesis. *J. Catal.* **2018**, *362*, 106–117. https://doi.org/10.1016/j.jcat.2018.03.034.

(87) Lu, F.; Chen, X.; Lei, Z.; Wen, L.; Zhang, Y. Revealing the Activity of Different Iron Carbides for Fischer-Tropsch Synthesis. *Appl. Catal. B* **2021**, *281*, 119521. https://doi.org/10.1016/j.apcatb.2020.119521.

(88) Xu, K.; Sun, B.; Lin, J.; Wen, W.; Pei, Y.; Yan, S.; Qiao, M.; Zhang, X.; Zong, B. ε-Iron Carbide as a Low-Temperature Fischer–Tropsch Synthesis Catalyst. *Nat. Commun.* **2014**, *5* (1), 5783. https://doi.org/10.1038/ncomms6783.

(89) Zhao, H.; Liu, J.-X.; Yang, C.; Yao, S.; Su, H.-Y.; Gao, Z.; Dong, M.; Wang, J.; Rykov, A. I.; Wang, J.; Hou, Y.; Li, W.-X.; Ma, D. Synthesis of Iron-Carbide Nanoparticles: Identification of the Active Phase and Mechanism of Fe-Based Fischer–Tropsch Synthesis. *CCS Chemistry* **2021**, *3* (11), 2712–2724. https://doi.org/10.31635/ccschem.020.202000555.

(90) de Smit, E.; Cinquini, F.; Beale, A. M.; Safonova, O. V.; van Beek, W.; Sautet, P.; Weckhuysen, B. M. Stability and Reactivity of ε−χ−θ Iron Carbide Catalyst Phases in Fischer−Tropsch Synthesis: Controlling μ_C. *J. Am. Chem. Soc.* **2010**, *132* (42), 14928–14941. https://doi.org/10.1021/ja105853q.

(91) Ordomsky, V. V.; Legras, B.; Cheng, K.; Paul, S.; Khodakov, A. Y. The Role of Carbon Atoms of Supported Iron Carbides in Fischer–Tropsch Synthesis. *Catal. Sci. Technol.* **2015**, *5* (3), 1433–1437. https://doi.org/10.1039/C4CY01631A.

(92) Li, Y.; Li, Z.; Ahsen, A.; Lammich, L.; Mannie, G. J. A.; Niemantsverdriet, J. W. H.; Lauritsen, J. V. Atomically Defined Iron Carbide Surface for Fischer–Tropsch Synthesis Catalysis. *ACS Catal.* **2019**, *9* (2), 1264–1273. https://doi.org/10.1021/acscatal.8b03684.

(93) Liu, X.-W.; Cao, Z.; Zhao, S.; Gao, R.; Meng, Y.; Zhu, J.-X.; Rogers, C.; Huo, C.-F.; Yang, Y.; Li, Y.-W.; Wen, X.-D. Iron Carbides in Fischer–Tropsch Synthesis: Theoretical and Experimental Understanding in Epsilon-Iron Carbide Phase Assignment. *The Journal of Physical Chemistry C* **2017**, *121* (39), 21390–21396. https://doi.org/10.1021/acs.jpcc.7b06104.

(94) Yang, Y.; Zhang, H.; Ma, H.; Qian, W.; Sun, Q.; Ying, W. Effect of Alkalis (Li, Na, and K) on Precipitated Iron-Based Catalysts for High-Temperature Fischer-Tropsch Synthesis. *Fuel* **2022**, *326*, 125090. https://doi.org/10.1016/j.fuel.2022.125090.

(95) Chang, Q.; Zhang, C.; Liu, C.; Wei, Y.; Cheruvathur, A. V.; Dugulan, A. I.; Niemantsverdriet, J. W.; Liu, X.; He, Y.; Qing, M.; Zheng, L.; Yun, Y.; Yang, Y.; Li, Y. Relationship between Iron Carbide Phases (ε-Fe_2C, Fe_7C_3, and χ-Fe_5C_2) and Catalytic Performances of Fe/SiO_2 Fischer–Tropsch Catalysts. *ACS Catal.* **2018**, *8* (4), 3304–3316. https://doi.org/10.1021/acscatal.7b04085.

(96) Guo, H.; Zhang, H.; Peng, F.; Yang, H.; Xiong, L.; Huang, C.; Wang, C.; Chen, X.; Ma, L. Mixed Alcohols Synthesis from Syngas over Activated Palygorskite Supported Cu–Fe–Co Based Catalysts. *Appl. Clay Sci.* **2015**, *111*, 83–89. https://doi.org/10.1016/j.clay.2015.03.009.

(97) Xu, J.; Wei, J.; Zhang, J.; Liu, N.; Ge, Q.; Sun, J. Precisely Synergistic Synthesis of Higher Alcohols from Syngas over Iron Carbides. *Chem Catalysis* **2023**, *3* (4). https://doi.org/10.1016/j.checat.2023.100584.

(98) Lohitharn, N.; Goodwin, J. G. Effect of K Promotion of Fe and FeMn Fischer–Tropsch Synthesis Catalysts: Analysis at the Site Level Using SSITKA. *J. Catal.* **2008**, *260* (1), 7–16. https://doi.org/10.1016/J.JCAT.2008.08.011.

(99) Santos, V. P.; Wezendonk, T. A.; Jaén, J. J. D.; Dugulan, A. I.; Nasalevich, M. A.; Islam, H.-U.; Chojecki, A.; Sartipi, S.; Sun, X.; Hakeem, A. A.; Koeken, A. C. J.; Ruitenbeek, M.; Davidian, T.; Meima, G. R.; Sankar, G.; Kapteijn, F.; Makkee, M.; Gascon, J. Metal Organic Framework-

Mediated Synthesis of Highly Active and Stable Fischer-Tropsch Catalysts. *Nat. Commun.* **2015**, *6* (1), 6451. https://doi.org/10.1038/ncomms7451.

(100) Meng, W.; Jong, B. C. A. de; Bovenkamp, H. van de; Boer, G.-J.; Leendert Bezemer, G.; Iulian Dugulan, A.; Xie, J. Selectivity Control between Reverse Water-Gas Shift and Fischer-Tropsch Synthesis in Carbon-Supported Iron-Based Catalysts for CO2 Hydrogenation. *Chemical Engineering Journal* **2024**, *489*, 151166. https://doi.org/10.1016/j.cej.2024.151166.

(101) de Smit, E.; Weckhuysen, B. M. The Renaissance of Iron-Based Fischer–Tropsch Synthesis: On the Multifaceted Catalyst Deactivation Behaviour. *Chem. Soc. Rev.* **2008**, *37* (12), 2758. https://doi.org/10.1039/b805427d.

(102) Claeys, M.; van Steen, E.; Botha, T.; Crous, R.; Ferreira, A.; Harilal, A.; Moodley, D. J.; Moodley, P.; du Plessis, E.; Visagie, J. L. Oxidation of Hägg Carbide during High-Temperature Fischer–Tropsch Synthesis: Size-Dependent Thermodynamics and *In Situ* Observations. *ACS Catal.* **2021**, *11* (22), 13866–13879. https://doi.org/10.1021/acscatal.1c03719.

(103) Ding, M.; Yang, Y.; Wu, B.; Li, Y.; Wang, T.; Ma, L. Study on Reduction and Carburization Behaviors of Iron Phases for Iron-Based Fischer–Tropsch Synthesis Catalyst. *Appl. Energy* **2015**, *160*, 982–989. https://doi.org/10.1016/j.apenergy.2014.12.042.

(104) Zhang, C.; Yang, Y.; Teng, B.; Li, T.; Zheng, H.; Xiang, H.; Li, Y. Study of an Iron-Manganese Fischer–Tropsch Synthesis Catalyst Promoted with Copper. *J. Catal.* **2006**, *237* (2), 405–415. https://doi.org/10.1016/j.jcat.2005.11.004.

(105) Zhu, J.; Wang, P.; Zhang, X.; Zhang, G.; Li, R.; Li, W.; Senftle, T. P.; Liu, W.; Wang, J.; Wang, Y.; Zhang, A.; Fu, Q.; Song, C.; Guo, X. *Dynamic Structural Evolution of Iron Catalysts Involving Competitive Oxidation and Carburization during CO 2 Hydrogenation*; 2022; Vol. 8. https://www.science.org.

(106) Jozwiak, W. K.; Kaczmarek, E.; Maniecki, T. P.; Ignaczak, W.; Maniukiewicz, W. Reduction Behavior of Iron Oxides in Hydrogen and Carbon Monoxide Atmospheres. *Appl. Catal. A Gen.* **2007**, *326* (1), 17–27. https://doi.org/10.1016/j.apcata.2007.03.021.

(107) Rommens, K. T.; Saeys, M. Molecular Views on Fischer–Tropsch Synthesis. *Chem. Rev.* **2023**, *123* (9), 5798–5858. https://doi.org/10.1021/acs.chemrev.2c00508.

(108) Sarkar, A.; Jacobs, G.; Ji, Y.; Hamdeh, H. H.; Davis, B. H. Fischer–Tropsch Synthesis: Characterization Rb Promoted Iron Catalyst. *Catal. Letters* **2008**, *121* (1–2), 1–11. https://doi.org/10.1007/s10562-007-9288-1.

(109) Ma, Z.; Ma, H.; Zhang, H.; Wu, X.; Qian, W.; Sun, Q.; Ying, W. Direct Conversion of Syngas to Light Olefins through Fischer–Tropsch Synthesis over Fe–Zr Catalysts Modified with Sodium. *ACS Omega* **2021**, *6* (7), 4968–4976. https://doi.org/10.1021/acsomega.0c06008.

(110) Kazansky, V. B.; Zaitsev, A. V.; Borovkov, V. Yu.; Lapidus, A. L. Infrared Diffuse Reflectance Study of Alkali Promoted Iron/Alumina and Cobalt/Alumina Fischer-Tropsch Catalysts Prepared by Decomposition of Carbonyls. *Appl. Catal.* **1988**, *40*, 17–25. https://doi.org/10.1016/S0166-9834(00)80422-4.

(111) Cornaro, U.; Rossini, S.; Montanari, T.; Finocchio, E.; Busca, G. K-Doping of Co/Al2O3 Low Temperature Fischer–Tropsch Catalysts. *Catal. Today* **2012**, *197* (1), 101–108. https://doi.org/10.1016/j.cattod.2012.07.005.

(112) Varvoutis, G.; Lykaki, M.; Papista, E.; Carabineiro, S. A. C.; Psarras, A. C.; Marnellos, G. E.; Konsolakis, M. Effect of Alkali (Cs) Doping on the Surface Chemistry and CO2 Hydrogenation Performance of CuO/CeO2 Catalysts. *Journal of CO2 Utilization* **2021**, *44*, 101408. https://doi.org/10.1016/j.jcou.2020.101408.

(113) Liotta, L. F.; Martin, G. A.; Deganello, G. The Influence of Alkali Metal Ions in the Chemisorption of CO and CO2on Supported Palladium Catalysts: A Fourier Transform Infrared Spectroscopic Study. *J. Catal.* **1996**, *164* (2), 322–333. https://doi.org/10.1006/jcat.1996.0388.

(114) Gartunkel, E. L.; Crowell, J. E.; Somorjai, G. A. *The Strong Influence of Potassium on the Adsorption of CO on Platinum Surfaces. A Thermal Desorption Spectroscopy and High-Resolution Electron Energy Loss Spectroscopy Study*; 1982; Vol. 86. https://pubs.acs.org/sharingguidelines.

(115) Yang, N.; Liu, X.; Asundi, A. S.; Nørskov, J. K.; Bent, S. F. The Role of Sodium in Tuning Product Distribution in Syngas Conversion by Rh Catalysts. *Catal. Letters* **2018**, *148* (1), 289–297. https://doi.org/10.1007/s10562-017-2223-1.

(116) Wu, W.; Luo, J.; Zhao, J.; Wang, M.; Luo, L.; Hu, S.; He, B.; Ma, C.; Li, H.; Zeng, J. Facet Sensitivity of Iron Carbides in Fischer-Tropsch Synthesis. *Nat. Commun.* **2024**, *15* (1), 6108. https://doi.org/10.1038/s41467-024-50544-1.

(117) Marinho, A. L. A.; Roussey, A.; Faucheux, V.; Benayad, A. Depth Resolving of Fe 2p Core-Level Photoemission during the CO2 Hydrogenation Reaction by Lab-Based Soft and Hard X-Ray Photoelectron Spectroscopy. *Appl. Surf. Sci.* **2024**, *672*, 160743. https://doi.org/10.1016/j.apsusc.2024.160743.

(118) Yoon, W.; Jo, H.; Ahmed, S.; Khan, M. K.; Irshad, M.; Lee, J.; Bibi, S. S.; Kim, J. Role of Alkali Metal in Maintaining Iron Integrity during Direct CO2 Hydrogenation. *Chemical Engineering Journal* **2024**, *495*, 153617. https://doi.org/10.1016/j.cej.2024.153617.

(119) Zhu, J.; Mu, M.; Liu, Y.; Zhang, M.; Zhang, G.; Cheng, Z.; Hang Yin, B.; Yip, A. C. K.; Song, C.; Guo, X. Unveiling the Promoting Effect of Potassium on the Structural Evolution of Iron Catalysts during CO2 Hydrogenation. *Chem. Eng. Sci.* **2023**, *282*, 119228. https://doi.org/10.1016/j.ces.2023.119228.

(120) Sun, K.; Gao, X.; Bai, Y.; Tan, M.; Yang, G.; Tan, Y. Synergetic Catalysis of Bimetallic Copper–Cobalt Nanosheets for Direct Synthesis of Ethanol and Higher Alcohols from Syngas. *Catal. Sci. Technol.* **2018**, *8* (15), 3936–3947. https://doi.org/10.1039/C8CY01074A.

(121) Kowalik, P.; Próchniak, W.; Borowiecki, T. The Effect of Alkali Metals Doping on Properties of Cu/ZnO/Al2O3 Catalyst for Water Gas Shift. *Catal. Today* **2011**, *176* (1), 144–148. https://doi.org/10.1016/j.cattod.2011.01.028.

(122) Li, H.; Chen, T.; Wang, G. The Effect of Alkali Metals Doping on Properties of CuMgCe for Isobutanol Synthesis from Syngas. *Appl. Catal. A Gen.* **2022**, *639*, 118607. https://doi.org/10.1016/j.apcata.2022.118607.

(123) Nørskov, J. K.; Bligaard, T.; Hvolbæk, B.; Abild-Pedersen, F.; Chorkendorff, I.; Christensen, C. H. The Nature of the Active Site in Heterogeneous Metal Catalysis. *Chem. Soc. Rev.* **2008**, *37* (10), 2163. https://doi.org/10.1039/b800260f.

(124) Hutu, A.-I.; Pervolarakis, E.; Remediakis, I. N.; Kristoffersen, H. H.; Rossmeisl, J. Scaling Relations on High-Entropy Alloy Catalyst Surfaces. *The Journal of Physical Chemistry C* **2024**, *128* (25), 10251–10258. https://doi.org/10.1021/acs.jpcc.4c01292.

(125) Medford, A. J.; Vojvodic, A.; Hummelshøj, J. S.; Voss, J.; Abild-Pedersen, F.; Studt, F.; Bligaard, T.; Nilsson, A.; Nørskov, J. K. From the Sabatier Principle to a Predictive Theory of Transition-Metal Heterogeneous Catalysis. *J. Catal.* **2015**, *328*, 36–42. https://doi.org/10.1016/j.jcat.2014.12.033.

(126) Liu, X.; Zhang, C.; Tian, P.; Xu, M.; Cao, C.; Yang, Z.; Zhu, M.; Xu, J. Revealing the Effect of Sodium on Iron-Based Catalysts for CO_2 Hydrogenation: Insights from Calculation and Experiment. *The Journal of Physical Chemistry C* **2021**, *125* (14), 7637–7646. https://doi.org/10.1021/acs.jpcc.0c11123.

(127) Zhong, L.; Hu, Q.; Li, C.; Ding, J.; Zhang, C.; Wan, H.; Wang, L.; Guan, G. Structural Regulation of Modified Fe_3O_4 Microspheres for Enhanced Synthesis of Linear α-Olefins by CO_2 Hydrogenation. *ACS Sustain. Chem. Eng.* **2025**, *13* (25), 9740–9752. https://doi.org/10.1021/acssuschemeng.5c02474.

(128) Cui, D.; Qin, T.; Lin, T.; Ti, J.; An, Y.; Zhong, L. K-Promoted Ru-Based Heterogeneous Catalysts for Ethylene Hydroformylation. *Chemical Engineering Journal* **2024**, *484*, 149419. https://doi.org/10.1016/j.cej.2024.149419.

(129) Orege, J. I.; Liu, N.; Amoo, C. C.; Wei, J.; Ge, Q.; Sun, J. Boosting CO2 Hydrogenation to High-Value Olefins with Highly Stable Performance over Ba and Na Co-Modified Fe Catalyst. *Journal of Energy Chemistry* **2023**, *80*, 614–624. https://doi.org/10.1016/j.jechem.2023.02.007.

(130) Orege, J. I.; Wei, J.; Han, Y.; Yang, M.; Sun, X.; Zhang, J.; Amoo, C. C.; Ge, Q.; Sun, J. Highly Stable Sr and Na Co-Decorated Fe Catalyst for High-Valued Olefin Synthesis from CO2 Hydrogenation. *Appl. Catal. B* **2022**, *316*, 121640. https://doi.org/10.1016/j.apcatb.2022.121640.

(131) Wang, R.; Chen, Y.; Shang, X.; Liang, B.; Zhang, X.; Zhuo, H.; Duan, H.; Li, X.; Yang, X.; Su, X.; Huang, Y.; Zhang, T. Reversing the Selectivity of Alkanes and Alkenes in Iron-Based Fischer–Tropsch Synthesis: The Precise Control and Fundamental Role of Sodium Promotor. *ACS Catal.* **2024**, *14* (14), 11121–11130. https://doi.org/10.1021/acscatal.4c02252.

(132) Paladino Lino, A. V.; Vieira, L. H.; Assaf, E. M.; Assaf, J. M. Effects of the Potassium Incorporation in Fe–Ce–Zr Based Catalysts and Activation Condition in CO2 Hydrogenation to C2/C3 Olefins at Atmospheric Pressure. *Int. J. Hydrogen Energy* **2024**, *51*, 1122–1140. https://doi.org/10.1016/j.ijhydene.2023.09.126.

(133) Zhang, Q.; Wang, S.; Shi, X.; Dong, M.; Chen, J.; Zhang, J.; Wang, J.; Fan, W. Conversion of CO2 to Higher Alcohols on K-CuZnAl/Zr-CuFe Composite. *Applied Catalysis B: Environment and Energy* **2024**, *346*, 123748. https://doi.org/10.1016/j.apcatb.2024.123748.

(134) Xu, J.; Wei, J.; Zhang, J.; Yao, R.; Ge, Q.; Ma, Q.; Sun, J. Highly Selective Production of Long-Chain Aldehydes, Ketones or Alcohols via Syngas at a Mild Condition. *Applied Catalysis B: Environment and Energy* **2022**, *307*, 121155. https://doi.org/10.1016/j.apcatb.2022.121155.

(135) Zhang, Z.; Yin, H.; Yu, G.; He, S.; Kang, J.; Liu, Z.; Cheng, K.; Zhang, Q.; Wang, Y. Selective Hydrogenation of CO2 and CO into Olefins over Sodium- and Zinc-Promoted Iron Carbide Catalysts. *J. Catal.* **2021**, *395*, 350–361. https://doi.org/10.1016/j.jcat.2021.01.036.

(136) Lu, X.; Tan, K. B.; Zhao, J.; Zhan, G. Advances in Integrated Catalysts for CO2 Thermal Hydrogenation to Multicarbon Products. *Chem Catalysis*. Cell Press March 20, 2025. https://doi.org/10.1016/j.checat.2025.101264.

(137) Wei, J.; Yao, R.; Han, Y.; Ge, Q.; Sun, J. Towards the Development of the Emerging Process of CO_2 Heterogenous Hydrogenation into High-Value Unsaturated Heavy Hydrocarbons. *Chem. Soc. Rev.* **2021**, *50* (19), 10764–10805. https://doi.org/10.1039/D1CS00260K.

(138) Vasconcelos, A. A.; Len, T.; de Oliveira, A. de N.; Costa, A. A. F. da; Souza, A. R. da S.; Costa, C. E. F. da; Luque, R.; Rocha Filho, G. N. da; Noronha, R. C. R.; Nascimento, L. A. S. do. Zeolites: A Theoretical and Practical Approach with Uses in (Bio)Chemical Processes. *Applied Sciences* **2023**, *13* (3), 1897. https://doi.org/10.3390/app13031897.

(139) Campanile, A.; Liguori, B.; Ferone, C.; Caputo, D.; Aprea, P. Zeolite-Based Monoliths for Water Softening by Ion Exchange/Precipitation Process. *Sci. Rep.* **2022**, *12* (1), 3686. https://doi.org/10.1038/s41598-022-07679-2.

(140) Tsai, W.-T.; Hsien, K.-J.; Hsu, H.-C. Adsorption of Organic Compounds from Aqueous Solution onto the Synthesized Zeolite. *J. Hazard. Mater.* **2009**, *166* (2–3), 635–641. https://doi.org/10.1016/j.jhazmat.2008.11.071.

(141) Yeritsyan, H.; Sahakyan, A.; Harutyunyan, V.; Nikoghosyan, S.; Hakhverdyan, E.; Grigoryan, N.; Hovhannisyan, A.; Atoyan, V.; Keheyan, Y.; Rhodes, C. Radiation-Modified Natural Zeolites for Cleaning Liquid Nuclear Waste (Irradiation against Radioactivity). *Sci. Rep.* **2013**, *3* (1), 2900. https://doi.org/10.1038/srep02900.

(142) Yue, B.; Liu, S.; Chai, Y.; Wu, G.; Guan, N.; Li, L. Zeolites for Separation: Fundamental and Application. *Journal of Energy Chemistry* **2022**, *71*, 288–303. https://doi.org/10.1016/j.jechem.2022.03.035.

(143) Luzanova, V. D.; Rozhmanova, N. B.; Lanin, S. N.; Nesterenko, P. N. Application of Zeolites in High-Performance Liquid Chromatography. *Journal of Analytical Chemistry* **2024**, *79* (10), 1353–1363. https://doi.org/10.1134/S1061934824700722.

(144) Kumar, S.; Srivastava, R.; Koh, J. Utilization of Zeolites as CO2 Capturing Agents: Advances and Future Perspectives. *Journal of CO2 Utilization* **2020**, *41*, 101251. https://doi.org/10.1016/j.jcou.2020.101251.

(145) Li, H.-X.; Donohue, J. M.; Chrmier, W. E.; Chu, Y. F. Application of Zeolites as Hydrocarbon Traps in Automotive Emission Controls; 2005; pp 1375–1382. https://doi.org/10.1016/S0167-2991(05)80487-2.

(146) Leman, A. M.; Jajuli, A.; Feriyanto, D.; Rahman, F.; Zakaria, S. Advanced Catalytic Converter in Gasoline Enginer Emission Control: A Review. *MATEC Web of Conferences* **2017**, *87*, 02020. https://doi.org/10.1051/matecconf/20178702020.

(147) Nakhli, S. A. A.; Delkash, M.; Bakhshayesh, B. E.; Kazemian, H. Application of Zeolites for Sustainable Agriculture: A Review on Water and Nutrient Retention. *Water Air Soil Pollut.* **2017**, *228* (12), 464. https://doi.org/10.1007/s11270-017-3649-1.

(148) Derakhshankhah, H.; Jafari, S.; Sarvari, S.; Barzegari, E.; Moakedi, F.; Ghorbani, M.; Shiri Varnamkhasti, B.; Jaymand, M.; Izadi, Z.; Tayebi, L. Biomedical Applications of Zeolitic Nanoparticles, with an Emphasis on Medical Interventions. *Int. J. Nanomedicine* **2020**, *Volume 15*, 363–386. https://doi.org/10.2147/IJN.S234573.

(149) Parsafard, N.; Shakor, Z. M. Advancements in Zeolite-Based Catalysts for the Isomerization of n-Alkanes: Mechanistic Insights and Future Directions. *Discover Applied Sciences* **2025**, *7* (5), 415. https://doi.org/10.1007/s42452-025-06842-4.

(150) Wei, L.; Wang, H.; Dong, Q.; Li, Y.; Xiang, H. A Review on the Research Progress of Zeolite Catalysts for Heavy Oil Cracking. *Catalysts* **2025**, *15* (4), 401. https://doi.org/10.3390/catal15040401.

(151) Research Nester. *Refinery Catalyst Marker-Historic Data (2019-2024), Global Trends 2025, Growth Forecasts 2037*; 2025. https://www.researchandmarkets.com/reports/5939379/refinery-catalyst-global-market-report?srsltid=AfmBOopx2CzE1yCR6A6TdRMJ3iqQS7KmZM2GvtQenPH6bgsKy3zKxGBe#product--summary (accessed 2025-12-30).

(152) Li, Y.; Yu, J. New Stories of Zeolite Structures: Their Descriptions, Determinations, Predictions, and Evaluations. *Chemical Reviews*. July 23, 2014, pp 7268–7316. https://doi.org/10.1021/cr500010r.

(153) Edañol, Y. D. G.; Usman, K. A. S.; Buenviaje, S. Jr. C.; Mantua, M. E.; Payawan, L. Jr. M. Utilizing Silica from Rice Hull for the Hydrothermal Synthesis of Zeolite Y. *KIMIKA* **2018**, *29* (1), 17–21. https://doi.org/10.26534/kimika.v29i1.17-21.

(154) Inchaurrondo, N. S.; Font, J. Clay, Zeolite and Oxide Minerals: Natural Catalytic Materials for the Ozonation of Organic Pollutants. *Molecules* **2022**, *27* (7), 2151. https://doi.org/10.3390/molecules27072151.

(155) Structure Commission of the International Zeolite Association. *IZA Structure Database*. https://www.iza-structure.org/ (accessed 2025-08-28).

(156) Cundy, C. S.; Cox, P. A. The Hydrothermal Synthesis of Zeolites: History and Development from the Earliest Days to the Present Time. *Chem. Rev.* **2003**, *103* (3), 663–702. https://doi.org/10.1021/cr020060i.

(157) Grand, J.; Awala, H.; Mintova, S. Mechanism of Zeolites Crystal Growth: New Findings and Open Questions. *CrystEngComm* **2016**, *18* (5), 650–664. https://doi.org/10.1039/C5CE02286J.

(158) Al-Nahari, S.; Dib, E.; Cammarano, C.; Saint-Germes, E.; Massiot, D.; Sarou-Kanian, V.; Alonso, B. Impact of Mineralizing Agents on Aluminum Distribution and Acidity of ZSM-5 Zeolites. *Angew. Chem. Int. Ed.* **2023**, *62* (7). https://doi.org/10.1002/anie.202217992.

(159) Kordala, N.; Wyszkowski, M. Zeolite Properties, Methods of Synthesis, and Selected Applications. *Molecules* **2024**, *29* (5), 1069. https://doi.org/10.3390/molecules29051069.

(160) Bregante, D. T.; Potts, D. S.; Kwon, O.; Ayla, E. Z.; Tan, J. Z.; Flaherty, D. W. Effects of Hydrofluoric Acid Concentration on the Density of Silanol Groups and Water Adsorption in Hydrothermally Synthesized Transition-Metal-Substituted Silicalite-1. *Chemistry of Materials* **2020**, *32* (17), 7425–7437. https://doi.org/10.1021/acs.chemmater.0c02405.

(161) Shah, M. A.; Nagornyy, T.; Aiwekhoe, S. E.; Hong, S.; Huy Tran, N. H.; Luo, S.; Chen, Z.; Auerbach, S. M.; Fan, W. Rapid Crystallization of Zeolites with Controllable Defects: Disentangling Fluoride Concentration and PH Using NH4F. *Cryst. Growth Des.* **2025**, *25* (6), 1821–1832. https://doi.org/10.1021/acs.cgd.4c01613.

(162) Oleksiak, M. D.; Rimer, J. D. Synthesis of Zeolites in the Absence of Organic Structure-Directing Agents: Factors Governing Crystal Selection and Polymorphism. *Reviews in Chemical Engineering* **2014**, *30* (1), 1–49. https://doi.org/10.1515/revce-2013-0020.

(163) Kim, Y.; Kim, K.; Ryoo, R. Cooperative Structure Direction of Diammonium Surfactants and Sodium Ions to Generate MFI Zeolite Nanocrystals of Controlled Thickness. *Chemistry of Materials* **2017**, *29* (4), 1752–1757. https://doi.org/10.1021/acs.chemmater.6b05338.

(164) Hijazi, N.; Bavykina, A.; Yarulina, I.; Shoinkhorova, T.; Ramos-Fernandez, E. V.; Gascon, J. Chemical Engineering of Zeolites: Alleviating Transport Limitations through Hierarchical Design and Shaping. *Chem. Soc. Rev.* **2025**, *54* (13), 6335–6384. https://doi.org/10.1039/D5CS00169B.

(165) van den Bergh, J.; Ban, S.; Vlugt, T. J. H.; Kapteijn, F. Diffusion in Zeolites: Extension of the Relevant Site Model to Light Gases and Mixtures Thereof in Zeolites DDR, CHA, MFI and FAU. *Sep. Purif. Technol.* **2010**, *73* (2), 151–163. https://doi.org/10.1016/j.seppur.2010.03.018.

(166) Gobin, O. C.; Reitmeier, S. J.; Jentys, A.; Lercher, J. A. Diffusion Pathways of Benzene, Toluene and p-Xylene in MFI. *Microporous and Mesoporous Materials* **2009**, *125* (1–2), 3–10. https://doi.org/10.1016/j.micromeso.2009.01.025.

(167) Miyamoto, M.; Iwatsuka, H.; Oumi, Y.; Uemiya, S.; Van den Perre, S.; Baron, G. V.; Denayer, J. F. M. Effect of Core-Shell Structuring of Chabazite Zeolite with a Siliceous Zeolite Thin Layer on the Separation of Acetone-Butanol-Ethanol Vapor in Humid Vapor Conditions. *Chemical Engineering Journal* **2019**, *363*, 292–299. https://doi.org/10.1016/j.cej.2019.01.106.

(168) Lanzafame, P.; Barbera, K.; Perathoner, S.; Centi, G.; Aloise, A.; Migliori, M.; Macario, A.; Nagy, J. B.; Giordano, G. The Role of Acid Sites Induced by Defects in the Etherification of HMF on Silicalite-1 Catalysts. *J. Catal.* **2015**, *330*, 558–568. https://doi.org/10.1016/j.jcat.2015.07.028.

(169) Janiszewska, E.; Macario, A.; Wilk, J.; Aloise, A.; Kowalak, S.; Nagy, J. B.; Giordano, G. The Role of the Defect Groups on the Silicalite-1 Zeolite Catalytic Behavior. *Microporous and Mesoporous Materials* **2013**, *182*, 220–228. https://doi.org/10.1016/j.micromeso.2012.12.013.

(170) Kubota, S.; Sumi, T.; Kitamura, H.; Miyake, K.; Uchida, Y.; Nishiyama, N. Promoted Propane Dehydrogenation over Co Confined within Core–Shell Silicalite-1 Zeolite Crystals. *Catal. Sci. Technol.* **2024**, *14* (5), 1201–1208. https://doi.org/10.1039/D3CY01637D.

(171) Zieliński, M.; Kot, M.; Pietrowski, M.; Wojcieszak, R.; Kowalska-Kuś, J.; Janiszewska, E. Studies of New Iridium Catalysts Supported on Modified Silicalite-1—Their Structure and Hydrogenating Properties. *Materials* **2021**, *14* (16), 4465. https://doi.org/10.3390/ma14164465.

(172) Ji, Y.; Yang, H.; Yan, W. Strategies to Enhance the Catalytic Performance of ZSM-5 Zeolite in Hydrocarbon Cracking: A Review. *Catalysts*. MDPI December 1, 2017. https://doi.org/10.3390/catal7120367.

(173) Monama, W.; Mohiuddin, E.; Thangaraj, B.; Mdleleni, M. M.; Key, D. Oligomerization of Lower Olefins to Fuel Range Hydrocarbons over Texturally Enhanced ZSM-5 Catalyst. *Catal. Today* **2020**, *342*, 167–177. https://doi.org/10.1016/j.cattod.2019.02.061.

(174) Yashnik, S. A.; Surovtsova, T. A.; Salnikov, A. V.; Parmon, V. N. Leaching Stability and Redox Activity of Copper-MFI Zeolites Prepared by Solid-State Transformations: Comparison with Ion-Exchanged and Impregnated Samples. *Materials* **2023**, *16* (2), 671. https://doi.org/10.3390/ma16020671.

(175) Palčić, A.; Valtchev, V. Analysis and Control of Acid Sites in Zeolites. *Appl. Catal. A Gen.* **2020**, *606*, 117795. https://doi.org/10.1016/j.apcata.2020.117795.

(176) Joshi, S. S. .; Ranade, V. V. . *Industrial Catalytic Processes for Fine and Specialty Chemicals*; Elsevier, 2016.

(177) Derouane, E. G.; Védrine, J. C.; Pinto, R. R.; Borges, P. M.; Costa, L.; Lemos, M. A. N. D. A.; Lemos, F.; Ribeiro, F. R. The Acidity of Zeolites: Concepts, Measurements and Relation to Catalysis: A Review on Experimental and Theoretical Methods for the Study of Zeolite Acidity. *Catalysis Reviews* **2013**, *55* (4), 454–515. https://doi.org/10.1080/01614940.2013.822266.

(178) Weitkamp, J. Zeolites and Catalysis. *Solid State Ion.* **2000**, *131* (1–2), 175–188. https://doi.org/10.1016/S0167-2738(00)00632-9.

(179) Derouane, E. G. New Aspects of Molecular Shape-Selectivity: Catalysis by Zeolite ZSM - 5; 1980; pp 5–18. https://doi.org/10.1016/S0167-2991(08)64860-0.

(180) Unnikrishnan, P.; Srinivas, D. Heterogeneous Catalysis. In *Industrial Catalytic Processes for Fine and Specialty Chemicals*; Elsevier, 2016; pp 41–111. https://doi.org/10.1016/B978-0-12-801457-8.00003-3.

(181) Mériaudeau, P.; Tuan, Vu. A.; Lefebvre, F.; Nghiem, Vu. T.; Naccache, C. Isomorphous Substitution of Silicon in the AlPO4 Framework with AEL Structure: N-Octane Hydroconversion. *Microporous and Mesoporous Materials* **1998**, *22* (1–3), 435–449. https://doi.org/10.1016/S1387-1811(98)00095-X.

(182) Arora, S. S.; Nieskens, D. L. S.; Malek, A.; Bhan, A. Lifetime Improvement in Methanol-to-Olefins Catalysis over Chabazite Materials by High-Pressure H2 Co-Feeds. *Nat. Catal.* **2018**, *1* (9), 666–672. https://doi.org/10.1038/s41929-018-0125-2.

(183) Wu, X.; Wei, Y.; Liu, Z. Dynamic Catalytic Mechanism of the Methanol-to-Hydrocarbons Reaction over Zeolites. *Acc. Chem. Res.* **2023**, *56* (14), 2001–2014. https://doi.org/10.1021/acs.accounts.3c00187.

(184) Lin, S.; Wei, Y.; Liu, Z. Autocatalytic Induction Period in Zeolite-Catalyzed Methanol Conversion. *Chem Catalysis*. Cell Press May 18, 2023. https://doi.org/10.1016/j.checat.2023.100597.

(185) Yarulina, I.; Chowdhury, A. D.; Meirer, F.; Weckhuysen, B. M.; Gascon, J. Recent Trends and Fundamental Insights in the Methanol-to-Hydrocarbons Process. *Nat. Catal.* **2018**, *1* (6), 398–411. https://doi.org/10.1038/s41929-018-0078-5.

(186) Olson, D. H.; Kokotailo, G. T.; Lawton, S. L.; Meier, W. M. *Crystal Structure and Structure-Related Properties of ZSM-5*; 1981; Vol. 85. https://pubs.acs.org/sharingguidelines.

(187) Brogaard, R. Y.; Weckhuysen, B. M.; Nørskov, J. K. Guest–Host Interactions of Arenes in H-ZSM-5 and Their Impact on Methanol-to-Hydrocarbons Deactivation Processes. *J. Catal.* **2013**, *300*, 235–241. https://doi.org/10.1016/j.jcat.2013.01.009.

(188) Yan, Z.; Chen, D.; Huang, L.; Liu, J.; Fu, H.; Xiao, Y.; Li, S. A Theoretical Insight into Diffusion Mechanism of Benzene-Methanol Alkylation Reaction in ZSM-5 Zeolite. *Microporous and Mesoporous Materials* **2022**, *337*, 111926. https://doi.org/10.1016/j.micromeso.2022.111926.

(189) Li, C.; Vidal-Moya, A.; Miguel, P. J.; Dedecek, J.; Boronat, M.; Corma, A. Selective Introduction of Acid Sites in Different Confined Positions in ZSM-5 and Its Catalytic Implications. *ACS Catal.* **2018**, *8* (8), 7688–7697. https://doi.org/10.1021/acscatal.8b02112.

(190) Kirschhock, C. E. A.; Ravishankar, R.; Verspeurt, F.; Grobet, P. J.; Jacobs, P. A.; Martens, J. A. Identification of Precursor Species in the Formation of MFI Zeolite in the TPAOH−TEOS−H $_2$ O System. *J. Phys. Chem. B* **1999**, *103* (24), 4965–4971. https://doi.org/10.1021/jp990297r.

(191) Zhang, W.; Wang, X.; Wu, Z.; Li, Z.; Yong, X.; Gu, Y.; Wang, J. Controlling the Morphologies and Crystal Growth Orientations of H-ZSM-5: Their Impact on the Structure-Diffusion-Performance Relationship in the Methanol-to-Propylene Reaction. *Catal. Sci. Technol.* **2024**, *14* (7), 1760–1774. https://doi.org/10.1039/D3CY01558K.

(192) Liu, C.; Kong, D.; Guo, H. The Morphology Control of Zeolite ZSM-5 by Regulating the Polymerization Degree of Silicon and Aluminum Sources. *Microporous and Mesoporous Materials* **2014**, *193*, 61–68. https://doi.org/10.1016/j.micromeso.2014.03.015.

(193) Shi, J.; Zhao, G.; Teng, J.; Wang, Y.; Xie, Z. Morphology Control of ZSM-5 Zeolites and Their Application in Cracking Reaction of C4 Olefin. *Inorg. Chem. Front.* **2018**, *5* (11), 2734–2738. https://doi.org/10.1039/c8qi00686e.

(194) Yokoi, T.; Mochizuki, H.; Namba, S.; Kondo, J. N.; Tatsumi, T. Control of the Al Distribution in the Framework of ZSM-5 Zeolite and Its Evaluation by Solid-State NMR Technique and Catalytic Properties. *Journal of Physical Chemistry C* **2015**, *119* (27), 15303–15315. https://doi.org/10.1021/acs.jpcc.5b03289.

(195) Wang, C.; Chu, Y.; Zheng, A.; Xu, J.; Wang, Q.; Gao, P.; Qi, G.; Gong, Y.; Deng, F. New Insight into the Hydrocarbon-Pool Chemistry of the Methanol-to-Olefins Conversion over Zeolite H-ZSM-5 from GC-MS, Solid-State NMR Spectroscopy, and DFT Calculations. *Chemistry – A European Journal* **2014**, *20* (39), 12432–12443. https://doi.org/10.1002/chem.201403972.

(196) Niyaj, D. S.; Sapali, S. N. Performance Evaluation of a Domestic Refrigerator with a Thermal Storage Arrangement Using Propane as a Refrigerant. *Energy Procedia* **2017**, *109*, 34–39. https://doi.org/10.1016/j.egypro.2017.03.045.

(197) Payne, A.; Garcia-Garcia, G.; Styring, P. Production of Propane and Propene *via* Carbon Capture Utilisation: Comparison of Its Environmental and Economic Performance against Conventional Production Methods. *Green Chemistry* **2023**, *25* (10), 4029–4057. https://doi.org/10.1039/D2GC04721G.

(198) *Hydrocarbon gas liquids explained Uses of hydrocarbon gas liquids*. U.S. Energy Information Administration.

(199) Lok, C. M.; Van Doorn, J.; Aranda Almansa, G. Promoted ZSM-5 Catalysts for the Production of Bio-Aromatics, a Review. *Renewable and Sustainable Energy Reviews* **2019**, *113*, 109248. https://doi.org/10.1016/j.rser.2019.109248.

(200) Sharifi, K.; Halladj, R.; Royaee, S. J. An Overview on the Effects of Metal Promoters and Acidity of ZSM-5 in Performance of the Aromatization of Liquid Hydrocarbons. *Reviews on Advanced Materials Science* **2020**, *59* (1), 188–206. https://doi.org/10.1515/rams-2020-0037.

(201) Ono, Y.; Adachi, H.; Senoda, Y. Selective Conversion of Methanol into Aromatic Hydrocarbons over Zinc-Exchanged ZSM-5 Zeolites. *Journal of the Chemical Society, Faraday Transactions 1: Physical Chemistry in Condensed Phases* **1988**, *84* (4), 1091. https://doi.org/10.1039/f19888401091.

(202) Wang, S.; Li, Z.; Qin, Z.; Dong, M.; Li, J.; Fan, W.; Wang, J. Catalytic Roles of the Acid Sites in Different Pore Channels of H-ZSM-5 Zeolite for Methanol-to-Olefins Conversion. *Chinese Journal of Catalysis* **2021**, *42* (7), 1126–1136. https://doi.org/10.1016/S1872-2067(20)63732-9.

(203) Fu, D.; Lucini Paioni, A.; Lian, C.; van der Heijden, O.; Baldus, M.; Weckhuysen, B. M. Elucidating Zeolite Channel Geometry–Reaction Intermediate Relationships for the Methanol-to-Hydrocarbon Process. *Angew. Chem. Int. Ed.* **2020**, *59* (45), 20024–20030. https://doi.org/10.1002/anie.202009139.

(204) Fu, D.; Maris, J. J. E.; Stanciakova, K.; Nikolopoulos, N.; van der Heijden, O.; Mandemaker, L. D. B.; Siemons, M. E.; Salas Pastene, D.; Kapitein, L. C.; Rabouw, F. T.; Meirer, F.; Weckhuysen, B. M. Unravelling Channel Structure–Diffusivity Relationships in Zeolite ZSM-5 at the Single-Molecule Level. *Angew. Chem. Int. Ed.* **2022**, *61* (5). https://doi.org/10.1002/anie.202114388.

(205) Liu, J.; Yang, C.; Li, S.; Zhang, J.; Bu, X.; Wang, H.; Ji, T.; Li, J.; Chang, C.-R.; Shi, Y.; Liu, J.; Xu, Z.; Gao, P. Low-Temperature CO2 Hydrogenation to Aromatics over ZnZrO Integrated with Boron-Modified ZSM-5. *Applied Catalysis B: Environment and Energy* **2025**, *377*, 125523. https://doi.org/10.1016/j.apcatb.2025.125523.

(206) Shang, X.; Liu, G.; Su, X.; Huang, Y.; Zhang, T. Preferential Synthesis of Toluene and Xylene from CO_2 Hydrogenation in the Presence of Benzene through an Enhanced Coupling Reaction. *ACS Catal.* **2022**, *12* (21), 13741–13754. https://doi.org/10.1021/acscatal.2c04314.

(207) Park, H.; Park, S.; Kim, N. S.; Kim, Y. T.; Chae, H.-J.; Kim, J.-C.; Kim, T.-W. Tandem Catalysts of Metal-Modified ZSM-5 with Na-Promoted Zinc Ferrite for CO2 Hydrogenation to Aromatics. *Catal. Today* **2026**, *461*, 115505. https://doi.org/10.1016/j.cattod.2025.115505.

(208) Dai, C.; Zhao, X.; Hu, B.; Zhang, J.; Hao, Q.; Chen, H.; Guo, X.; Ma, X. Hydrogenation of CO_2 to Aromatics over Fe–K/Alkaline Al_2O_3 and P/ZSM-5 Tandem Catalysts. *Ind. Eng. Chem. Res.* **2020**, *59* (43), 19194–19202. https://doi.org/10.1021/acs.iecr.0c03598.

(209) Xing, S.; Turner, S.; Fu, D.; van Vreeswijk, S.; Liu, Y.; Xiao, J.; Oord, R.; Sann, J.; Weckhuysen, B. M. Silicalite-1 Layer Secures the Bifunctional Nature of a CO_2 Hydrogenation Catalyst. *JACS Au* **2023**, *3* (4), 1029–1038. https://doi.org/10.1021/jacsau.2c00621.

(210) Valecillos, J.; Elordi, G.; Aguayo, A. T.; Castaño, P. The Intrinsic Effect of Co-Feeding Water on the Formation of Active/Deactivating Species in the Methanol-to-Hydrocarbons Reaction on ZSM-5 Zeolite. *Catal. Sci. Technol.* **2021**, *11* (4), 1269–1281. https://doi.org/10.1039/D0CY02497J.

(211) Hughes, A. E.; Easton, C. D.; Gengenbach, T. R.; Biesinger, M. C.; Laleh, M. Interpretation of Complex X-Ray Photoelectron Peak Shapes. I. Case Study of Fe 2p3/2 Spectra. *Journal of Vacuum Science & Technology A* **2024**, *42* (5). https://doi.org/10.1116/6.0003804.

(212) Biesinger, M. C. Advanced Analysis of Copper X-ray Photoelectron Spectra. *Surface and Interface Analysis* **2017**, *49* (13), 1325–1334. https://doi.org/10.1002/sia.6239.

(213) Ravel, B.; Newville, M. *ATHENA* , *ARTEMIS* , *HEPHAESTUS*: Data Analysis for X-Ray Absorption Spectroscopy Using *IFEFFIT*. *J. Synchrotron Radiat.* **2005**, *12* (4), 537–541. https://doi.org/10.1107/S0909049505012719.

(214) Klencsár, Z. Mössbauer Spectrum Analysis by Evolution Algorithm. *Nucl. Instrum. Methods Phys. Res. B* **1997**, *129* (4), 527–533. https://doi.org/10.1016/S0168-583X(97)00314-5.

(215) Wezendonk, T. A.; Santos, V. P.; Nasalevich, M. A.; Warringa, Q. S. E.; Dugulan, A. I.; Chojecki, A.; Koeken, A. C. J.; Ruitenbeek, M.; Meima, G.; Islam, H.-U.; Sankar, G.; Makkee, M.; Kapteijn, F.; Gascon, J. Elucidating the Nature of Fe Species during Pyrolysis of the Fe-BTC MOF into Highly Active and Stable Fischer–Tropsch Catalysts. *ACS Catal.* **2016**, *6* (5), 3236–3247. https://doi.org/10.1021/acscatal.6b00426.

(216) Coats, A. W.; Redfern, J. P. *Thermogravimetric Analysis A Review**; Vol. 88.

(217) Saadatkhah, N.; Carillo Garcia, A.; Ackermann, S.; Leclerc, P.; Latifi, M.; Samih, S.; Patience, G. S.; Chaouki, J. Experimental Methods in Chemical Engineering: Thermogravimetric Analysis—TGA. *Can. J. Chem. Eng.* **2020**, *98* (1), 34–43. https://doi.org/10.1002/cjce.23673.

(218) Katnani, A. D.; Papathomas, K. I. Kinetics and Initial Stages of Oxidation of Aluminum Nitride: Thermogravimetric Analysis and x-Ray Photoelectron Spectroscopy Study. *Journal of Vacuum Science & Technology A: Vacuum, Surfaces, and Films* **1987**, *5* (4), 1335–1340. https://doi.org/10.1116/1.574765.

(219) Menczel, J. D.; Prime, R. B. *THERMAL ANALYSIS OF POLYMERS - Fundamentals and Applications*; John Wiley & Sons, Inc.: Hoboken, New Jersey, 2009.

(220) WANG, B.; MANOS, G. A Novel Thermogravimetric Method for Coke Precursor Characterisation. *J. Catal.* **2007**, *250* (1), 121–127. https://doi.org/10.1016/j.jcat.2007.05.018.

(221) Deboucha, W.; Leklou, N.; Khelidj, A.; Oudjit, M. N. Hydration Development of Mineral Additives Blended Cement Using Thermogravimetric Analysis (TGA): Methodology of Calculating the Degree of Hydration. *Constr. Build. Mater.* **2017**, *146*, 687–701. https://doi.org/10.1016/j.conbuildmat.2017.04.132.

(222) Goetze, J.; Meirer, F.; Yarulina, I.; Gascon, J.; Kapteijn, F.; Ruiz-Martínez, J.; Weckhuysen, B. M. Insights into the Activity and Deactivation of the Methanol-to-Olefins Process over Different Small-Pore Zeolites As Studied with Operando UV–Vis Spectroscopy. *ACS Catal.* **2017**, *7* (6), 4033–4046. https://doi.org/10.1021/acscatal.6b03677.

(223) Goetze, J.; Weckhuysen, B. M. Spatiotemporal Coke Formation over Zeolite ZSM-5 during the Methanol-to-Olefins Process as Studied with *Operando* UV-Vis Spectroscopy: A Comparison between H-ZSM-5 and Mg-ZSM-5. *Catal. Sci. Technol.* **2018**, *8* (6), 1632–1644. https://doi.org/10.1039/C7CY02459B.

(224) Van Speybroeck, V.; Hemelsoet, K.; De Wispelaere, K.; Qian, Q.; Van der Mynsbrugge, J.; De Sterck, B.; Weckhuysen, B. M.; Waroquier, M. Mechanistic Studies on Chabazite-Type Methanol-to-Olefin Catalysts: Insights from Time-Resolved UV/Vis Microspectroscopy Combined with Theoretical Simulations. *ChemCatChem* **2013**, *5* (1), 173–184. https://doi.org/10.1002/cctc.201200580.

(225) Dahl, I. M.; Kolboe, S. On the Reaction Mechanism for Propene Formation in the MTO Reaction over SAPO-34. *Catal. Letters* **1993**, *20* (3–4), 329–336. https://doi.org/10.1007/BF00769305.

(226) Martínez-Espín, J. S.; Topsøe, H. *Mechanistic and Kinetic Investigations on the Role of Methanol and Dimethyl Ether in the Methanol-To-Hydrocarbons Reaction*. https://www.researchgate.net/publication/319833921.

(227) Jacobs, G.; Pendyala, V. R. R.; Martinelli, M.; Shafer, W. D.; Gnanamani, M. K.; Khalid, S.; MacLennan, A.; Hu, Y.; Davis, B. H. Fischer–Tropsch Synthesis: XANES Spectra of Potassium in Promoted Precipitated Iron Catalysts as a Function of Time On-Stream. *Catal. Letters* **2017**, *147* (8), 1861–1870. https://doi.org/10.1007/s10562-017-2090-9.

(228) Krausser, L.; Kondratenko, V. A.; Lund, H.; Bartling, S.; Fedorova, E. A.; Yang, Q.; Kondratenko, E. V. Formation and Role of Iron-Containing Phases in CO_2 Hydrogenation to Higher Hydrocarbons. *ACS Catal.* **2025**, *15* (12), 10627–10638. https://doi.org/10.1021/acscatal.4c07946.

(229) Han, Y.; Fang, C.; Ji, X.; Wei, J.; Ge, Q.; Sun, J. Interfacing with Carbonaceous Potassium Promoters Boosts Catalytic CO_2 Hydrogenation of Iron. *ACS Catal.* **2020**, *10* (20), 12098–12108. https://doi.org/10.1021/acscatal.0c03215.

(230) Ramirez, A.; Ould-Chikh, S.; Gevers, L.; Chowdhury, A. D.; Abou-Hamad, E.; Aguilar-Tapia, A.; Hazemann, J.; Wehbe, N.; Al Abdulghani, A. J.; Kozlov, S. M.; Cavallo, L.; Gascon, J. Tandem Conversion of CO_2 to Valuable Hydrocarbons in Highly Concentrated Potassium Iron Catalysts. *ChemCatChem* **2019**, *11* (12), 2879–2886. https://doi.org/10.1002/cctc.201900762.

(231) Panzone, C.; Philippe, R.; Nikitine, C.; Vanoye, L.; Bengaouer, A.; Chappaz, A.; Fongarland, P. Catalytic and Kinetic Study of the CO_2 Hydrogenation Reaction over a Fe–K/Al_2O_3 Catalyst toward Liquid and Gaseous Hydrocarbon Production. *Ind. Eng. Chem. Res.* **2021**, *60* (46), 16635–16652. https://doi.org/10.1021/acs.iecr.1c02542.

(232) Abebe, B.; Murthy, H. C. A.; Amare, E. Summary on Adsorption and Photocatalysis for Pollutant Remediation: Mini Review. *Journal of Encapsulation and Adsorption Sciences* **2018**, *08* (04), 225–255. https://doi.org/10.4236/jeas.2018.84012.

(233) Biesinger, M. C.; Payne, B. P.; Grosvenor, A. P.; Lau, L. W. M.; Gerson, A. R.; Smart, R. St. C. Resolving Surface Chemical States in XPS Analysis of First Row Transition Metals, Oxides and Hydroxides: Cr, Mn, Fe, Co and Ni. *Appl. Surf. Sci.* **2011**, *257* (7), 2717–2730. https://doi.org/10.1016/j.apsusc.2010.10.051.

(234) Zhou, Y.; Wang, Y.; Lu, H.; Liu, T.; Hong, X.; Liu, G. Highly Dispersed K- and Pd-Comodified Fe Catalyst for CO_2 Hydrogenation to Higher Alcohols. *ACS Sustain. Chem. Eng.* **2024**, *12* (8), 3322–3330. https://doi.org/10.1021/acssuschemeng.3c08044.

(235) Xu, D.; Fan, H.; Hou, G.; Liu, K.; Li, Y.; Huang, S.; Ding, M. Constructing Stable Cu-Fe5C2 Interfaces for Efficient Syngas Conversion to Higher Alcohols. *Chemical Engineering Journal* **2024**, *499*, 155624. https://doi.org/10.1016/j.cej.2024.155624.

(236) Wang, J.; Wang, T.; Xi, Y.; Gao, G.; Sun, P.; Li, F. In-Situ-Formed Potassium-Modified Nickel-Zinc Carbide Boosts Production of Higher Alcohols beyond CH_4 in CO_2 Hydrogenation. *Angew. Chem. Int. Ed.* **2023**, *62* (42). https://doi.org/10.1002/anie.202311335.

(237) Rousseau, B.; Estrade-Szwarckopf, H. Evolution of K-, Rb- and Cs-Graphite Intercalation Compounds Surfaces under Controlled Oxidization: An XPS Study. *Solid State Commun.* **1993**, *88* (1), 1–4. https://doi.org/10.1016/0038-1098(93)90757-E.

(238) Yang, S.-J.; Bates, C. W. The Role of Cesium Suboxides in Low-Work-Function Surface Layers Studied by x-Ray Photoelectron Spectroscopy: Ag-O-Cs. *Appl. Phys. Lett.* **1980**, *36* (8), 675–677. https://doi.org/10.1063/1.91620.

(239) Ebbinghaus, G.; Simon, A. Electronics Structures of Rb, Cs and Some of Their Metallic Oxides Studied by Photoelectron Spectroscopy. *Chem. Phys.* **1979**, *43* (1), 117–133. https://doi.org/10.1016/0301-0104(79)80111-1.

(240) Caracciolo, L.; Madec, L.; Martinez, H. XPS Analysis of K-Based Reference Compounds to Allow Reliable Studies of Solid Electrolyte Interphase in K-Ion Batteries. *ACS Appl. Energy Mater.* **2021**, *4* (10), 11693–11699. https://doi.org/10.1021/acsaem.1c02400.

(241) Gao, J.; Huang, Z.; Chen, Y.; Wan, J.; Gu, X.; Ma, Z.; Chen, J.; Tang, X. Activating Inert Alkali-Metal Ions by Electron Transfer from Manganese Oxide for Formaldehyde Abatement. *Chemistry – A European Journal* **2018**, *24* (3), 681–689. https://doi.org/10.1002/chem.201704398.

(242) Moulder, J. F.; Stickle, W. F.; Sobol, P. E. ’; Bomben, K. D.; Chastain, J. *Handbook of X-Ray Photoelectron Spectroscopy AReference Book of Standard Spectra for Identification and Interpretation of XPS Data*.

(243) Courcot, D.; Gengembre, L.; Guelton, M.; Barbaux, Y.; Grzybowska, B. *Effect of Potassium on the Surface Potential of Titania*; 1994.

(244) Joseph, Y.; Ketteler, G.; Kuhrs, C.; Ranke, W.; Weiss, W.; Schlögl, R. On the Preparation and Composition of Potassium Promoted Iron Oxide Model Catalyst Films. *Physical Chemistry Chemical Physics* **2001**, *3* (18), 4141–4153. https://doi.org/10.1039/b104263g.

(245) Rodriguez, J. A.; Clendening, W. D.; Campbell, C. T. Adsorption of Carbon Monoxide Carbon Dioxide on Clean and Cesium-Covered Copper(110). *J. Phys. Chem.* **1989**, *93* (13), 5238–5248. https://doi.org/10.1021/j100350a040.

(246) Henn, F. C.; Rodriguez, J. A.; Campbell, C. T. Adsorption and Reaction of HCOOH on Doped Cu(110): Coadsorption with Cesium, Oxygen, and Csa + Oa. *Surf. Sci.* **1990**, *236* (3), 282–312. https://doi.org/10.1016/0039-6028(90)90475-N.

(247) Zhou, X. L.; White, J. M. Coadsorption and Reaction of Phosphorus Trifluoride with Potassium on Silver(111). *J. Phys. Chem.* **1991**, *95* (2), 887–896. https://doi.org/10.1021/j100155a073.

(248) Wesner, D. A.; Linden, G.; Bonzel, H. P. Alkali Promotion on Cobalt: Surface Analysis of the Effects of Potassium on Carbon Monoxide Adsorption and Fischer-Tropsch Reaction. *Appl. Surf. Sci.* **1986**, *26* (3), 335–356. https://doi.org/10.1016/0169-4332(86)90074-7.

(249) Brodén, G.; Bonzel, H. P. Potassium Adsorption on Fe(110). *Surf. Sci.* **1979**, *84* (1), 106–120. https://doi.org/10.1016/0039-6028(79)90282-6.

(250) Bertolini, J. C.; Duvault, J. L.; Jugnet, Y.; Ruiz, Ph.; Tardy, B. Potassium on Ni(111): Quantitative Determination and Electronic Structure. *J. Chem. Phys.* **1988**, *88* (1), 394–398. https://doi.org/10.1063/1.454614.

(251) Solymosi, F.; Berkó, A.; Tóth, Z. Adsorption and Dissociation of CH3OH on Clean and K-Promoted Pd(100) Surfaces. *Surf. Sci.* **1993**, *285* (3), 197–208. https://doi.org/10.1016/0039-6028(93)90430-R.

(252) Krix, D.; Nienhaus, H. Low-Temperature Oxidation of Alkali Overlayers: Ionic Species and Reaction Kinetics. *Appl. Surf. Sci.* **2013**, *270*, 231–237. https://doi.org/10.1016/j.apsusc.2013.01.008.

(253) Hamlyn, R. C. E.; Mahapatra, M.; Orozco, I.; Waluyo, I.; Hunt, A.; Rodriguez, J. A.; White, M. G.; Senanayake, S. D. Structure and Chemical State of Cesium on Well-Defined Cu(111) and Cu2O/Cu(111) Surfaces. *Journal of Physical Chemistry C* **2020**, *124* (5), 3107–3121. https://doi.org/10.1021/ACS.JPCC.9B10608/ASSET/IMAGES/MEDIUM/JP9B10608_0009.GIF.

(254) Moretti, G.; Palma, A.; Paparazzo, E.; Satta, M. Auger Parameter and Wagner Plot Studies of Small Copper Clusters. *Surf. Sci.* **2016**, *646*, 298–305. https://doi.org/10.1016/j.susc.2015.07.018.

(255) Cao, X.; Prozorov, R.; Koltypin, Yu.; Kataby, G.; Felner, I.; Gedanken, A. Synthesis of Pure Amorphous Fe $_2$ O $_3$. *J. Mater. Res.* **1997**, *12* (2), 402–406. https://doi.org/10.1557/JMR.1997.0058.

(256) Machala, L.; Zboril, R.; Gedanken, A. Amorphous Iron(III) OxideA Review. *J. Phys. Chem. B* **2007**, *111* (16), 4003–4018. https://doi.org/10.1021/jp064992s.

(257) van Diepen, A. M.; Popma, Th. J. A. Temperature Dependence of the Hyperfine Field in Amorphous Fe2O3. *Solid State Commun.* **1978**, *27* (2), 121–125. https://doi.org/10.1016/0038-1098(78)90814-1.

(258) Zhang, Y.; Cao, C.; Zhang, C.; Zhang, Z.; Liu, X.; Yang, Z.; Zhu, M.; Meng, B.; Xu, J.; Han, Y.-F. The Study of Structure-Performance Relationship of Iron Catalyst during a Full Life Cycle for CO2 Hydrogenation. *J. Catal.* **2019**, *378*, 51–62. https://doi.org/10.1016/j.jcat.2019.08.001.

(259) Kaczmarczyk, J.; Zasada, F.; Janas, J.; Indyka, P.; Piskorz, W.; Kotarba, A.; Sojka, Z. Thermodynamic Stability, Redox Properties, and Reactivity of Mn_3O_4, Fe_3O_4, and Co_3O_4 Model Catalysts for N_2O Decomposition: Resolving the Origins of Steady Turnover. *ACS Catal.* **2016**, *6* (2), 1235–1246. https://doi.org/10.1021/acscatal.5b02642.

(260) Yang, T.; Wen, X.-D.; Li, Y.-W.; Wang, J.; Jiao, H. Interaction of Alkali Metals with the Fe3O4(111) Surface. *Surf. Sci.* **2009**, *603* (1), 78–83. https://doi.org/10.1016/j.susc.2008.10.020.

(261) Petersen, M. A.; Cariem, M. J.; Claeys, M.; van Steen, E. A DFT Perspective of Potassium Promotion of χ-Fe5C2(1 0 0). *Appl. Catal. A Gen.* **2015**, *496*, 64–72. https://doi.org/10.1016/j.apcata.2015.02.008.

(262) Xia, W.; Abdalrahman, R. A.; Fiallos, L. M. F.; Al-Dhalimy, A. M. B.; Bains, P. S.; Shather, A. H.; Radi, U. K.; Alawadi, A.; Elmasry, Y. Investigation on Bare ZnO Nanotubes and Nanosheet as Electrode Materials for Potassium-Ion Batteries: A DFT Search. *Inorg. Chem. Commun.* **2024**, *161*, 112063. https://doi.org/10.1016/j.inoche.2024.112063.

(263) Padilla-Campos, L.; Toro-Labbé, A. Theoretical Study of the Diffusion of Alkali Metals on a Cu(111) Surface. *Journal of Molecular Structure: THEOCHEM* **1997**, *390* (1–3), 183–192. https://doi.org/10.1016/S0166-1280(96)04773-2.

(264) Doskocil, E. J.; Bordawekar, S. V; Davis, R. J. *Alkali-Support Interactions on Rubidium Base Catalysts Determined by XANES, EXAFS, CO 2 Adsorption, and IR Spectroscopy*; 1997; Vol. 169.

(265) Shou, H.; Davis, R. J. Reactivity and in Situ X-Ray Absorption Spectroscopy of Rb-Promoted Mo2C/MgO Catalysts for Higher Alcohol Synthesis. *J. Catal.* **2011**, *282* (1), 83–93. https://doi.org/10.1016/j.jcat.2011.05.028.

(266) Caddeo, F.; Loche, D.; Casula, M. F.; Corrias, A. Evidence of a Cubic Iron Sub-Lattice in t-CuFe2O4 Demonstrated by X-Ray Absorption Fine Structure. *Sci. Rep.* **2018**, *8* (1), 797. https://doi.org/10.1038/s41598-017-19045-8.

(267) Li, Y.; Gao, W.; Peng, M.; Zhang, J.; Sun, J.; Xu, Y.; Hong, S.; Liu, X.; Liu, X.; Wei, M.; Zhang, B.; Ma, D. Interfacial Fe5C2-Cu Catalysts toward Low-Pressure Syngas Conversion to Long-Chain Alcohols. *Nat. Commun.* **2020**, *11* (1), 61. https://doi.org/10.1038/s41467-019-13691-4.

(268) PARRATT, L. G. Electronic Band Structure of Solids by X-Ray Spectroscopy. *Rev. Mod. Phys.* **1959**, *31* (3), 616–645. https://doi.org/10.1103/RevModPhys.31.616.

(269) Bordiga, S.; Groppo, E.; Agostini, G.; van Bokhoven, J. A.; Lamberti, C. Reactivity of Surface Species in Heterogeneous Catalysts Probed by In Situ X-Ray Absorption Techniques. *Chem. Rev.* **2013**, *113* (3), 1736–1850. https://doi.org/10.1021/cr2000898.

(270) Xiang, H.; Xin, R.; Prasongthum, N.; Natewong, P.; Sooknoi, T.; Wang, J.; Reubroycharoen, P.; Fan, X. Catalytic Conversion of Bioethanol to Value-Added Chemicals and Fuels: A Review. *Resources Chemicals and Materials* **2022**, *1* (1), 47–68. https://doi.org/10.1016/j.recm.2021.12.002.

(271) Rosmaninho, M. G.; Moura, F. C. C.; Souza, L. R.; Nogueira, R. K.; Gomes, G. M.; Nascimento, J. S.; Pereira, M. C.; Fabris, J. D.; Ardisson, J. D.; Nazzarro, M. S.; Sapag, K.; Araújo, M. H.; Lago, R. M. Investigation of Iron Oxide Reduction by Ethanol as a Potential Route to Produce Hydrogen. *Appl. Catal. B* **2012**, *115–116*, 45–52. https://doi.org/10.1016/j.apcatb.2011.11.038.

(272) Zaki, T. Catalytic Dehydration of Ethanol Using Transition Metal Oxide Catalysts. *J. Colloid Interface Sci.* **2005**, *284* (2), 606–613. https://doi.org/10.1016/j.jcis.2004.10.048.

(273) Iwamoto, M.; Tanaka, M.; Hirakawa, S.; Mizuno, S.; Kurosawa, M. Pulse and IR Study on the Reaction Pathways for the Conversion of Ethanol to Propene over Scandium-Loaded Indium Oxide Catalysts. *ACS Catal.* **2014**, *4* (10), 3463–3469. https://doi.org/10.1021/cs5006822.

(274) Meunier, F. C. Relevance of IR Spectroscopy of Adsorbed CO for the Characterization of Heterogeneous Catalysts Containing Isolated Atoms. *The Journal of Physical Chemistry C* **2021**, *125* (40), 21810–21823. https://doi.org/10.1021/acs.jpcc.1c06784.

(275) Du, P.; Ait El Fakir, A.; Zhao, S.; Dostagir, N. H. M. D.; Pan, H.; Ting, K. W.; Mine, S.; Qian, Y.; Shimizu, K.; Toyao, T. Ethanol Synthesis *via* Catalytic CO_2 Hydrogenation over Multi-Elemental KFeCuZn/ZrO_2 Catalyst. *Chem. Sci.* **2024**, *15* (38), 15925–15934. https://doi.org/10.1039/D4SC02588A.

(276) Orege, J. I.; Yu, Y.; Wei, J.; Fan, Q.; Zhang, J.; Song, L.; Ge, Q.; Sun, J. Engineering the Microenvironment in Ba-Doped Fe Catalyst with Alkali Metal Promoters for Enhanced CO2 Hydrogenation to α-Olefins. *Chemical Engineering Journal* **2025**, *505*. https://doi.org/10.1016/j.cej.2025.159301.

(277) Khan, M. K.; Butolia, P.; Jo, H.; Irshad, M.; Han, D.; Nam, K. W.; Kim, J. Selective Conversion of Carbon Dioxide into Liquid Hydrocarbons and Long-Chain α-Olefins over Fe-Amorphous AlO XBifunctional Catalysts. *ACS Catal.* **2020**, *10* (18), 10325–10338. https://doi.org/10.1021/acscatal.0c02611.

(278) Gu, H.; Ding, J.; Zhong, Q.; Zeng, Y.; Song, F. Promotion of Surface Oxygen Vacancies on the Light Olefins Synthesis from Catalytic CO2 Hydrogenation over Fe K/ZrO2 Catalysts. *Int. J. Hydrogen Energy* **2019**, *44* (23), 11808–11816. https://doi.org/10.1016/j.ijhydene.2019.03.046.

(279) Li, T.; Zhao, H.; Guo, L.; Liu, G.; Wu, J.; Xing, T.; Li, T.; Liu, Q.; Sui, J.; Han, Y.; Liang, J.; He, Y.; Tsubaki, N. Construction of Highly Active Fe5C2-FeCo Interfacial Sites for Oriented Synthesis of Light Olefins from CO2 Hydrogenation. *ACS Catal.* **2025**, *15* (2), 1112–1122. https://doi.org/10.1021/acscatal.4c06001.

(280) Zhou, S.; Wen, Y.; Wang, B.; Fan, M.; Ren, L.; Cui, Z.; Huang, W.; Li, J.; Guo, J. Regulation of CuFeZn Catalysts by K3PO4 and Its Effect on CO2 Hydrogenation to C2+ Alcohols. *Chemical Engineering Journal* **2024**, *487*, 150425. https://doi.org/10.1016/j.cej.2024.150425.

(281) Ding, L.; Shi, T.; Gu, J.; Cui, Y.; Zhang, Z.; Yang, C.; Chen, T.; Lin, M.; Wang, P.; Xue, N.; Peng, L.; Guo, X.; Zhu, Y.; Chen, Z.; Ding, W. CO2 Hydrogenation to Ethanol over Cu@Na-Beta. *Chem* **2020**, *6* (10), 2673–2689. https://doi.org/10.1016/j.chempr.2020.07.001.

(282) Hauchecorne, B.; Terrens, D.; Verbruggen, S.; Martens, J. A.; Van Langenhove, H.; Demeestere, K.; Lenaerts, S. Elucidating the Photocatalytic Degradation Pathway of Acetaldehyde: An FTIR in Situ Study under Atmospheric Conditions. *Appl. Catal. B* **2011**, *106* (3–4), 630–638. https://doi.org/10.1016/j.apcatb.2011.06.026.

(283) Zhang, Q.; Wang, S.; Geng, R.; Wang, P.; Dong, M.; Wang, J.; Fan, W. Hydrogenation of CO2 to Higher Alcohols on an Efficient Cr-Modified CuFe Catalyst. *Appl. Catal. B* **2023**, *337*, 123013. https://doi.org/10.1016/j.apcatb.2023.123013.

(284) Chen, W.; Ding, Y.; Song, X.; Wang, T.; Luo, H. Promotion Effect of Support Calcination on Ethanol Production from CO Hydrogenation over Rh/Fe/Al2O3 Catalysts. *Appl. Catal. A Gen.* **2011**, *407* (1–2), 231–237. https://doi.org/10.1016/j.apcata.2011.08.044.

(285) He, K.; Li, Y.; Li, Z.; Chen, J.; Tan, L.; Qiu, T.; Li, X.; Ma, X.; Dai, C. Enhanced Ethanol Synthesis via CO2 Hydrogenation Using La-Doped CuFeOx Catalysts. *Chemical Engineering Journal* **2024**, *501*, 157608. https://doi.org/10.1016/j.cej.2024.157608.

(286) Huang, J.; Zhang, G.; Zhu, J.; Wang, M.; Ding, F.; Song, C.; Guo, X. Boosting the Production of Higher Alcohols from CO_2 and H_2 over Mn- and K-Modified Iron Carbide. *Ind. Eng. Chem. Res.* **2022**, *61* (21), 7266–7274. https://doi.org/10.1021/acs.iecr.2c00720.

(287) Ren, X.; Men, Z.; Wang, P.; Filot, I. A. W.; Hensen, E. J. M. The Nature of K Promotion of χ-Fe5C2 for High Chain-Growth Probability in the Fischer–Tropsch Reaction. *Applied Catalysis B: Environment and Energy* **2025**, *374*, 125403. https://doi.org/10.1016/j.apcatb.2025.125403.

(288) Nie, X.; Meng, L.; Wang, H.; Chen, Y.; Guo, X.; Song, C. DFT Insight into the Effect of Potassium on the Adsorption, Activation and Dissociation of CO_2 over Fe-Based Catalysts. *Physical Chemistry Chemical Physics* **2018**, *20* (21), 14694–14707. https://doi.org/10.1039/C8CP02218F.

(289) Mehar, V.; Liao, W.; Mahapatra, M.; Shi, R.; Lim, H.; Barba-Nieto, I.; Hunt, A.; Waluyo, I.; Liu, P.; Rodriguez, J. A. Morphology Dependent Reactivity of CsO_x Nanostructures on Au(111): Binding and Hydrogenation of CO_2 to HCOOH. *ACS Nano* **2023**, *17* (22), 22990–22998. https://doi.org/10.1021/acsnano.3c08324.

(290) Liao, W.; Liu, P. Methanol Synthesis from CO_2 Hydrogenation over a Potassium-Promoted Cu_xO/Cu(111) ($x \leq 2$) Model Surface: Rationalizing the Potential of Potassium in Catalysis. *ACS Catal.* **2020**, *10* (10), 5723–5733. https://doi.org/10.1021/acscatal.9b05226.

(291) Xie, J.; Zeng, Y.; Sun, Z.; Liu, J.; Zhang, C.; Wang, Y.; Sun, W.; Wang, J.; Cao, D.; Guo, Q.; Guo, J. Potassium-Promoted Formic Acid Dehydrogenation on Cu(111): Visualizing $HCOO^-$-K^+ Intermediates. *JACS Au* **2025**, *5* (7), 3366–3373. https://doi.org/10.1021/jacsau.5c00462.

(292) Ma, Y.-P.; Wang, G.-C. Systematic Theoretical Study of CO Activation over Clean and Potassium-Modified Transition Metals. *The Journal of Physical Chemistry C* **2023**, *127* (1), 265–278. https://doi.org/10.1021/acs.jpcc.2c07380.

(293) Sun, W.; Yang, P.; Jiang, Y.; Zhang, J.; Zhang, H.; Jin, Q.; Zhang, C.; Zhang, Z.; Feng, H.; Du, Y.; Wang, Z.; Cao, D.; Wu, F.; Jiang, Y.; Guo, J. Visualizing Alkali Metal Aggregation-Induced Coordination in CO2 Activation on Copper. *Nat. Commun.* **2025**, *16* (1), 9463. https://doi.org/10.1038/s41467-025-64499-4.

(294) Ren, X.; Krösschell, R. D. E.; Men, Z.; Wang, P.; Filot, I. A. W.; Hensen, E. J. M. A Computational Study of K Promotion of CO Dissociation on Hägg Carbide. *Catal. Sci. Technol.* **2025**, *15* (11), 3262–3274. https://doi.org/10.1039/D4CY01463D.

(295) Bera, P.; Cámara, A. L.; Hornés, A.; Martínez-Arias, A. Comparative in Situ DRIFTS-MS Study Of12CO- And 13CO-TPR on CuO/Cep2 Catalyst. *Journal of Physical Chemistry C* **2009**, *113* (24), 10689–10695. https://doi.org/10.1021/jp9020504.

(296) Xu, M.; Liu, X.; Song, G.; Cai, Y.; Shi, B.; Liu, Y.; Ding, X.; Yang, Z.; Tian, P.; Cao, C.; Xu, J. Regulating Iron Species Compositions by Fe-Al Interaction in CO2 Hydrogenation. *J. Catal.* **2022**, *413*, 331–341. https://doi.org/10.1016/j.jcat.2022.06.030.

(297) Li, P.; Miser, D. E.; Rabiei, S.; Yadav, R. T.; Hajaligol, M. R. The Removal of Carbon Monoxide by Iron Oxide Nanoparticles. *Appl. Catal. B* **2003**, *43* (2), 151–162. https://doi.org/10.1016/S0926-3373(02)00297-7.

(298) Pillai, U. R.; Deevi, S. Room Temperature Oxidation of Carbon Monoxide over Copper Oxide Catalyst. *Appl. Catal. B* **2006**, *64* (1–2), 146–151. https://doi.org/10.1016/j.apcatb.2005.11.005.

(299) Fan, Z.; Gao, F.; Zhang, J.; Yi, L.; Luo, N.; Yi, H.; Tang, X. Advances in CO Catalytic Oxidation on Typical Metal Oxide Catalysts: Performance, Mechanism, and Optimization. *J. Mater. Chem. A Mater.* **2025**, *13* (32), 26129–26165. https://doi.org/10.1039/D5TA03067F.

(300) Yu, X.; Zhang, X.; Jin, L.; Feng, G. CO Adsorption, Oxidation and Carbonate Formation Mechanisms on Fe $_3$ O $_4$ Surfaces. *Physical Chemistry Chemical Physics* **2017**, *19* (26), 17287–17299. https://doi.org/10.1039/C7CP02760E.

(301) Bang, G.; Jin, S.; Kim, H.; Kim, K.-M.; Lee, C.-H. Mg-Incorporated Sorbent for Efficient Removal of Trace CO from H2 Gas. *Nat. Commun.* **2023**, *14* (1), 7045. https://doi.org/10.1038/s41467-023-42871-6.

(302) Zhao, J.; Shi, R.; Waterhouse, G. I. N.; Zhang, T. Selective Photothermal CO2 Reduction to CO, CH4, Alkanes, Alkenes over Bimetallic Alloy Catalysts Derived from Layered Double Hydroxide Nanosheets. *Nano Energy* **2022**, *102*. https://doi.org/10.1016/j.nanoen.2022.107650.

(303) Guglielminotti, E. *Spectroscopic Characterization of the Fe/ZrOi System. 1. CO Adsorption*; 1994; Vol. 98. https://pubs.acs.org/sharingguidelines.

(304) Hadjiivanov, K.; Knözinger, H. FTIR Study of CO and NO Adsorption and Coadsorption on a Cu/SiO2 Catalyst: Probing the Oxidation State of Copper. *Physical Chemistry Chemical Physics* **2001**, *3* (6), 1132–1137. https://doi.org/10.1039/b009649k.

(305) Dulaurent, O.; Courtois, X.; Perrichon, V.; Bianchi, D. Heats of Adsorption of CO on a Cu/Al $_2$ O $_3$ Catalyst Using FTIR Spectroscopy at High Temperatures and under Adsorption Equilibrium Conditions. *J. Phys. Chem. B* **2000**, *104* (25), 6001–6011. https://doi.org/10.1021/jp9943629.

(306) Lemire, C.; Meyer, R.; Henrich, V. E.; Shaikhutdinov, Sh.; Freund, H.-J. The Surface Structure of Fe3O4(111) Films as Studied by CO Adsorption. *Surf. Sci.* **2004**, *572* (1), 103–114. https://doi.org/10.1016/j.susc.2004.08.033.

(307) Lu, F.; Chen, X.; Wen, L.; Wu, Q.; Zhang, Y. The Synergic Effects of Iron Carbides on Conversion of Syngas to Alkenes. *Catal. Letters* **2021**, *151* (7), 2132–2143. https://doi.org/10.1007/s10562-020-03505-4.

(308) Boudjemaa, A.; Daniel, C.; Mirodatos, C.; Trari, M.; Auroux, A.; Bouarab, R. In Situ DRIFTS Studies of High-Temperature Water-Gas Shift Reaction on Chromium-Free Iron Oxide Catalysts. *Comptes Rendus Chimie* **2011**, *14* (6), 534–538. https://doi.org/10.1016/j.crci.2010.11.007.

(309) Weiß, J.; Yang, Q.; Bentrup, U.; Kondratenko, E. V.; Brückner, A.; Kubis, C. Operando DRIFT and In Situ Raman Spectroscopic Studies on Aspects of CO $_2$ Fischer-Tropsch Synthesis Catalyzed by Bulk Iron Oxide-Based Catalysts. *ChemCatChem* **2022**, *14* (22). https://doi.org/10.1002/cctc.202200577.

(310) Wang, Y.-X.; Wang, G.-C. A Systematic Theoretical Study of Water Gas Shift Reaction on Cu(111) and Cu(110): Potassium Effect. *ACS Catal.* **2019**, *9* (3), 2261–2274. https://doi.org/10.1021/acscatal.8b04427.

(311) Omojola, T.; van Veen, A. C. Competitive Adsorption of Oxygenates and Aromatics during the Initial Steps of the Formation of Primary Olefins over ZSM-5 Catalysts. *Catal. Commun.* **2020**, *140*, 106010. https://doi.org/10.1016/j.catcom.2020.106010.

(312) Rojo-Gama, D.; Nielsen, M.; Wragg, D. S.; Dyballa, M.; Holzinger, J.; Falsig, H.; Lundegaard, L. F.; Beato, P.; Brogaard, R. Y.; Lillerud, K. P.; Olsbye, U.; Svelle, S. A Straightforward Descriptor for the Deactivation of Zeolite Catalyst H-ZSM-5. *ACS Catal.* **2017**, *7* (12), 8235–8246. https://doi.org/10.1021/acscatal.7b02193.

(313) Seremak, A.; Capel Berdiell, I.; Arstad, B.; Fjermestad, T.; Svelle, S. Investigating the Flexibility of H-ZSM-5 Zeolite Upon Adsorption of Coke Precursors: A Theoretical and Experimental

Approach. *The Journal of Physical Chemistry C* **2025**, *129* (2), 1183–1197. https://doi.org/10.1021/acs.jpcc.4c07349.

(314) Barbera, K.; Bonino, F.; Bordiga, S.; Janssens, T. V. W.; Beato, P. Structure–Deactivation Relationship for ZSM-5 Catalysts Governed by Framework Defects. *J. Catal.* **2011**, *280* (2), 196–205. https://doi.org/10.1016/j.jcat.2011.03.016.

(315) Gulková, D.; Šolcová, O.; Zdražil, M. Preparation of MgO Catalytic Support in Shaped Mesoporous High Surface Area Form. *Microporous and Mesoporous Materials* **2004**, *76* (1–3), 137–149. https://doi.org/10.1016/j.micromeso.2004.07.039.

(316) Bhattacharjya, D.; Selvamani, T.; Mukhopadhyay, I. Thermal Decomposition of Hydromagnesite. *J. Therm. Anal. Calorim.* **2012**, *107* (2), 439–445. https://doi.org/10.1007/s10973-011-1656-9.

(317) Fan, H.-X.; Cui, T.-Y.; Rajendran, A.; Yang, Q.; Feng, J.; Yue, X.-P.; Li, W.-Y. Comparative Study on the Activities of Different MgO Surfaces in CO2 Activation and Hydrogenation. *Catal. Today* **2020**, *356*, 535–543. https://doi.org/10.1016/j.cattod.2020.03.010.

(318) Xu, G.; Xia, Q.-H.; Lu, X.-H.; Zhang, Q.; Zhan, H.-J. Selectively Catalytic Epoxidation of Styrene with Dry Air over the Composite Catalysts of Co-ZSM-5 Coordinated with Ligands. *J. Mol. Catal. A Chem.* **2007**, *266* (1–2), 180–187. https://doi.org/10.1016/j.molcata.2006.10.052.

(319) Rastogi, C. K.; Saha, S.; Sivakumar, S.; Pala, R. G. S.; Kumar, J. Kinetically Stabilized Aliovalent Europium-Doped Magnesium Oxide as a UV Sensitized Phosphor. *Physical Chemistry Chemical Physics* **2015**, *17* (6), 4600–4608. https://doi.org/10.1039/C4CP05205F.

(320) Fulmer, G. R.; Miller, A. J. M.; Sherden, N. H.; Gottlieb, H. E.; Nudelman, A.; Stoltz, B. M.; Bercaw, J. E.; Goldberg, K. I. NMR Chemical Shifts of Trace Impurities: Common Laboratory Solvents, Organics, and Gases in Deuterated Solvents Relevant to the Organometallic Chemist. *Organometallics* **2010**, *29* (9), 2176–2179. https://doi.org/10.1021/om100106e.

(321) Zachariou, A.; Hawkins, A. P.; Howe, R. F.; Barrow, N.; Bradley, J.; Collier, P.; Lennon, D.; Parker, S. F. A Spectroscopic Paradox: The Interaction of Methanol with ZSM-5 at Room Temperature. *Top. Catal.* **2021**, *64* (9–12), 672–684. https://doi.org/10.1007/s11244-021-01462-9.

(322) Dutta Chowdhury, A.; Houben, K.; Whiting, G. T.; Mokhtar, M.; Asiri, A. M.; Al-Thabaiti, S. A.; Basahel, S. N.; Baldus, M.; Weckhuysen, B. M. *Supporting Information Initial Carbon-Carbon Bond Formation during the Early Stages of the Methanol-to-Olefin Process Proven by Zeolite-Trapped Acetate and Methyl Acetate*.

(323) Salehirad, F.; Anderson, M. Solid-State NMR Studies of Adsorption Complexes and Surface Methoxy Groups on Methanol-Sorbed Microporous Materials. *J. Catal.* **1998**, *177* (2), 189–207. https://doi.org/10.1006/jcat.1998.2096.

(324) Hunger, M.; Horvath, T. Adsorption of Methanol on Brønsted Acid Sites in Zeolite H-ZSM-5 Investigated by Multinuclear Solid-State NMR Spectroscopy. *J. Am. Chem. Soc.* **1996**, *118* (49), 12302–12308. https://doi.org/10.1021/ja962425k.

(325) Haase, F.; Sauer, J. Interaction of Methanol with Broensted Acid Sites of Zeolite Catalysts: An Ab Initio Study. *J. Am. Chem. Soc.* **1995**, *117* (13), 3780–3789. https://doi.org/10.1021/ja00118a014.

(326) Chowdhury, A. D.; Houben, K.; Whiting, G. T.; Chung, S. H.; Baldus, M.; Weckhuysen, B. M. Electrophilic Aromatic Substitution over Zeolites Generates Wheland-Type Reaction Intermediates. *Nat. Catal.* **2018**, *1* (1), 23–31. https://doi.org/10.1038/s41929-017-0002-4.

(327) Holmes, C. E. C. A. ; Ruttink, J. L. ; Schaftenaar, P. J. A. ; Terlouw, G. ; Chem, J. K.; White, J. L.; Beck, L. W.; Haw, J. F. *53) Hop*; Chichester, 1992; Vol. 114. https://pubs.acs.org/sharingguidelines.

(328) Chowdhury, A. D.; Houben, K.; Whiting, G. T.; Mokhtar, M.; Asiri, A. M.; Al-Thabaiti, S. A.; Basahel, S. N.; Baldus, M.; Weckhuysen, B. M. Initial Carbon–Carbon Bond Formation during the Early Stages of the Methanol-to-Olefin Process Proven by Zeolite-Trapped Acetate and Methyl Acetate. *Angew. Chem. Int. Ed.* **2016**, *55* (51), 15840–15845. https://doi.org/10.1002/anie.201608643.

(329) Xu, M.; Harris, K. D. M.; Thomas, J. M. Mapping the Evolution of Adsorption of Water in Nanoporous Silica by in Situ Solid-State ^{1}H NMR Spectroscopy. *J. Am. Chem. Soc.* **2008**, *130* (18), 5880–5882. https://doi.org/10.1021/ja8007243.

(330) Xu, M.; Harris, K. D. M.; Thomas, J. M. In Situ Solid-State 1H NMR Studies of Hydration of the Solid Acid Catalyst ZSM-5 in Its Ammonium Form. *Solid State Nucl. Magn. Reson.* **2009**, *35* (2), 93–99. https://doi.org/10.1016/j.ssnmr.2008.12.011.

(331) Lesthaeghe, D.; Horré, A.; Waroquier, M.; Marin, G. B.; Van Speybroeck, V. Theoretical Insights on Methylbenzene Side-Chain Growth in ZSM-5 Zeolites for Methanol-to-Olefin Conversion. *Chemistry – A European Journal* **2009**, *15* (41), 10803–10808. https://doi.org/10.1002/chem.200901723.

(332) Ribeiro, M. C.; Jacobs, G.; Davis, B. H.; Cronauer, D. C.; Kropf, A. J.; Marshall, C. L. Fischer-Tropsch Synthesis: An In-Situ TPR-EXAFS/XANES Investigation of the Influence of Group I Alkali Promoters on the Local Atomic and Electronic Structure of Carburized Iron/Silica Catalysts. https://doi.org/10.1021/jp911856q.

(333) Tsang, S. C. E.; Zheng, J. Decomposition of Polyolefins, September 25, 2025.

(334) Ding, Y.; Zhang, S.; Liu, C.; Shao, Y.; Pan, X.; Bao, X. CO2-Facilitated Upcycling of Polyolefin Plastics to Aromatics at Low Temperature. *Natl. Sci. Rev.* **2024**, *11* (5). https://doi.org/10.1093/nsr/nwae097.

(335) Chen, W.; Jiao, Y.; Liu, Y.; Wang, M.; Zhang, F.; Ma, D. One-Pot Upgrading Polyethylene and CO_2 to Aromatics via Tandem Catalysis. *CCS Chemistry* **2024**, *6* (6), 1422–1429. https://doi.org/10.31635/ccschem.023.202303518.

(336) Sun, C.; Wang, Y. Catalytic Upcycling Plastics with CO2: A Novel Strategy for Carbon Waste Valorization. *Chem Catalysis* **2024**, *4* (3), 100934. https://doi.org/10.1016/j.checat.2024.100934.

(337) Santatiwongchai, J.; Faungnawakij, K.; Hirunsit, P. Comprehensive Mechanism of CO_2 Electroreduction toward Ethylene and Ethanol: The Solvent Effect from Explicit Water–Cu(100) Interface Models. *ACS Catal.* **2021**, *11* (15), 9688–9701. https://doi.org/10.1021/acscatal.1c01486.

(338) Zimmermann, N. E. R.; Haranczyk, M. History and Utility of Zeolite Framework-Type Discovery from a Data-Science Perspective. *Cryst. Growth Des.* **2016**, *16* (6), 3043–3048. https://doi.org/10.1021/acs.cgd.6b00272.

Appendix

List of Figures

Chapter 2

Figure S1| Schematic representation of the catalytic plug flow reactor.

Figure S2| Valve diagram with valve 4 in channel 1 in OFF position.

Figure S3| Valve diagram channel 1 with valve 4 in ON position.

Figure S4| Valve diagram channel 2 with valve 2 and 3 in OFF position.

Figure S5| Valve diagram channel 2 with valve 2 in ON and 3 in OFF position.

Figure S6| Valve diagram channel 2 with valve 2 and 3 in ON position.

Figure S7| Valve diagram channel 2 with valve 2 in ON and 3 in OFF position.

Figure S8| Valve diagram channel 3 (not used for analysis) with valve 1 in OFF position.

Figure S9| Valve diagram channel 3 (not used for analysis) with valve 1 in OFF position.

Figure S10| GC traces obtained from mixing a calibration gas with different ratios of N_2.

Figure S11| Example of a typical obtained during CO_2 hydrogenation over CZF.

Figure S12| Example of a typical obtained during CO_2 hydrogenation over Cs-CZF.

Chapter 3

Figure S13| Diffractogram of calcined CZF sample.

Figure S14| Catalytic repeatability results of CZF and Cs-CZF.

Figure S15| Reaction time point selectivity data for CZF (left) and Rb-CZF (right).

Figure 16| Non-fitted ASF function $\ln(W_n/n)$ applied to catalytic data obtained from alkali metal doped and undoped CZF without offset.

Figure 17| Non-fitted ASF function $\ln[(W_n/n)]$ applied to catalytic data obtained from alkali metal doped and undoped CZF with a small offset.

Figure S18| Linear relationship between HA selectivity and C_2/C_3 ratio.

Figure S19| Raw data obtained on Cu LMM spectra of doped and undoped samples before and after reaction.

Figure S20| Cu LMM spectra of doped and undoped samples before and after reaction.

Figure S21| Fe 2p XPS spectra of reduced samples.

Figure S22| Raw data obtained for Fe 2p spectra obtained from doped and undoped catalysts after reduction in 5% H_2 at 360 °C.

Figure S23| Raw data obtained for Fe 2p spectra obtained from doped and undoped catalysts after CO_2 hydrogenation.

Figure S24| XPS spectra of AMs of spent samples.

Figure S25| Mössbauer spectra of reduced and spent samples.

Figure S26| Mössbauer spectrum of calcined samples at 26.85 °C.

Figure S27| Mössbauer spectrum of calcined samples at 4.2 K.

Figure S28| Transmission Electron Microscope image of CZF and Rb-CZF after reaction.

Figure S29| Simulated Electron diffraction pattern of Fe_3O_4.

Figure S30| Wavelet transformed EXAFS data of Rb-CZF after reaction.

Chapter 4

Figure S31| Heating and cooling during CO-DRIFTS over Cs-CZF.

Figure S32| Additional CO adsorption DRIFTS experiment.

Figure S33| Maximum b-CO intensity over CZF, K-CZF, Rb-CZF and Cs-CZF.

Chapter 5

Figure S34| De-gassed pristine ZSM-5 analysed by ssNMR.

Figure S35| 1D ^{13}C ssNMR of composite catalyst after CO_2 hydrogenation co-fed with ^{13}C benzene (N2).

Figure S36| The complete 1D ^{13}C ssNMR of composite catalyst after low pressure $^{13}CO_2$ hydrogenation in the absence of co-fed benzene (N4).

Figure S37| Example of chromatogram of CO_2 hydrogenation hydrocarbon products in the presence of 50 mg benzene.

Figure S38| Chromatogram of $CO_2 + H_2$ control experiment in the absence of the $RhIn/MgO_x$ catalyst in the presence of 200 mg benzene.

List of Tables

Chapter 2

Table S1| Valve turning sequence during CO_2 hydrogenation GC gas analysis.

Chapter 5

Table S2| All trace liquid products retrieved after CO_2 hydrogenation as identified by GC-MS.

Chapter 2

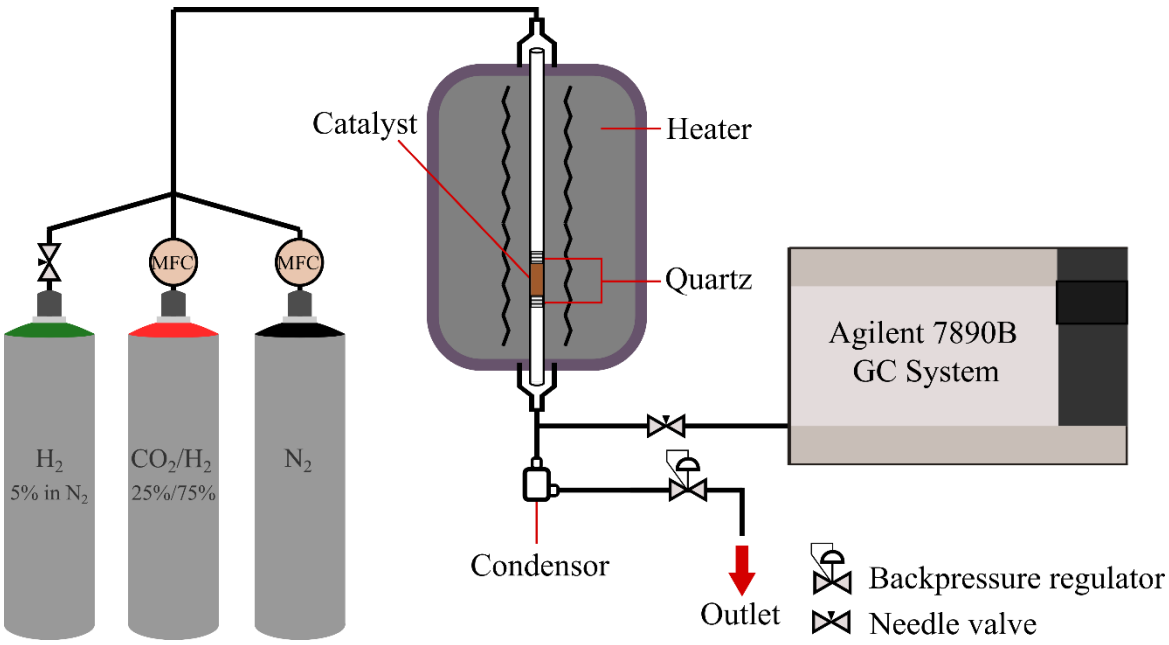

Figure S1| Schematic representation of the catalytic plug flow reactor. The reactor body is composed of a stainless steel outer tube (with 12.7 mm diameter) in which a quartz inner tube (with 8mm diameter) is placed to hold the catalyst. The reactor sits inside a three-stage heater. The catalyst is pressed between quartz wool and positioned in the centre of the third heating stage. The reductant gas (5% H_2 in N_2) is supplied to the reactor by a needle valve. The high pressure gasses (CO_2/H_2 mixture and pure N_2) are supplied by mass flow controllers (MFC). Back pressure is by a manual back pressure regulator (BPR). A condenser is used to prevent heavy hydrocarbons from entering the BPR. The analyte gas flow to the GC is regulated by a needle valve.

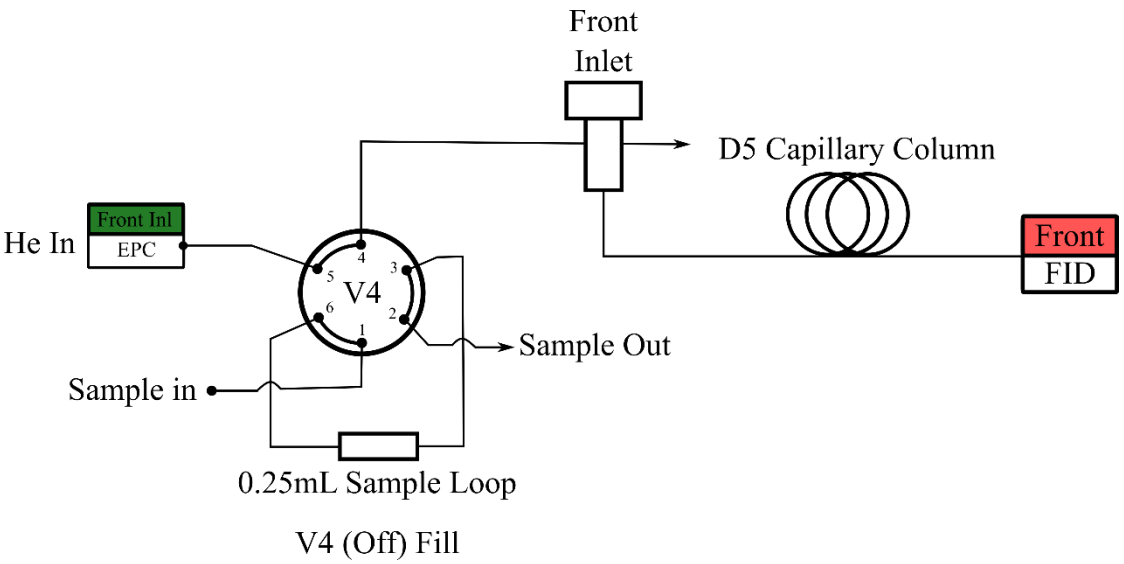

Figure S2| Valve diagram with valve 4 in channel 1 **in OFF position.** In this position, the sample gas flows through the 6-way valve such that the sample loop is filled, while only carrier gas flows to the FID detector.

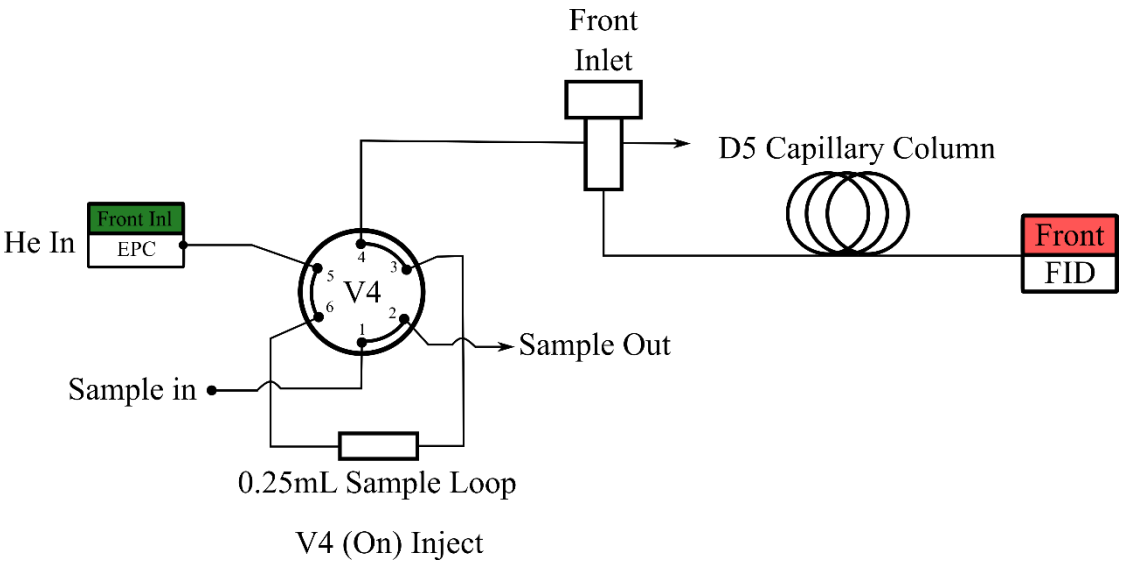

Figure S3| Valve diagram channel 1 **with valve 4 in ON position.** In this position, the sample gas from the sample loop is injected into the Split/Splitless inlet in Split mode, after which the sample is separated on the non-polar DB-5 column. After separation and elution the sample components are detected by the FID.

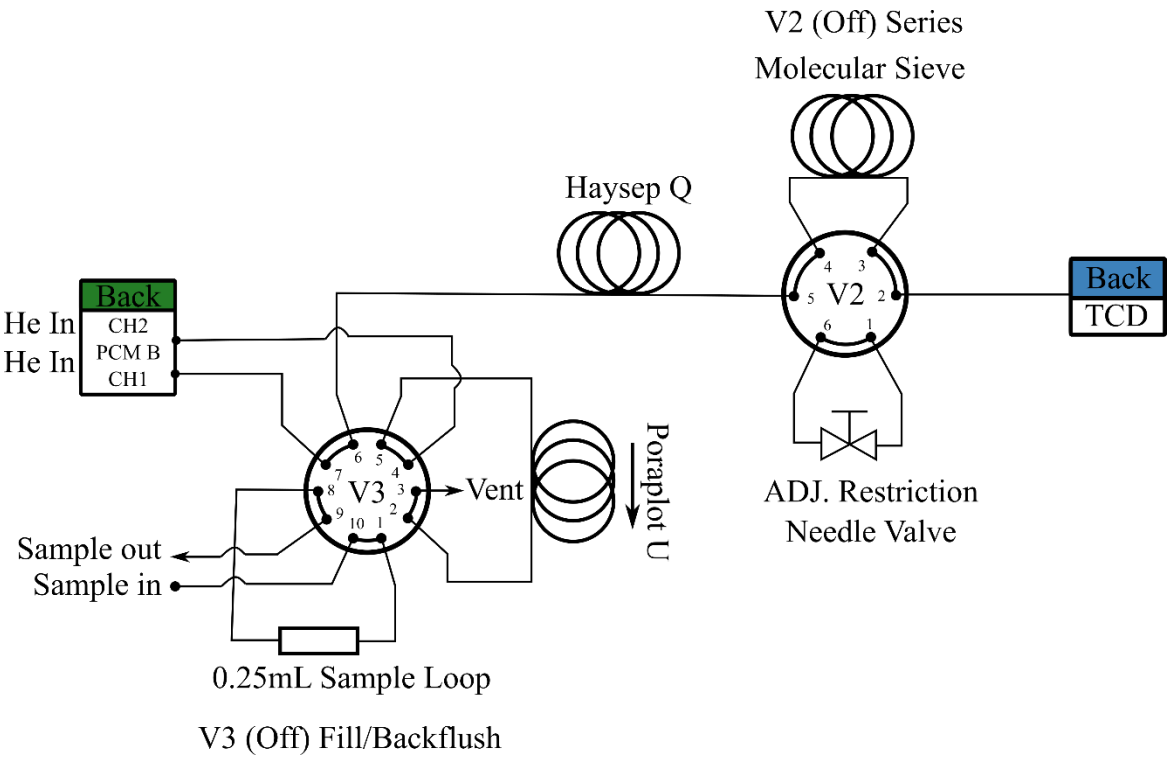

Figure S4| Valve diagram channel 2 with valve 2 and 3 in OFF position. In this position, the sample gas flows through the 10-way valve such that the sample loop is filled, while only carrier gas flows to TCD detector and through all columns. Any gas remaining in the Poraplot U column is vented in this position.

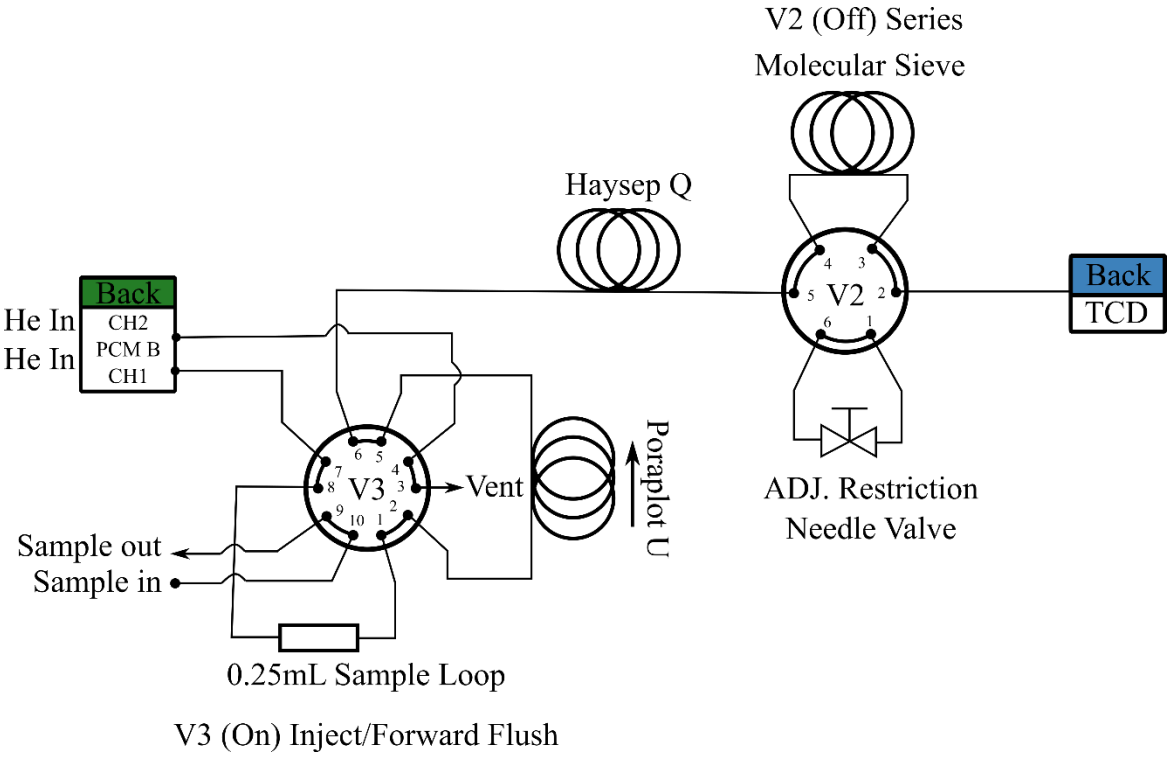

Figure S5| Valve diagram channel 2 with valve 2 in ON and 3 in OFF position. In this position, the sample gas is injected from the 10-way valve into the polar porous polymer (Poraplot U) backflushing column. After the initial separation the gas is further separated by the packed Hayesep Q and Molecular Sieve columns and finally is detected by the TCD.

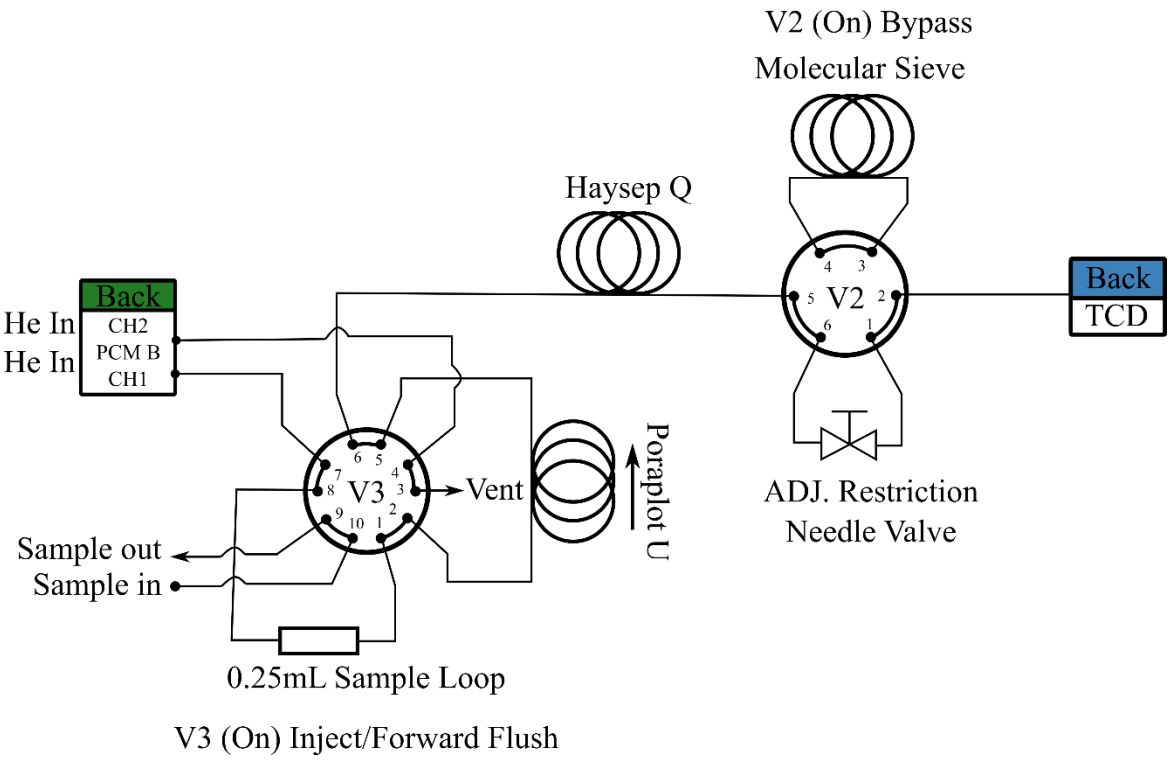

Figure S6| Valve diagram channel 2 **with valve 2 and 3 in ON position.** In this position, the sample gas is injected from the 10-way valve into the polar porous polymer (Poraplot U) backflushing column. After the initial separation the gas is further separated by the Hayesep Q. Instead of being introduced into the Molecular Sieve column, the sample components travel through a restrictor, which equalizes the pressure across valve 2. Finally the sample is detected by the TCD.

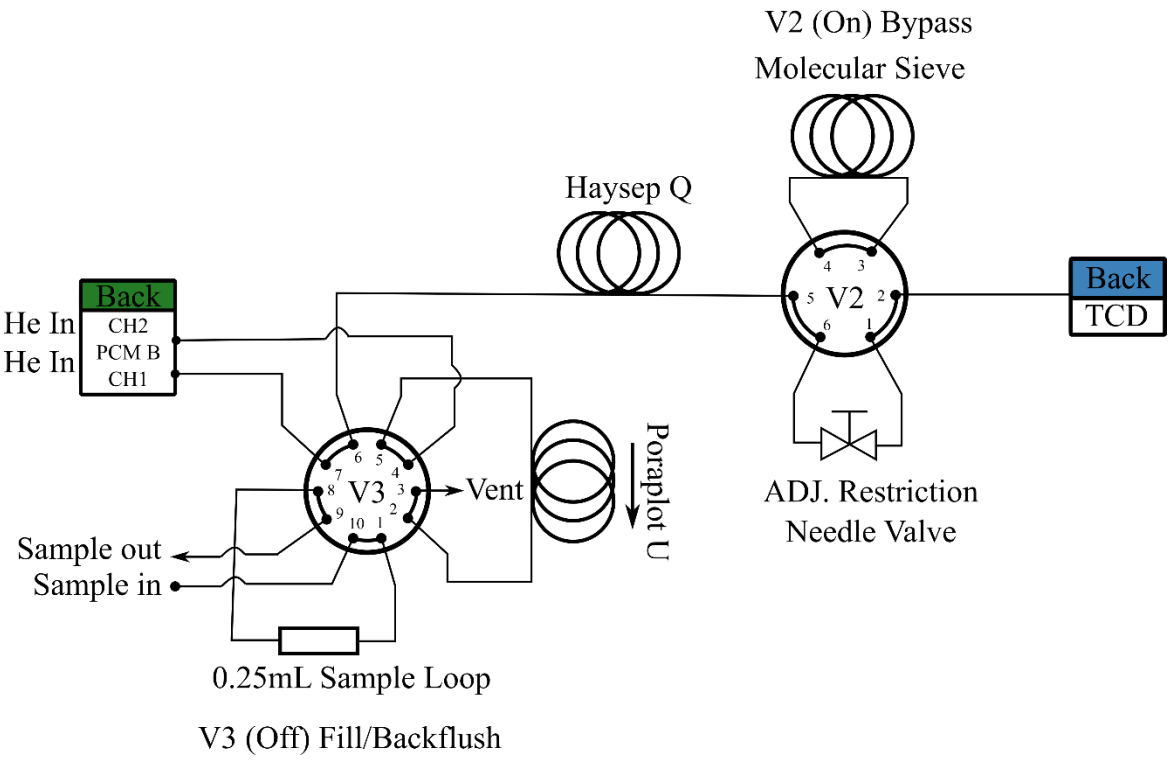

Figure S7| Valve diagram channel 2 **with valve 2 in ON and 3 in OFF position.** In this position, the sample gas is reintroduced into the sample loop, while any remaining sample gas is vented from the backflushing Poraplot U column. Any gas eluted earlier from the Poraplot U column is separated by the packed Hayesep Q column. The Molecular Sieve column is by-passed. Instead, the sample components travel through a restrictor, which equalizes the pressure across valve 2. Finally the sample is detected by the TCD.

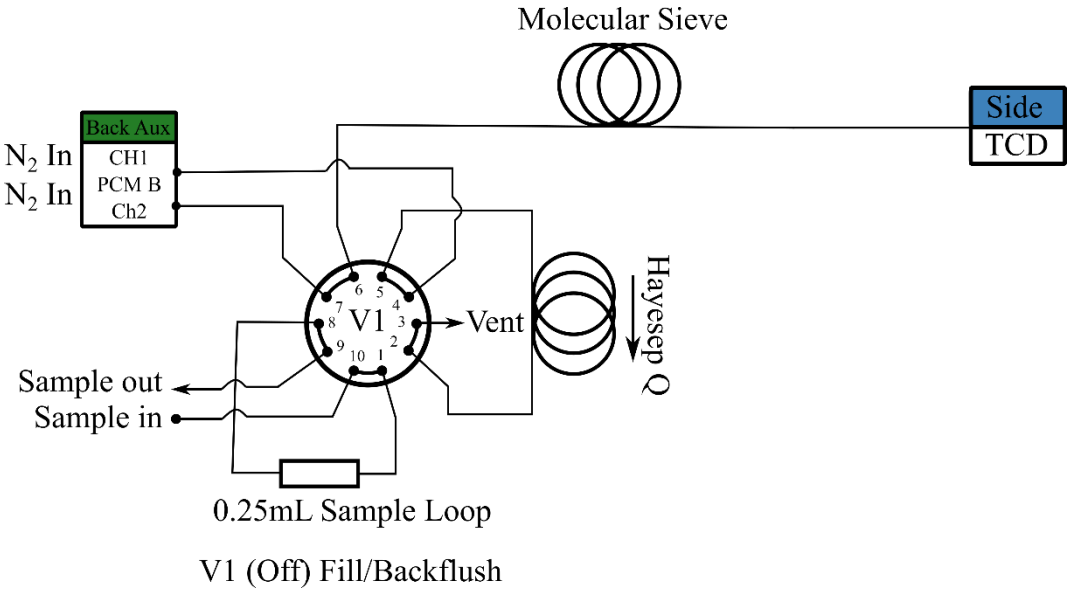

Figure S8| Valve diagram channel 3 (not used for analysis) with valve 1 in OFF position. In this position, the sample gas flows through the 10-way valve such that the sample loop is filled, while only carrier gas flows to the FID detector. In case any sample is present in the Hayesep Q column it is vented in this position

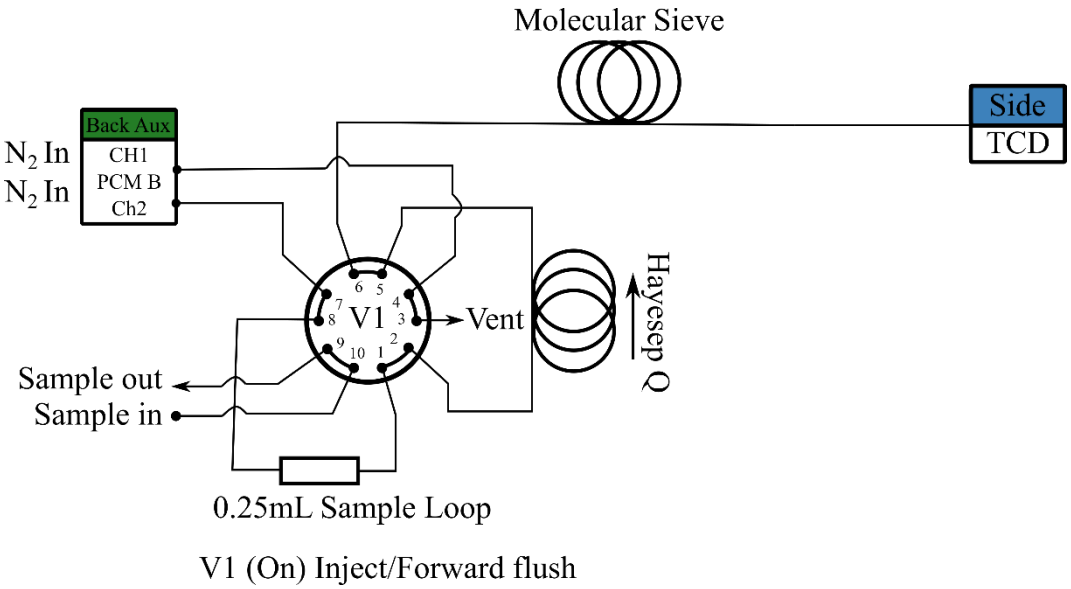

Figure S9| Valve diagram channel 3 (not used for analysis) with valve 1 in OFF position. In this position, the sample gas is injected from the 10-way valve into the packed Hayesep Q backflushing column. After the initial separation the gas is further separated by a Molecular Sieve column and finally is detected by the TCD.

Table S1| Valve turning sequence during CO_2 hydrogenation GC gas analysis.

Time [Min]	*Channel*	*Valve*	*Event*
0.01	*1*	*4*	*ON*
0.01	*2*	*3*	*ON*
0.01	*3*	*1*	*ON*
0.2	*3*	*1*	*OFF*
1.3	*2*	*2*	*ON*
8	*1*	*4*	*OFF*
14	*2*	*3*	*OFF*
29	*2*	*2*	*OFF*

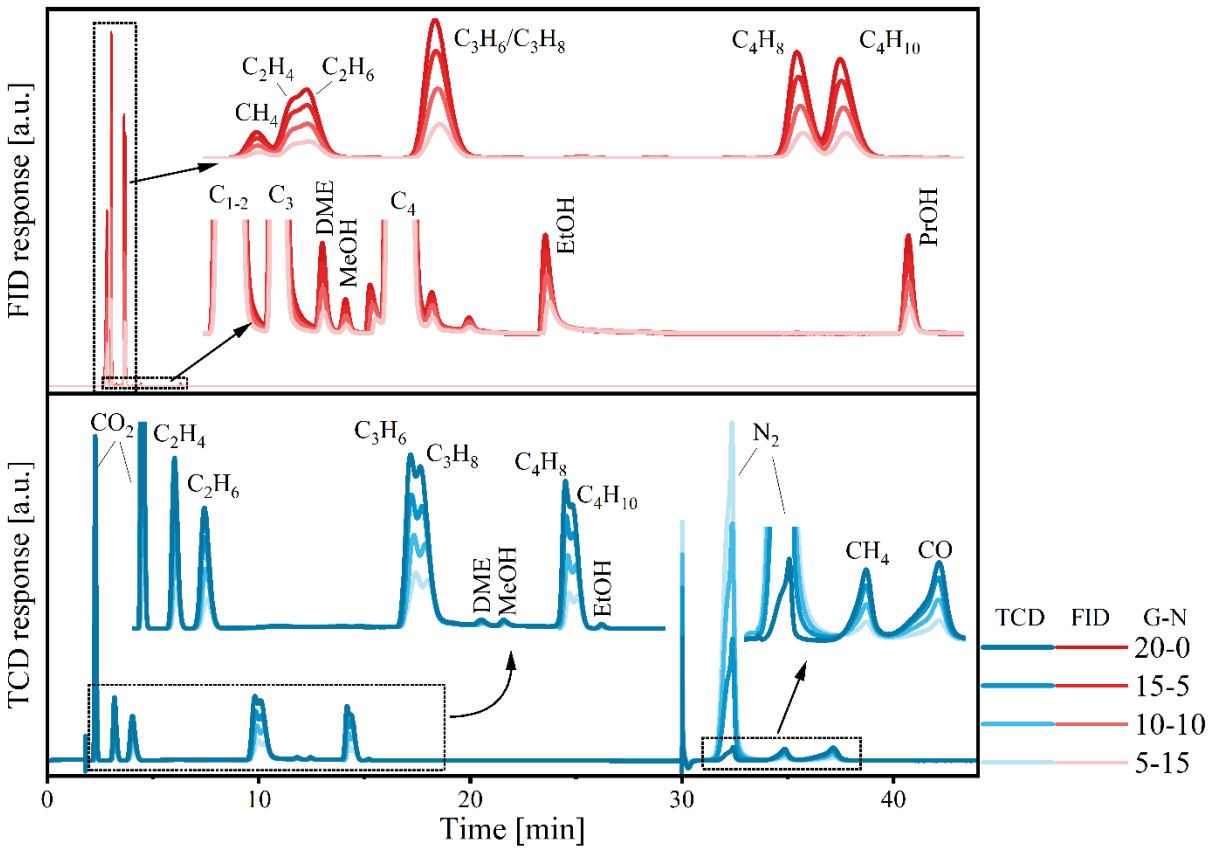

Figure S10| GC traces obtained from mixing a calibration gas with different ratios of N_2. To obtain the relative response factors of expected CO_2 hydrogenation product molecules, the change in their peak area upon dilution with N_2 was monitored. The gas-to-nitrogen ratio (G-N) is varied from 20 to 0 mL/min respectively to 5 to 15 mL/min respectively. The top and bottom panels show the obtained FID and TCD results respectively. The insets in the top panel show enlarged portions of the FID chromatograph from 2.65 to 3.9 minutes and from 2.65 to 6.6 minutes. The insets in the bottom panel show enlarged portions of the TCD chromatograph from 2 to 17 minutes and from 31 to 38 minutes. Labels indicate the molecules which each peak represent.

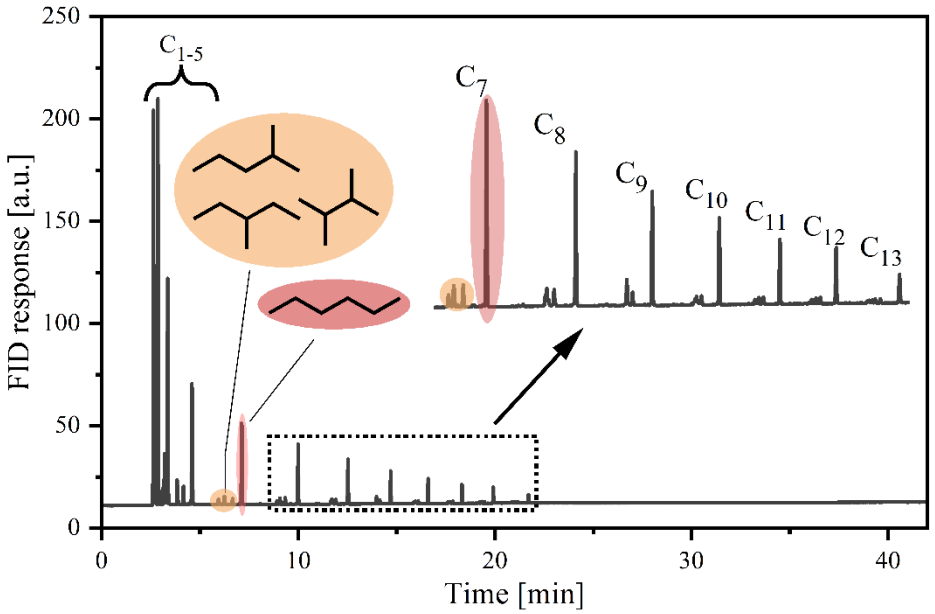

Figure S11| Example of a typical obtained during CO_2 hydrogenation over CZF. The FID trace shows the formation of C_1 to C_{13} hydrocarbons with linear (red) and branched structure (orange). In correspondence with their lower boiling point the branched hydrocarbons are eluted from the non-polar DB-5 column before their linear isomer.

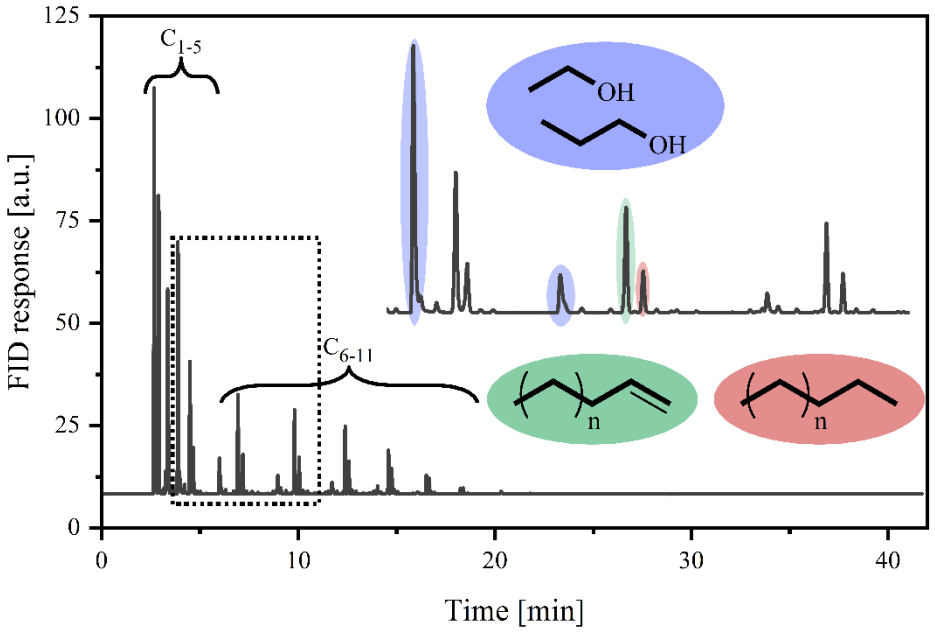

Figure S12| Example of a typical obtained during CO_2 hydrogenation over Cs-CZF. The FID trace shows the formation of C_1 to C_{11} paraffins (red) and olefins (green),). In correspondence with their lower affinity to the non-polar DB-5 column, olefins are eluted before their saturated equivalent. Furthermore, higher alcohols (blue) are identified by their tailing peak shape.

Chapter 3

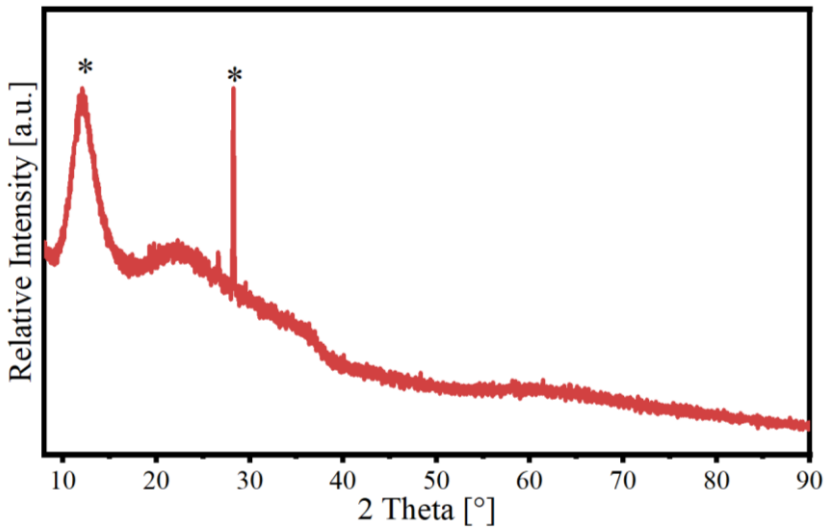

Figure S13| Diffractogram of calcined CZF sample. The peaks indicated by * are attributed to the sample holder.

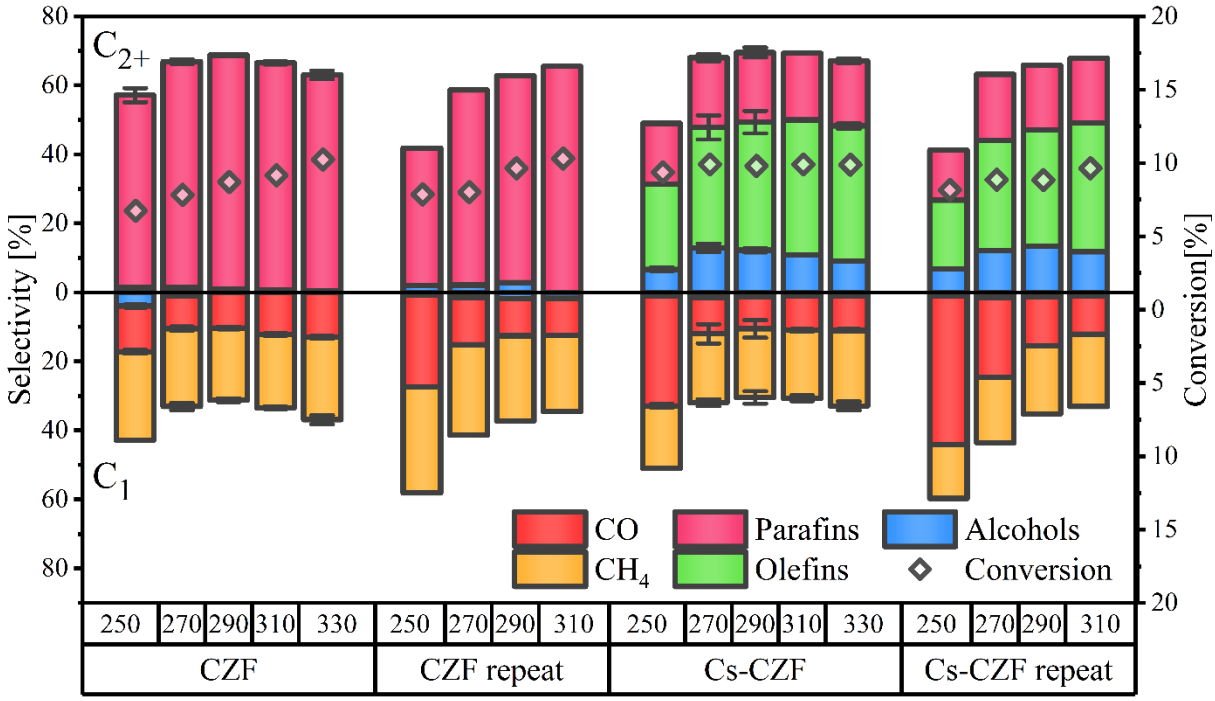

Figure S14| Catalytic repeatability results of CZF and Cs-CZF. The catalytic results of the originally synthesized CZF and Cs-CZF materials are shown next to the catalytic results obtained for a second batch of each catalyst. The repeat experiments were only carried out up to 310 °C. Error-bars are indicated for the originally obtained data showing relatively low variability between subsequent measurements. The CO_2 conversion is plotted with diamonds; The product distribution is shown as stacked columns. Products with a carbon number of 1 are plotted using negative values. The figure shows the repeatability of the original data. Although relatively more C1 products are obtained at 250 °C temperatures for the repeated samples, the effect of Cs-doping on the material is the same.

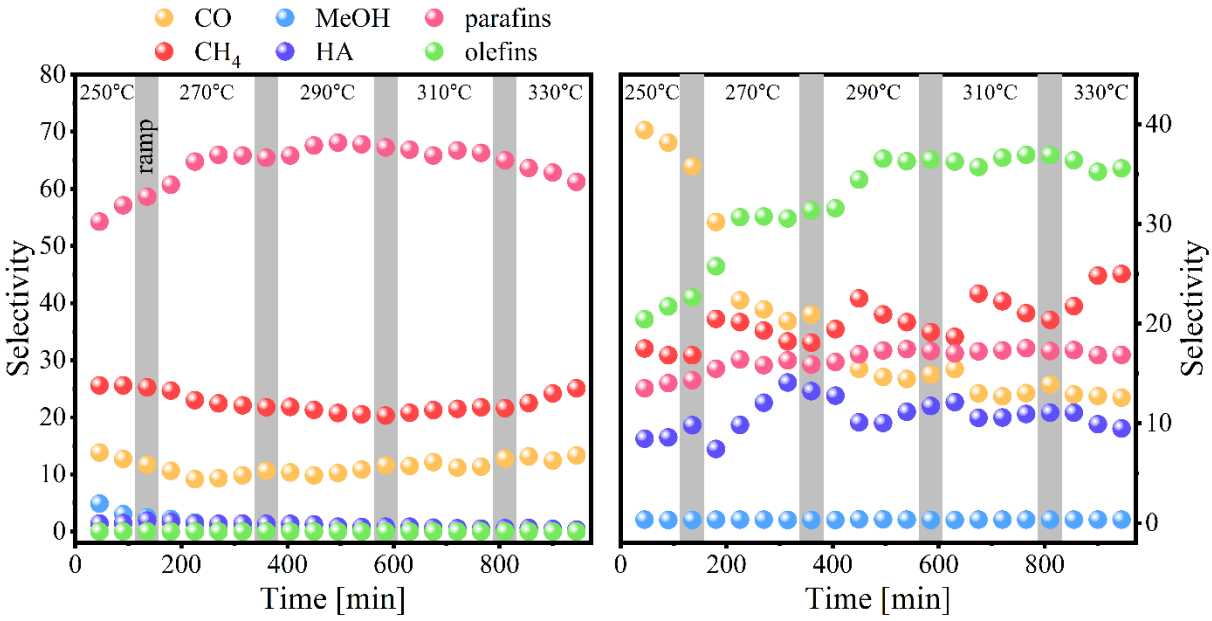

Figure S15| Reaction time point selectivity data for CZF (left) and Rb-CZF (right). The CO_2 hydrogenation reaction product selectivity is shown for each GC injection separately. The selectivity to CO, methanol, CH_4, C_{2+} paraffins, olefins and higher alcohols are indicated by the yellow, light blue, orange, red, green and dark blue spheres respectively. The data points in de shaped area were obtained during temperature ramping.

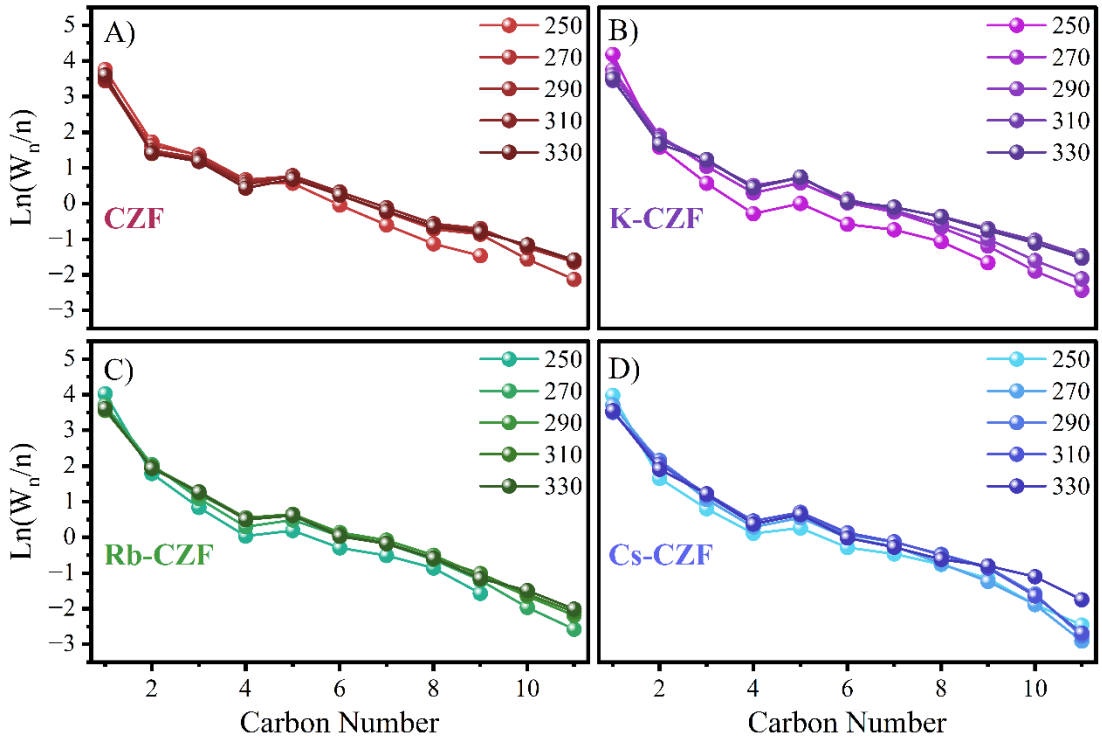

Figure S16| Non-fitted ASF function $ln(W_n/n)$ applied to catalytic data obtained from alkali metal doped and undoped CZF without offset.

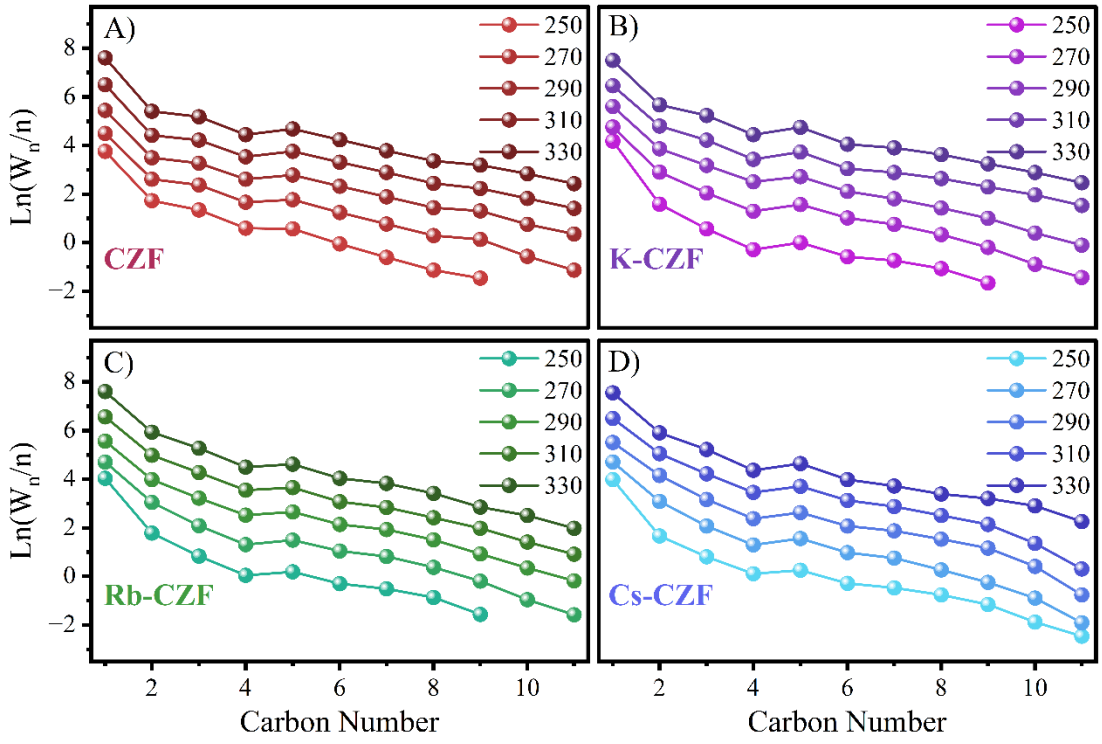

Figure S17| Non-fitted ASF function $ln(W_n/n)$ applied to catalytic data obtained from alkali metal doped and undoped CZF with a small offset.

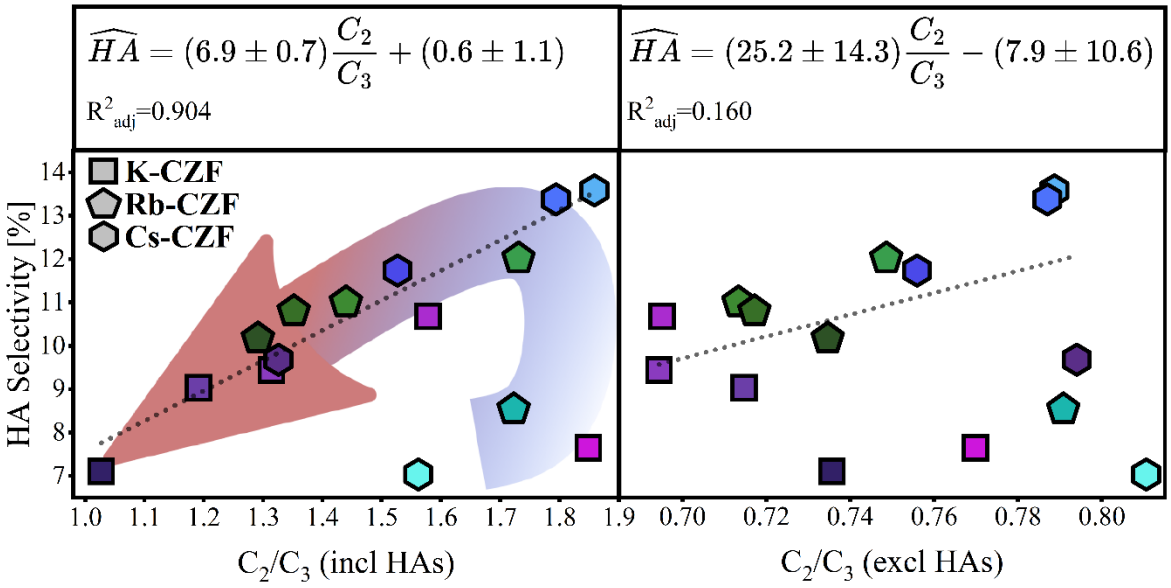

Figure S18| Linear relationship between HA selectivity and C_2/C_3 ratio. The figure shows the higher alcohols selectivity plotted against the C_2/C_3 ratio. On the left the C_2/C_3 ratio is taken to include higher alcohols; on the right the C_2/C_3 is shown excluding higher alcohols. The data for K-CZF, Rb-CZF and Cs-CZF are indicated by squares, pentagons and hexagons respectively. Data obtained at higher temperatures are indicated in darker colours. The arrow follows the general trajectory as the temperature is increased from 250 to 330 °C. Linear fitting is applied to the data obtained at temperatures above 250 °C, the resulting linear function is given by $\widehat{HA}$.

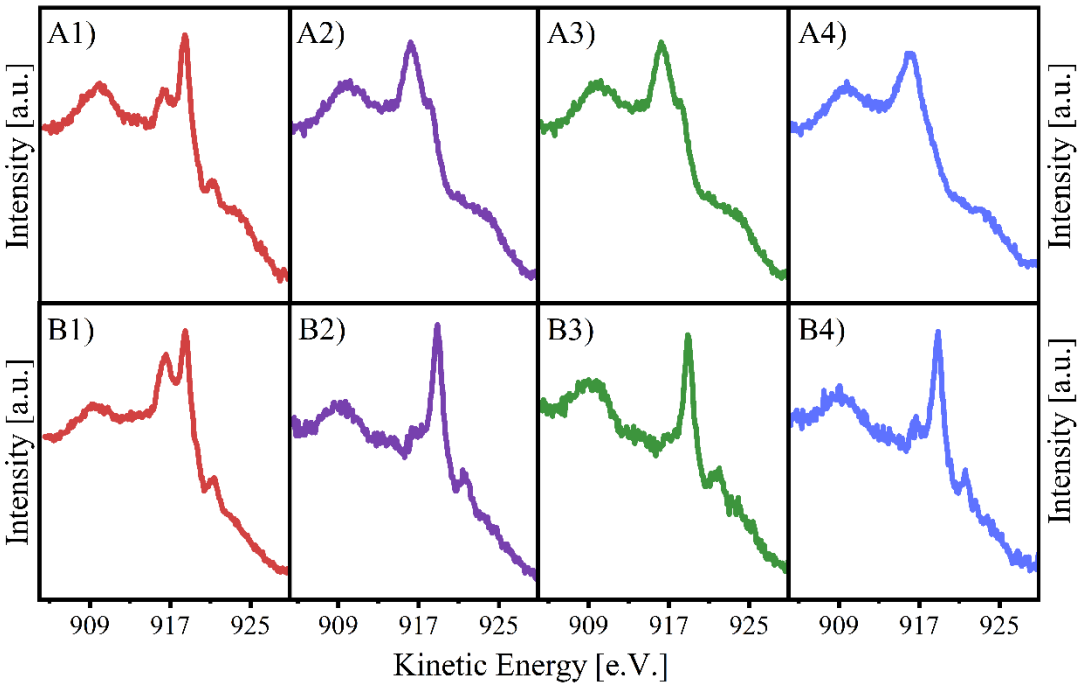

Figure S19| Raw data obtained on Cu LMM spectra of doped and undoped samples before and after reaction. Panels A1, 2, 3 and 4 show the Cu LMM spectra of CZF, K-CZF, Rb-CZF and Cs-CZF after reduction in red, purple, green and blue respectively. Panels B1, 2, 3 and 4 show the Cu LMM spectra of CZF, K-CZF, Rb-CZF and Cs-CZF after reaction in red, purple, green and blue respectively. The spectral broadening observed in A4 is due to samples charging.

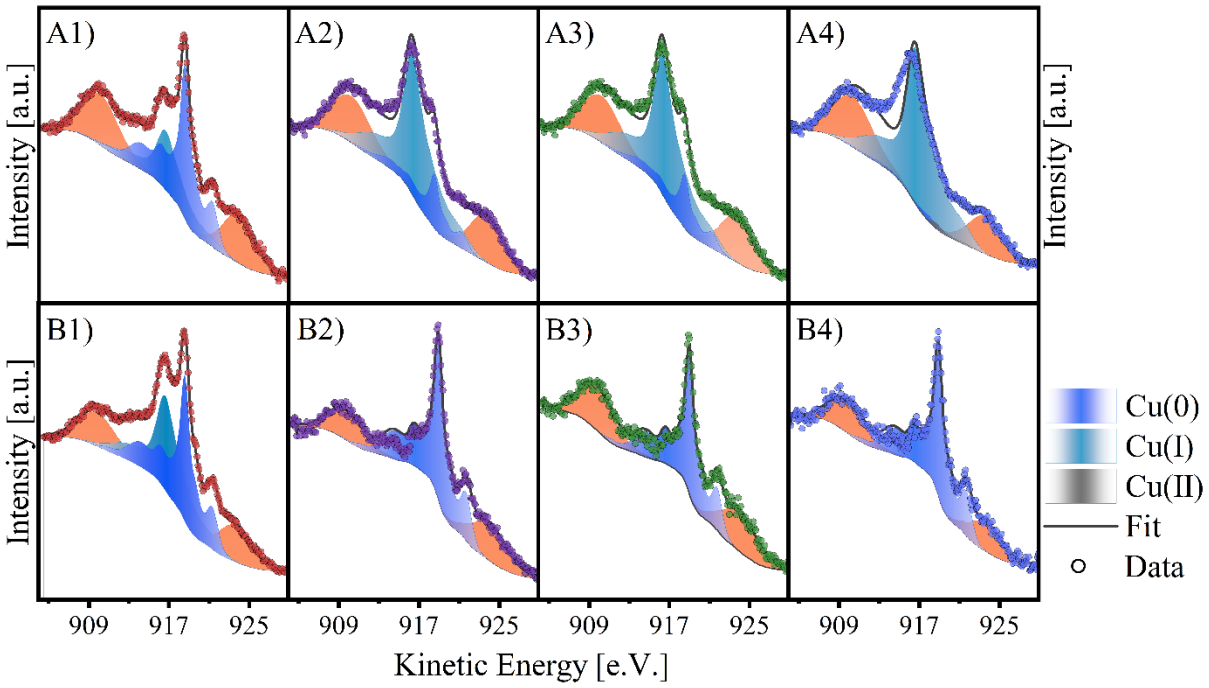

Figure S20| Cu LMM spectra of doped and undoped samples before and after reaction. Panels A1, 2, 3 and 4 show the Cu LMM spectra of CZF, K-CZF, Rb-CZF and Cs-CZF after reduction in red, purple, green and blue respectively. Panels B1, 2, 3 and 4 show the Cu LMM spectra of CZF, K-CZF, Rb-CZF and Cs-CZF after reaction in red, purple, green and blue respectively. The Cu^0, Cu^{1+} and Cu^{2+} peak model envelopes are shown by the dark blue, light blue and grey areas respectively. The orange area is related to overlapping Zn peaks. The poor fitting in panel A4 is due to samples charging.

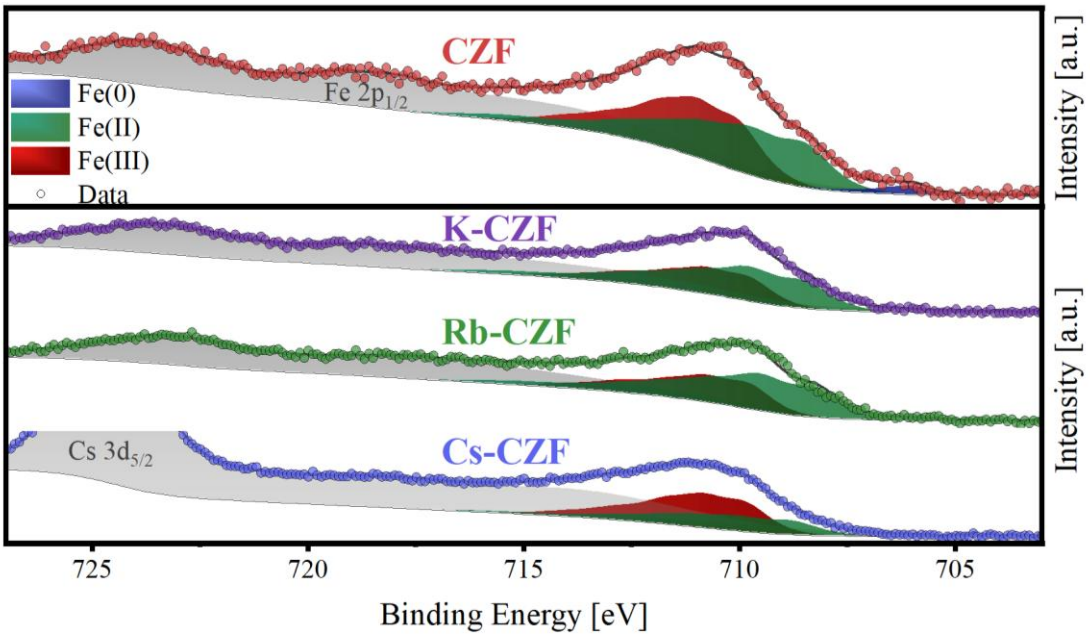

Figure S21| Fe 2p XPS spectra of reduced samples. The spectra obtained for CZF, K-CZF, Rb-CZF and Cs-CZF are plotted in red, purple, green and blue respectively. The contribution of Fe^0, Fe^{2+} and Fe^{3+} is illustrated by the blue, green and red areas respectively. The grey area indicates the arbitrarily fitted $2p_{1/2}$ region. A grey line indicates the fit.

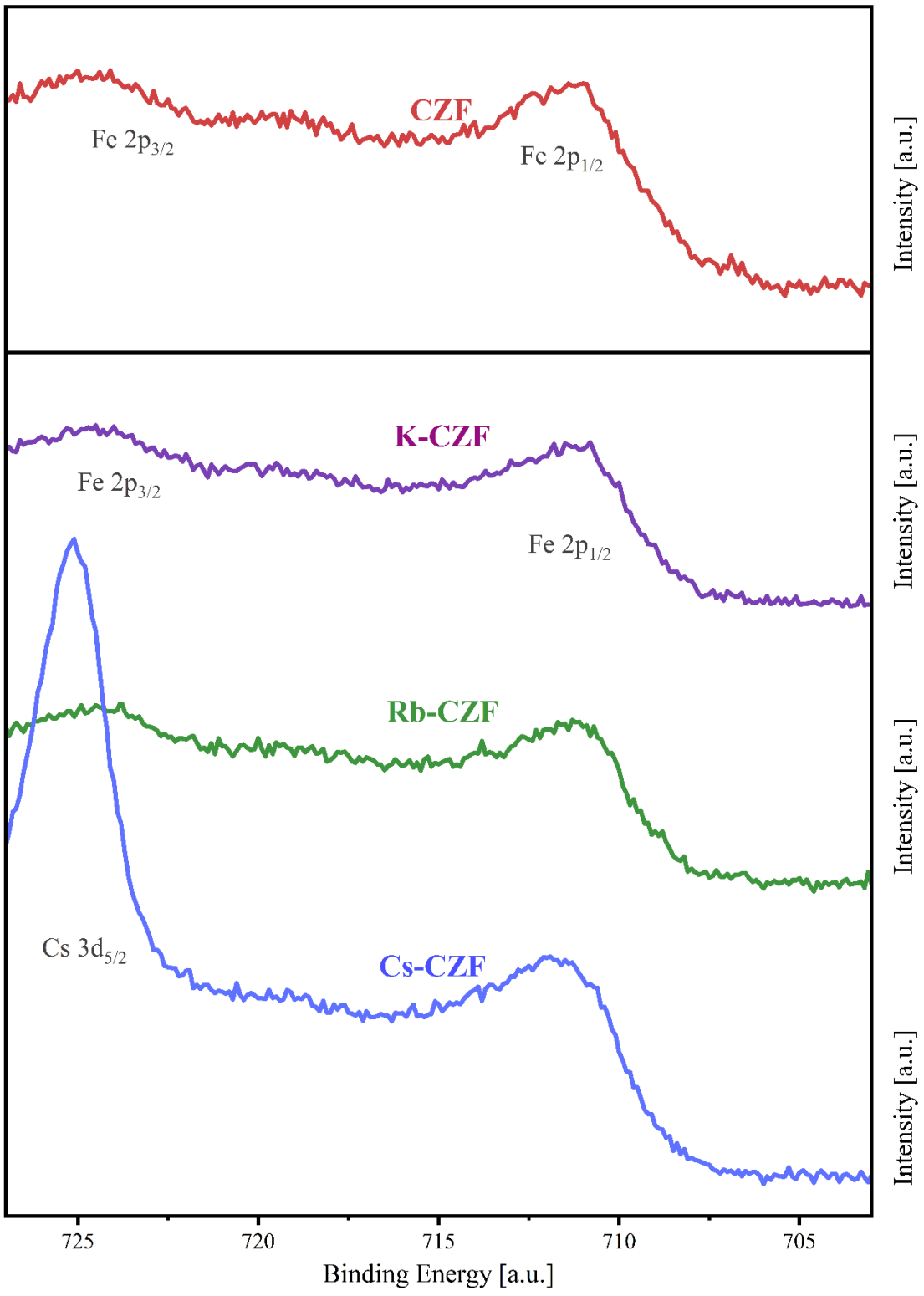

Figure S22| Raw data obtained for Fe 2p spectra obtained from doped and undoped catalysts after reduction in 5% H_2 at 360 °C.

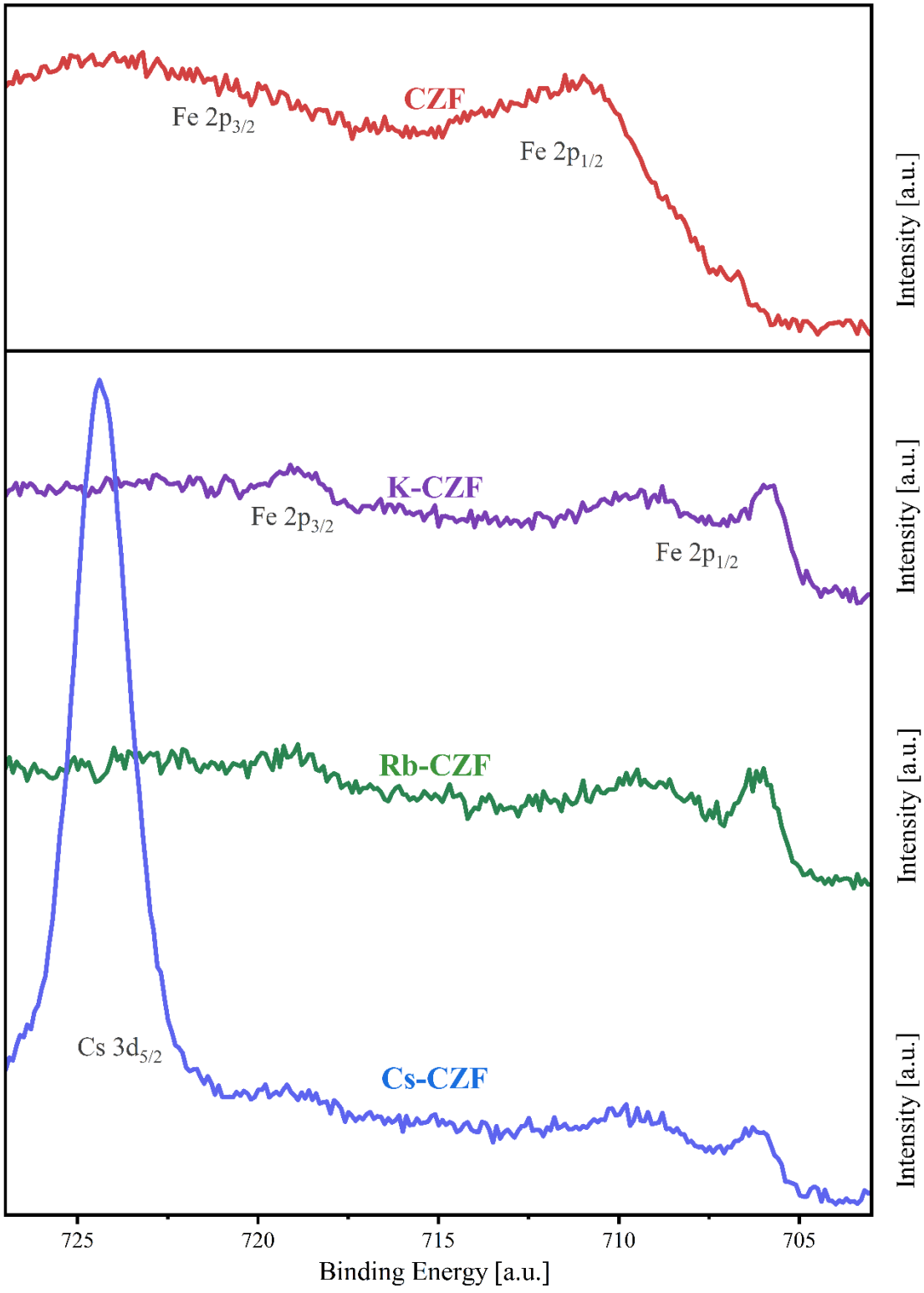

Figure S23| Raw data obtained for Fe 2p spectra obtained from doped and undoped catalysts after CO_2 hydrogenation.

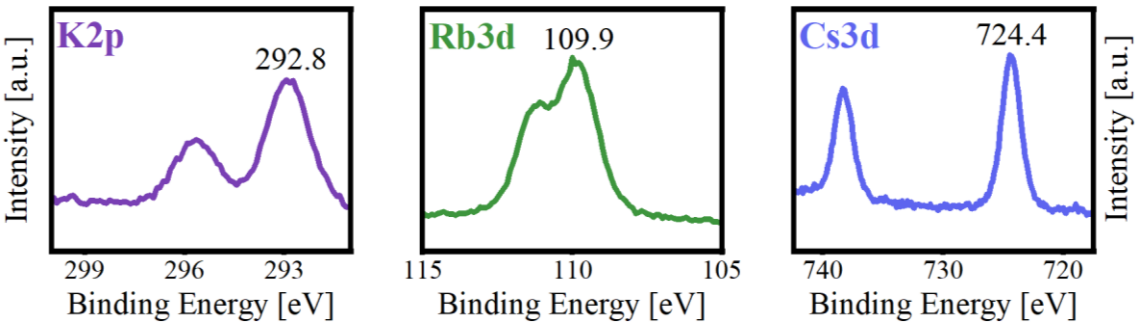

Figure S24| XPS spectra of AMs of spent samples. From left to right the spectra obtained for K, Rb and Cs are shown in purple, green and blue respectively. The position of the peak maximum is indicated.

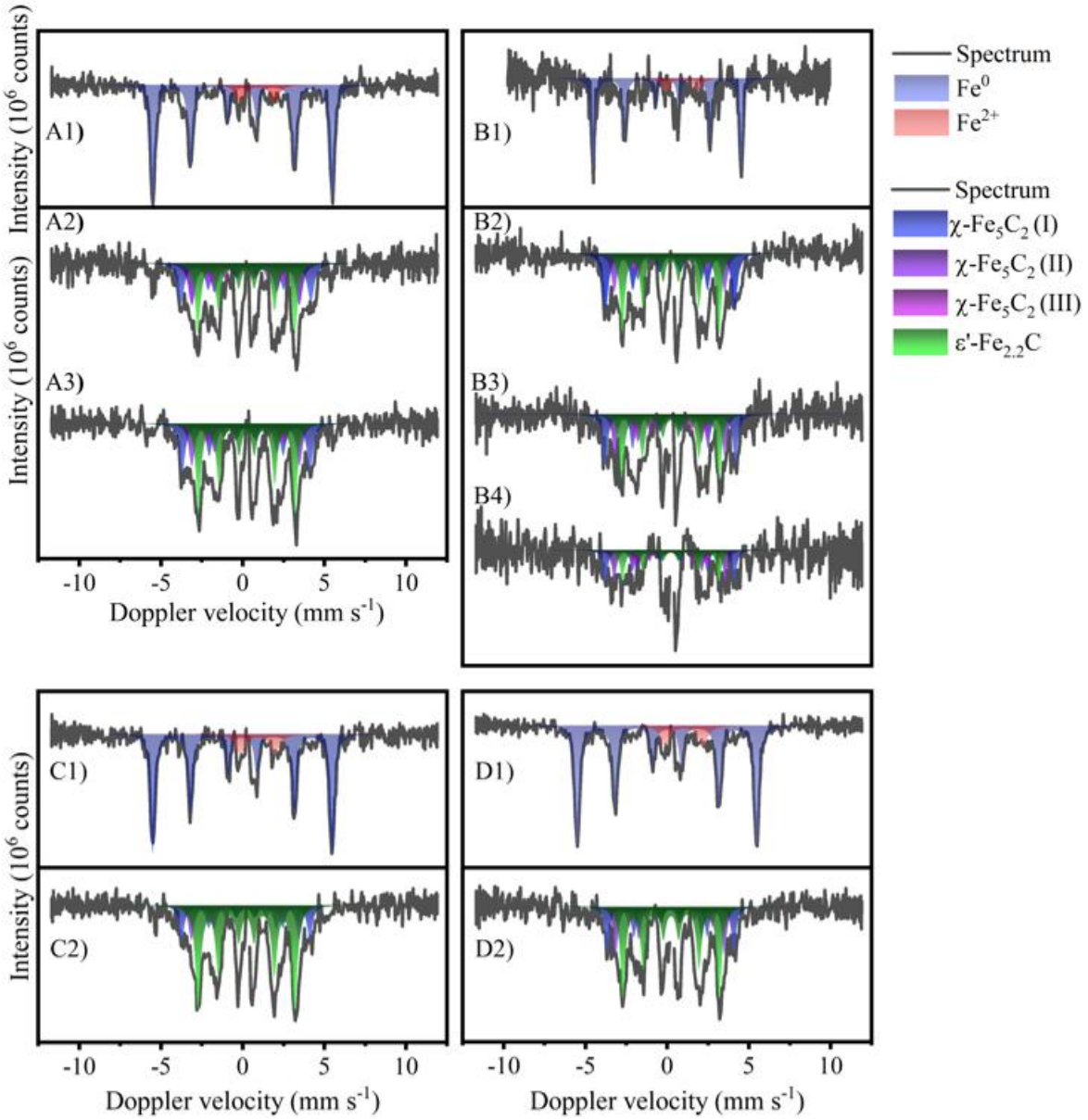

Figure S25| Mössbauer spectra of reduced and spent samples. Panels A1, B1, C1 and D1 show the collected spectra for CZF, Cs-CZF, Rb-CZF and K-CZF after reduction. The spectra in A2-3, B2-4, C2 and D2 show the spectra of the catalyst after reaction. For details see the methods Section 2.2.2.5.

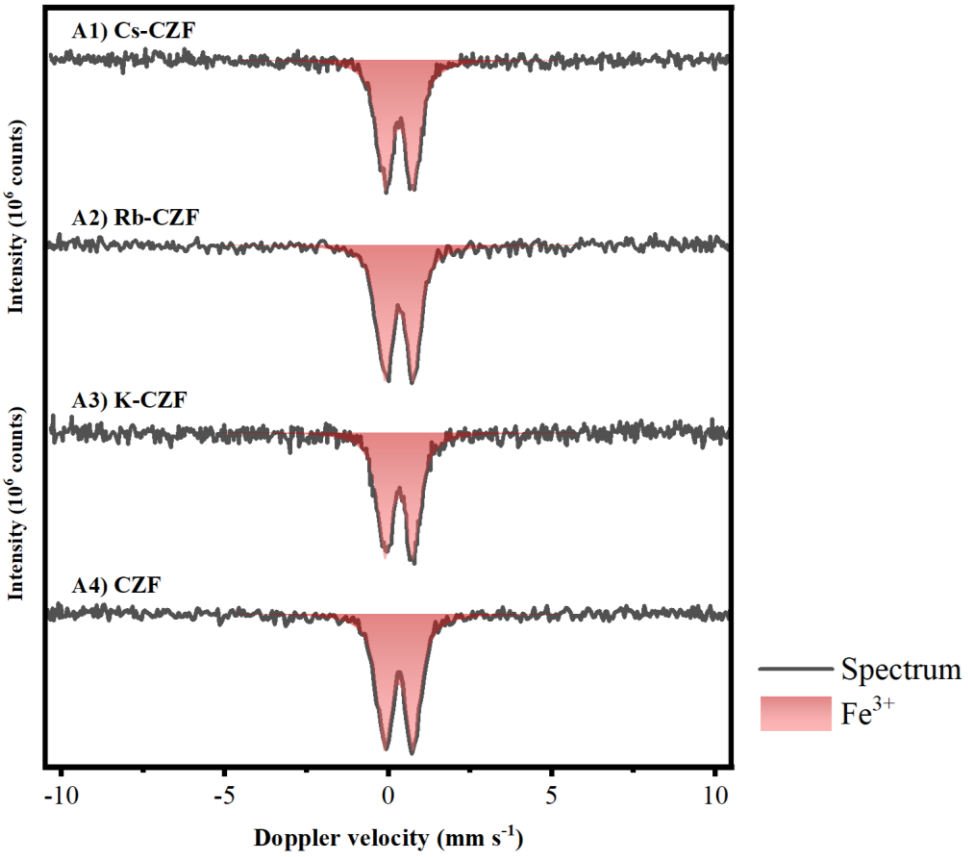

Figure S26| Mössbauer spectrum of calcined samples at 26.85 °C. The spectra obtained for Cs-CZF, Rb-CZF, K-CZF and CZF are plotted in A1, A2, A3 and A4 respectively. All spectra are fitted with a single doublet.

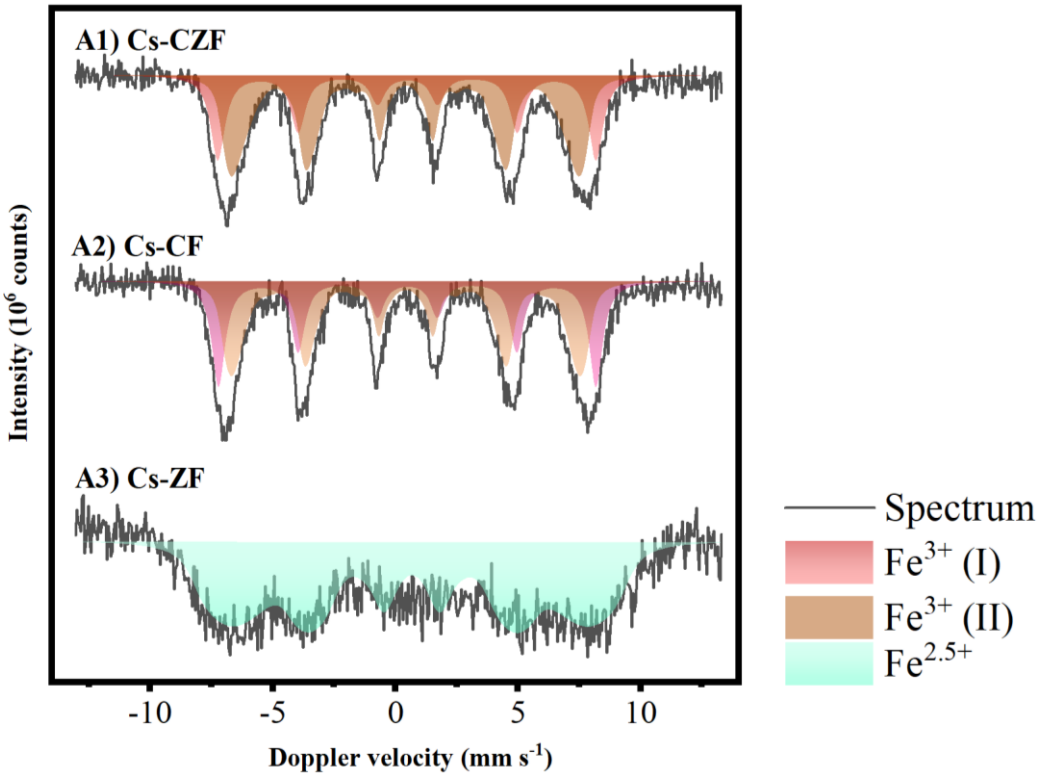

Figure S27| Mössbauer spectrum of calcined samples at 4.2 K. The spectra obtained for Cs-CZF and reference materials Cs-CF and Cs-ZF K-CZF are plotted in A1, A2 and A3 respectively. All spectra are fitted with a single doublet.

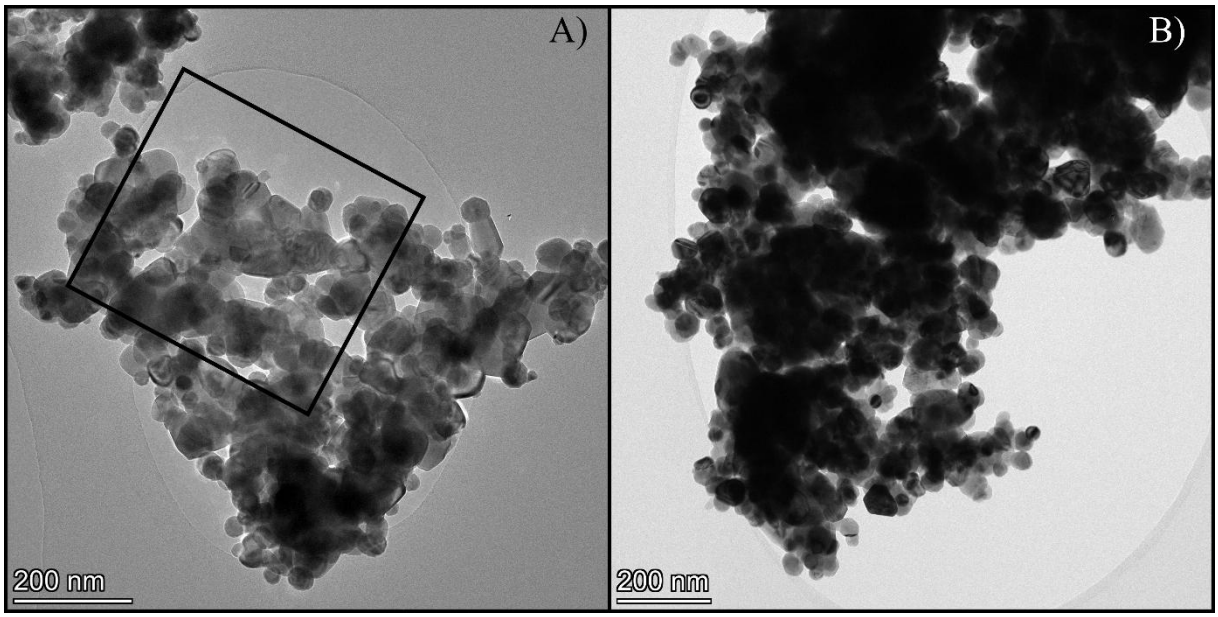

Figure S28|Transmission Electron Microscope image of CZF and Rb-CZF after reaction. Panels A and B show the morphology of CZF and Rb-CZF after reaction respectively. The box in panel A indicates the region analysed in detail in Figure 27.

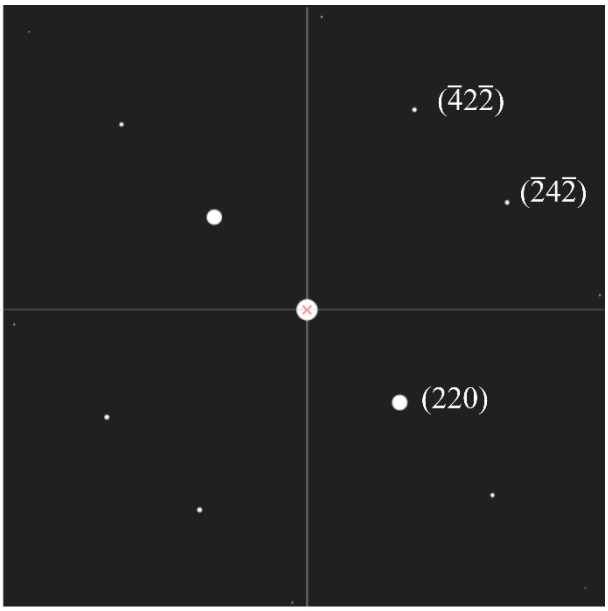

Figure S29| Simulated Electron diffraction pattern of Fe_3O_4.

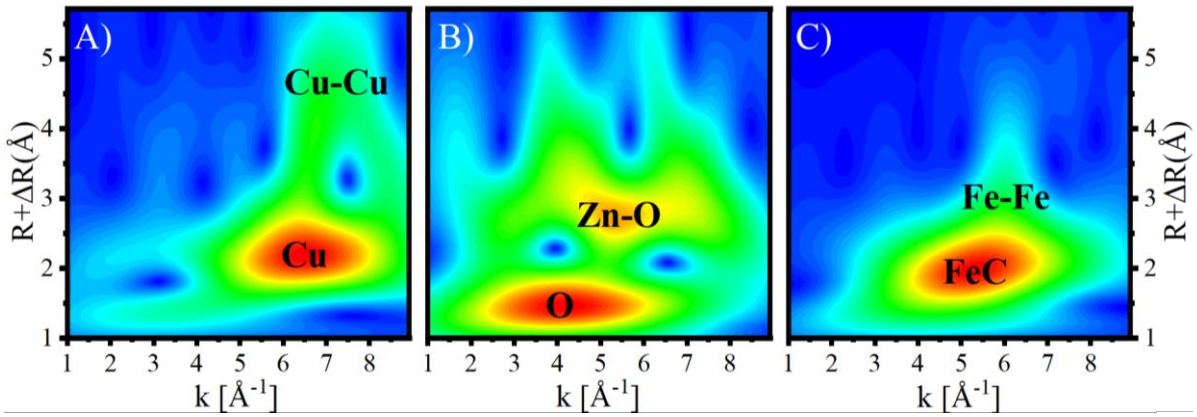

Figure S30| Wavelet transformed EXAFS data of Rb-CZF after reaction. Panel A, B and C show the wavelet transform of the Cu, Zn and Fe K-edge respectively. The atoms involved in the scattering paths are indicated.

Chapter 4

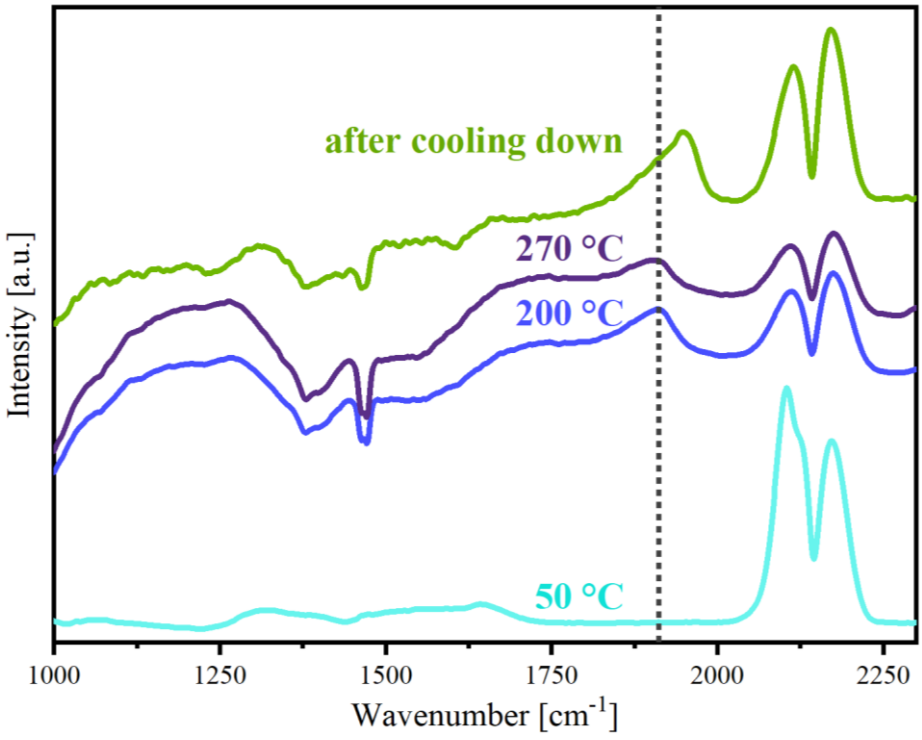

Figure S31| Heating and cooling during CO-DRIFTS over Cs-CZF. The spectra in cyan, blue and purple were taken while flowing 1% CO in N_2 at 50, 200 and 270 °C respectively and are identical to those presented in the main text. The green spectrum was obtained after cooling down to 25 °C after the completion of the temperature ramping procedure.

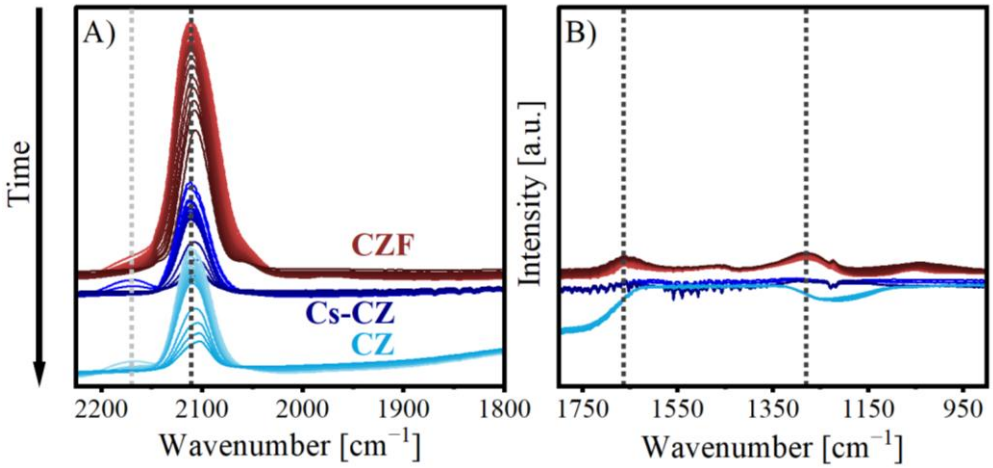

Figure S32| Additional CO adsorption DRIFTS experiment. The figure shows the evolution of the DRIFT absorption bands during the desorption of CO from CZF (red/top), Cs-CZ (dark blue/middle) and CZ (light blue/bottom) under continuous flushing with N_2. For comparison the black dotted reference lines are centred at the initial band positions for CZF. The grey reference line indicates the CO band which can be exclusively be attributed to the gas phase. The regions for CO and carbonate like species are shown in panel A and B respectively.

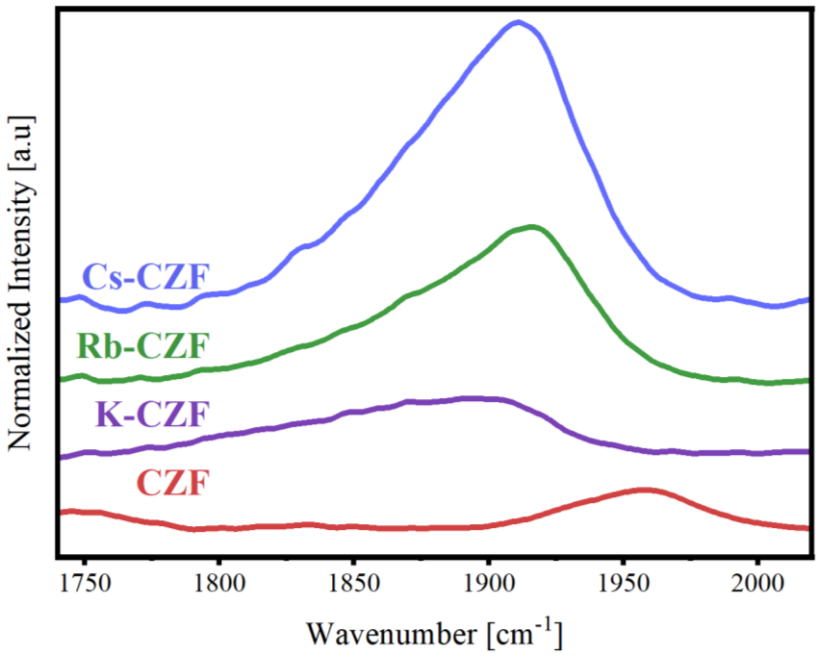

Figure S33| Maximum b-CO intensity over CZF, K-CZF, Rb-CZF and Cs-CZF. The figure shows the maximum b-CO band intensity obtained over Cs-CZF (at 190 °C), Rb-CZF (at 230 °C), K-CZF (at 230 °C) and CZF (at 240 °C) in blue, green, purple and red respectively. The spectra are normalised to the background measured at 2635 cm^{-1}

Chapter 5

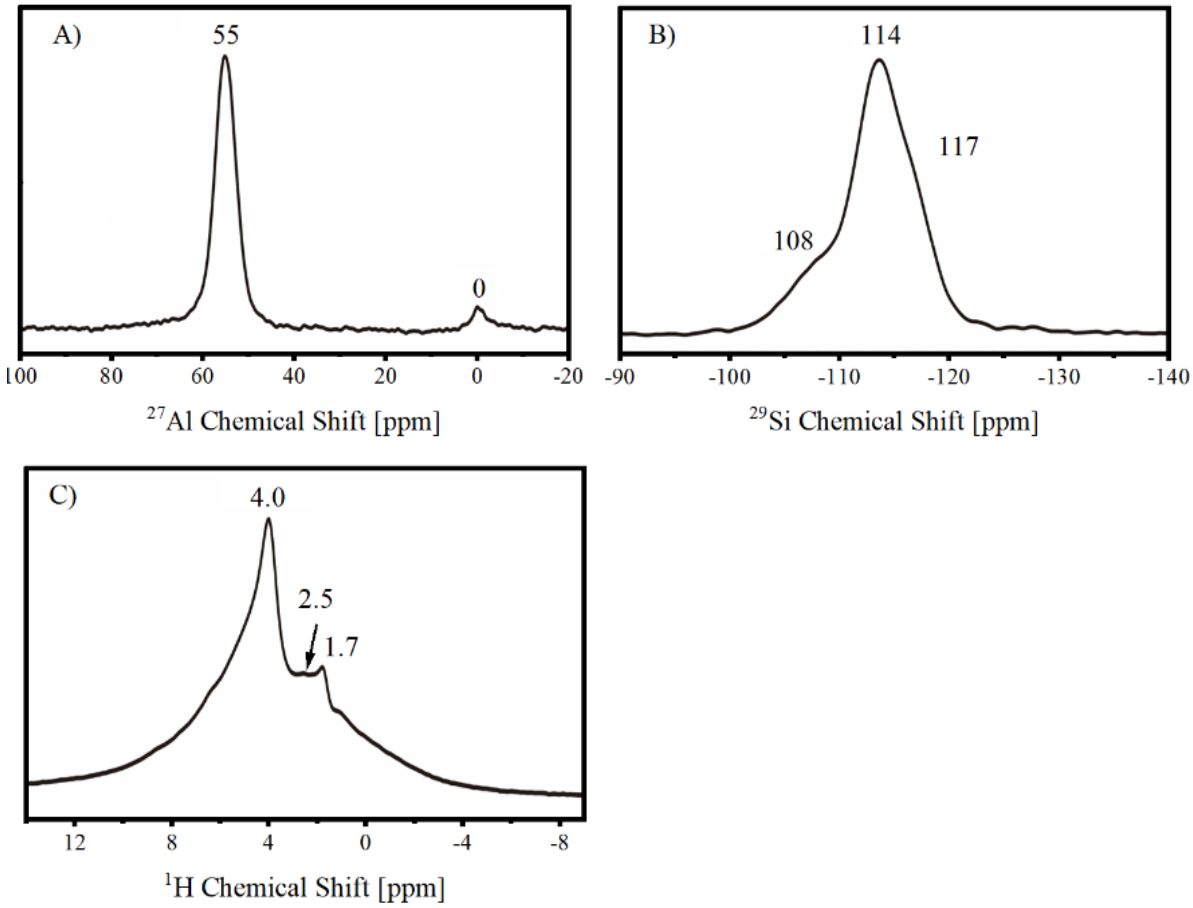

Figure S34| De-gassed pristine ZSM-5 analysed by ssNMR. Panel A shows the spectrum of ^{27}Al. Panel B shows the spectrum of ^{29}Si. Panel C shows the spectrum of ^{1}H.

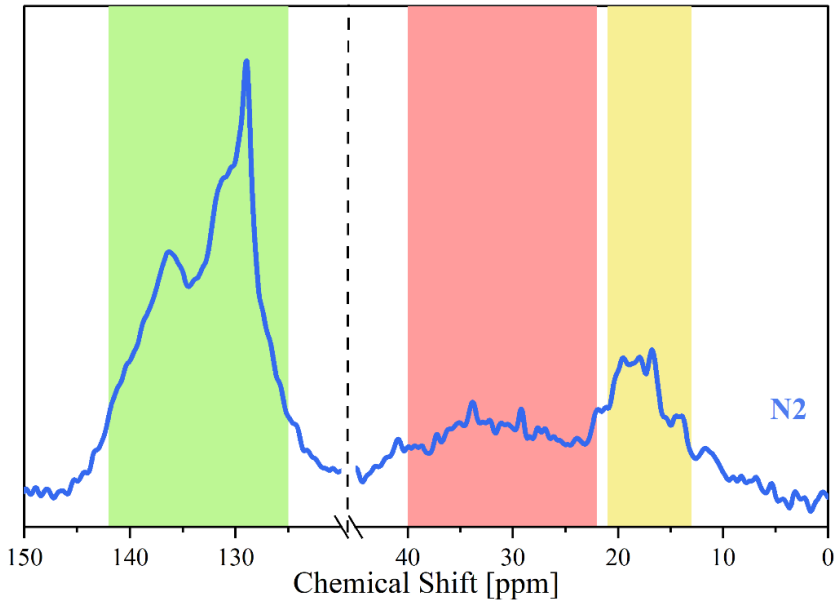

Figure S35| 1D ^{13}C ssNMR of composite catalyst after CO_2 hydrogenation co-fed with ^{13}C benzene (N2).

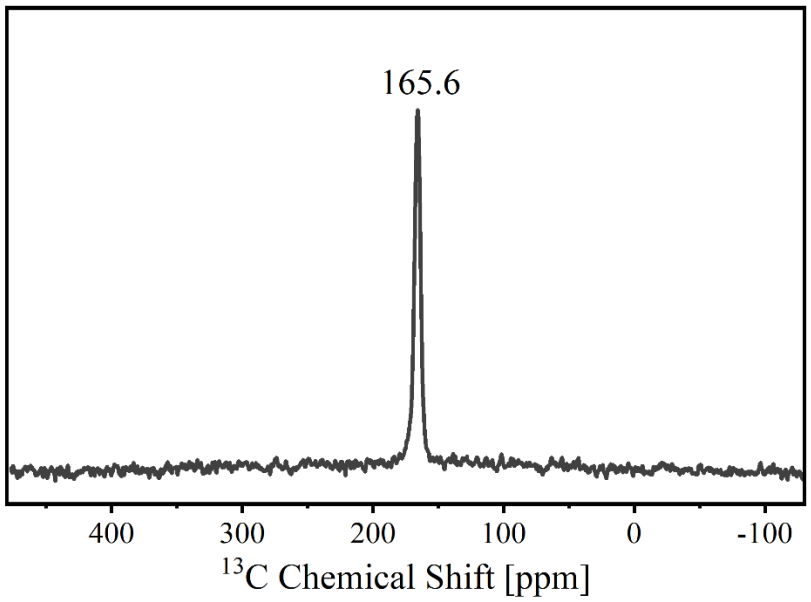

Figure S36| The complete 1D ^{13}C ssNMR of composite catalyst after low pressure $^{13}CO_2$ hydrogenation in the absence of co-fed benzene (N4).

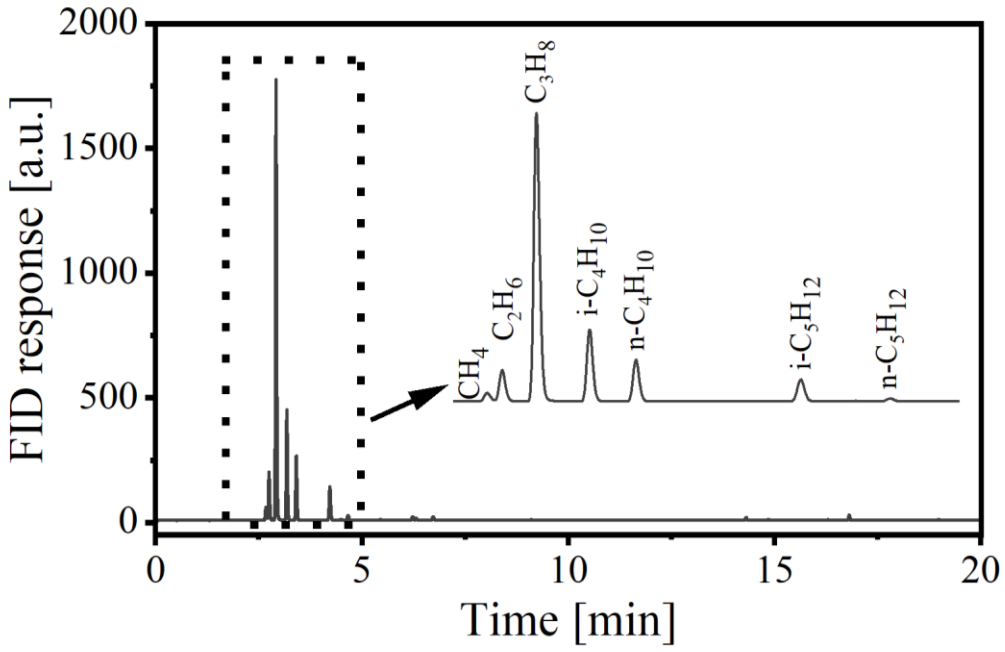

Figure S37| Example of chromatogram of CO_2 hydrogenation hydrocarbon products in the presence of 50 mg benzene. The FID response is shown for the first 20 minutes of the measurements. The region associated with gas products is enlarged and labelled. The prefix *i*- and *n*- indicate linear and branched hydrocarbons respectively.

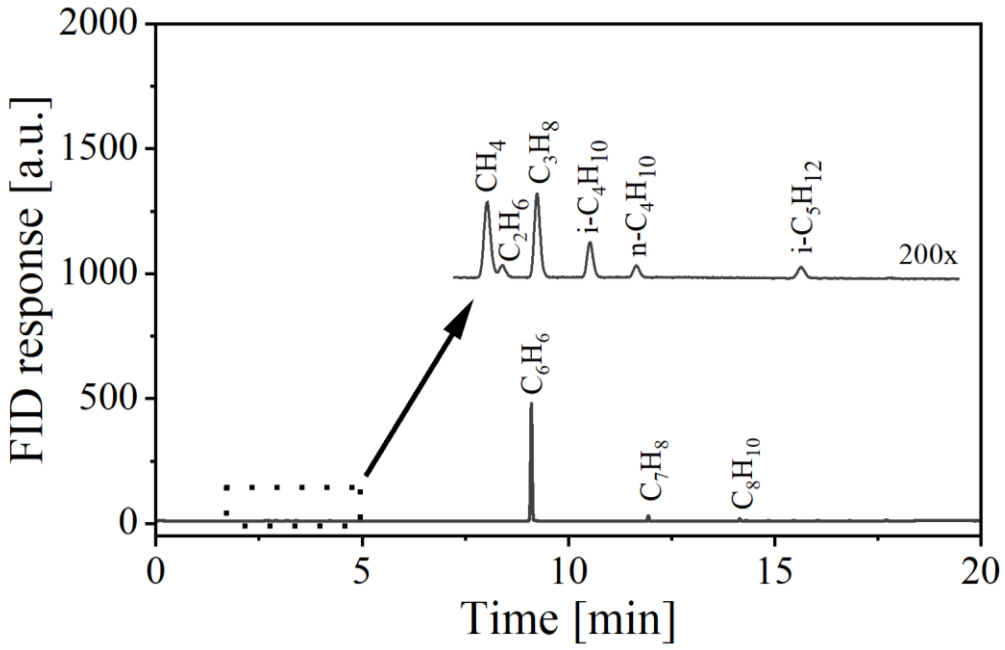

Figure S38| Chromatogram of CO_2 + H_2 control experiment in the absence of the RhIn/MgO_x catalyst in the presence of 200 mg benzene. The region associated with gas products are enlarged and labelled. The prefix *i*- and *n*- indicate linear and branched hydrocarbons respectively. Note that the signal is increased by a factor 200 to reveal the trace amounts of gas products.

APPENDIX: CHAPTER 5

Table S2| All trace liquid products retrieved after CO_2 hydrogenation as identified by GC-MS. The products are listed in the order at which they appear during analysis and are grouped by their carbon number.

Carbon number	Product
6	Benzene
7	toluene
8	1,3-dimethylbenzene
	1,4-dimethylbenzene
	1,2-dimethylbenzene
9	1-ethyl-2-methyl-benzene
	propyl benzene
	1-ethyl-methylbenzene
	1,2,3-trimethylbenzene
	mesitylene
	1,3,5-trimethylbenzene
10	1,4-diethylbenzene
	n-butylbenzene
	1,2,4,5-tetramethylbenzene